

## ABSTRACT

In this thesis, an integrated monitoring device for use on 11 kV overhead lines has been developed. Uniquely, the devices use an optimised form of Power Line Communication to enable a low latency communication network. It is shown that such a network is able to facilitate new and improved applications and offer tangible benefits to the network operator. One such application is fault location. It is shown that a strategic placement of the monitoring devices allows the implementation of a highly accurate fault location scheme, even on branched networks. Underpinning the system concept is the low latency communication scheme. To guarantee robust, error-free communication, it has been shown that “off the shelf” chips are not appropriate and modifications need to be made to existing modulation schemes to cope with the severe channel impairments on the HV network. A modulator/demodulator has been designed and developed, and a bespoke multiplexing scheme ensures that a message can be received from each device in a large network in a short period of time. Crucially, this period of time does not exceed the protection time of the distribution network, so information about the fault can be proliferated faster than the time it takes for the network’s protection scheme to operate. Prototype devices have been built and it is demonstrated that these devices can implement an extremely low latency communication scheme. A GPS timing module and highly optimised digital logic is able to rapidly timestamp the arrival time of high frequency fault induced transients and, subsequently, prepare and send a communication symbol bearing the timestamp information. The ability of the system to use, process and communicate information extremely quickly could, it is argued, have far reaching applications smart grids of the future.

An Integrated Monitoring and Communication Device for  
use on 11 kV Overhead Lines

by

Stephen Robson

Dissertation submitted to Cardiff School of Engineering  
Cardiff University, in partial fulfillment  
of the requirements for the degree of  
Doctor of Philosophy  
2012

Advisory Committee:  
Professor Manu Haddad, First Supervisor  
Dr. Huw Griffiths, Second Supervisor

## Acknowledgments

I would like to first express my appreciation to Prof. Manu Haddad and Dr. Huw Griffiths for continued help and guidance and for having the vision to conceive the principles underpinning this project. Without them, this thesis would not have been possible.

To the academics and engineers of the Power Networks Research Academy for funding the project and generally taking steps to ensure that the challenges of today are the achievements of tomorrow.

I would also like to thank Gaurab Mitra of UK Power Networks for offering helpful practical advice throughout the project and for arranging several invaluable placements within the company.

# Table of Contents

List of Figures	vii
List of Abbreviations	xi
Bibliography	xii
1 Introduction	1
1.1 The OHMS Concept . . . . .	1
1.2 Contributions in the Thesis . . . . .	5
1.3 Thesis Structure . . . . .	7
2 Power Line Communication and Fault Location: A Review	8
2.1 Monitoring of Distribution Networks . . . . .	8
2.2 Power Line Communication . . . . .	12
2.3 Fault Location . . . . .	14
2.4 Exploitation of Electronic Hardware in Remote Monitoring . . . . .	18
2.5 Summary . . . . .	19
3 Communication Aspects in Overhead Lines and its Application to 11 kV Networks	21
3.1 Introduction . . . . .	21
3.2 Key Factors of Communication of Information . . . . .	22
3.3 Modelling of Propagation Modes on Overhead Lines . . . . .	25
3.4 Development of a Representative Model for a Rural 11 kV Network . . . . .	30
3.5 Determination of Channel Characteristics for 11 kV Networks . . . . .	36
3.5.1 Additive White Gaussian Noise . . . . .	37
3.5.2 Channel Impulse Response and Delay Spread on the HV PLC Channel . . . . .	38
3.6 Exploitation of Orthogonal Frequency Division Multiplexing (OFDM) for the OHMS System . . . . .	46
3.6.1 Key Aspects of OFDM for the OHMS System . . . . .	46
3.6.2 Synchronisation and Timing . . . . .	55
3.6.3 Assessment of Subcarrier Spacing Effects . . . . .	58
3.7 Conclusion . . . . .	59
4 Assessment of Proposed Narrowband Power Line Communication for the OHMS System	62
4.1 Introduction . . . . .	62
4.2 Modelling of the OFDM System on the 11 kV Network and Simulation Methodology . . . . .	62
4.2.1 Development of the OFDM Modulator for the ATP Models Platform . . . . .	65

4.2.2	Simulation of the Test Network in the ATP/EMTP and Matlab Domains . . . . .	69
4.3	Effect of OFDM Parameters: Simulation Results . . . . .	70
4.3.1	Bit Error Rate Due to Symbol Timing Offsets . . . . .	70
4.3.2	Performance of Synchronisation Schemes on the Test Network	73
4.3.2.1	Shape of the Autocorrelation metric, $P(d)$ . . . . .	74
4.3.2.2	Mean and Variance of the Timing Estimator . . . . .	77
4.4	Performance of OFDM: Effect of Number of Subcarriers, Length of Cyclic Prefix and Modulation Scheme . . . . .	80
4.5	Concentration of Bit Errors . . . . .	85
4.6	Effect of Multipath on Received Signal Strength . . . . .	85
4.7	Effect of Coupling Scheme . . . . .	87
4.8	Proposed OFDM Scheme for the OHMS System . . . . .	88
4.9	Proposed OFDM Modulation Scheme . . . . .	91
4.10	Conclusion . . . . .	92
5	Application of the OHMS Concept for Fault Location on 11 kV Networks	94
5.1	Introduction . . . . .	94
5.2	Proposal for a New Multi-ended Fault Location Scheme . . . . .	94
5.2.1	Principles of Proposed Approach . . . . .	94
5.2.2	Network Parameters Required for Proposed Approach . . . . .	98
5.2.3	Detailed Aspects of the Proposed Multi-Ended Fault Location	99
5.3	Application of Proposed Method to Distribution Networks . . . . .	107
5.3.1	One Branch Network . . . . .	107
5.3.2	Multiple Branch Networks . . . . .	109
5.4	Sensitivity to Errors in Networks with the Same Line Configuration .	114
5.5	Adaptation of Method for Networks with Cable sections . . . . .	115
5.6	Improved Accuracy using Travel Times Between Installed OHMS De- vices . . . . .	118
5.6.1	Generalisation for Large Networks . . . . .	123
5.7	Optimisation of the Number of OHMS Devices for Fault Location . .	125
5.8	Timestamping of Fault Induced Transients . . . . .	127
5.9	Conclusion . . . . .	129
6	Appraisal of Proposed Modes of Operation for the OHMS Device	134
6.1	Introduction . . . . .	134
6.2	Possible Modes of Operation for the OHMS Device . . . . .	135
6.2.1	Mode 1: Transient Timestamp Only . . . . .	139
6.2.2	Mode 2: Transient Timestamp and Synchrophasor . . . . .	143
6.2.3	Mode 3: Transient Timestamp, Synchrophasor and Condition Monitoring . . . . .	144
6.3	Appraisal of Operating Mode 1 . . . . .	144
6.3.1	Proof of Concept . . . . .	144
6.3.2	Pre-fault Calculations . . . . .	145
6.3.3	Scenario 1: Fault on the main line (all overhead line network)	148

6.3.4	Scenario 2: Fault on a Sub-branch . . . . .	154
6.3.5	Scenario 3: Fault on the main line (all overhead line network), reduced number of OHMS devices . . . . .	158
6.4	Conclusion . . . . .	159
7	Hardware and Software Development . . . . .	162
7.1	Introduction . . . . .	162
7.2	Hardware Requirements of the System . . . . .	162
7.2.1	Communication Requirements . . . . .	162
7.2.2	Timestamping Requirements . . . . .	164
7.2.3	Processing Requirements . . . . .	164
7.2.4	Transducer Requirements . . . . .	164
7.3	Overview of the Design Software for System Development . . . . .	165
7.4	Elements of the OHMS Transmitter . . . . .	165
7.4.1	Overview . . . . .	165
7.4.2	Mapper . . . . .	167
7.4.3	Modulator . . . . .	168
7.4.4	Cyclic Prefix Insertion . . . . .	169
7.4.5	Quadrature Mixer and Upconverter . . . . .	174
7.4.6	GPS Timestamping Module . . . . .	174
7.4.7	Synchrophasor Module . . . . .	176
7.4.8	Packet Generation . . . . .	176
7.5	Elements of the OHMS Receiver . . . . .	177
7.5.1	Overview . . . . .	177
7.5.2	Realisation of the Timing Estimator . . . . .	178
7.5.3	FFT and Demapper . . . . .	184
7.6	Implementation of the Bluetooth Interface . . . . .	188
7.7	Development of the Software User Interface . . . . .	189
7.8	Selection and Implementation of Coupling Device . . . . .	191
7.9	External Circuitry . . . . .	191
7.9.1	ADC/DAC Card . . . . .	191
7.9.2	Protective Circuitry . . . . .	192
7.9.3	GPS Module Circuitry . . . . .	192
7.9.4	Power Amplifier . . . . .	192
7.10	Timing Performance of the OHMS Elements . . . . .	196
7.11	Development of a Prototype . . . . .	196
7.12	Conclusion . . . . .	198
8	Field Trials and System Testing . . . . .	201
8.1	Overview . . . . .	201
8.2	Laboratory Based Testing of the OHMS concept . . . . .	202
8.2.1	An FPGA Based Transient Generator and Network Model for Testing Purposes . . . . .	202
8.2.2	Overview of the Experimental Setup . . . . .	203
8.2.3	Demonstration of OHMS Symbol Generation . . . . .	205

8.2.4	Demonstration of the Timestamping Module . . . . .	206
8.2.5	Performance of the OHMS Concept with Direct Connections .	208
8.2.6	Full concept verification using the FPGA based network model	210
8.2.7	Partial Demonstration of the OHMS Concept: Sending a Location and Displaying it in the OHMS HMI . . . . .	211
8.3	Field Based Tests on 11 kV Lines . . . . .	213
8.4	Conclusion . . . . .	213
9	General Conclusion and Future Work	215
9.1	Discussion and Future Work . . . . .	215
9.2	Conclusion . . . . .	219
A	Code Listings	221
B	Resource Usage	255
C	Contents of the Accompanying CD	259
	Bibliography	260

## List of Figures

1.1	Overview of the OHMS concept . . . . .	3
1.2	High level block diagram of the OHMS concept . . . . .	4
2.1	Example of three synchrophasor measurements. Retrieval of the phasors from all measurements can give a network wide snapshot of network conditions and a continuous feed of this information shows dynamic changes in these conditions . . . . .	10
3.1	A 3-phase distribution line . . . . .	25
3.2	Diagrammatic representation of the current direction in the ground mode (a), and the two aerial modes (b) and (c). . . . .	28
3.3	Visualisation of the natural modes in a three conductor system . . . . .	28
3.4	Comparison of attenuation experienced on an infinite (reflection free) distribution line (geometry shown in Table 3.1) by signals in Mode 1 (ground mode) and the aerial modes (modes 2 and 3) at a frequency of 400 kHz . . . . .	29
3.5	11 kV line of wood pole construction showing the conductor height, $h$ , and the conductor spacing, $d$ . . . . .	33
3.6	The example network . . . . .	35
3.7	Diagram showing a typical impulse response and RMS delay spread . . . . .	39
3.8	Diagram showing Intersymbol Interference (ISI). The dashed line represents the delayed (reflected) parts of the incident signal . . . . .	39
3.9	Method to Obtain Frequency Response, $H(f)$ from the Impulse Response, $h(t)$ . . . . .	42
3.10	Phase response of a reflection-free channel . . . . .	45
3.11	Phase responses between 0 and 2 MHz for communication between selected nodes on the test network. . . . .	47
3.12	Magnitude responses (up to 2 MHz) between selected nodes on the test network (Ground Mode) . . . . .	48
3.13	Magnitude responses (up to 2 MHz) between selected nodes on the test network (Mode 2) . . . . .	49
3.14	Functional OFDM System: Transmitter . . . . .	51
3.15	Functional OFDM System: Receiver . . . . .	52
3.16	Diagram showing cyclic prefix inserion and the useful part of the OFDM symbol . . . . .	52
3.17	Transmitted Constellation Points . . . . .	54
3.18	FFT sampling period: Optimum timing and early timing . . . . .	56
3.19	Proportion of relative phase rotations between neighbouring points exceeding the decision boundary in a frequency range between 200 kHz and 800 kHz for DBPSK, DQPSK and D8PSK. The solid line represents the mean values for all channel responses between nodes A to E and dashed lines represent one standard deviation. The decision bounday is $\pm \pi/8$ , $\pm \pi/4$ and $\pm \pi/2$ for D8PSK, DQPSK and DBPSK respectively. . . . .	60

4.1	Block diagram showing the simulation methodology . . . . .	64
4.2	Fortran code for the IDFT part of the OFDM modulator. . . . .	66
4.3	Fortran code to perform the cyclic prefix insertion. . . . .	66
4.5	Diagrammatic Representation of Network Flow in the OFDM Transmitter Model . . . . .	68
4.4	Fortran code showing a 4 <sup>th</sup> order low pass digital reconstruction filter and the quadrature mixer (see Appendix A.6 for full Fortran code). . . . .	68
4.6	BER due to symbol timing offset in the DBPSK system . . . . .	71
4.7	BER due to symbol timing offset in the DQPSK system . . . . .	72
4.8	BER due to symbol timing offset in the D8PSK system . . . . .	72
4.9	$P(d)^2$ and $P_f(d)^2$ for communication between selected nodes. . . . .	75
4.10	$P(d)$ at different SNR values with various symbol timing offsets . . . . .	76
4.11	Timing Estimator Mean and Variance for communication between nodes A,B and C and all other nodes. . . . .	78
4.12	Timing Estimator Mean and Variance for communication between nodes A,B and C and all other nodes. . . . .	79
4.13	Timing metric and associated histograms from 1000 simulation runs at an SNR of 10 dB . . . . .	81
4.14	Scatter diagram showing average BER versus maximum permissible data rate for the schemes outlined in Table 4.2. . . . .	83
4.15	Scatter diagram showing BER versus OHMS symbol duration rate for the schemes outlined in Table 4.2. . . . .	84
4.16	Bit Error Rate by subcarrier using a system with centre frequency 460 kHz and a bandwidth of 166.7 kHz . . . . .	86
4.17	Attenuation between nodes on the Test Network . . . . .	87
4.18	Configuration of possible coupling schemes on a three conductor line . . . . .	89
4.19	Voltage phasors induced into the modes for different coupling schemes . . . . .	90
5.1	Induced modal components for different fault scenarios . . . . .	98
5.2	Representation of the a discretised one branch network with $p$ points and a branch, $X$ , originating at point $n = b_x$ . . . . .	99
5.3	Example Network . . . . .	105
5.4	Procedure for finding the location of a fault using the multi-ended method . . . . .	106
5.5	ATP/EMTP representation of one branch network, including high pass filter and modal transform models ( $F_i=130$ ). . . . .	108
5.6	R-ratios plotted as a function of position index for one branch network . . . . .	110
5.7	W metric for one branch network . . . . .	111
5.8	R-ratios plotted as a function of position index for two branch network . . . . .	112
5.9	W metric for two branch network . . . . .	113
5.10	Sensitivity analysis in the one branch and two branch network . . . . .	116
5.11	Elements of the Matrix <b>D</b> . . . . .	125
5.12	Hypothetical network with OHMS devices at positions $A, B, C, D$ and $E$ and four possible fault positions labelled $FP1, FP2, FP3$ and $FP4$ . . . . .	127

5.13	Generation of transients in Matlab for testing the peak detector algorithm (all magnitudes are normalised to 1, $F_s=50$ MHz)	130
5.14	Peak detect algorithm with sampling frequency, $F_s$	131
5.15	Example waveforms from Matlab simulation of a Gaussian pulse with rise time of 4 $\mu$ s and a sampling frequency, $F_s$ , of 50 MHz. The SNR of the transient is 10 dB.	132
6.1	Diagrammatic representation of the proposed multiplexing scheme	136
6.2	Number of OHMS Transmitters versus $T_{tot}$	138
6.3	Decision diagram to implement scheme 1: timestamp only	142
6.4	Test network showing positions of the OHMS devices	146
6.5	W metric from the multi-ended method for the fault at position index 166.	150
6.6	Histograms derived from 10,000 simulation runs at differing values of standard deviation, $\sigma$ , of the imposed error on each of the 15 OHMS devices involved in the multi-ended fault location method for the fault at position index 166.	151
6.7	Histograms derived from 10,000 simulation runs at differing values of standard deviation, $\sigma$ , of the imposed error on each of the 15 OHMS devices involved in the multi-ended fault location method for the fault at position index 166.	152
6.8	Plots to show effect of a large individual error on the resultant $W(n)$ (all 15 OHMS devices involved in the method).	154
6.9	W metric from the multi-ended method for the fault at position index 642.	155
6.10	Histograms derived from 10,000 simulation runs at differing values of standard deviation, $\sigma$ , of the imposed error on each of the 15 OHMS devices involved in the multi-ended fault location method for the fault at position index 642.	156
6.11	Histograms derived from 10,000 simulation runs at differing values of standard deviation, $\sigma$ , of the imposed error on each of the 15 OHMS devices involved in the multi-ended fault location method for the fault at position index 642.	157
6.12	W metric for fault at position index 166 for a reduced number of OHMS devices.	160
7.1	High level block diagram of the OHMS transmitter	166
7.2	Block Diagram showing the design of the OHMS Modulator	170
7.3	Selected waveforms of the simulated IFFT core	170
7.4	Selected waveforms of the simulated Cyclic Prefix module	172
7.5	Quartus Block Diagram of the Cyclic Prefix Insertion Design. Code for the cyclic prefix block is shown in Appendix C.1	173
7.6	Selected waveforms of the Quadrature Mixer Module	175
7.7	High level block diagram of the OHMS receiver	177
7.8	Computation of $r_{d+N}^* r_{d+2N}$	179

7.9	Recursive Implementation of the Moving Sum . . . . .	179
7.10	Quartus Block Diagram of the Moving Sum Part of the Timing Estimator . . . . .	180
7.11	Overview of the method used to determine start time of FFT in the OFDM demodulator . . . . .	182
7.12	Selected waveforms to show functionality of the Find Max logic and generation of the start packet flag . . . . .	183
7.13	Block diagram of the CORDIC and Demapper process . . . . .	187
7.14	Selected waveforms to show functionality of the CORDIC and demapper processes . . . . .	187
7.15	Example Screenshot of the OHMS HMI Design . . . . .	190
7.16	Coupling Capacitor . . . . .	191
7.17	GPS Timestamping module PCB including the M12M Timing Receiver and the RS-232 interface to to the FPGA . . . . .	193
7.18	Biasing circuitry for the OPA564 Operational Amplifier. $S_1, S_2=1N4757$ Zener diode. . . . .	194
7.19	The OPA564 and biasing circuitry PCB board including 24V supply, input/output sma connectors and wires leading to “on/off” switch for external mounting . . . . .	195
7.20	Timing analysis from transient detection to communication symbol transmission . . . . .	197
7.21	OHMS Transmitter prototype . . . . .	199
8.1	Experimental setup possibilities . . . . .	204
8.2	OHMS Transmitter message burst: Synchronisation symbol followed by an information symbol (real part, with one subcarrier switched on)	206
8.3	Zoomed view of the real part of the synchronisation symbol, showing repetition in the time domain . . . . .	207
8.4	Screenshot of HMI plotting the fractional second of the received timestamp . . . . .	208
8.5	Experimental setup with OHMS devices directly connected . . . . .	209
8.6	OHMS HMI output in the bit errors experiment . . . . .	210
8.7	Performance on the real time test network with a varying cyclic prefix (166.7 KHz bandwidth system) . . . . .	211
8.8	Screenshot of the HMI set to detect and display the GPS co-ordinates in the received symbol . . . . .	212
A.1	Resources used in the OHMS Receiver FPGA . . . . .	254
B.1	Resources used in the OHMS Transmitter FPGA . . . . .	256
B.2	Resources used in the OHMS Receiver FPGA . . . . .	257
B.3	Illustrative cost breakdown of the OHMS Transmitter and Receiver .	258

## List of Abbreviations

$\alpha$	alpha
$\beta$	beta
$B_c$	50% Coherence Bandwidth
$f_c$	Carrier Frequency
$f_s$	Sampling Frequency
$\gamma$	Propagation Constant
$[\Lambda]$	Voltage Propagation Matrix
$[T_v]$	Voltage Transformation Matrix
$[T_i]$	Current Transformation Matrix
$\Phi_e$	Phase Error
k	Number of Subcarriers
$\sigma_t$	RMS Delay Spread
ASIC	Application Specific Integrated Circuit
ATP	Alternative Transients Program
AWGN	Additive White Gaussian Noise
BER	Bit Error Rate
BPL	Broadband Over Power Line
CP	Cyclic Prefix
DLC	Distribution Line Carrier
DFT	Discrete Fourier Transform
DNO	Distribution Network Operator
DPSK	Differential Phase Shift Keying
EMTP	Electromagnetic Transients Program
FFT	Fast Fourier Transform
FPGA	Field Programmable Gate Array
GPS	Global Positioning Satellite
HMI	Human Machine Interface
ICI	Intercarrier Interference
ISI	Intersymbol Interference
LPF	Low Pass Filter
MV	Medium Voltage
NPLC	Narrowband Power Line Communication
PCB	Printed Circuit Board
PLC	Power Line Communication
PSK	Phase Shift Keying
OFDM	Orthogonal Frequency Division Multiplexing
OHMS	Overhead Line Monitoring System
QAM	Quadrature Amplitude Modulation
RMS	Root Mean Squared
SNR	Signal to Noise Ratio
TDR	Time Domain Reflectometry

## List of Publications

### References

- [1] S. Robson, A. Haddad, and H. Griffiths, “Simulation of narrowband power line communication using atp-empt,” in *North American Power Symposium (NAPS), 2009*, pp. 1 –6, Oct. 2009.
- [2] S. Robson, H. Griffiths, and A. Haddad, “Narrowband power line communications: Channel characteristics and modulation,” in *Universities Power Engineering Conference (UPEC), 2010 45th International*, pp. 1 –6, 31 2010-Sept. 3 2010.
- [3] S. Robson, A. Haddad, and H. Griffiths, “Simulation of power line communication using atp-empt and matlab,” in *Innovative Smart Grid Technologies Conference Europe (ISGT Europe), 2010 IEEE PES*, pp. 1 –8, Oct. 2010.
- [4] S. Robson, A. Haddad, and H. Griffiths, “Fault location on branches networks using a multi-ended approach,” *Power Delivery, IEEE Transactions on*, [Submitted]
- [5] S. Robson, A. Haddad, and H. Griffiths, “An overhead line monitoring system for rural distribution networks,” *Power Delivery, IEEE Transactions on*, [Final Revision]
- [6] S. Robson, A. Haddad, and H. Griffiths, “Communication between remote nodes on distribution networks,” *Power Line Communications, IEEE International Symposium on*, [Final Revision]

# Chapter 1

## Introduction

### 1.1 The OHMS Concept

In the coming decades, it is widely accepted that electricity distribution networks will be subject to significant changes. These changes will be driven primarily by the requirement of networks to adapt to developments in the way electricity is generated and consumed. The idea of totally centralised electricity generation and a passive grid is set to make way for an “active” grid that facilitate more efficient operation and the enabling of an ever increasing uptake of embedded generation. Key to this transition is way information is gathered, disseminated and used.

This thesis is based on the development of an integrated monitoring system for use on rural 11 kV networks. What sets this system apart, however, is its ability to gather, process and exchange information. If a system, for example, has the ability to gather information (e.g. with voltage or current transducers), use information (e.g. through the use of onboard computational ability) and disseminate this information (through a communication system), a myriad of new possibilities emerge. In fact, it will be shown that by exploiting modern electronics, the speed at which the system operates (gathering, using and disseminating) is less than the time it takes for a typical network’s protection scheme to operate. It will be shown that this ability enables a new fault location technique that is effective on branched networks.

The concept of using a number of integrated overhead line monitoring systems with the ability to communicate with each other is known as the OHMS system<sup>1</sup>. The devices making up the OHMS system are known as OHMS devices. A summary of the aims of this thesis are set out below:

- Implementaton of an improved fault location scheme
- Remote monitoring of voltage, current and condition monitoring of plant
- Development of a cost effective communication link between remote nodes and the primary substation, or an access point to the DNO's main communication infrastructure.

To achieve these aims, each OHMS device is to integrate GPS capability (or a proven means of achieving accurate timing) and a highly optimised communication system to transfer the collected information. It should be noted that the vulnerabilities of GPS, especially in critical applications, are well known so suitable backup mechanisms should be sought as a fail safe in case of GPS signal failure [1]. Nevertheless, GPS is a very widely used technology and provides a very capable means of distributing a synchronised clock source in large networks. For a distributuon network, this is shown diagrammatically in Fig. 1.1.

There are many potential applications in the OHMS concept and they are usually thought of as separate, however, significant similarities exist in the implementation of these functions. Sensor information, for example, can be shared between several parallel processes occuring simultaneously on the same chip. Furthermore,

---

<sup>1</sup>OHMS is an acronym of OverHead line Monitoring System.

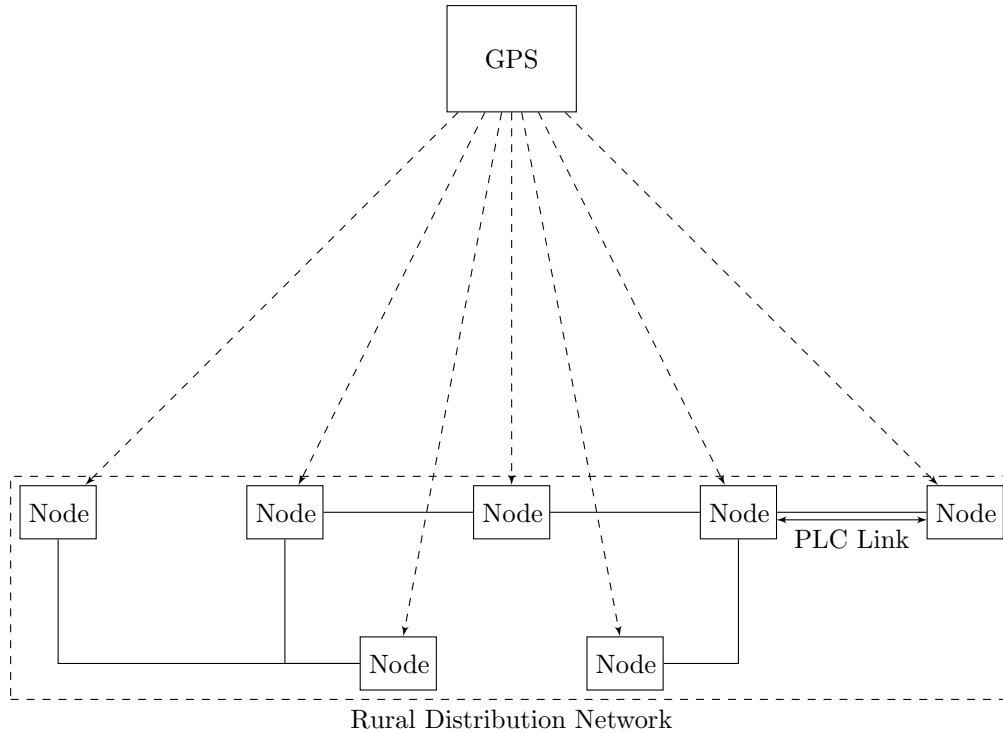


Figure 1.1: Overview of the OHMS concept

there is potential for hardware re-use for digital circuits implementing certain processing functions (e.g., the FFT). The implementation of a dedicated communication channel between each of the OHMS devices also opens up a new range of possibilities in terms of automation options or local monitoring of network conditions independent of the control room. Bandwidth requirements may be significantly reduced if each device can intelligently process and use information in a closed loop. Many of the synergies between functions arise because the basic processing requirements and analysis methods are similar. For example:

- Synergies between digital modulation techniques and wide area monitoring, for example, can the synchronisation schemes used to signal the arrival time of a

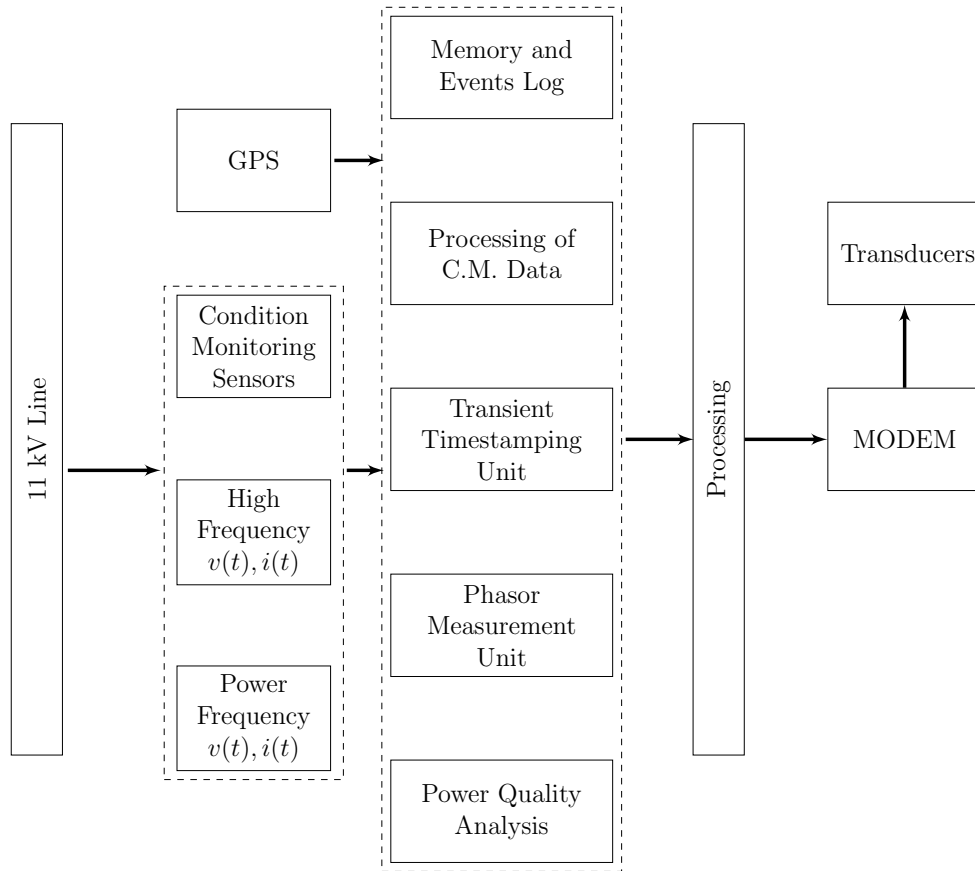


Figure 1.2: High level block diagram of the OHMS concept

symbol also be used to "share" a single GPS clock between many neighbouring nodes? (for example, using the IEEE 1588 standard [2]).

- Is it possible to use channel estimation information, routinely used in OFDM, to monitor changes in network conditions (e.g. a fault condition)?

Fig. 1.2 shows a block diagram of the conceptual OHMS device. It is observed that many different tasks can run in parallel but may share the same sensory information.

The idea of incorporating a large number of sensor equipped nodes on rural

networks coupled with their communication capability opens up new possibilities that have the potential to offer tangible benefits, especially in large rural networks where “observability” is extremely low. The duplication of equipment inherent in a multi-node monitoring system means that cost is likely to be an issue, so it is important to be mindful that a comparison between likely benefits and potential cost must always weigh in favour of the former.

## 1.2 Contributions in the Thesis

To implement the OHMS concept, research was carried out in several key areas. Firstly, communication was recognised as a fundamental barrier to the OHMS concept, and to smart grids in general. The key problem was the lack of an existing technology that could offer an ultra-low latency<sup>2</sup> direct link between remote nodes on a network. Wireless techniques, for instance the Short Message Service (SMS) defined in the GSM, have extremely high latency (in the order of seconds) [3]. Existing Power Line Communication (PLC) techniques, e.g. Broadband over Power Line (BPL) also have an extremely high latency but also suffer from the problem of requiring frequent repeaters. To resolve the problem, a highly optimised communication scheme was developed. The scheme, based on a narrowband version of PLC, is shown to offer a low latency, direct link between remote nodes and, importantly, does not require repeaters. The OHMS concept, as will be shown, is well suited to operation in the high kHz, low MHz frequency range. A comparison of the OHMS

---

<sup>2</sup>Latency is defined here as the time taken for information to be transmitted from one point to another point.

Table 1.1: Existing PLC frequency bands and proposed OHMS frequency band

Band	Frequency Range	Use
No Band	3-9 kHz	Reserved for utilities
CENELEC A	9-95 kHz	Energy suppliers
CENELEC B	95-125 kHz	Consumer use
CENELEC C	125-140 kHz	Consumer use
CENELEC D	140-148.5 kHz	Consumer use
BPL Frequencies	2-30 MHz	Broadband over Power Line
OHMS Frequencies	0.5-2 MHz	Proposed OHMS bandwidth

frequency range and some existing PLC bands are shown in Table 1.1.

Another contribution in this thesis is the development of a novel fault location scheme based on the travelling wave method. The technique is shown to provide extremely accurate fault location, even on highly branched networks. The effectiveness of the method is demonstrated using a simulation model of a “typical” rural distribution network.

The OHMS concept is embodied in a pair of prototype devices that demonstrate, under lab conditions, the effectiveness of the OHMS concept. The implementation of the OHMS concept is reliant on the use of Field Programmable Gate Array (FPGA) chips, offering very fast clock rates and high degrees of parallelism. The logic within the FPGA has been carefully engineered to offer extremely fast response times. For example, the device has been designed to create and send an information burst containing relevant information just a few  $\mu\text{s}$  after a fault induced transient has been detected. The success of the laboratory based trials, where communication between the prototype systems and effectiveness of the timestamping module has been verified has prompted the organisation of a field trial on a part of

the UK Power Networks 11 kV network in a rural part of Hertfordshire, England. Final preparations are being made for a full system test to be carried out on this network.

### 1.3 Thesis Structure

In Chapter 2, a literature review is carried on topics relevant to OHMS concept, including fault location, monitoring on distribution networks and power line communication. In Chapter 3, key concepts in communications are investigated and a test network is proposed in order to effectively model the OHMS system. The Chapter concludes by arguing that Orthogonal Frequency Division Multiplexing (OFDM) is the most suitable communication scheme to enable the OHMS system. In Chapter 4, OFDM is simulated on the test network and a recommendation is made for the specifics of a communication scheme for the OHMS system. In Chapter 5, a new multi-ended fault location algorithm is proposed based on the retrieval of high frequency fault induced transients. In Chapter 6, the specific aspects of the OHMS system are formalised and appraised through simulation and theoretical examination. It is demonstrated that the new multi-ended fault location algorithm is capable of locating faults on branched networks. In Chapter 7, hardware and software is developed to meet the requirements stipulated in the preceding analyses. This hardware and software is trialed in Chapter 8 before the thesis draws to a conclusion in Chapter 9.

## Chapter 2

### Power Line Communication and Fault Location: A Review

#### 2.1 Monitoring of Distribution Networks

The monitoring of distribution networks is an activity regarded by network owners as an important means of managing ageing assets and delivering power in an efficient manner. There are many ways in which networks can be monitored, ranging from the condition monitoring of individual assets, to the holistic monitoring of an entire grid using sophisticated methods and specialist software.

Post privatisation, there has been a shift in the way electricity companies manage and operate grids. The philosophy of “fit and forget” has made way for a more pro-active approach that places more emphasis on active management, optimisation and control of network assets.

A growing theme in condition monitoring is the detection and characterisation of high frequency transients within the line itself or airborne in the form of electromagnetic waves or sound vibrations. These methods take advantage of “tell-tale” signals emitted in the physical process of an event. A classic example of this is the detection of Partial Discharge (PD). In [4] [5] a non-intrusive method based on the detection of Ultra High Frequency (UHF) energy symptomatic of PD in power transformers has been shown to be effective. One significant advantage of this type of method is the ability to not only detect the presence of an event, but also to

pinpoint its location. This is normally achieved by measuring the arrival time of a signal at multiple locations in a network of strategically placed sensors connected to some form of synchronised clock. The emergence of the Global Positioning Satellite (GPS) system has increased the feasibility of these methods over large geographical areas. A useful example of this is in the location of lightning strikes based on the arrival time of a characteristic burst of radiation generated in the return stroke [6]. The system has been successfully utilised by both the UK MET office and National Grid. Ultimately, the emergence of clock synchronised measurements has led to the development of wide-area monitoring techniques, increasing the possibilities in terms of the scale and applicability of gathered information from Phasor Measurement Units (PMUs) [7] [8].

In network operations, one of the most promising technologies to emerge in recent years has been that of the synchrophasor. Synchrophasors facilitate the simultaneous measurement of voltage and current phasors on a network scale (Fig. 2.1). The addition of a communication link between each synchrophasor device and the network operator's control room provides a snapshot of all phasors at a particular moment in time, leading to significant improvement in power quality control, load shedding schemes and demand response actions.

The predominant experience of synchrophasor schemes in operational duties have been for post event monitoring, owing much to the high cost and complexity of communicating the acquired synchrophasors to a central location in a timescale that made possible a fast response to the measured data. Recently, implementations of synchrophasors with telemetry capability have emerged, mostly in WAM trial

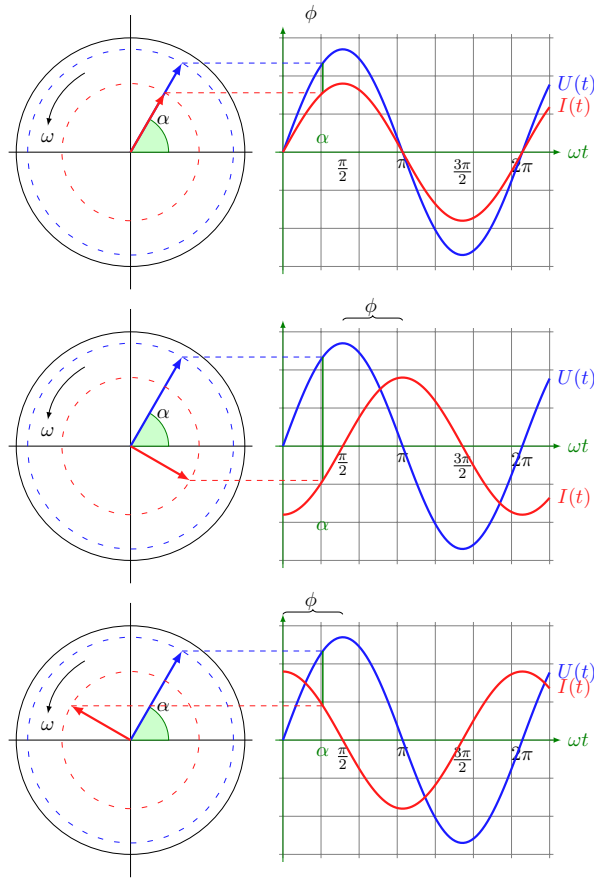


Figure 2.1: Example of three synchrophasor measurements. Retrieval of the phasors from all measurements can give a network wide snapshot of network conditions and a continuous feed of this information shows dynamic changes in these conditions .

schemes on transmission networks. For distribution networks, the challenges are more severe. The geographically sprawling nature of the network combined with lack of access to conventional communication infrastructure (at least downstream of the 33/11 kV substation) makes any attempt at implementing a WAM scheme extremely expensive. A major technological hurdle is the difficulty in providing a dedicated communication channel between the network operator's SCADA system and the remote PMUs. A second problem is the vast duplication in cost necessary to provide a density of PMU coverage deemed useful to the network operator. Overcoming

these problems could pave the way to an economically justifiable implementation of, and the associated benefits of WAM in distribution networks.

In transmission networks, i.e. those operating at 400 kV and 275 kV in the UK, there is a high degree of condition monitoring of major plant (e.g. transformers, busbars, capacitor banks etc.). The substations in these networks are hubs in a large communication network with high bandwidth connections provided by fibre optics. The SCADA system [9] standardises the process of acquiring and retrieving information over large networks and utilities have made significant investments in an effort to improve the way condition monitoring information is gathered, processed and stored. New standards, for example IEC61850 [10], aim to further leverage new innovations in communication and monitoring technology. Although modern standards can improve interoperability in conventional wired networks, the situation in large, rural type sensor networks is still to take form. These types of networks are common in High Voltage distribution systems where the task of achieving any meaningful wide area monitoring information without access to the main communication infrastructure seems daunting. The obvious solution is wireless. In [11], a large scale General Packet Radio Services (GPRS) based telecontrol network was implemented, with 1000 remote switches interfaced to the existing SCADA system of the DNO. Another notable attempt at providing a solution to retrieving monitoring information include the "Power Donut", an integrated current and temperature measurement device with wireless capability [12]. Other attempts at providing a suitable communication link have emphasised the weaknesses in "standardised" wireless protocols in achieving both the required latency and throughput to support

the sensor networks envisaged in future smart grids [13].

## 2.2 Power Line Communication

Later in the thesis, Power Line Communication will be presented as a viable method to implement a low latency, dedicated communication link between remote nodes in a rural distribution network. First, the historical role of PLC in protection schemes on distribution networks will be explained.

The first implementations of PLC in network operation applications was in the 1940s, but PLC itself was well known and widely used in telephony as far back as the 1920s<sup>1</sup> [14] [15]. The first primitive PLC setup used by DNOs actually performed an important task and built up a reputation within the industry of being a robust, reliable method of communicating low latency, low bandwidth packets of data [16]. In the earliest implementations, the information transferred by the PLC link was one-way switching signals to remote relays [17]. In the 1950s and 1960s, PLC implementations increased in sophistication and quickly became a standard method of providing the intertrip signal to the remote end in distance protection schemes [18]. These systems used an arrangement of line traps and tuners operating in narrow frequency bands with the capability to send very low throughput information; usually just an “on” or “off” signal. Nevertheless, the low-latency and high reliability of the system secured it longevity, with such schemes still in use to the present day.

---

<sup>1</sup>It could be argued that PLC has existed for as long as power lines themselves have existed. The “information” carried by the power line is whether or not a generator is connected at the other end

The onset of the “digital revolution” in the 1980s and the development of new modulation techniques paved the way for the introduction of Broadband over Power Line (BPL), a way of sending high bandwidth digitally modulated signals over the power line without the need for the bulky and expensive line traps of the previous systems. Its ability to supply broadband connections to rural areas is the main reason BPL received so much attention from the research community in recent years [19] [20]. However, if an analysis was to be made regarding why BPL has not been widely deployed, the reason would probably be cost. BPL requires repeaters every mile or so to amplify and re-transmit the signal. In fact, BPL’s greatest strength is also its greatest weakness; high data throughput from high bandwidth necessitates the use of relatively high frequency carrier waves (up to 30 MHz). At these frequencies, the skin depth of the conductor is extremely small, leading to very high attenuation. The repeaters needed to continuously compensate for the attenuation of the signals add a duplication of cost that weakens the business model of internet provision via BPL. Recently, there has been a trend towards using BPL to implement smart grid solutions in distribution networks [21]. Initial trials seem promising but highlight another major weakness of BPL; high latency.

A trade off between the high attenuation of BPL and the low bandwidth of Power Line Carrier is possible if the bandwidth is restricted to less than about 500 kHz and the carrier frequency is also kept as low as possible. These PLC MODEMS are often described as Narrowband PLC (NPLC). The crucial advantage of NPLC over BPL (at least for monitoring applications) is that NPLC has an extremely low latency, and equipped with a general purpose MODEM and free from the burdens of

the delays caused by standard protocols, a designer may be naive enough to envisage a network of remote nodes connected via a direct, dedicated communication link. There have, in fact, been a number of high profile commercial projects aimed at developing NPLC chipsets. In [22], a chipset was created specifically for the sub-500 kHz channel in distribution networks, but results on their trials indicated the difficulty in establishing reliable communication links. The OFDM based chipsets were shown to be capable of data rates up to 576 kbps but do not facilitate a burst-like transmission mode where several radios can be multiplexed. More recently, NPLC implementations have been based on Internet Protocol (IP) based solutions. In [23], a system designed to recover smart metering information is described. Interestingly, the system also enables the transmission of real time video over the PLC network. The packet based IP solution, however, increases the latency beyond what would be acceptable in the OHMS system.

Later on in this thesis, a highly optimised form of NPLC will be shown to provide such a link combined with a reasonable bandwidth and no requirement for repeaters.

### 2.3 Fault Location

The aim of fault location is to locate, as accurately as possible, the location of the part of the network responsible for the fault itself. The primary motivation for implementing a fault location method is to expedite the restoration of the line back to normal operating conditions. Another reason is to provide the network

operator better information as to what manual adjustments should be made to the operating configuration of the network to minimise CMLs and CIs and maintain public safety. The introduction of performance incentives in the last few decades has focused DNOs interest on achieving better fault location and the research output in this field has increased significantly during this time.

There are currently 3 major categories of fault location methods:

- Impedance based methods
- Travelling wave methods
- “Knowledge” based methods.

Impedance based methods rely on the measurement of the fundamental frequency component of voltage and current post fault and/or pre fault. The idea had its beginning with distance protection schemes that attempt to differentiate between faults in a nearby zone, and faults further away [24]. Early efforts concentrated on what was possible with information from only the distance relay at the immediate terminal. Takagi’s approach [25] was one of the first formalised methods for pinpointing the location of a fault in this way, and provided a crude approximation of the fault location. Improvements on Takagi’s benchmark were quick to follow with the advent of two-terminal approaches, requiring voltage and current measurements from both ends of a faulted line [26]. Today, impedance based methods are still widely used but inherent weaknesses limit the accuracy to approximately 1% of the line length (under ideal conditions) [27]. Although some effort has been made to

apply impedance based methods on branched networks [28], it is extremely problematic to apply the techniques to anything other than point to point transmission line type networks.

Travelling wave methods ignore the fundamental frequency component and instead use either the travelling wave initiated by the fault disturbance or the reflection characteristics of an artificially generated wave [29], [30]. This, again, can be done either from one of the terminals or, with increased accuracy, from two terminals of a point to point line. The use of the high-frequency fault-generated component has received a good deal of attention because it can provide a fault estimate that is insensitive to fault inception angle, fault type, fault resistance and system parameters [31]. Single-ended methods are popular because, unlike two-ended methods, they do not require any form of synchronisation (e.g. GPS) or a communication link. It is customary to classify single ended methods as either Type A or Type C. A Type A system estimates the location of the fault by measuring the time it takes for the fault-generated wave to travel from the busbar to the fault and back again. Type C systems introduce a pulse into the line and locates the fault based on the time of the reflection. The major problem with single ended methods, even in point to point lines, is that the fault induced travelling wave is easily lost or obscured by the presence of other disturbances or reflections not related to the fault [32]. The problem is exacerbated as the the number of branches in the network increases. The use of the wavelet transform is a way to improve the discrimination between fault transient arrivals [33].

Multi-ended methods also go some way to alleviating the difficulties inherent

in single ended methods. A Type B method uses a synchronisation signal sent between the two ends of the line. Type D methods remove the need for this signal through the use of a synchronised clock. More recently, a new class of fault recorder has emerged based on the signal induced by the circuit breaker operation. These are known as Type E methods [34].

Many notable contributions to the advancement of fault location technology use elements of multiple methods. In [35], a device capable of operating as a Type A, B, C and D fault locator was built. Advances in both the affordability and capability of commercially available electronics has led to some to think about retrieving information from multiple locations in the network, rather than just from the ends of the main lines. Such an approach may make possible the implementation of new algorithms that perform better in radial networks. In [36], a travelling wave method based on arrival time recordings from the end of each line, and post-processing with the wavelet transform, has shown good results. An attempt has been made at using the travelling wave method, in conjunction with the wavelet transform, to locate faults on the IEEE 34-Bus network [37]. Promising results have been reported, but the error margin is still high and the operational complexity and cost of the system means the method is still unjustifiable in practice.

Knowledge based methods encompass a wide range of techniques. A common method of knowledge based fault location is the trivial task of interpreting customer information in the form of phone calls. Often, unusual network conditions are spotted and reported by the public. The sum total of customer calls can paint a picture of the likely fault location and type. Expert systems have been developed

based on key customer information, network topology and a rule base acting on a database [38] [39].

## 2.4 Exploitation of Electronic Hardware in Remote Monitoring

Field Programmable Gate Array (FPGA) technology is well suited to applications requiring speed and parallelism [40]. Unlike microprocessors and ASICs, they also have the property of configurability, easing the prototyping process. These properties can be put to good use in an integrated monitoring system. To fully realise the OHMS concept, remote computational power and speed are important factors. Also important is the ability to carry out multiple tasks simultaneously because the resources on an FPGA can be divided and separated in a way that is not possible in CPUs<sup>2</sup>. In this sense, it is possible to "react" to a stimulus (perhaps in the form of a trigger condition being set) within a few clock cycles. Furthermore, the number of, and combinations of the different stimuli that can be monitored is extremely large in an FPGA, maybe only limited by the number of pins connecting the chip. The computational power of FPGAs are boosted by the availability of extremely efficient hardware representations of digital signal processing functions such as the FFT and filtering and the combination of fast acting circuitry with efficient processing and falling costs has led to a surge in FPGA/ASIC based solutions to condition monitoring problems [41] [42].

---

<sup>2</sup>Simultaneous computational threads are possible in multiple core CPUs but come nowhere near the "parallelism" of gate array chips.

## 2.5 Summary

This chapter has provided a summary of the main research fields underpinning the OHMS concept. The monitoring of distribution networks is a rapidly evolving research area with new techniques and ideas attempting to bridge the gap between capabilities of current methods and the substantially more advanced systems required to meet the demands of future networks. There is still a lot of uncertainty about what, exactly, the grids of tomorrow will look like and the way they will be operated. What is not uncertain is the requirement for better methods of communication and new ways to use this information.

PLC is not a new concept, but advances in recent decades have transformed what it can offer in terms of real time monitoring of electricity networks. BPL is now a well established technology, but it has several weaknesses that arguably hold it back as a viable option in smart grid applications. NPLC seems more likely to fill this niche and several implementations have been deployed on distribution networks with variable success, with the main application being remote metering. The author believes that the most crucial advantage of NPLC, i.e. low latency, has yet to be fully exploited.

An extremely low latency communication link between remote nodes on large, rural networks could solve a major problem in another field of study: fault location. There are many good methods that can successfully locate a fault in simple point-to-point networks, but in branches networks, there has yet to be a convincing, practical solution for rural networks without access to communication infrastructure.

In the next chapter, the most important enabler of smart grid technologies, communication, will be discussed.

## Chapter 3

# Communication Aspects in Overhead Lines and its Application to 11 kV Networks

### 3.1 Introduction

Power Line Communication is a proven method of conveying information between two points separated by a multi-conductor power line structure. Successful PLC systems have been used for decades in protective relaying schemes, where the signal must travel for many miles [18]. More recently, BPL systems have been developed, making possible the transfer of information at several Mbps [43]. In contrast to the protective relaying schemes which use a carrier frequency in the kHz range and a narrow bandwidth, BPL uses carrier frequencies of several MHz and a bandwidth of around 30 MHz. Despite the possibility of high data rates, BPL has been fairly slow to be adopted because of the high cost of deployment.

In general, the power line (for instance the one shown in Fig. 3.1) is a very good medium for the transmission of communication signals, even at modestly high frequencies. As will be explained in this section, a number of "balanced" modes exist in multiconductor transmission lines. Crucially, the balanced nature of these modes explains why only a small portion of the total energy is radiated away from the line structure. At low frequencies, the impedance of the line is low, and PLC signals can

propagate over large distances in the balanced modes. At higher frequencies, for example those used in BPL systems, the impedance of the line increases to such a degree that the PLC signal is no longer capable of travelling long distances<sup>1</sup>. In this case, repeaters are necessary every km or so, increasing the system cost dramatically.

The strategy adopted by the OHMS system is to use a relatively low carrier frequency (less than 1 MHz) yet a bandwidth large enough to carry a meaningful stream of information. In this Chapter, the communication system of the OHMS system is to be specified by examining the properties of the channel and the behaviour of the PLC signal at the chosen frequencies. It will be shown that the requirement to communicate in branched networks complicates the design of the MODEM such that the analog modulation schemes used in the “old fashioned” PLC schemes are inadequate. Furthermore, it will be demonstrated that a highly optimised version of a modern communication method can provide an effective communication link between many remote nodes on a branched network.

### 3.2 Key Factors of Communication of Information

This section will briefly highlight some basic concepts and introduce key terminology in the field of communication theory. Communication is the conveying of information through some medium. This medium connects two devices that wish to communicate. For communication to be successful, the transmitter must find some means of encoding information into a message and the receiver must, in turn, decode this message to recover the information. In modern digital communication

---

<sup>1</sup>This is due to skin depth effects.

systems, there are several ways to encode information. One popular method works by digitally encoding information into the phase of a carrier wave. This is known as *phase modulation*. Assume, for example, that there are two possible phases and they are set  $180^\circ$  apart, say at  $90^\circ$  and  $270^\circ$ . This system is able to encode 1 bit of information because there are two possible states. At the receiver, a decision must be made on whether the phase of the carrier of the incoming message is closer to  $90^\circ$  or  $270^\circ$ . To convey more information, the transmitter could attempt to increase the possible number of states from 2 to 4, so 2 bits can be sent per message. This now requires 4 phases, say  $90^\circ$ ,  $180^\circ$ ,  $270^\circ$  and  $360^\circ$ . Every attempt at sending a message is known as a *symbol*. Every time the transmitter attempts to send a new message, the phase of the carrier wave is changed to encode the new information. The rate at which the transmitter changes the sent symbol is known as the symbol rate, or the *signalling rate*. The higher the signalling rate, the more information that can be sent per unit of time. Similarly, the greater the possible number of states in a symbol, the more information that can be sent per symbol and per unit of time.

The path between the transmitter and the receiver is known as the *channel*. The channel is often characterised by its *magnitude response* and *phase response*. The magnitude response is the attenuation a signal will experience between the transmitter and receiver. The phase response is the change in phase a signal will experience between the transmitter and receiver. Almost always, the magnitude and phase responses of a channel are dependent on frequency, so it is useful to plot them as a function of frequency.

In phase modulation, the channel is a source of impairment because the phase of the a signal at the receiver will be different to the phase of the signal sent by the transmitter. Some systems have receivers that attempt to correct for the channel to restore the received signal such that is closer to that sent by the transmitter. A less complex solution is to encode the information not in the absolute phase of the carrier, but in the *difference* between the phase of the current and previous symbol. This is known as *differential phase modulation*. Differential phase modulation can be done in time, where the phase of the current and previous symbols are compared, or in frequency, where the phases of two separate carriers (at different carrier frequencies) are compared. For the latter, the nature of the phase response is important because the two carrier signals may experience different phase impairments due to the channel. This is a particular problem in PLC and will be investigated in more detail later in this chapter.

When the decoded symbol differs from the transmitted symbol, an error has occurred and a number of bits received will differ in some way to the bits that were sent. The chance of receiving an incorrect bit for a particular communication channel is known as the *Bit Error Rate* (BER). The BER for a particular channel depends on channel impairments, signal to noise ratio (SNR) and the nature of the coding scheme used by the modulator/demodulator (MODEM). For a given SNR, symbols with a high number of states, thus including more information per symbol, are more prone to bit errors than schemes employing fewer possible states.

### 3.3 Modelling of Propagation Modes on Overhead Lines

The analysis of high frequency signals propagating on a multi-conductor power line structure (for example, in Fig. 3.1) is simplified by applying the theory of natural modes [44] [45]. Modal theory states that any set of phase conductor current and voltage existing at any point of a lossy and reflection-free 3-phase line can be resolved into three sets of natural mode components. The modes are independent and there is no intermodal coupling [44].

First, the well known equations relating the phase voltage and the line parameters (R and C) are obtained:

$$\frac{\partial^2 V(x)}{\partial x^2} = \gamma^2 V(x) \quad (3.1)$$

The equivalent Equation for current is given by:

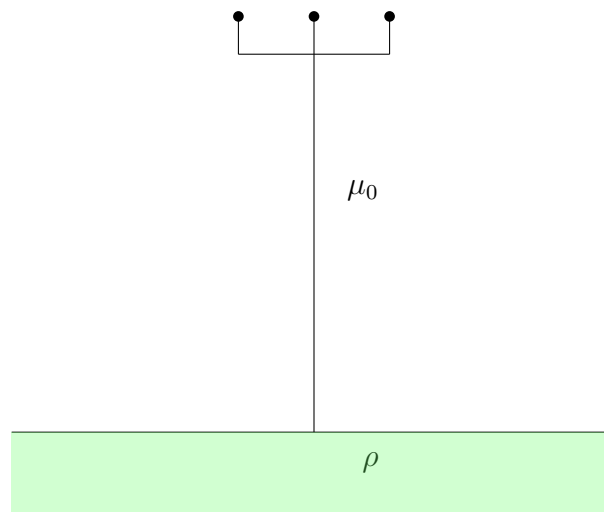


Figure 3.1: A 3-phase distribution line

$$\frac{\partial^2 I(x)}{\partial x^2} = \gamma^2 I(x) \quad (3.2)$$

Where  $x$  is position and  $\gamma$  is the propagation constant. For lossy lines, the propagation constant is:

$$\gamma = \sqrt{(R + j\omega L)(G + j\omega C)} \quad (3.3)$$

The propagation constant can also be expressed in terms of the attenuation constant  $\alpha$  and the phase constant  $\beta$ :

$$\gamma = \alpha + j\beta \quad (3.4)$$

To convert from the phase to the modal domain, a transformation matrix,  $[T_V]$ , is introduced. The values in  $[T_V]$  diagonalise the product of the impedance and admittance matrices ( $[Z]$  and  $[Y]$ ). The relationship between  $[V_{phase}]$  and  $[V_{mode}]$  is given by:

$$[V_{phase}] = [T_V] \cdot [V_{mode}] \quad (3.5)$$

Combining Equation (3.5) with Equation (3.1) leads to:

$$\left( \frac{\partial^2 V_{mode}(x)}{\partial x^2} \right) = [\Lambda] \cdot [V_{mode}] \quad (3.6)$$

Where:

$$[\Lambda] = [T_V]^{-1} \cdot [Z_{phase}] \cdot [Y_{phase}] \cdot [T_V] \quad (3.7)$$

$[\Lambda]$  is the voltage propagation matrix containing the diagonal elements that are the eigenvalues of  $[Z] \cdot [Y]$ . Each column of  $[\Lambda]$  represents a mode. Taking column  $k$ :

$$\left( \frac{\partial^2 V_{mode(k)}(x)}{\partial x^2} \right) = [\gamma_{mode(k)}] \cdot [V_{mode(k)}] \quad (3.8)$$

Where  $\gamma_{mode(k)}$  is the square root of the eigenvalue  $\gamma_k$  and can be named the modal propagation constant for mode  $k$ . It is clear that each mode will be associated with a different modal propagation constant. In a three conductor Overhead Transmission Line (OHTL), for example that shown in Fig. 3.2, three modes can exist. Each mode is characterised by an independent propagation constant. Mode 1, also known as the ground mode, is the most attenuated of the three modes and can be described as current flow in the same direction for all three conductors and a return path via the ground. Mode 2 can be visualised as current flow of opposite polarities in the two outer conductors only. Mode 3, the least attenuated mode, involves current flow in the forward direction in the centre conductor and return current flow in the two outer conductors. The phenomenon of modal propagation is best visualised diagrammatically, as in Fig. 3.3.

Fig. 3.3 shows that the voltage (or current) on a given phase will be the superposition of the modal voltages (or currents) associated with that phase. For example, the voltage on phase A or C (an outer conductor) will be made up of

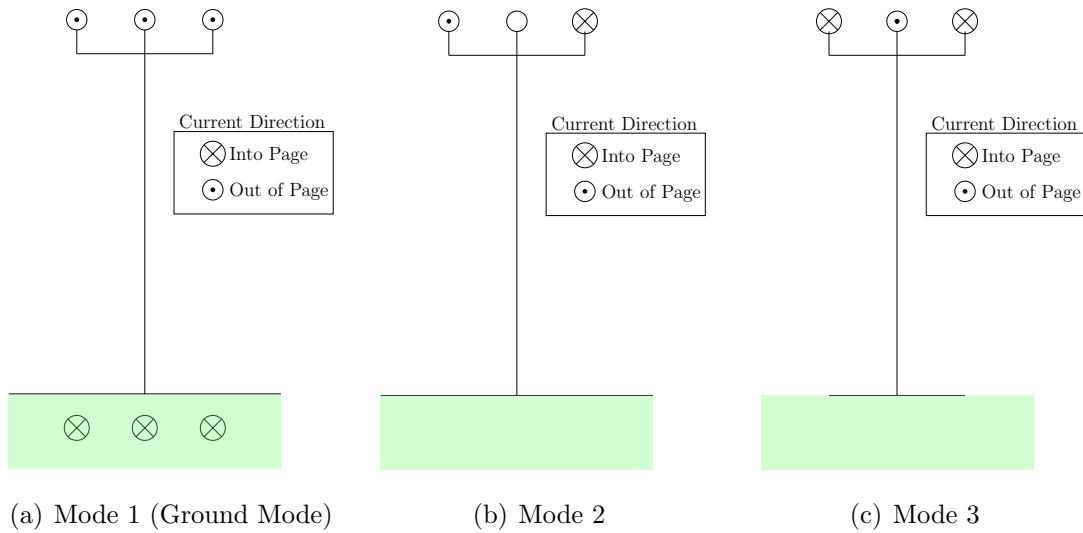


Figure 3.2: Diagrammatic representation of the current direction in the ground mode (a), and the two aerial modes (b) and (c).

a ground mode element, a mode 2 element and a mode 3 element. Phase B (the centre conductor) has no mode 2 component. In the analysis of PLC propagation over large distances (i.e. exceeding 15 km), the physical significance of modes is clear. At such distances, the power in the ground mode tends to diminish quickly, leaving only the aerial modes. Consequently, the design of a PLC coupling scheme for operation over long distances should aim to minimise power coupled into the ground mode whilst maximising power into the aerial modes. This phenomenon is

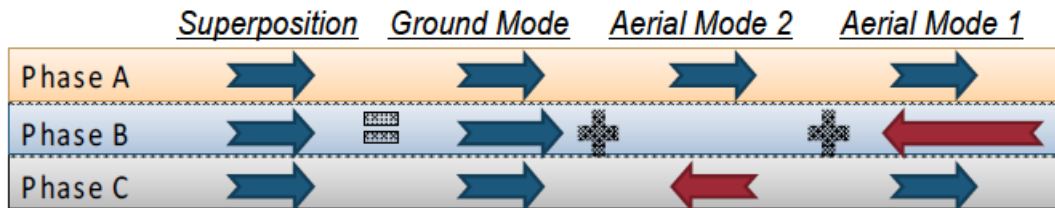


Figure 3.3: Visualisation of the natural modes in a three conductor system

shown clearly in Fig. 3.4, where a simulation of the propagation of all three modes have been compared on a long (reflection-free) line in the Electromagnetic Transients Program-Alternative Transient program (ATP/EMTP). The characteristics of the line used in the simulation are shown later in Table 3.1. It should be noted that the attenuation in the modes is highly dependent on frequency.

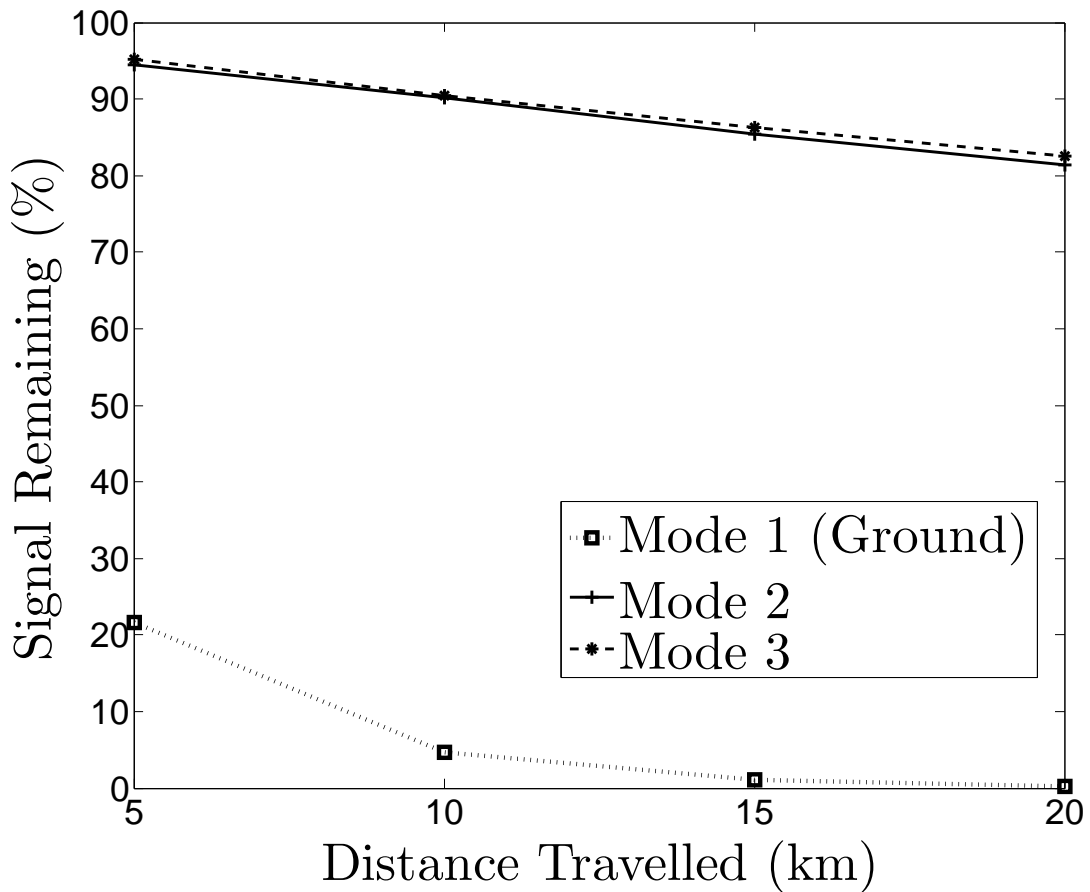


Figure 3.4: Comparison of attenuation experienced on an infinite (reflection free) distribution line (geometry shown in Table 3.1) by signals in Mode 1 (ground mode) and the aerial modes (modes 2 and 3) at a frequency of 400 kHz

### 3.4 Development of a Representative Model for a Rural 11 kV Network

The ATP/EMTP is widely used for transient analysis of power systems but the theory and models underpinning the program are also applicable to the simulation of PLC [46]. The J.Marti line model [8] was developed as a computationally efficient means of simulating the frequency dependent parameters of the line. In the phase domain, the impedance matrix is frequency dependent making its calculation awkward and computationally expensive. In the modal domain, however, there is no inter-mode coupling and a frequency dependent model can be constructed with synthetic networks. A constant transformation matrix is assumed and modal propagation constants are calculated over a wide frequency range. For narrowband PLC, the usefulness of the simulation is limited to how well it can replicate real life conditions. One particular challenge is the modelling of the earth. The ATP/EMTP uses Carson's formula [47], which assumes a homogeneous earth with uniform resistivity; a good approximation at low frequencies but questionable at frequencies exceeding several MHz [48] [49] [50]. Nonetheless, Carson's formula has been shown to be reasonably accurate over the narrowband PLC frequency range [51]. A further shortfall is the assumption of a real and constant transformation matrix. In [52], it is suggested that this assumption may lead to inaccuracies if a wide frequency range is being simulated. This is due in part to the sensitivity of the calculated propagation matrix to the chosen value of the real and constant transformation matrix. The choice of the frequency at which to calculate the transformation matrix may

also lead to inaccuracies due to the presence of eigenvector switchovers.

Despite there being several sources of inaccuracy, it must be noted that the ATP/EMTP has previously been used in Power Line Carrier studies. Comparisons with a number of published studies in the area of PLC propagation for the Distribution Line Carrier (DLC) system (occupying a frequency range that does not exceed 50 KHz) corroborate the general attenuation levels generated by the J.Marti line models [53]. In [54], a very good agreement between the ATP/EMTP simulation results and experimental results was observed. This study, however, was limited to the CENELEC D frequency band (140-148.5 kHz) and therefore reveals nothing about the performance of the J.Marti line model at frequencies of greater than 200 kHz. Despite the uncertainty in the accuracy of the J.Marti line model at such high frequencies, it is deemed that the expected error bounds fall within that necessary to draw useful conclusions from simulation of communication type scenarios.

A disproportionate number of customer interruptions originate on the 11 kV rural type network yet fault location on these types of network is still especially problematic due to their branched nature and the lack of communication infrastructure. With this reasoning, this type of network is chosen as the main focus of study. The line model parameters shown in Table 3.1, and in Fig. 3.5, are based on data obtained from DNO literature regarding 11 kV wood pole overhead lines typically used in rural areas. The resultant voltage and current transformation matrices, as calculated by the ATP/EMTP, are displayed in Equations (3.9) and (3.10) respectively.

Table 3.1: Characteristics of the OHTL under test  
11 kV Wood Pole Overhead Line

Height, $h$	9m
Height at mid-span, $h_{mid}$	7.5m
Conductor separation, $d$	1.5m
Conductor name	Dingo
Conductor resistivity	0.1814 $\Omega$ /km DC

$$[T_v] = \begin{bmatrix} 0.6027 & -0.7071 & -0.4089 \\ 0.52299 & 0 & 0.8158 \\ 0.6027 & 0.7071 & -0.4089 \end{bmatrix} \quad (3.9)$$

$$[T_i] = \begin{bmatrix} 0.5782 & -0.7071 & -0.3706 \\ 0.5796 & 0 & 0.8642 \\ 0.5782 & 0.7071 & -0.3706 \end{bmatrix} \quad (3.10)$$

The chosen network is based on generic networks devised by the United Kingdom Generic Distribution System (UKGDS) project [55]. The UKGDS-EHV2 “Large Rural Network” is chosen as the basis for the example network. Data, including branch lengths and line model information is translated from the UKGDS network and reproduced as an ATP/EMTP model with J.Marti frequency dependent line models. It is noted that a number of the branch lengths in the UKGDS-EHV2 network are the same. This situation is extremely unlikely in practical networks and may lead to a situation whereby the channel impulse response is unrealistic (due to similarities in path lengths<sup>2</sup>). The branch lengths are therefore “randomised” to  $\pm 10\%$  from the listed values in the UKGDS-EHV2 network. Fig. 3.6 shows the

---

<sup>2</sup>Path lengths usually drop off exponentially with distance, as would be the case in most “real world” networks. Identical branch lengths may conspire to produce large, unrealistic rays in the impulse response.

layout of the example network after the randomisation process.

It is shown in [56] that the presence of transformers and their loadings have little effect on the propagation behaviour of the DLC signal as, in effect, the signal is contained within the network and the transformers are open circuits. A negligible portion of the signal energy propagates through the transformer (although the use of capacitors between the primary and secondary windings can facilitate a low impedance path). It is inferred from these results, which were taken at 50 kHz and below, that the connected transformers can be accurately modelled as open circuits at frequencies beyond 100 kHz, simplifying the ATP/EMTP model.

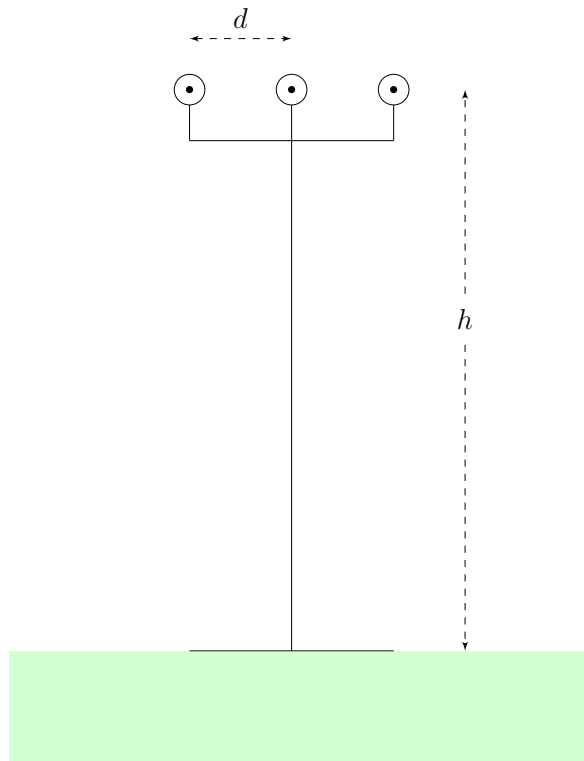


Figure 3.5: 11 kV line of wood pole construction showing the conductor height,  $h$ , and the conductor spacing,  $d$ .

The resultant ATP/EMTP test network allows the simultaneous assessment of modulation scheme performance on a network scale. The advantage of this method (rather than a generalised approach relying on channel models) is that well known frequency dependent line models can be used and there is practically no limit on the complexity of the simulated system.

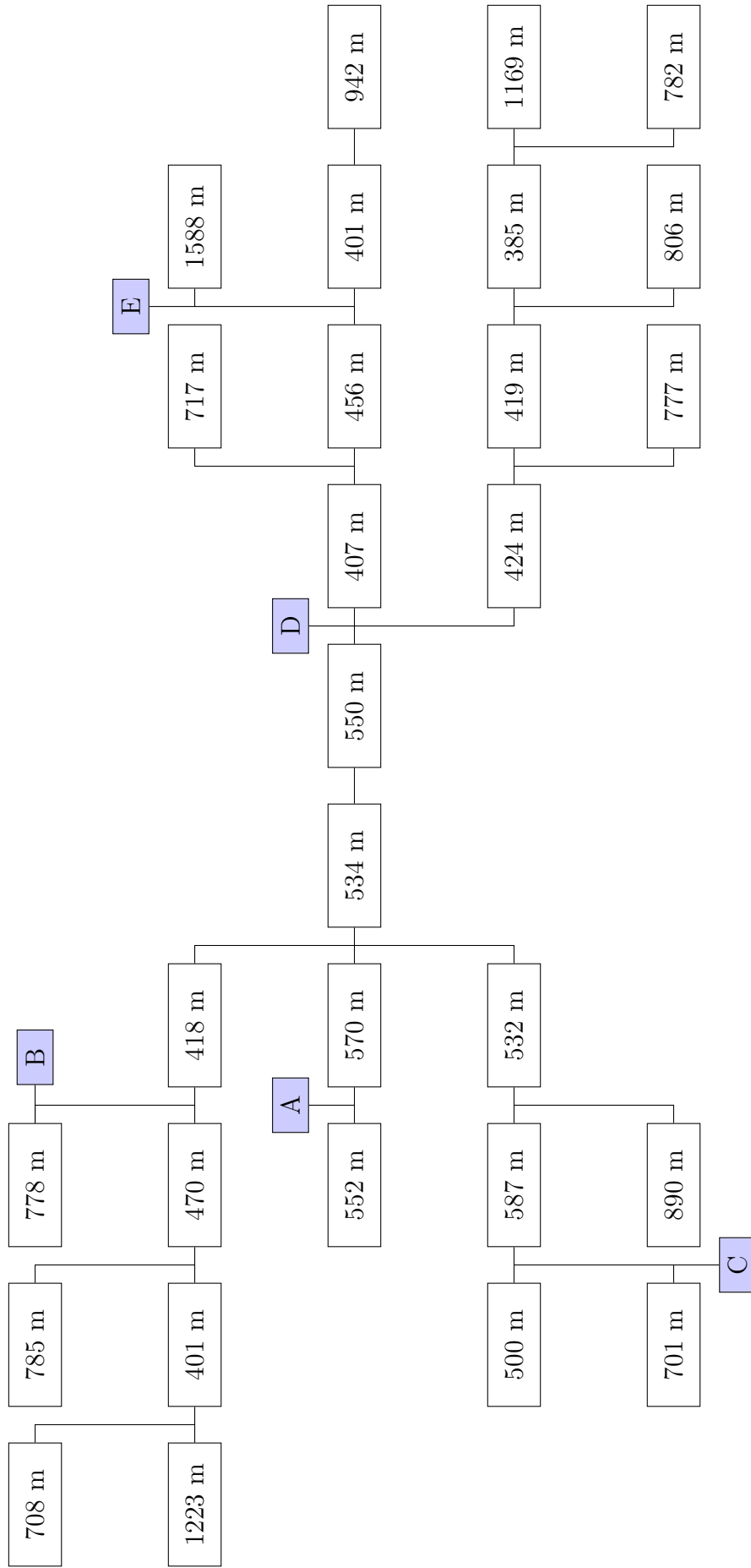


Figure 3.6: The example network

### 3.5 Determination of Channel Characteristics for 11 kV Networks

The sub-MHz channel is often neglected in PLC studies because it falls between the BPL frequencies and the Narrowband PLC, (NPLC) range of frequencies. Despite this, it is suggested in this thesis that the frequency range just below 1 MHz can offer the best trade-off between data-rate, bandwidth and the required number of repeaters to accommodate the system. In this work, the range of frequencies between 200 kHz and 800 kHz is examined to determine the performance of the commonly used Orthogonal Frequency Division Multiplexing (OFDM) modulation scheme. The design of a communication scheme for the transfer of information between nodes on a power network requires the careful specification of several key parameters such as the required bit-rate, the acceptable BER, the amount of information to be transferred and, importantly for latency specific applications, the time it takes for a given amount of information to be transferred between one node and all other nodes.

There have been numerous studies examining the channel characteristics of the power line. Some have concentrated on obtaining empirical measurements of the RMS delay spread and impulse response, mainly on LV channels and at frequencies beyond 30 MHz [57] [58]. Others aim to construct a useful channel model based on these empirical results [59] [60] [61]. However, one may generally assume that prior to the deployment of a communication device on an HV power line, detailed knowledge of the channel response between any two arbitrary points is not available, as is demonstrated by the lack of published results in the literature. It is also notable

that results indicating delay spread at low frequencies (i.e. <1 MHz) are rare.

In the following sections, the example network shown in Fig. 3.6 is used to obtain channel characteristics between representative point to point channels, where a channel is defined as the physical medium between the points.

### 3.5.1 Additive White Gaussian Noise

Additive White Gaussian Noise (AWGN) is wideband noise with a flat and constant spectral density. This type of noise places an immediate and unavoidable limitation on the achievable BER in a given channel. According to the Shannon-Hartley theorem [62], the channel capacity,  $C$ , can be expressed as a function of channel bandwidth,  $B$ , received power,  $S$ , and the noise level,  $N$ .

$$C = B \log_2 \left( 1 + \frac{S}{N} \right) \quad (3.11)$$

Therefore, the channel capacity is limited by the used bandwidth and the signal to noise ratio. The noise power on the HV power line has been measured empirically in several studies [63] [64]. It was established that the noise is Gaussian at frequencies above approximately 100 kHz and has a power spectral density of around -110 dBm/Hz.

### 3.5.2 Channel Impulse Response and Delay Spread on the HV PLC Channel

Frequency selective fading is caused by multipath interference and results in an increased BER. The problem of frequency selective fading is emphasised in the power line channel because the transmitted signal is bound by the power line structure ensuring that there will be at least as many time-delayed reflections reaching the receiver as there are branches and, typically, more as the signal continues to propagate throughout the network. The power of the time-delayed version of the transmitted signal is attenuated and time delayed, giving rise to a less powerful and more spread signal at the receiver. This effect is usually referred to as the RMS delay spread of the channel, and is displayed in Fig. 3.7. The significance of the RMS delay spread is best explained when considering what happens when the signalling rate of the transmitter modulator is faster than the RMS delay spread of the channel. At the receiver, the previous symbol's energy will be smeared alongside the current symbol's energy (as can be seen in Fig. 3.8, resulting in significant impairment and a greatly increased BER. To avoid this impairment, the symbol duration can be set to greater than the RMS delay spread of the channel. The RMS delay spread therefore sets a limit on the signalling rate in single carrier modulation schemes and has prompted the use of multi-carrier modulation schemes such as OFDM.

The impulse response of a channel is defined in terms of the input,  $u(t)$ , output,  $y(t)$  and the delay spread function,  $h(t, \tau)$ .

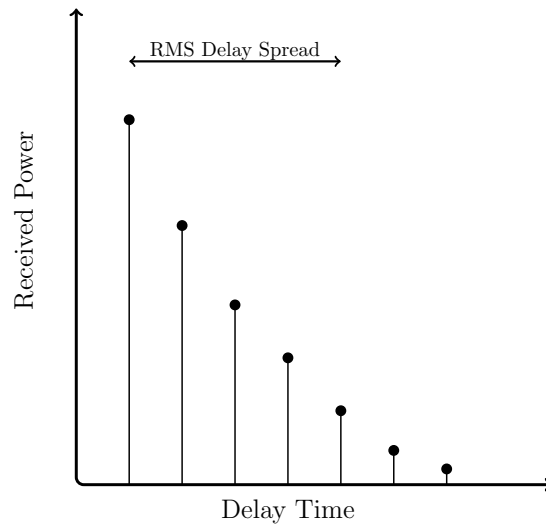


Figure 3.7: Diagram showing a typical impulse response and RMS delay spread

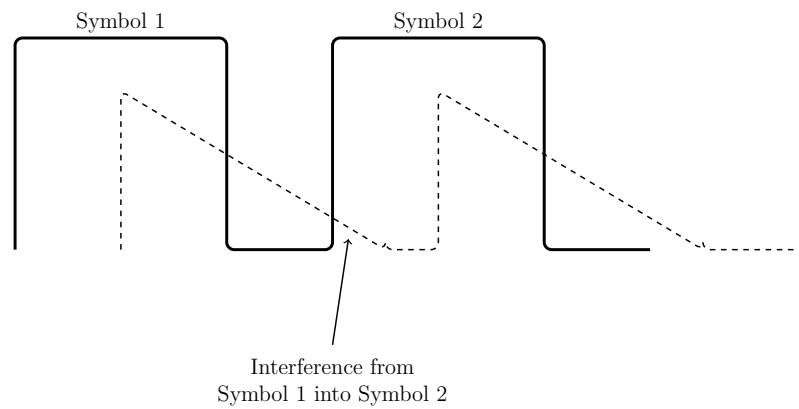


Figure 3.8: Diagram showing Intersymbol Interference (ISI). The dashed line represents the delayed (reflected) parts of the incident signal

$$y(t) = u(t) \star h(t, \tau) = \int_{-\infty}^{\infty} h(t, \tau)u(t - \tau).d\tau \quad (3.12)$$

The impulse response can also be used to calculate the RMS delay spread.

The first moment of the Power Delay Profile (PDP) is defined as:

$$\bar{\tau} = \frac{\sum_k P(\tau_k)\tau_k}{\sum_k P(\tau_k)} \quad (3.13)$$

Where  $\tau_k$  is the delay time and  $P(\tau_k)$  the power in the  $k_{th}$  impulse.  $\bar{\tau}$  is the mean excess delay. The square root of the second central moment of the PDP is given by:

$$\sigma_\tau = \sqrt{\frac{\sum_k [\tau_k - \bar{\tau}]^2 P(\tau_k)}{\sum_k P(\tau_k)}} \quad (3.14)$$

Where  $\sigma_\tau$  is the RMS delay spread. From the RMS delay spread, one may also calculate the coherence bandwidth. Here, the definition in the following equation is used:

$$B_c = \frac{1}{5\sigma_\tau} \quad (3.15)$$

Where  $B_c$  is the 50% coherence bandwidth. The coherence bandwidth can be described as a statistical measure of the range of frequencies over which the channel can be considered “flat”. If this figure is large, the channel has a flat frequency spectrum over a large frequency span, a desirable property because a signal sent using similar frequencies will experience similar amplitude fading due to the channel.

In differential modulation schemes, information is encoded in the phase *difference* between neighbouring carriers, so a coherence bandwidth at least as great as the frequency separation between these two carriers is necessary.

Equations (3.14) and (3.15) can be used to calculate the RMS delay spread and the coherence bandwidth from the recorded impulse response of a particular channel.

The modal impulse responses (e.g. for mode 1, 2 and 3) can be calculated directly within the ATP/EMTP, where phase quantities are readily available. First, however, these phase quantities are converted to modal values using, in this case, the transformation matrix for current,  $[T_i]$ .

$$[I_{phase}] = [T_i][I_{mode}] \quad (3.16)$$

$[T_i]$  is calculated by the ATP/EMTP using the geometry of the line structure (see Equation (3.9)). A model can be used to convert phase quantities to modal quantities during the simulation run time using the values of  $[T_i]$ , which is a 3 by 3 matrix in a 3 conductor line. The code for the model is shown in Appendix A.1.

Several test points are placed at various points of the example network (shown in Fig. 3.6). These points are labelled A-E. The impulse response and RMS delay spread are found by injecting a pulse of short duration at one point (exciting all three modes) and measuring the received power, P, at all other points. It is convenient to use a coupling scheme that excites all three modes. This can be achieved by coupling simultaneously to the centre conductor and one of the outer conductors.

The magnitude of the induced signal into each phase is unimportant because for channel evaluation, only a comparison between the input and output signals needs to be made.

The method used in this analysis is summarised in Fig. 3.9. Tables 3.2-3.4 show the calculated RMS delay spread for modes 1, 2 and 3 respectively. It is worth noting that an immediate analysis shows that the delay spread between any two points is unrelated to the distance between these two points. The coherence bandwidths between all possible node pairs are shown in Tables 3.5-3.7. The code used to calculate these values is shown in Appendix A.4

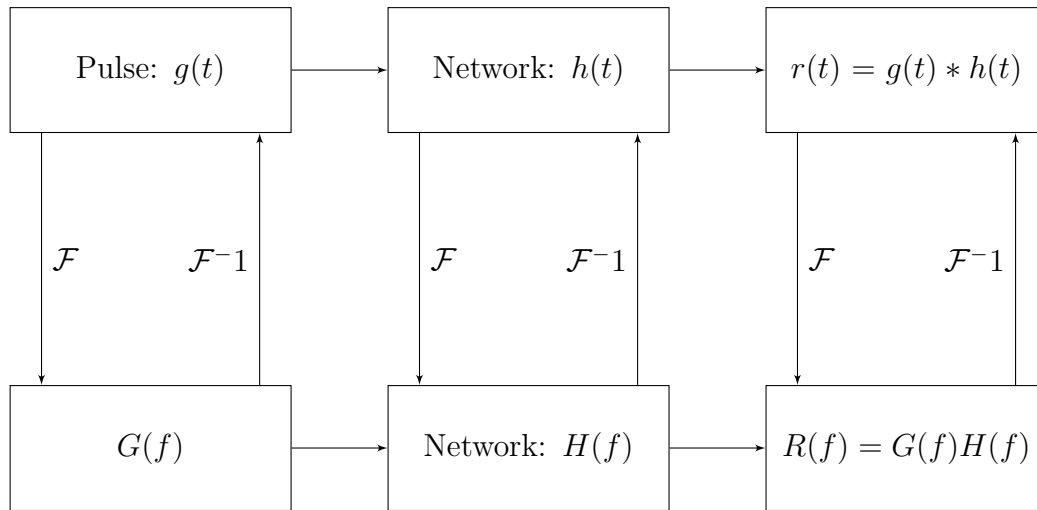


Figure 3.9: Method to Obtain Frequency Response,  $H(f)$  from the Impulse Response,  $h(t)$

Table 3.2: RMS Delay Spread Between Points for Mode 1 ( $\mu\text{s}$ )

-	A	B	C	D	E
A	-	267	169	265	196
B	316	-	323	213	169
C	133	150	-	164	125
D	219	120	230	-	185
E	124	117	99	129	-

Table 3.3: RMS Delay Spread Between Points for Mode 2 ( $\mu\text{s}$ )

-	A	B	C	D	E
A	-	974	613	916	805
B	963	-	680	885	650
C	592	637	-	748	880
D	914	663	740	-	1200
E	829	686	906	1200	-

Table 3.4: RMS Delay Spread Between Points for Mode 3 ( $\mu\text{s}$ )

-	A	B	C	D	E
A	-	789	495	740	665
B	800	-	547	728	530
C	508	578	-	655	740
D	735	541	641	-	1000
E	669	547	736	1000	-

Table 3.5: Coherence Bandwidth Between Points for Mode 1 ( $\text{Hz}$ )

-	A	B	C	D	E
A	-	1124	1369	1026	1504
B	966	-	913	1360	1739
C	1439	1325	-	1198	1852
D	1266	1667	935	-	803
E	1980	1695	2174	1613	-

Table 3.6: Coherence Bandwidth Between Points for Mode 2 ( $Hz$ )

-	A	B	C	D	E
A	-	279	304	275	244
B	282	-	330	299	286
C	305	334	-	266	212
D	279	302	272	-	167
E	245	278	212	167	-

Table 3.7: Coherence Bandwidth Between Points for Mode 3 ( $Hz$ )

-	A	B	C	D	E
A	-	353	379	344	291
B	348	-	398	372	347
C	372	390	-	308	252
D	342	370	312	-	182
E	291	342	251	182	-

The phase response between points on the test network can be obtained by taking the angle of the magnitude response. The phase response can be thought of as the change in phase a sinusoid experiences as it travels between two points on the network. In communication systems, where the information is encoded in the phase difference between two sinusoidal subcarriers, the phase response is extremely important. The channel adds distortion such that there is phase difference between adjacent subcarriers that is caused by the channel itself. For a channel with no reflections, the impulse response consists of a single impulse and the channel exhibits a linear phase response, as shown in Fig. 3.10. The smooth transition in phase makes it easy for the receiver to correct for the channel distortion, or, alternatively, accept the small discrepancy in phase at the expense of a slightly lower BER.

Here, the angle of the FFT of the impulse response at the receiving node is

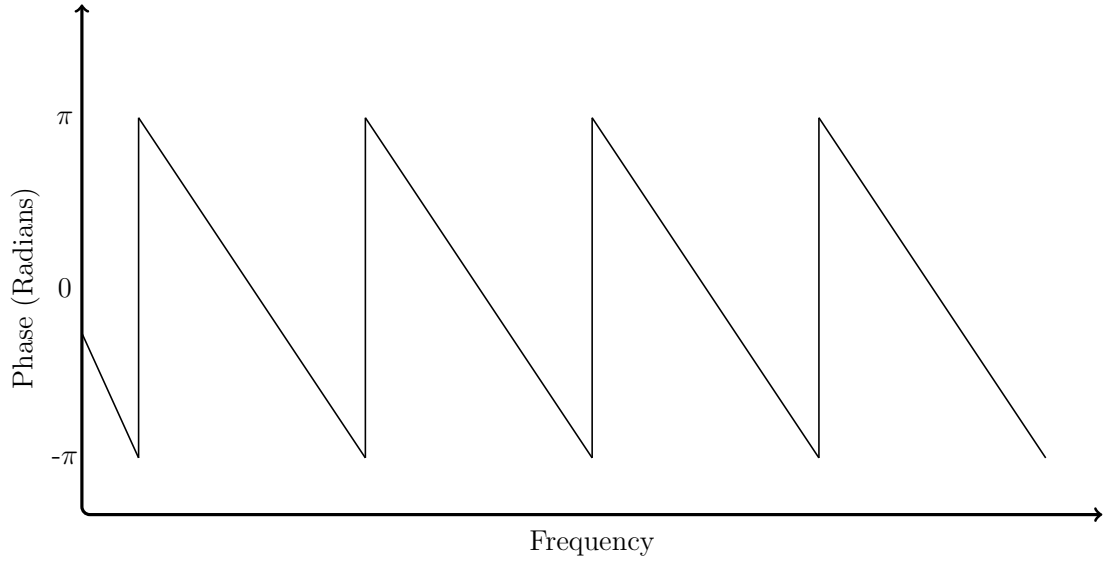


Figure 3.10: Phase response of a reflection-free channel

computed and plotted for all node combinations on the test network. Fig. 3.11 shows the phase response between selected node pairs (mode 2). It is observed that the phase response is extremely non-linear and erratic, especially at lower frequencies. If this phase response was to be compared to one belonging to a wireless channel or the channel giving the phase response in Fig. 3.10, the difference would be stark. In wireless channels, there tend to be fewer strong reflections so the phase difference is more linear as a function of frequency. The practical significance of this result is the possibility of phase rotations acting as a channel impairment. In differential modulation schemes, the information is encoded in the phase of adjacent subcarriers. Differences in phase rotations experienced by two adjacent subcarriers will alter the phase difference between the two subcarriers, decreasing the BER performance.

In OFDM systems, subcarrier spacing is an important consideration and will be further discussed in the next section.

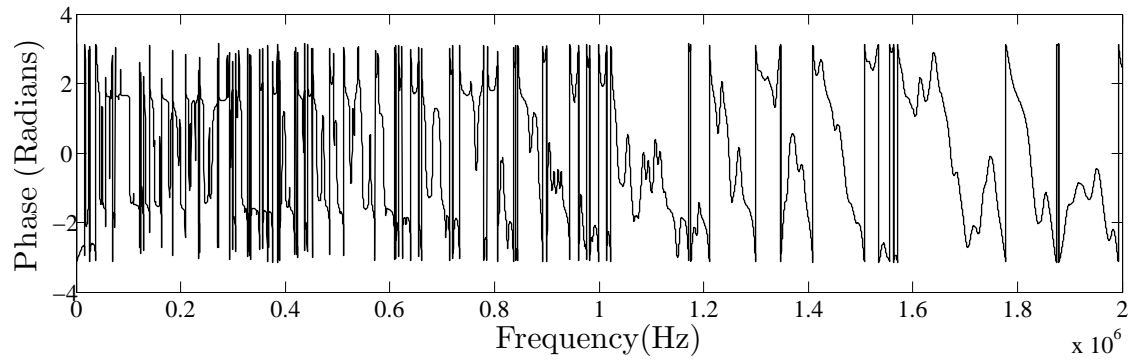
The magnitude response can be obtained by taking the absolute value of the FFT of the impulse response at the receiving node. This computation is performed for all node combinations in the example network and selected plots, for both the ground mode and mode 2, are shown in Figures 3.12 and 3.13, respectively.

The magnitude responses for the aerial modes show regions of high attenuation over a narrow frequency range. These are known as deep fades and are symptomatic of a channel suffering multipath interference. For the ground mode, there are fewer deep fades but the general attenuation is lower. In PLC, the transmit power of the transmitter is often limited, making it difficult to achieve a suitable SNR at the receiver. A power efficient strategy to solving the problem of deep fades is to allocate power based on the channel response, with more power being delivered to frequencies with deep fades [65]. Despite adding cost and complexity to the MODEM, this approach could be an invaluable tool in achieving a target data rate in the HV channels discussed earlier.

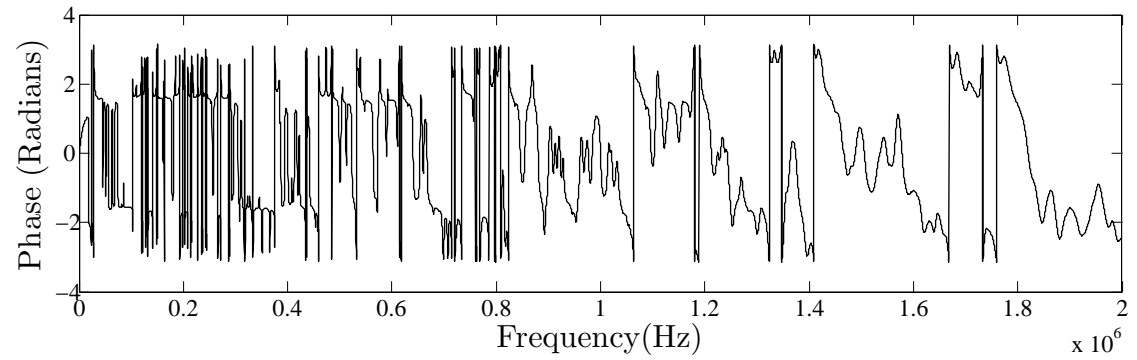
## 3.6 Exploitation of Orthogonal Frequency Division Multiplexing (OFDM) for the OHMS System

### 3.6.1 Key Aspects of OFDM for the OHMS System

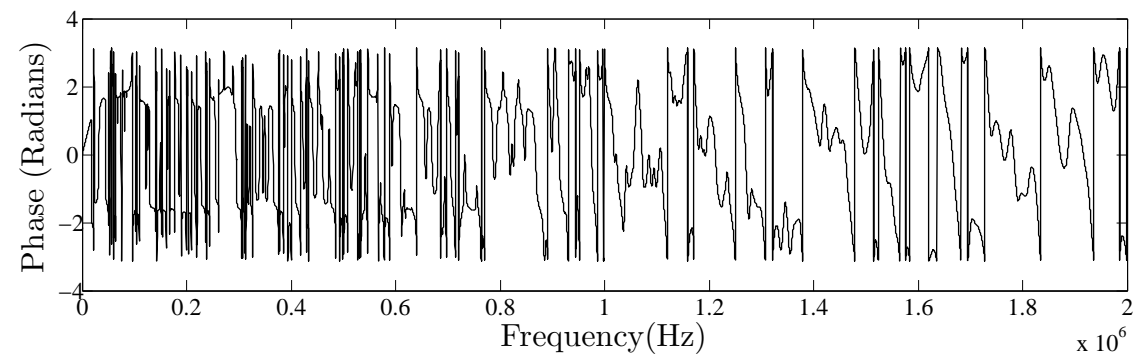
The channel characteristics of the HV power line channel make it difficult to use single carrier modulation schemes. This is due to Intersymbol Interference (ISI), where the previous symbol's energy smears over into the current symbol energy, causing errors at the receiver. The severity of ISI is dependent on the RMS delay



(a) Phase Response Between Nodes A and B of the Test Network

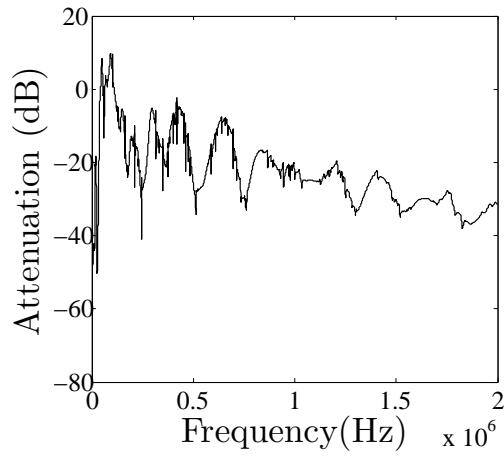


(b) Phase Response Between Nodes B and D of the Test Network

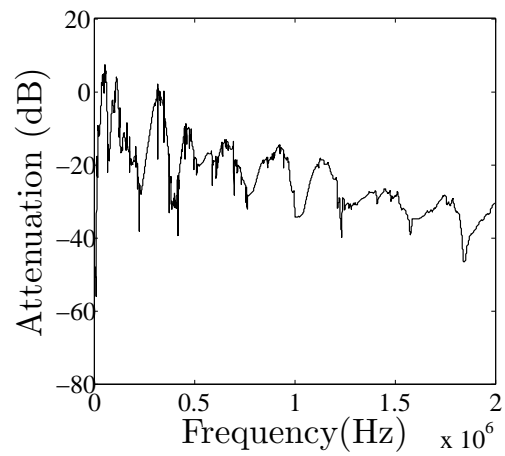


(c) Phase Response Between Nodes E and A of the Test Network

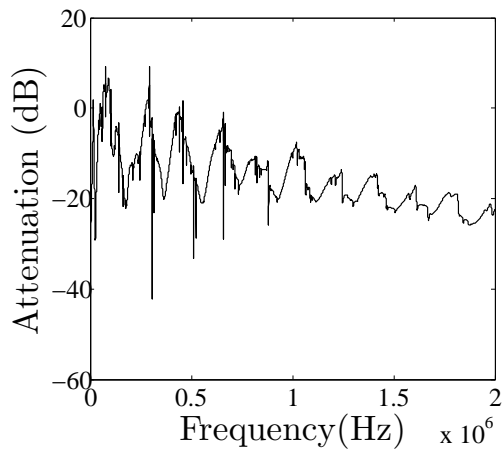
Figure 3.11: Phase responses between 0 and 2 MHz for communication between selected nodes on the test network.



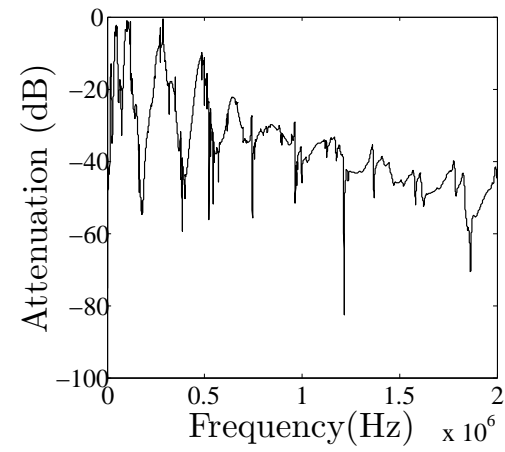
(a) Ground mode (A to B)



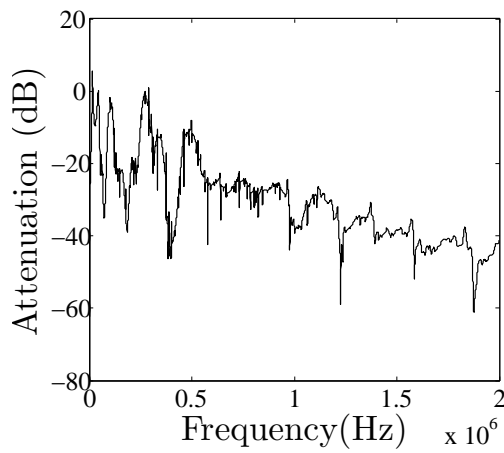
(b) A to C



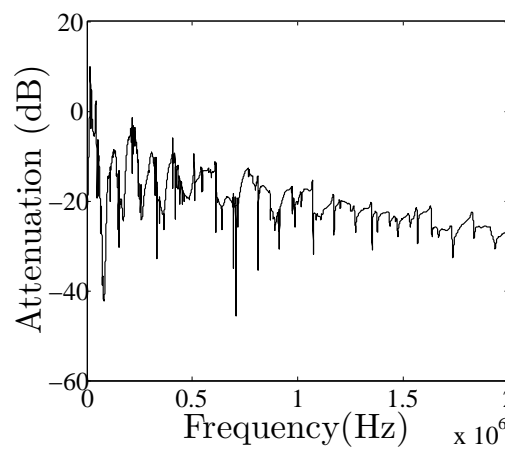
(c) B to D



(d) C to B

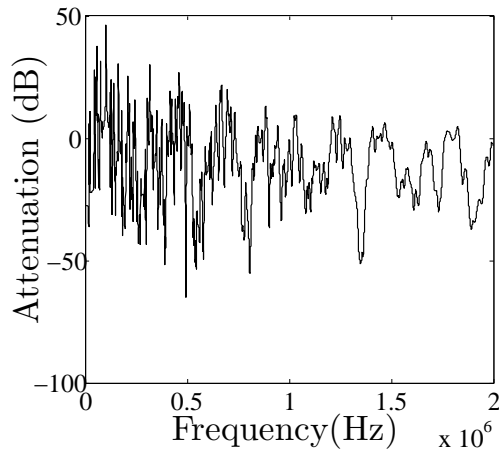


(e) D to C

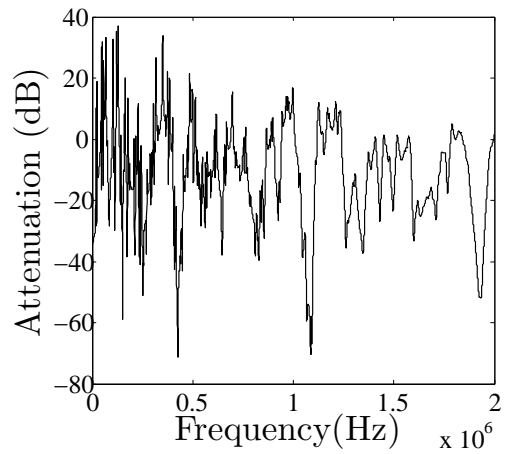


(f) E to D

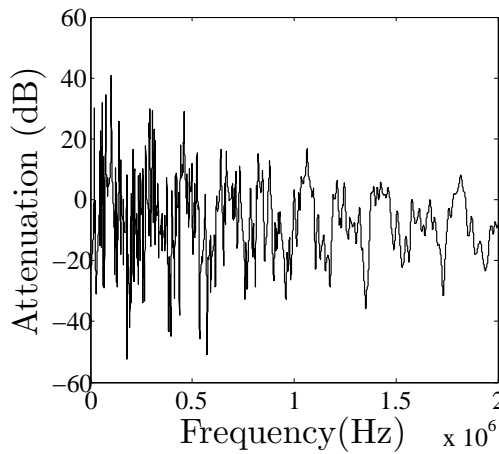
Figure 3.12: Magnitude responses (up to 2 MHz) between selected nodes on the test network (Ground Mode)



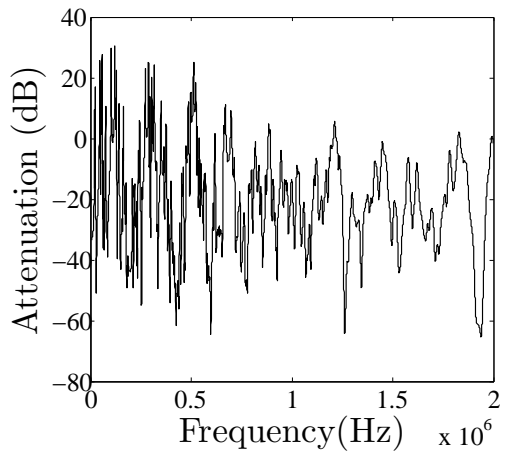
(a) Mode 2 (A to B)



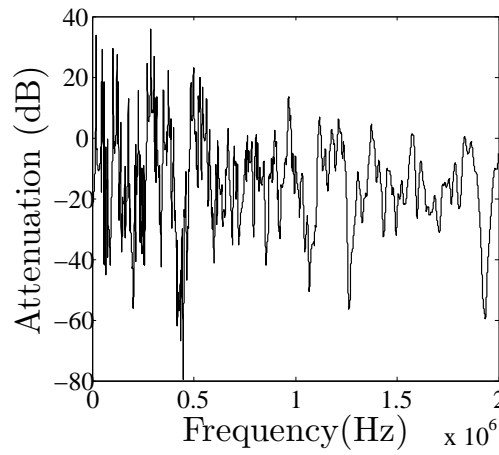
(b) A to C



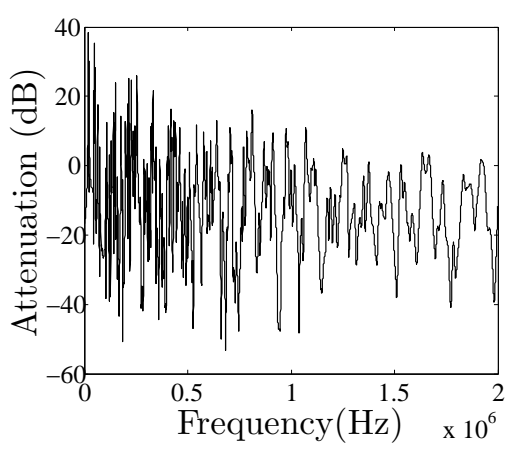
(c) B to D



(d) C to B



(e) D to C



(f) E to D

Figure 3.13: Magnitude responses (up to 2 MHz) between selected nodes on the test network (Mode 2)

spread of the channel. One simple solution to this problem is to increase the symbol period by reducing the signalling rate [66]. If the symbol duration is significantly greater than the delay spread of the channel, ISI is minimised. A drawback of this approach is the reduction in the data rate. The first paper to suggest the principle of orthogonal multiplexing as a means of maintaining high data rates, spectral efficiency and ensure a low signalling rate was [67]. The basic principle of frequency multiplexing relies on a bank of  $N - 1$  separate modulators with different carrier frequencies. For spectral efficiency, the carrier frequencies are chosen such that they are orthogonal to one another, giving a separation of  $\Delta f$  and a total used bandwidth,  $W$ , of  $N\Delta f$ . In OFDM systems, the serial data stream is converted into  $N$  parallel symbols,  $S_0, S_1, \dots, S_{N-1}$ . The parallel symbols are modulated by the bank of modulators and combined to give the OFDM symbol for transmission. This is shown in Fig. 3.14. Demodulation is done via a bank of demodulators set at the same carrier frequencies as the modulators at the transmitter, as is shown in Fig. 3.15. Orthogonality ensures that there is no interference between the carriers (known as Inter-Carrier Interference).

A major disadvantage of OFDM is the requirement for  $N$  separate modulator/demodulator pairs. It is, therefore, convenient that the process of modulation and demodulation in OFDM can also be achieved using the IDFT/DFT [68], or using the more computationally efficient IFFT/FFT. Each symbol,  $S_k$ , may be defined in terms of its real and imaginary parts:

$$S_k = I_k + jQ_k \tag{3.17}$$

For  $N - 1$  complex symbols, an  $N - 1$  point IDFT is required. A single OFDM symbol has a useful period  $T$  preceded by a cyclic prefix of length  $T_g$ , as can be seen in Fig. 3.16. For ISI free communication, the cyclic prefix length,  $T_g$ , is longer than the channel impulse response. The OFDM time domain signal is defined as:

$$v(t) = \sum_{k=-N}^N S_k e^{j2\pi kt/T}, -T_g \leq t \leq T \quad (3.18)$$

Where  $S_k$  are the data symbols,  $N$  is the number of subcarriers and  $T$  is the OFDM symbol time. The frequencies of the complex exponentials are defined as:

$$f_k = \frac{k}{T}, -N \leq k \leq N \quad (3.19)$$

Prior to transmission, the signal is quadrature modulated (modulation onto two carriers of the same frequency but  $90^\circ$  out of phase) and up-converted. The total useful period,  $T$ , increases as the number of sub-carriers,  $k$  increases and is

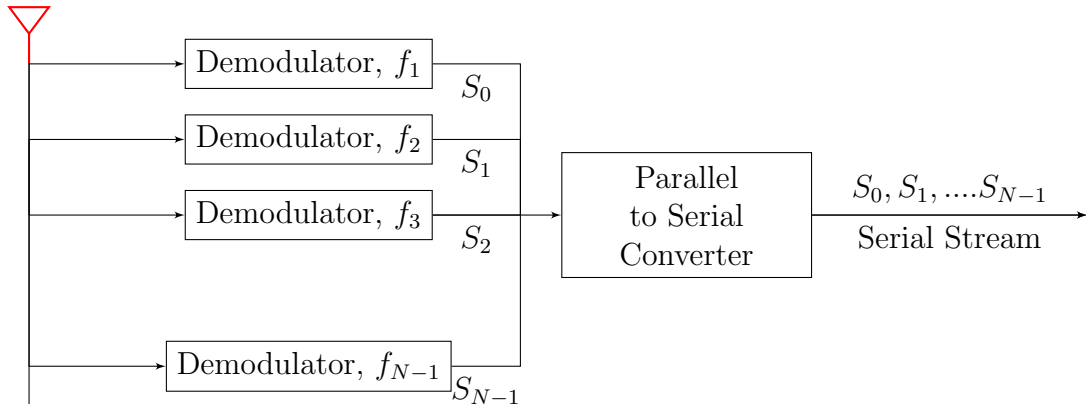


Figure 3.14: Functional OFDM System: Transmitter

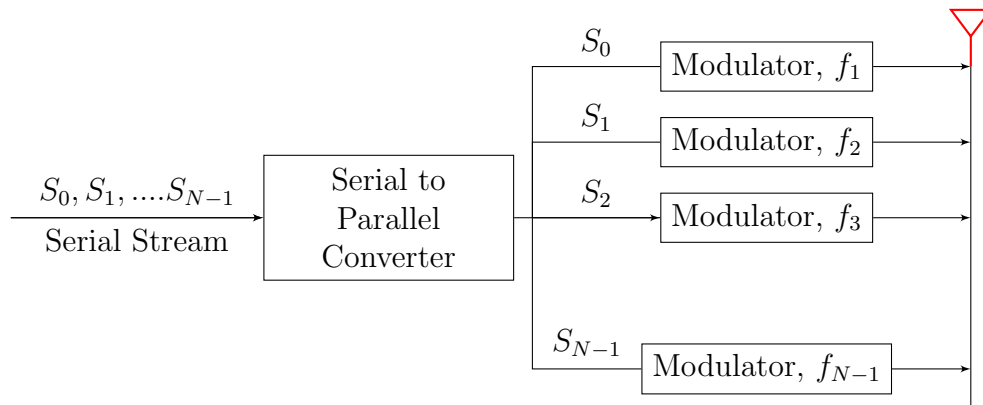


Figure 3.15: Functional OFDM System: Receiver

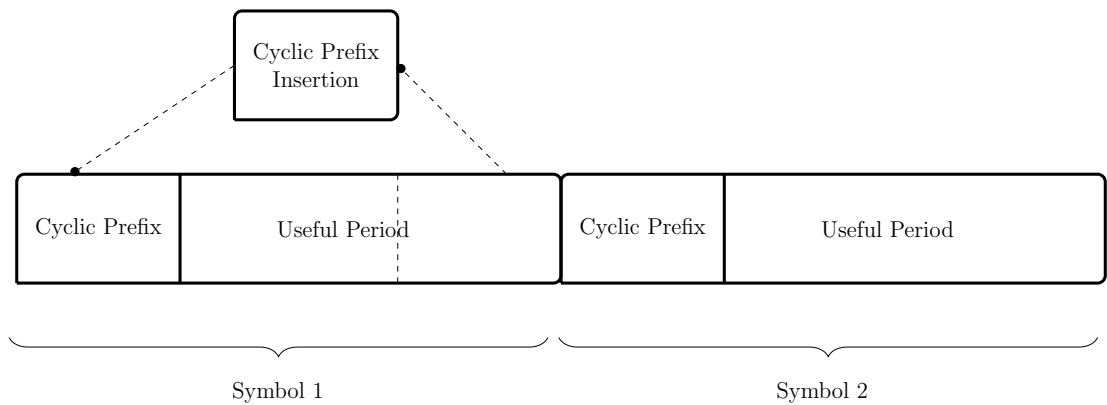


Figure 3.16: Diagram showing cyclic prefix inserion and the useful part of the OFDM symbol

related by the sampling frequency,  $f_s$ .

$$T = \frac{k}{f_s} \quad (3.20)$$

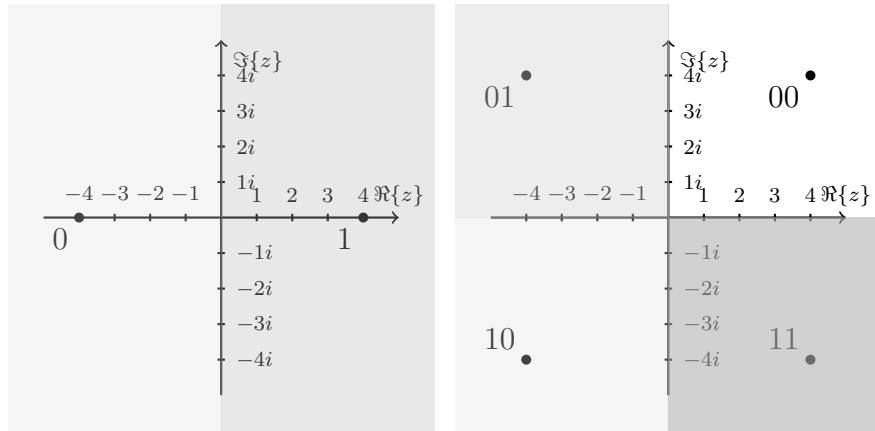
The above equation highlights the trade-off between the symbol period, the used bandwidth and the data rate. An increase in the data rate can be achieved by increasing  $k$  or  $f_s$ . Increasing  $k$  has the side effect of increasing the symbol period. Increasing  $f_s$  decreases the symbol period at the expense of an increased used bandwidth.

Each subcarrier in an OFDM system has the potential to carry information, in fact, OFDM can be thought of as  $k$  separate MODEMS running in parallel. Each subcarrier is modulated using a conventional modulation scheme. One popular modulation scheme, often used in OFDM schemes, is known as Quadrature Amplitude Modulation (QAM). In QAM, two digital streams of information can be modulated simultaneously by two carrier waves set at the same frequency but  $180^\circ$  out of phase (in quadrature) from one another. Information is encoded in the amplitude of the two carrier waves. The phasor sum of the two quadrature signals can be positioned, as a point, in the complex plane. Each point is characterised by an amplitude and a phase. 4-QAM, otherwise known as Quadrature Phase Shift Keying (QPSK), modulates two bits of information onto one of four possible points in the complex plane. 2-QAM, or Binary Phase Shift Keying (BPSK) is capable of modulating 1 bit of information onto one of two possible points. 8-QAM, known as 8 Phase Shift Keying (8PSK) has a constellation of 8 possible points in the complex plane, so is

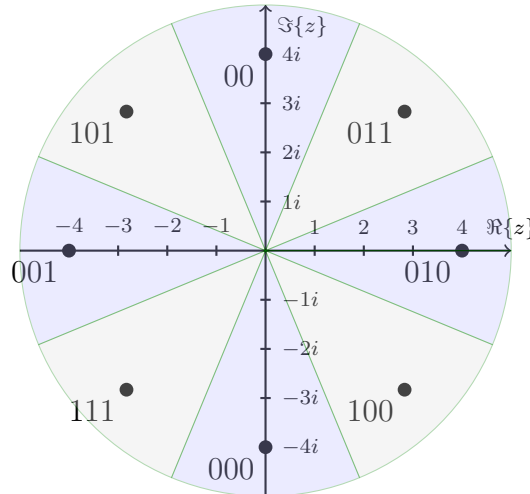
able to modulate 3 bits of information per symbol. Fig. 3.17 shows the constellation diagrams for these three modulation schemes.

The total information sent per OFDM symbol is the sum of the information sent per subcarrier. Therefore, denser constellations allow more information to be sent per OFDM symbol. Beyond 8PSK, progressively denser constellations are possible by increasing the number of possible constellation points<sup>3</sup>. The pri-

<sup>3</sup>Digital Video Broadcasting (DVB), the standard used by “Freeview” in the UK, uses a maxi-



(a) Transmitted constellation points of a BPSK symbol (b) Transmitted constellation points of a QPSK symbol



(c) Transmitted constellation points of an 8PSK symbol

Figure 3.17: Transmitted Constellation Points

mary drawback of using denser constellations is less robustness to noise and phase rotations caused by the channel.

The role of the demodulator is to determine the position of the received complex symbols and decide the bit(s) of information this symbol position encodes. In practice, the received symbol will be different to the transmitted symbol. This is due to phase rotations and fading in the channel between the transmitter and receiver. A coherent OFDM detector attempts to correct for the channel by using known pilot signals on one or more of the subcarriers. A simpler implementation is non-coherent (differential) detection. Here, the information is encoded not in the absolute position of a symbol but in the phase difference between adjacent subcarriers. This can be done either in the time or frequency domain. The obvious advantage of differential modulation is pilot subcarriers are not required<sup>4</sup>. A second advantage is robustness to phase rotations caused by the channel if the subcarrier spacing is less than the coherence bandwidth [69].

### 3.6.2 Synchronisation and Timing

As previously stated, in differential OFDM systems, the information is encoded in the phase difference between adjacent subcarriers. Phase rotations caused by the channel are unavoidable and may lead to bit errors at the receiver. Another source of error is incorrect timing [70]. It is necessary to start the sampling of the incoming OFDM signal close to the start of the useful part of the symbol. To explain this,

---

4A pilot is a “known” subcarrier used at the receiver to correct for channel impairments.

consider the case, in Fig. 3.18, where sampling starts too early, for example, within the cyclic prefix. This manifests itself as a cyclic shift of all demodulated symbols because the FFT window is not aligned on the useful part of the symbol. The severity of the phase rotation is dependent on the number of subcarriers and the sample offset.

Coherent demodulation schemes suffer severe degradation as a result of sampling time misalignments and cannot operate without phase correction. In contrast, differential demodulation techniques generally suffer less degradation as a result of timing errors. In differential demodulation, the phase error is:

$$\Phi_e = e^{\frac{2\pi}{k}} \quad (3.21)$$

where  $e$  is the number of sample interval misalignments and is valid for delayed timing errors that result in the FFT timing window starting in the quasi-periodically extended cyclic prefix. The error resulting in the FFT timing window going beyond

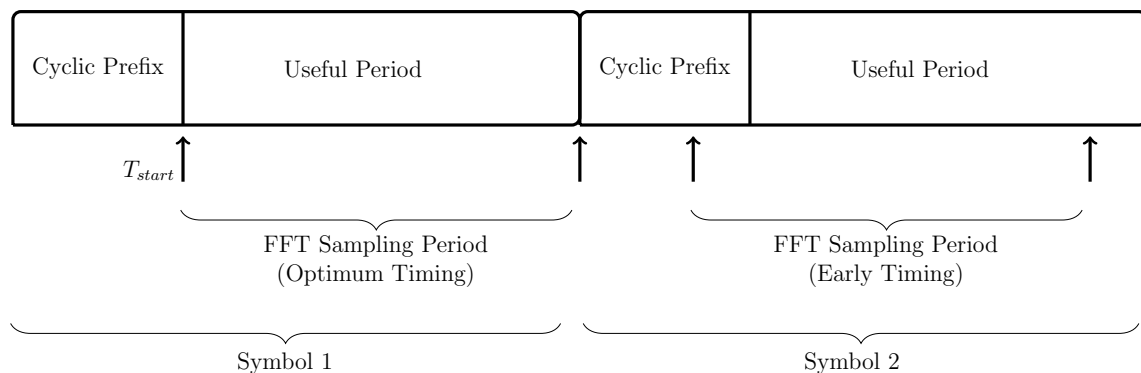


Figure 3.18: FFT sampling period: Optimum timing and early timing

the end of the information symbol (and into the following symbol) has a far more severe BER penalty. There are several possible schemes used to locate the starting point of the information symbol, shown as  $T_{start}$  in Fig. 3.18. The most popular use the principle of correlation between two parts of a repetitive signal. In the Schmidl/Cox method [71], a synchronisation symbol with two identical halves in the time domain precedes the information symbol. The receiver performs an auto-correlation on the sequence of received samples, with a delay of exactly half the number of samples in a symbol. The auto-correlation metric is defined as  $P(d)$ . The Schmidl/Cox method also advocates a normalisation term,  $R(d)$ , defined as the power in the current half symbol of samples. The metric,  $M(d)$  is expressed as:

$$M(d) = \frac{|P(d)|^2}{(R(d))^2} , \quad (3.22)$$

The metric,  $M(d)$ , approximates to 1 at the end of the synchronisation symbol. In the presence of noise, the peak value reduces. The auto-correlation function,  $P(d)$  can be found recursively and efficiently realised in hardware as a moving sum. Given that:

$$P(d) = \sum_{m=0}^{N-1} (r_{d+m}^* r_{d+m+N}) , \quad (3.23)$$

Where  $N$  is the number of samples in half a symbol. A recursive implementation can be reached via the following:

$$P(d+1) = P(d) + r_{d+N}^* r_{d+2N} - r_d^* r_{d+N} , \quad (3.24)$$

The result is a correlation peak occurring at the final sample of the synchronisation symbol. Because the information symbols arrive in sequence, after the synchronisation symbol, the correlation peak acts as a useful flag to the receiver and feeds its decision as to when the FFT should begin taking samples.

### 3.6.3 Assessment of Subcarrier Spacing Effects

Theory suggests that the subcarrier spacing used in the communication scheme should be less than the coherence bandwidth of the channel, else ISI will occur [66]. For incoherent OFDM systems, the transmitted information is encoded in the relative phase difference between either two adjacent subcarriers in the same symbol or concurrent subcarriers in the time domain. Here, an assessment is made of the impact the channel has on the relative phase rotation between two adjacent subcarriers in the same symbol. The phase response between all possible node pairs of the test network is obtained. Subsequently, the relative phase difference is calculated between neighbouring frequency points spaced apart by a varying amount. Frequencies between 200 kHz and 800 kHz are considered and the results shown in Fig. 3.19. As expected, the proportion of relative phase rotations between neighbouring points exceeding the decision boundaries are lower at short spacings between neighbouring points and progressively higher as the spacing increases. Furthermore, it is observed that the Differential Binary Phase Shift Keying (DBPSK) scheme performs best and Differential 8 Phase Shift Keying (D8PSK) performs worst. This is unsurprising given that less interference power is required to push the received symbol away from

the intended point as the constellation becomes more dense.

The results shown in Fig. 3.19 have practical significance in the design of an OFDM communication scheme. For example, in differential schemes it is desirable to minimise the difference in phase rotations between adjacent subcarriers. In channels severely impaired by multipath interference, the spacing between subcarriers should be set to be smaller than the coherence bandwidth. Here, it is shown that the subcarrier spacing should be lower than 200 Hz to minimise channel induced phase rotation differences between subcarriers. This subcarrier spacing is exceptionally low when compared with typical wireless channels [72], and places a significant constraint on the design of an OFDM system to be used on this network.

### 3.7 Conclusion

In this Chapter, the key aspects of digital communication theory have been introduced. Multi-carrier schemes, for example OFDM, are well suited to the power line channel because they may have a longer symbol duration and a large cyclic prefix. If the cyclic prefix is larger than the RMS delay spread of the channel, the negative effects of multipath interference are minimised. The problem is multipath for frequencies in the sub-MHz range is difficult to gauge because there are very few published results in this area. To examine the problem in more detail, a simulation model was developed based on well known frequency dependent line models making up a “typical” rural network. Initial simulations on this network suggest that the problem of multipath interference is severe and RMS delay spreads are considerably

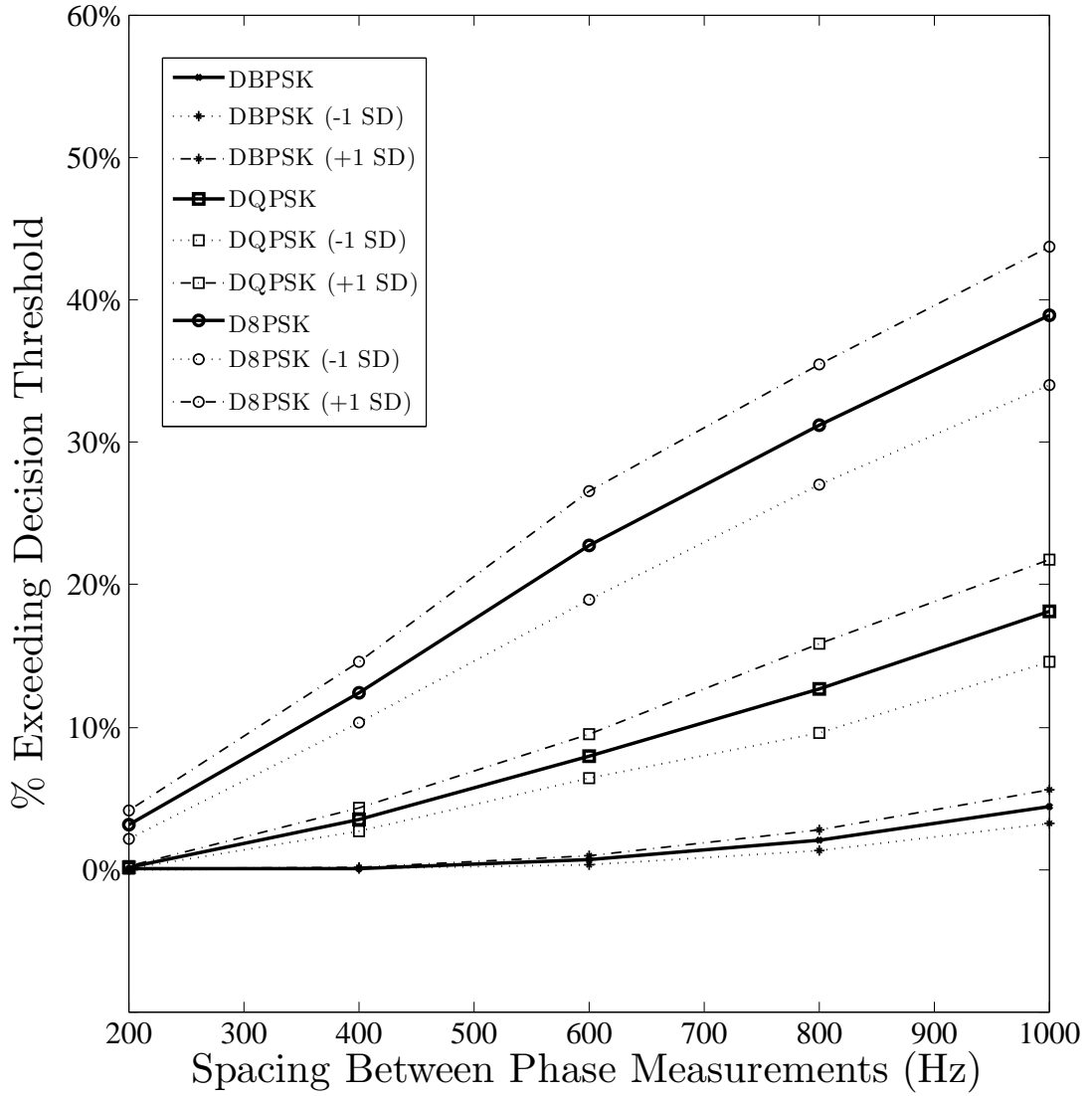


Figure 3.19: Proportion of relative phase rotations between neighbouring points exceeding the decision boundary in a frequency range between 200 kHz and 800 kHz for DBPSK, DQPSK and D8PSK. The solid line represents the mean values for all channel responses between nodes A to E and dashed lines represent one standard deviation. The decision boundary is  $\pm \pi/8$ ,  $\pm \pi/4$  and  $\pm \pi/2$  for D8PSK, DQPSK and DBPSK respectively.

larger than published figures for wireless channels and BPL PLC channels. This indicates that existing off the shelf communication chips may not be suitable for the low latency link demanded by the OHMS concept.

In the next Chapter, the test network will be used to examine the suitability of various OFDM modulation schemes with the view to selecting the basic key requirements for the system.

## Chapter 4

# Assessment of Proposed Narrowband Power Line Communication for the OHMS System

### 4.1 Introduction

The OHMS concept requires a low latency communication link between remote nodes on a distribution network. It was observed in Chapter 3 that the design of such a system should be based around due cognisance of the important parameters defining the channel. Failure to set the subcarrier spacing to below a critical value, for instance, will result in an immediate BER penalty even before the effects of noise are accounted for. In this Chapter, the test network is used to simulate NPLC and a suitable communication scheme, able to meet the performance requirements of the OHMS system, will be suggested.

### 4.2 Modelling of the OFDM System on the 11 kV Network and Simulation Methodology

It is expensive, time consuming and logistically difficult to trial new modulation schemes or communication systems directly on the electricity network. Therefore, in the PLC design process, simulation plays an important role. To be useful, the simulation scheme must be able to replicate the actual 11 kV network with high

accuracy. The ATP/EMTP software is the most widely used transient simulation packages and has been shown to faithfully simulate transient propagation on HV networks. In this work, the software is required to simulate the propagation of PLC signals, however, published results on the accuracy of ATP/EMTP for PLC type simulations are limited. Despite this, it should be recognised that the phenomenon of high frequency propagation throughout a network is fairly well understood<sup>1</sup>, and the confidence in the line models used for transient simulations can extend to PLC simulations too.

The ATP/EMTP software has a diverse suite for modelling common power system elements. For unusual cases, a user may specify behaviour using a Fortran based coding language known as the models language. This feature makes it possible to model a fully functional OFDM modulator within the simulation itself. In addition to the OFDM modulator, a quadrature mixer and LPF model has been constructed. Later in this section, the code and structure of the OFDM modulator and quadrature mixer/Low Pass Filter (LPF) model will be discussed.

The OFDM signal can be coupled to the test network at any point. Likewise, it is possible to obtain the voltage and current readings at any point in the network. To complete the simulation, the signals at the chosen receiver points are exported to Matlab, where a model of a synchronisation scheme and OFDM demodulator resides. Matlab is a feature rich software environment with particularly powerful capability in digital signal processing and digital communication.

---

<sup>1</sup>Although the phenomenon is well understood, the accuracy of travelling wave based line models decreases as the frequency increases. Cable models are notoriously poor [73].

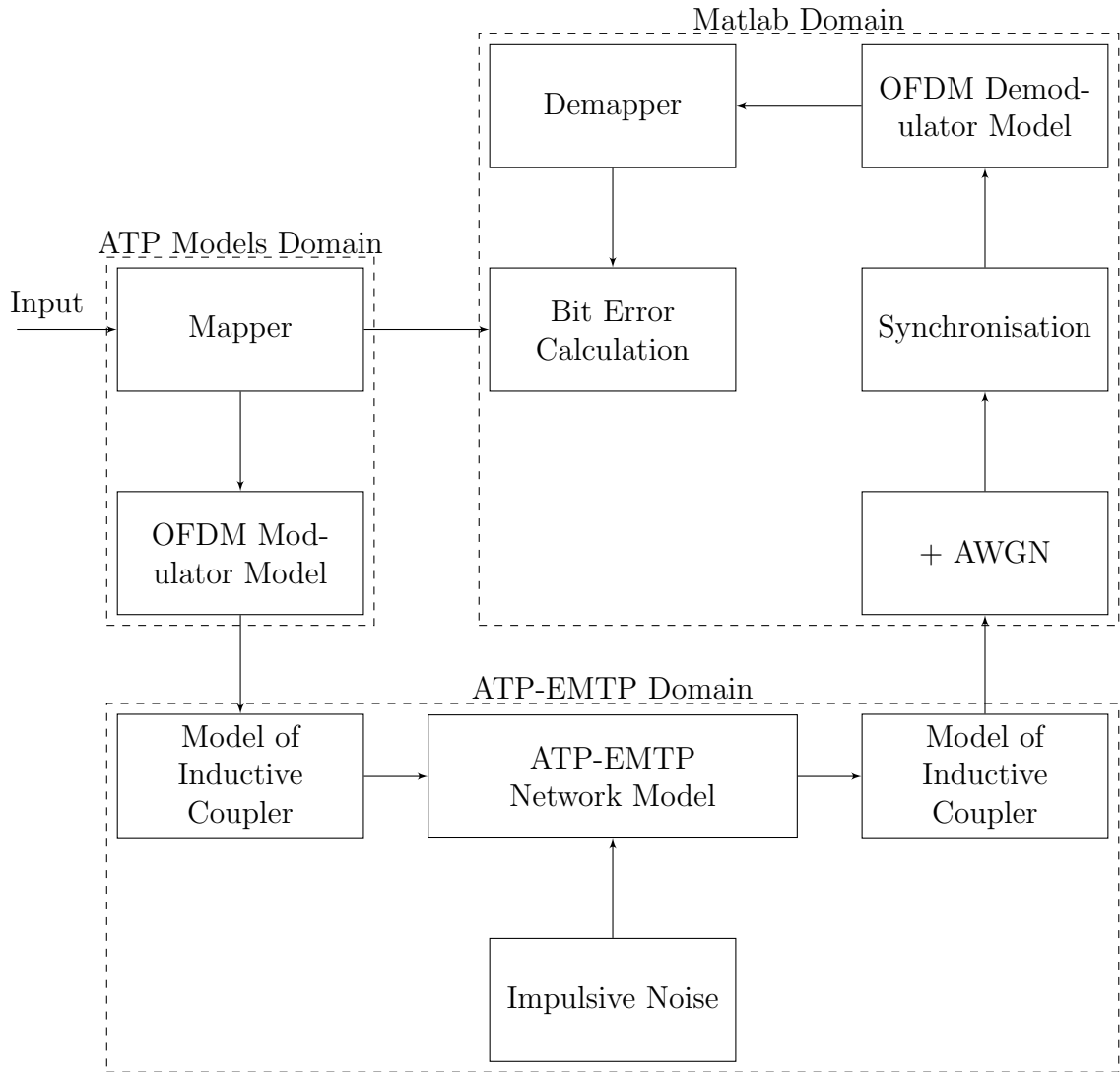


Figure 4.1: Block diagram showing the simulation methodology

Fig. 4.1 shows a block diagram summarising the simulation scheme. A multi-platform approach has been chosen. In the ATP/EMTP domain, the example network (introduced in Chapter 3) is implemented. Running alongside this is the ATP models domain, where several bespoke models have been created to perform the functions required to implement the OFDM transmitter. Synchronisation and demodulation takes place in the Matlab domain.

## 4.2.1 Development of the OFDM Modulator for the ATP Models Platform

It is assumed that the example network shown in Fig. 3.6 contains a number of Transmitter/Receiver units positioned at nodes A to E. The aim of simulating this example network is to assess the feasibility of communication between these nodes. To achieve this, a model of an OFDM modulator is created using the Fortran based Models language within ATP/EMTP. To replicate the modulator, the output timestep from the modulator model must be less than simulation timestep. This is achieved using the `TIMESTEP MAX` command within the OFDM modulator model. Setting the `TIMESTEP MAX` parameter to 1.2E-5 and the simulation timestep to 1E-7 means that the modulator model outputs a new value every 60 simulation timesteps. This effectively sets the output frequency of the OFDM modulator model to 166.7 kHz. Changing the `TIMESTEP MAX` changes the output frequency of the OFDM modulator model according to the following formula:

$$f_{mod} = \frac{2}{T_{max}} \quad (4.1)$$

The OFDM modulator model, listed in Appendix A.5, works by computing the N point IDFT of a randomly generated stream of data. The entire IDFT operation occurs during a single timestep and produces N output samples to be outputted in time sequence. In the Fortran models language, the IDFT is computed with the following code:

```

FOR p:=0 to y DO
  FOR n:=0 to y DO
    SR:=cos(p*(n/(y+1))*2*PI)
    SI:=-sin(p*(n/(y+1))*2*PI)
    FFrrr[p] := (FFrrr[p]+FFr[n]*SR)-((FFi[n]*SI))
    FFiii[p] := (FFiii[p]+FFr[n]*SI)+((FFi[n]*SR))
  ENDFOR
ENDFOR
FOR p:=0 to y DO
  FFrrr[p] :=((1/(y+1))*FFrrr[p])*3
  FFiii[p] :=-((1/(y+1))*FFiii[p])*3
ENDFOR

```

Figure 4.2: Fortran code for the IDFT part of the OFDM modulator.

The code in Fig. 4.2 performs a complex IDFT on the real input symbols,  $FFr$  and the imaginary input symbols,  $FFi$ . The real part of the output is  $FFrrr$  and the imaginary part is  $FFiii$

Cyclic prefix insertion is also handled in the OFDM modulator model. The final “*cyc*” samples are copied and inserted to the start of the symbol and the first “*y*” samples are shifted, creating a new symbol with length  $y + cyc$ , where *cyc* is the length of the cyclic prefix and *y* is the length of the useful part of the symbol. The variable *cyc* can be declared in the models dialog box, allowing flexibility in the size of the cyclic prefix.

```

FFiii[cyc..y+cyc]:=FFiii[0..y]
FFrrr[cyc..y+cyc]:=FFrrr[0..y]
FFiii[0..cyc-1]:=FFiii[y+1..y+cyc]
FFrrr[0..cyc-1]:=FFrrr[y+1..y+cyc]

```

Figure 4.3: Fortran code to perform the cyclic prefix insertion.

After the OFDM symbol is computed and the cyclic prefix is inserted, the model outputs the samples at a rate specified by the `TIMESTEP MAX` command. Two internal counters,  $r$  and  $R2$ , control whether a new symbol should be constructed and the indexing of output samples from the current symbol. The counter  $r$  resets to zero after a symbol has been constructed whereas  $R2$  continues to increment, allowing the model to control the timing of various events.

The outputs of the OFDM modulator model are the real and imaginary parts of the OFDM symbol (including the cyclic prefix). These values are passed onto the filter/quadrature mixer model. This model runs at the same timestep as the simulation meaning that the samples from the OFDM modulator have a “staircase” appearance. Two low pass reconstruction filters are used to remove high frequency aliases and smooth the appearance of the OFDM output. The filters are realised using the Z-function capability of the models language, allowing any digital filter to be replicated. Finally, the pass band OFDM signal is created by multiplying the real and imaginary waveform by the cosine, and sine of a carrier frequency, as shown in Fig. 4.4, where a carrier frequency of 600 kHz and an amplification factor of 100 is used. A summary of the simulation setup is shown in Fig, 4.5 and Table 4.1.

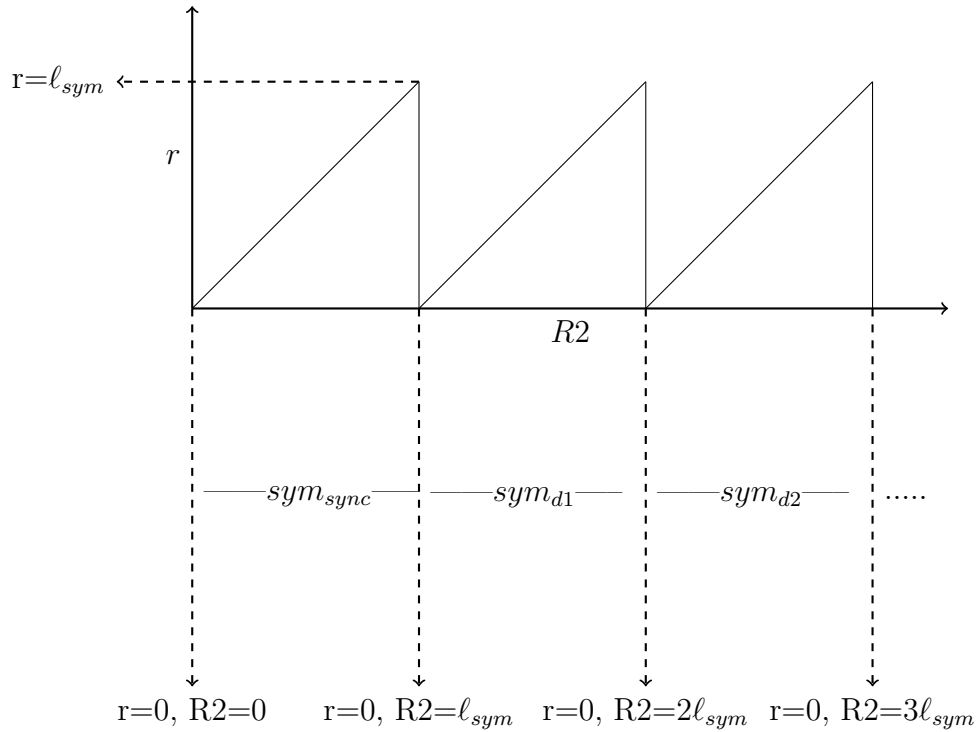


Figure 4.5: Diagrammatic Representation of Network Flow in the OFDM Transmitter Model

```

COMBINE AS po2
zfun(ar/B) := (0.0000954|z0 +0.0002863|z-1
+0.0002863|z-2
+0.0000954E-3|z-3)/(1|z0 -2.8116|z-1
+2.6405|z-2 -0.8281|z-3)
ENDCOMBINE
p:=br*sin(2*pi*T*600000)
q:=ar*cos(2*pi*T*600000)
sig:= p+q
JUMP:=100*sig
ENDEXEC
ENDMODEL

```

Figure 4.4: Fortran code showing a 4<sup>th</sup> order low pass digital reconstruction filter and the quadrature mixer (see Appendix A.6 for full Fortran code).

Table 4.1: Summary of logical flow in the OFDM transmitter model

$r$	$R2$	Action	Description
0	0	Generate Synchronisation Symbol, $sym_{syn}$	Perform IDFT on even sub-carriers of random constellation points.
$\ell_{sym} > N > 0$	0 to $\ell_{sym}$	Output samples	Output one sample per timestep, T.
0	$\ell_{sym}$	Generate Data Symbol, $sym_{d1}$	Perform IDFT on stream of random constellation points.
$\ell_{sym} > N > 0$	$\ell_{sym}$ to $2\ell_{sym}$	Generate Data Symbol, $sym_{d1}$	Perform IDFT on stream of random constellation points.

#### 4.2.2 Simulation of the Test Network in the ATP/EMTP and Matlab Domains

The test network introduced in Chapter 3, and detailed in Fig. 3.6 is used as the basis for the ATP/EMTP models domain outlined in Fig. 4.1. The output of the OFDM transmitter model is coupled to the line using a coupled inductive model. The inductive model is a mutually coupled RL element with a mutual inductance of 0.001 mH and a self inductance of 0.01 mH. The OFDM signal then propagates throughout the network and the received signal at each receiver node is demodulated using a demodulator model in Matlab (for the code of the Matlab OFDM demodulator, see Appendix A.2, and Appendix A.3 for the Schmidl/Cox synchronisation module). This process can be repeated to simulate communication between each node pair. The OFDM parameters are set to minimise the effect of the multipath interference by setting the subcarrier spacing to less than the coherence bandwidth of the channel. A centre frequency of 440 kHz is chosen with a 512

subcarrier symbol and a cyclic prefix larger than the worst case delay spread.

## 4.3 Effect of OFDM Parameters: Simulation Results

### 4.3.1 Bit Error Rate Due to Symbol Timing Offsets

For differentially coded OFDM, small timing offsets result in linear phase rotations across the subcarriers. For the case where the information is encoded in the phase difference between adjacent subcarriers in the same symbol, timing offsets result in a phase difference that deviates from that sent by the modulator. Increasing the timing offset increases the amount by which one subcarrier's phase will rotate compared to the subcarrier that precedes it, in turn increasing the likelihood that the received constellation point will move across the decision threshold, resulting in bit errors. For negative symbol timing offsets that fall within the cyclic prefix of the OFDM symbol, orthogonality may still be preserved. For positive timing errors, ISI and Intercarrier Interference (ICI) result in random phase fluctuations of the demodulated symbol and an inevitable and unpredictable increase in the BER. For channels impaired by multipath interference, the situation is further complicated. Each subcarrier experiences a phase shift due to the channel, however, a problem exists when adjacent subcarriers experience significantly different phase shifts, leading to the potential of an additional BER penalty.

The BER due to symbol timing offsets and multipath interference are examined for communication in the test network between node A and all other nodes. Separate simulations are performed for DBPSK, QPSK and 8PSK. The sample with an offset

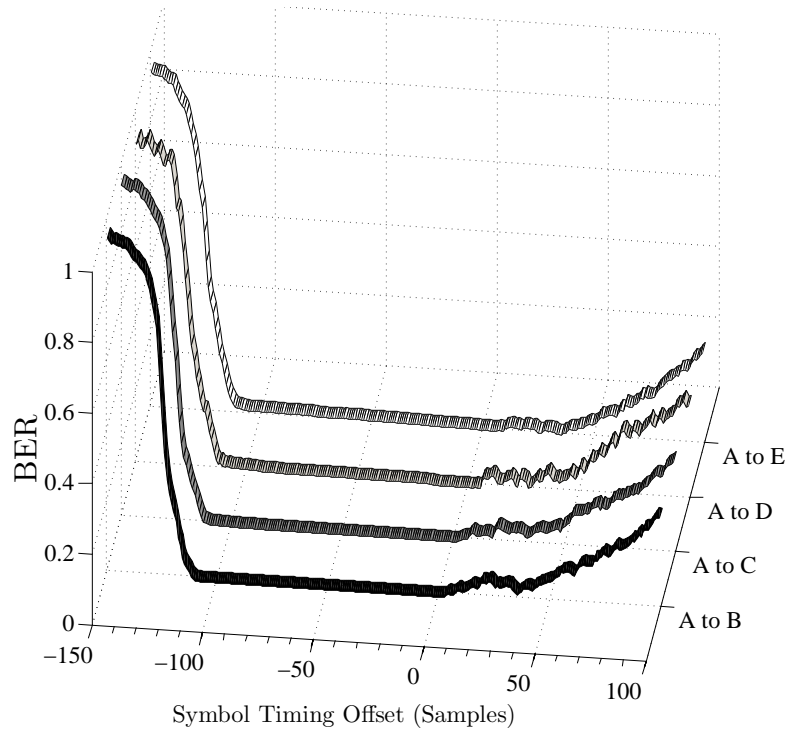


Figure 4.6: BER due to symbol timing offset in the DBPSK system

of zero is determined manually using the propagation time and distances between the nodes. Fig. 4.6 shows the BER for timing offsets in the case of DBPSK. The corresponding plots for DQPSK and Q8PSK are shown in Fig. 4.7 and Fig. 4.8 respectively.

The results confirm that there is an immediate BER penalty for positive timing offsets for all three modulation schemes. For negative timing offsets, the BER is unaffected until a critical point is reached. This period of grace where no significant BER penalty is incurred is longest for DBPSK ( $\approx 100$  samples, i.e. two thirds of the CP length) and shortest in the D8PSK scheme ( $\approx 15$  samples). Beyond this critical point, the BER quickly rises to above 0.5, suggesting that the linear phase rotation has crossed the decision threshold. For positive timing offsets, there is an

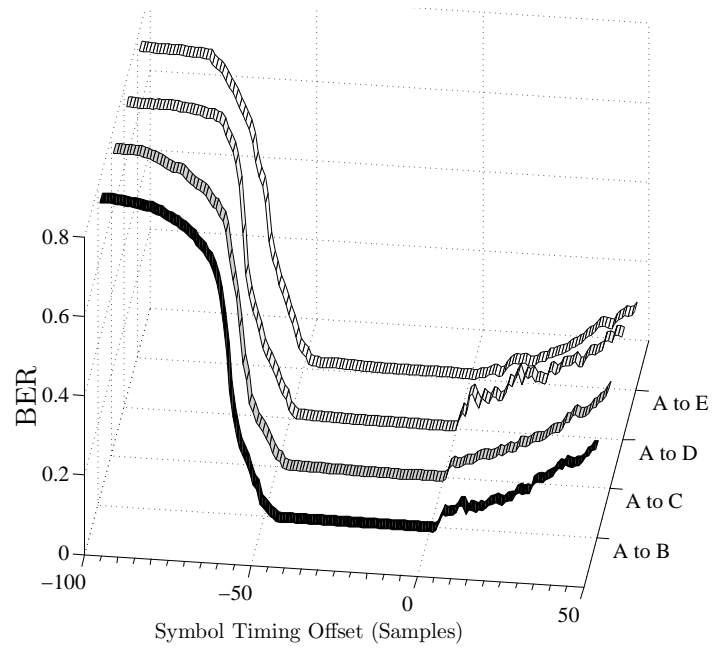


Figure 4.7: BER due to symbol timing offset in the DQPSK system

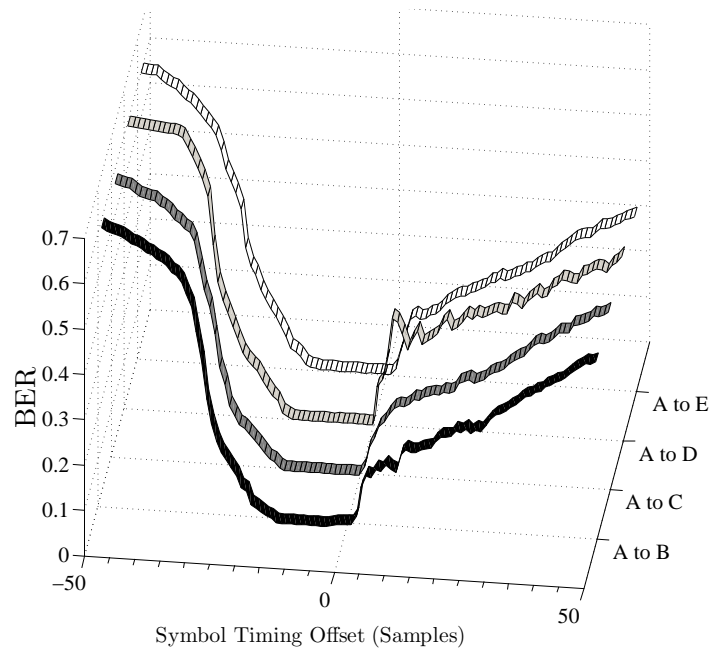


Figure 4.8: BER due to symbol timing offset in the D8PSK system

immediate, but gradual increase in BER. Again, the performance of the DBPSK shows more robustness than the modulation schemes with denser constellations.

### 4.3.2 Performance of Synchronisation Schemes on the Test Network

A Schmidl/Cox timing estimator is modelled as the front end of the demodulator in the Matlab environment. In the modulator model (in the ATP Models domain shown in Fig. 4.1), a synchronisation symbol with two equal halves in the time domain is produced by transmitting only on the odd subcarriers. This synchronisation symbol precedes the information symbol. The analysis is furthered by considering a number of refinements to the Schmidl/Cox estimation algorithm. The first, in response to a tendency of the timing metric,  $M(d)$  to reach false peaks, is to use only the correlation term metric,  $P(d)^2$ . A further refinement can be made to avoid erroneous peaks at points along the plateau caused by the presence of the cyclic prefix. Passing  $P(d)^2$  through a low pass filter of length approximately equal to half the cyclic prefix length (in samples) gives rise to a new metric,  $P_f(d)^2$  with the desirable property of peaking at approximately the end of the plateau. Furthermore, another refinement can be made by introducing a "back off" of a pre-designated number of samples to decrease the likelihood of a positive symbol timing estimate whilst remaining in the area where the BER is not significantly raised. Here, the method of using a low pass filter and subsequent finding of the peak of  $P_f(d)^2$  is used. A "back off" may be applied later.

Assume a 500 subcarrier, 512 point FFT OFDM system is used. The cyclic

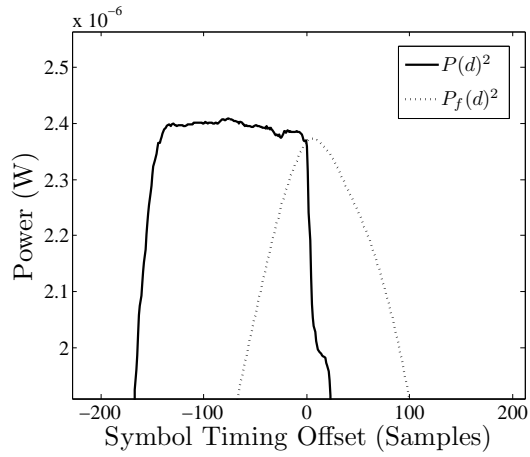
prefix length is chosen as 167 samples, translating to a time of 1 ms in a system with a sampling frequency of 166.7 kHz. The total symbol length, including cyclic prefix, is 4 ms.

#### 4.3.2.1 Shape of the Autocorrelation metric, $P(d)$

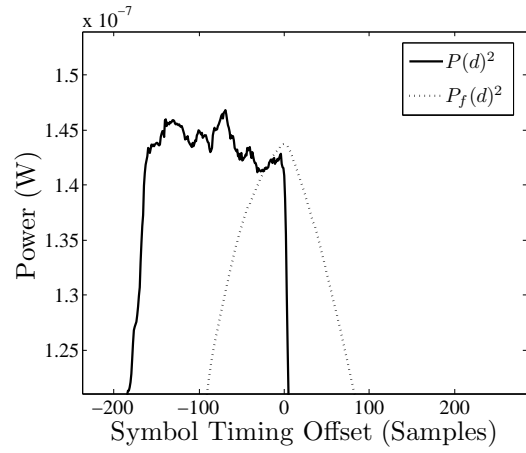
The shape of  $P(d)$  is of critical importance to the overall performance of the timing estimator. The presence of the plateau in the metric complicates the task of detecting the start of the information symbol because the actual peak may appear anywhere on the plateau, whereas the ideal timing point (corresponding to a timing offset of zero) is the final sample of the plateau. The idea of using an LPF to construct a new metric,  $P_f(d)^2$ , may help by peaking at approximately the final sample of the plateau.

Communication is attempted between all node pairs on the test network and the metric  $P(d)$  is observed. The metric  $P_f(d)^2$  is also computed and overlaid on  $P(d)$ . It can be seen in Fig. 4.9 that the peak of  $P_f(d)^2$  aligns with the end of the plateau.

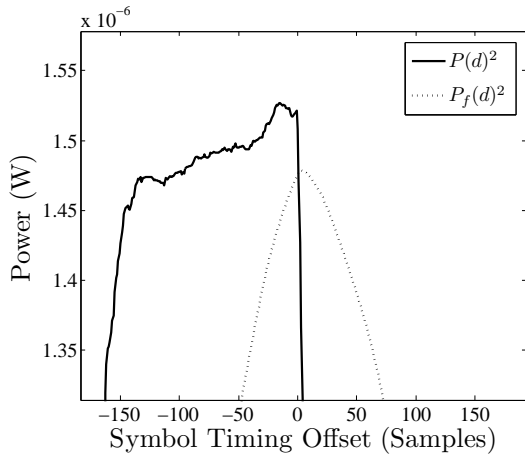
The shape of  $P(d)$  is variable and depends on a number of factors. First, the SNR determines how flat the plateau is. Another factor is the positions of the communicating nodes. A very noticeable phenomenon is the tendency of the plateau of  $P(d)$ , for communication between some nodes, to extend beyond the optimum timing point. This results in positive symbol timing offsets. The tendency of the timing estimate to extend seems to be unrelated to the SNR, rather it is



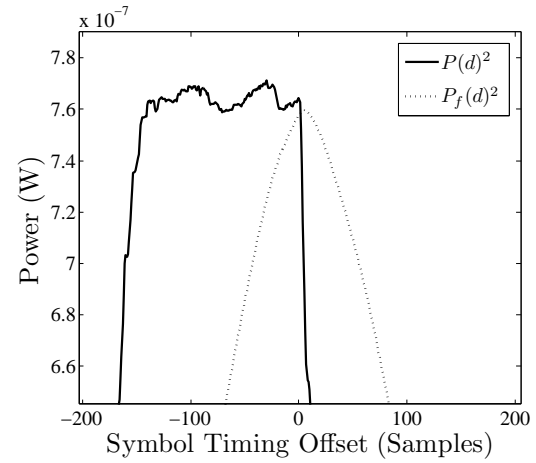
(a) Node A to B



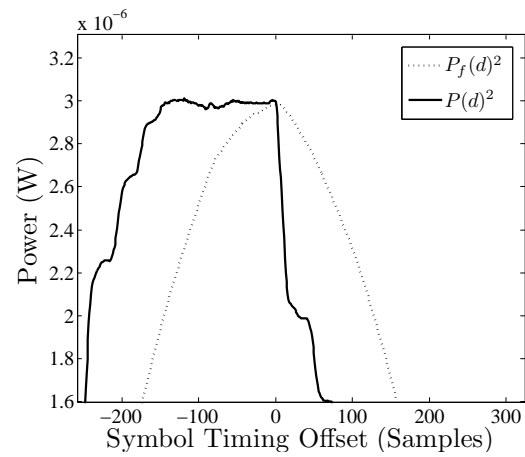
(b) Node A to C



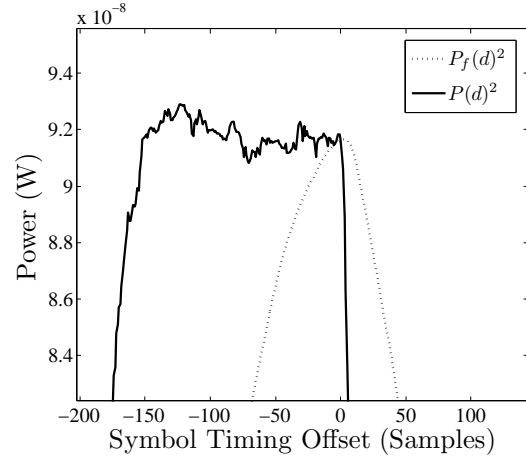
(c) Node A to D



(d) Node A to E



(e) Node B to A



(f) Node B to C

Figure 4.9:  $P(d)^2$  and  $P_f(d)^2$  for communication between selected nodes.

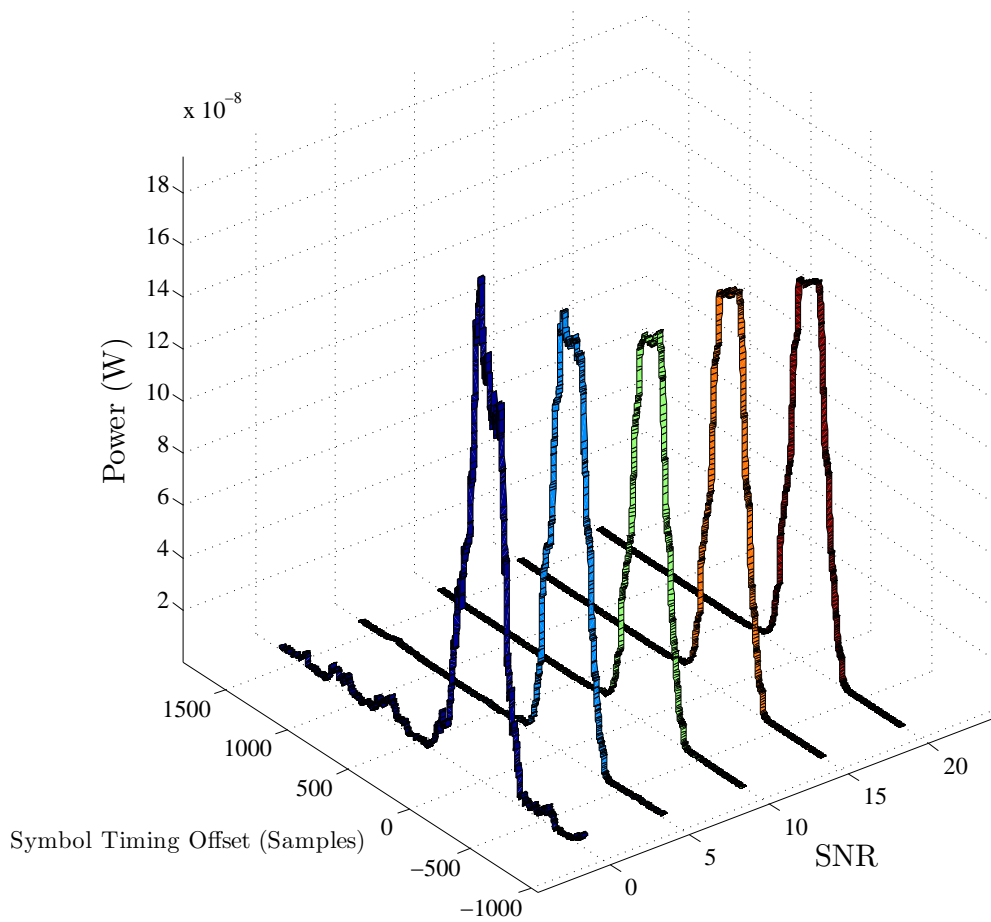


Figure 4.10:  $P(d)$  at different SNR values with various symbol timing offsets

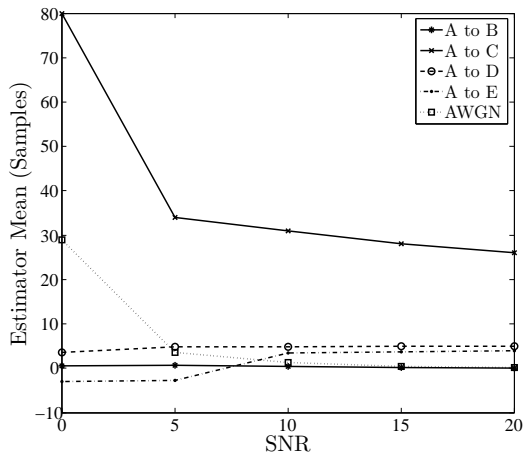
the particular combination of reflections at that point. This phenomena will be discussed in more detail in the following section, where the mean and variance of the timing estimates are shown.

To demonstrate the effect of SNR on the shape of  $P(d)$ , a three dimensional plot showing a family of  $P(d)$  metrics at different SNR values is shown in Fig. 4.10. As can be seen in Fig 4.10, it is clear that the plateau is flatter at higher SNR values. At an SNR of 0, the metric has no clear plateau.

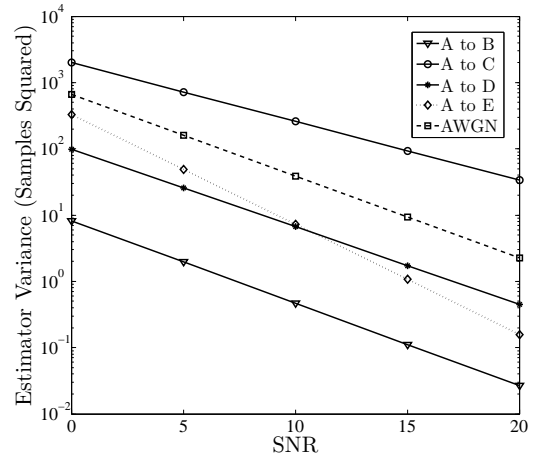
### 4.3.2.2 Mean and Variance of the Timing Estimator

The mean and variance between all node pairings involving A, B, C, D and E are shown in Fig. 4.11 and Fig. 4.12. There is an exponential relationship between SNR and the timing estimator variance. Both the mean and variance of the timing estimates are highly dependent on the shape of the correlation term,  $P(d)^2$ . In some cases, the expected drop in the correlation term is disrupted by the presence of reflections. This leads to the peak of the low pass filtered term being pushed to beyond the optimum timing point. This increases the likelihood of a positive symbol timing offset and explains the positive mean value for communication between A and C, as shown in Fig. 4.11(a). As discussed in section 4.4.2.1, increasing the SNR does little to reduce the mean because the correlation function is affected by reflections of the correlation symbol itself. In practice, this decreases the performance of the timing estimator between some node pairings at particular frequencies. It is noted that the tendency for disruption in the falling part of the correlation term is highly dependent on frequency. For instance, communication between A and C using a centre frequency of 480 kHz (as opposed to 440 kHz) results in a mean that is very close to 0 over the SNR range of 0 to 20 dB.

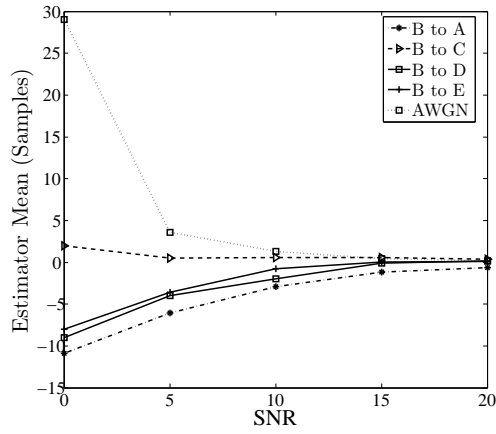
To highlight the importance of the shape of the correlation term on the timing estimator performance, three node pairings are compared. As can be seen in Fig. 4.13(a) and Fig. 4.13(b), for communication between A and C at an SNR of 10 dB, most of the estimates (out of 1000 simulation runs) are positive. Fig. 4.13(c) and Fig. 4.13(d) suggests that the same applies, but to a lesser degree, for commu-



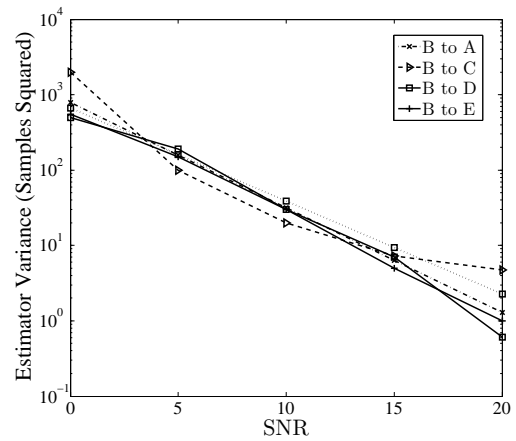
(a) Mean



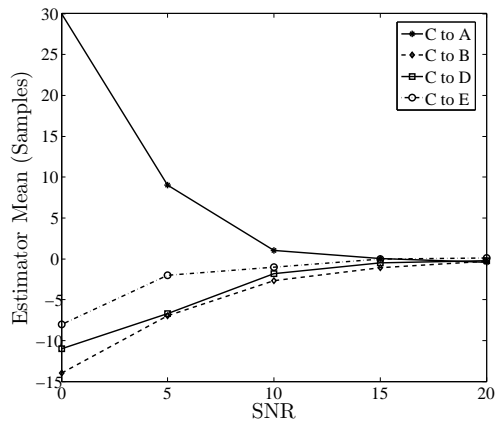
(b) Variance



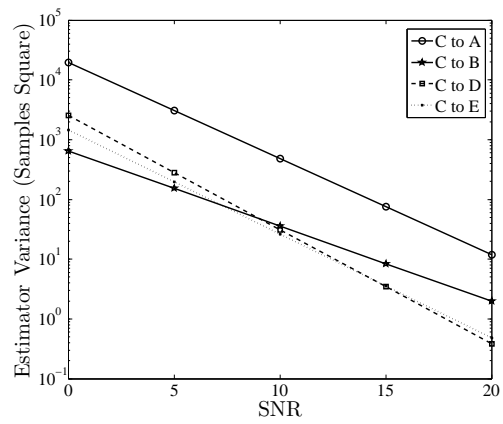
(c) Mean



(d) Variance

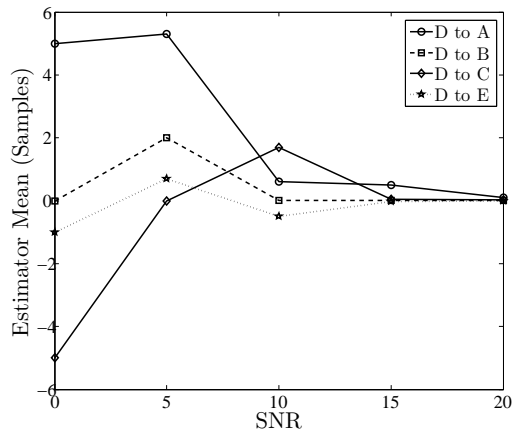


(e) Mean

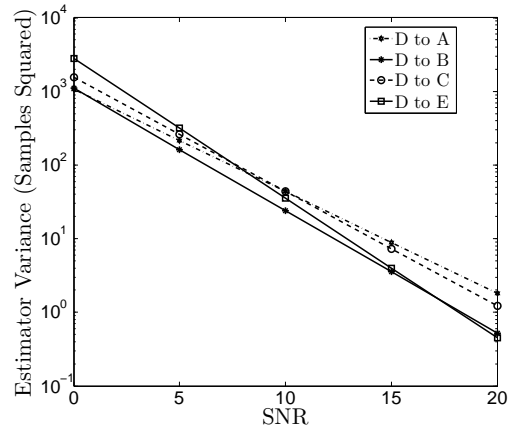


(f) Variance

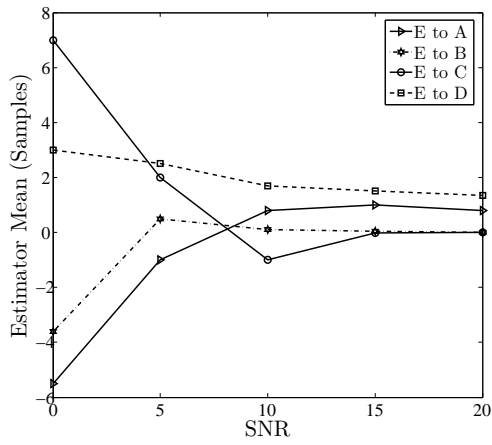
Figure 4.11: Timing Estimator Mean and Variance for communication between nodes A, B and C and all other nodes.



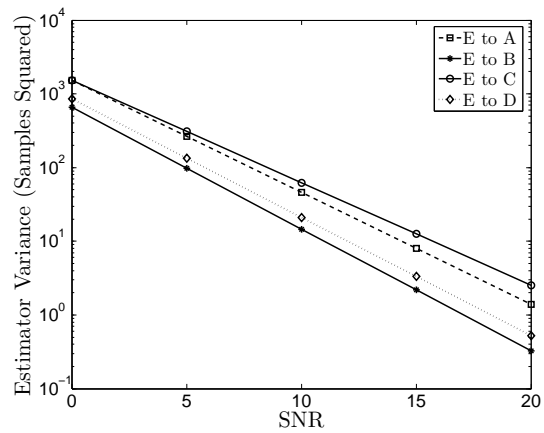
(a) Mean



(b) Variance



(c) Mean



(d) Variance

Figure 4.12: Timing Estimator Mean and Variance for communication between nodes A, B and C and all other nodes.

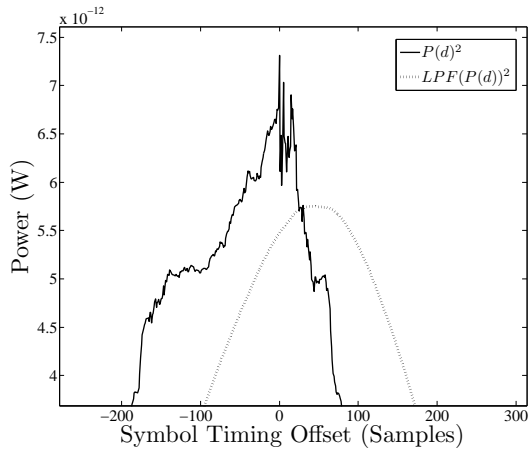
nication between nodes A and B. For communication between A and D, shown in Fig. 4.13(e) and Fig. 4.13(f), the estimates are equally distributed between positive and negative.

#### 4.4 Performance of OFDM: Effect of Number of Subcarriers, Length of Cyclic Prefix and Modulation Scheme

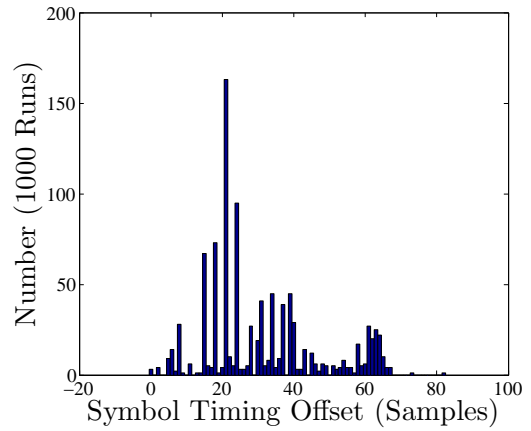
The most important parameters affecting the performance of an OFDM modulation scheme are the number of subcarriers, the length of the cyclic prefix and the choice of subcarrier modulation scheme [74]. It was shown in Fig. 3.19 that the coherence bandwidth of the test network which represents a typical rural 11 kV network, is relatively low compared to typical wireless communication channels. Differential modulation schemes operating over this channel must have a subcarrier spacing that is less than the coherence bandwidth to avoid a large BER penalty. The relationship between the number of subcarriers ( $N_{carr}$ ), the sampling frequency ( $f_s$ ) and the subcarrier spacing ( $S_{spacing}$ ) is given by:

$$S_{spacing} = \frac{f_s}{N_{carr}} \quad (4.2)$$

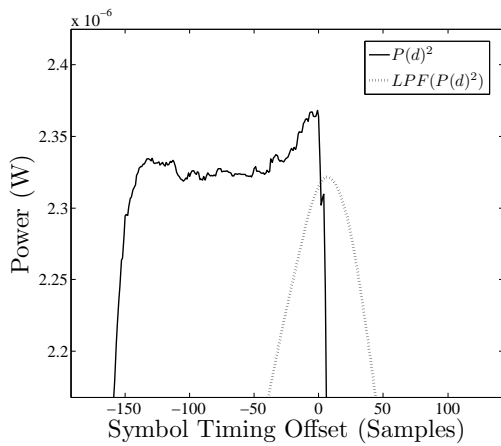
Equation (4.2) suggests that the subcarrier spacing is proportional to the sampling frequency and inversely proportional to the number of subcarriers. For the OHMS concept, this presents a dilemma. On one hand, it would be desirable to decrease  $N_{carr}$  to shorten the symbol period, yet on the other,  $N_{carr}$  should be lengthened to minimise the subcarrier spacing. The sampling frequency is limited



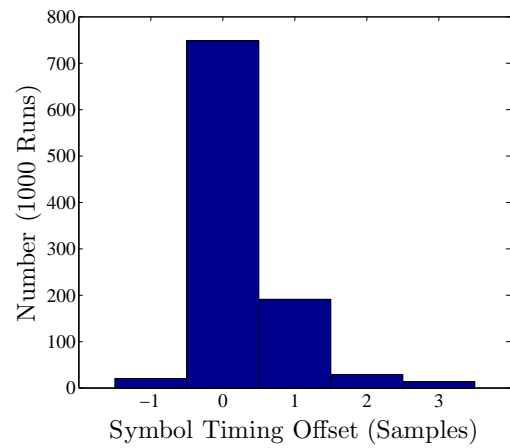
(a) A to C (SNR=10 dB)



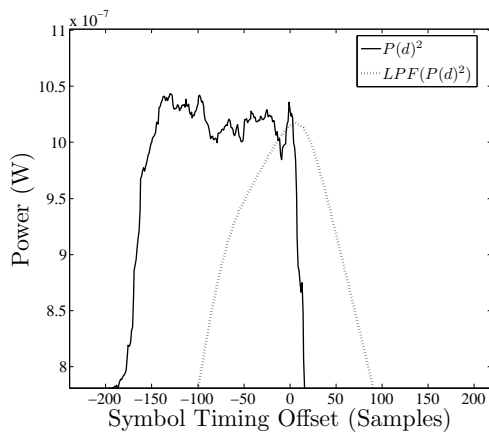
(b) Histogram of timing estimates: A to C (10 dB)



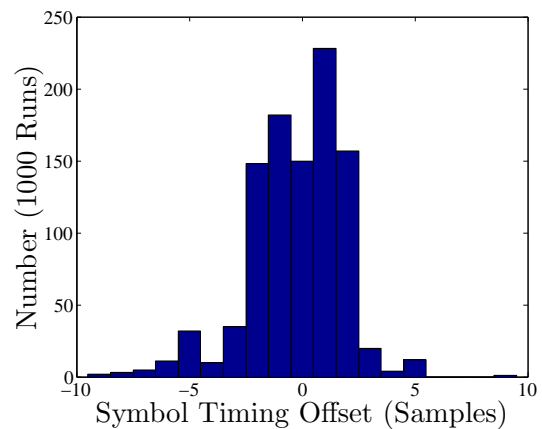
(c) A to B (SNR=10 dB)



(d) Histogram of timing estimates: A to B (10 dB)



(e) A to D (SNR=10 dB)



(f) Histogram of timing estimates: A to D (10 dB)

Figure 4.13: Timing metric and associated histograms from 1000 simulation runs at an SNR of 10 dB

Table 4.2: Table to show the OFDM modulation schemes under study

Scheme	Subcarriers	Cyclic Prefix Duration		Symbol Duration ( $\mu\text{s}$ )
		Samples	Time ( $\mu\text{s}$ )	
A	128	25	150	768
B	128	75	450	768
C	128	150	900	768
D	256	25	150	1536
E	256	75	450	1536
F	256	150	900	1536
G	512	25	150	3072
H	512	75	450	3072
I	512	150	900	3072

by the available bandwidth.

In Table 4.2, a number of possible OFDM schemes are listed. The number of subcarriers<sup>2</sup> is limited to 128, 256 and 512. A sampling frequency of 166.7 kHz is used. The cyclic prefix lengths are chosen as 25, 75 and 150 samples, translating to a duration of 150, 450 and 900  $\mu\text{s}$  respectively. These are chosen to be similar to typical RMS delay spreads of the channel, as calculated for the test network in Section 3.5.2.

Fig. 4.14 shows a scatter diagram of the BER performance (averaged for  $f_c=400, 440, 480, 520, 560$  and  $600$  kHz and with no noise) versus the maximum permissible bit rate (assuming every subcarrier is used to carry information, symbols are sent continuously and there is no synchronisation symbol). The figure is colour coded to show the difference for DBPSK, DQPSK and D8PSK schemes. It is is

<sup>2</sup>Choosing  $N_{carr}$  to conform to  $2^n$  allows the FFT algorithm to be used.

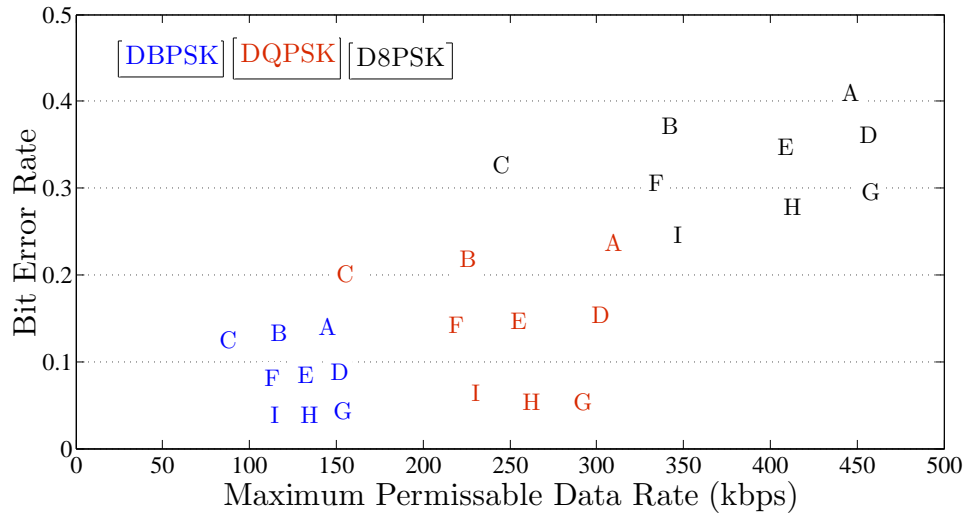


Figure 4.14: Scatter diagram showing average. BER versus maximum permissible data rate for the schemes outlined in Table 4.2.

observed that there is a trade-off between data rate and BER, indicated by the high BERs experienced by D8PSK schemes but relatively low BERs in DBPSK schemes. Another noticeable trend is the link between the number of subcarriers and BER. The lowest BERs, for example, tended to be with those schemes using 512 subcarriers whereas the worst BER performance was in schemes using 128 subcarriers. This can be explained with reference to Equation 4.2. For a 128 subcarrier scheme, the subcarrier spacing is approximately 1300 Hz compared to 325 Hz in the 512 subcarrier scheme. Increasing the number of subcarriers even further, say to 1024, would lead to a subcarrier spacing of 162 Hz below the 200 Hz suggested maximum figure (set out in Section 3.6.3. However, a 1024 subcarrier symbol (requiring a symbol duration of 1024 samples) would increase the symbol duration and limit the speed of communication required in the OHMS concept.

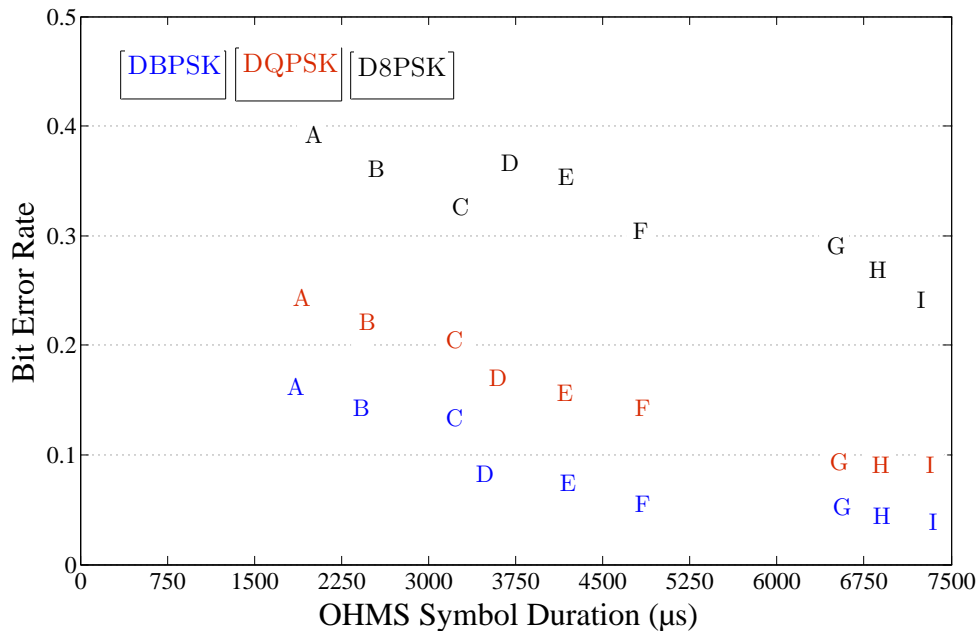


Figure 4.15: Scatter diagram showing BER versus OHMS symbol duration rate for the schemes outlined in Table 4.2.

To examine the performance of each scheme in terms of its symbol duration, another scatter diagram is plotted and shown in Fig. 4.15. Here, the symbol duration is considered to be the duration of a complete communication “burst” (e.g. a synchronisation symbol followed by an information symbol, with both symbols appended by a cyclic prefix, known henceforth as an “OHMS” symbol.). In this case, the lower subcarrier schemes offer the best performance because an OHMS symbol can be sent in the quickest time. Schemes using 512 subcarrier have the largest OHMS symbol durations. Overall, this analysis has shown that there is a trade-off between symbol duration, BER and achievable data transfer per transmission.

## 4.5 Concentration of Bit Errors

Errors due to multipath interference tend to be concentrated on specific areas in the frequency spectrum where large phase rotations, caused by the channel, push the received constellation point away from the sent constellation point. Adaptive OFDM is an attempt to improve throughput by, first, actively avoiding transmitting on subcarriers that experience large phase rotations and second, using denser constellation modulation schemes for the subcarriers with a high SNR and relatively unaffected by phase rotations. The results shown in Fig. 3.19 show that there are a large number of sizeable phase rotations for subcarrier spacings less than 1 kHz, indicating that the PLC HV channel would benefit from the implementation of adaptive techniques. This is also shown in Fig. 4.16, where the BER per subcarrier is plotted for communication between different nodes. Fig. 4.16 suggests that the errors are concentrated at certain frequencies, supporting the view that an adaptive scheme would offer considerable benefits in performance.

## 4.6 Effect of Multipath on Received Signal Strength

It is well established that the attenuation experienced by a signal travelling between two points on a network is unpredictable because the signal strength at any point is highly dependent on the multipath characteristics rather than the attenuation per unit length of the power line. Therefore, a problem may emerge if one node attempts to send an OFDM symbol to all other nodes simultaneously (broadcast). An acceptable SNR may be achieved at one node, but at another, the highly

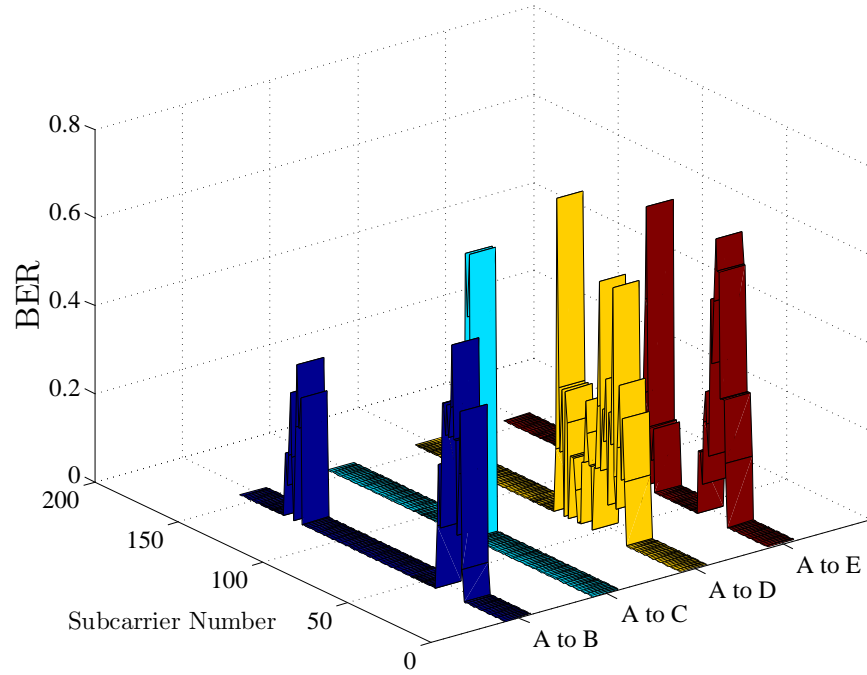


Figure 4.16: Bit Error Rate by subcarrier using a system with centre frequency 460 kHz and a bandwidth of 166.7 kHz

frequency selective channel may attenuate the signal to a received power falling below the requirements for a target BER. Fig. 4.17 shows the attenuation experienced when node A broadcasts an OFDM symbol to all other nodes on the network. It can be clearly seen from Fig. 4.17 that there is a large variation in attenuation for the channels existing between the possible node pairings. This makes it difficult to specify the power requirements of the OHMS transmitter to achieve a target BER.

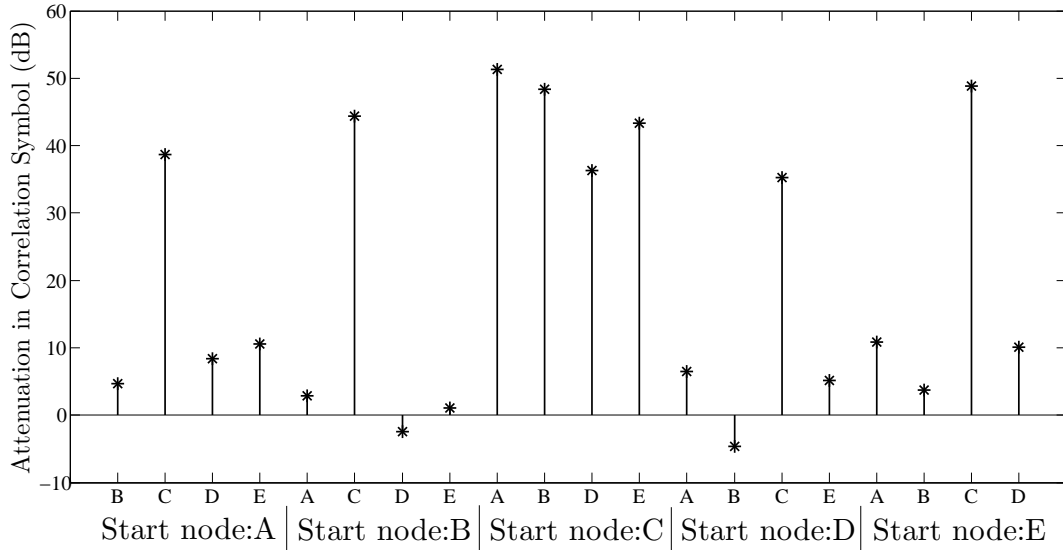


Figure 4.17: Attenuation between nodes on the Test Network

## 4.7 Effect of Coupling Scheme

The coupling scheme chosen determines how much of each mode is excited. The previous analysis in this chapter has assumed that the three modes are separate, and considered each one in isolation. In reality, a coupling scheme will excite at least two and sometimes even all three modes. This may be problematic for communication over large distances because each mode travels at a slightly different speed, leading to deterioration of the intended signal if it is taken from a single conductor.

Fig. 4.18 shows a number of possible coupling schemes using one or two coupling devices. With the line model shown in Fig. 3.1, an inductive RL model is used to model the couplers in ATP/EMTP and the amount of signal energy entering each mode is examined for each of the coupling schemes shown in Fig. 4.18. The results

are shown in the form of phasor diagrams plotted in Fig. 4.19.

It is worth noting that the amount of energy excited into each mode is dependent on the dimensions of the line, however, the proportion of energy entering each mode for a given scheme will be similar for lines with similar geometry. It is interesting to note from Fig. 4.19 that schemes using only a single conductor tend to excite all 3 modes. This is due to lines of magnetic flux (created by the coupler induced current) inducing voltage in all three modes for the three conductor geometry (as a result of Faraday's law of induction). In centre phase coupling (Fig. 4.18(a)), the majority of the energy is excited in mode 1 (ground mode). In contrast, when outer phase coupling is used (Fig. 4.18(b)), the majority of the energy is coupled into mode 2 (an aerial mode). This is an important result because it shows that a viable coupling scheme is possible with only a single coupler placed on one of the outer conductors. It is possible with a coupler on each conductor operating in "push-pull" mode, i.e.  $180^\circ$  out of phase, to couple with high efficiency into mode 2. Although efficient coupling into the aerial modes is possible using more than one coupler, the duplication of cost and added complexity makes multiple coupler coupling schemes undesirable.

## 4.8 Proposed OFDM Scheme for the OHMS System

A number of key points can be derived from the simulation results discussed in this chapter:

- The BER penalty for symbol timing errors is variable, depending on whether

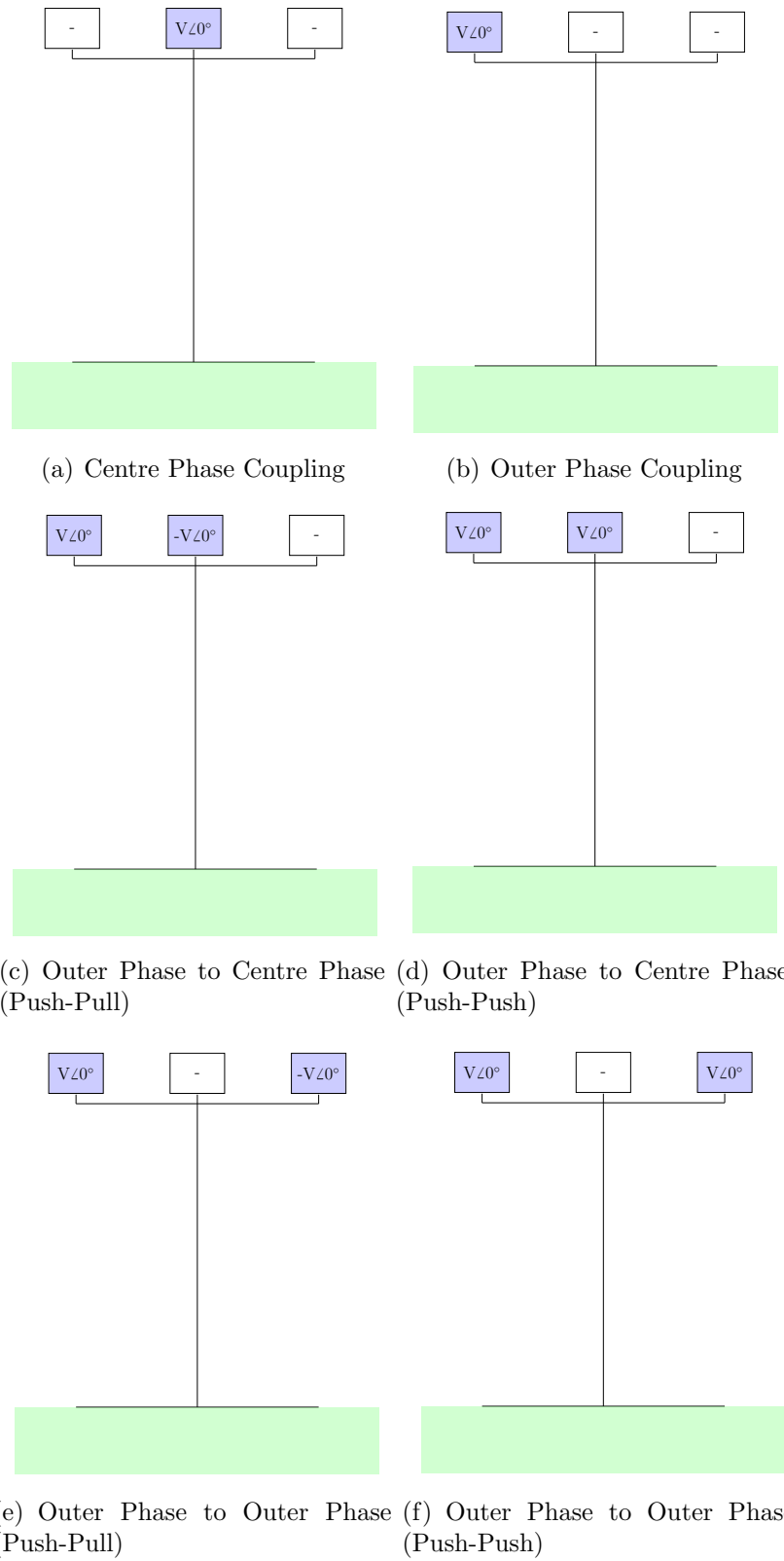
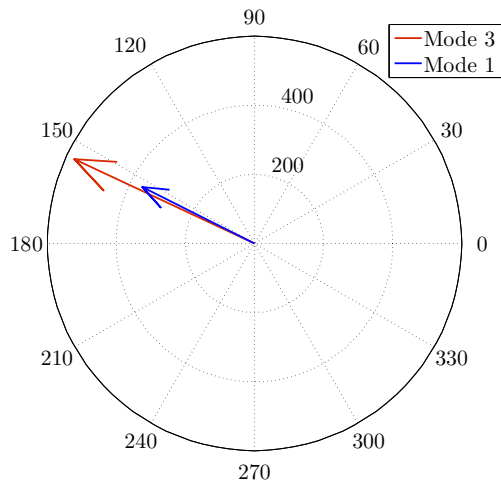
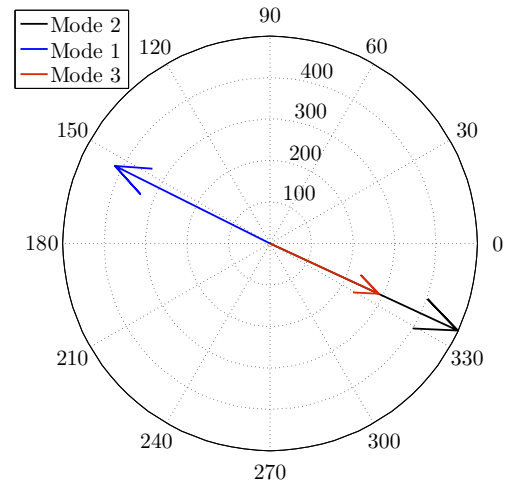


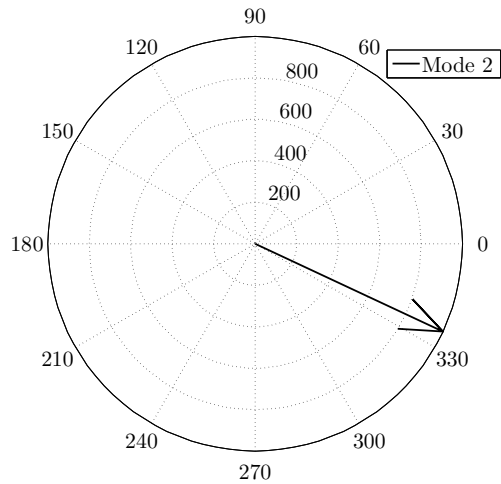
Figure 4.18: Configuration of possible coupling schemes on a three conductor line



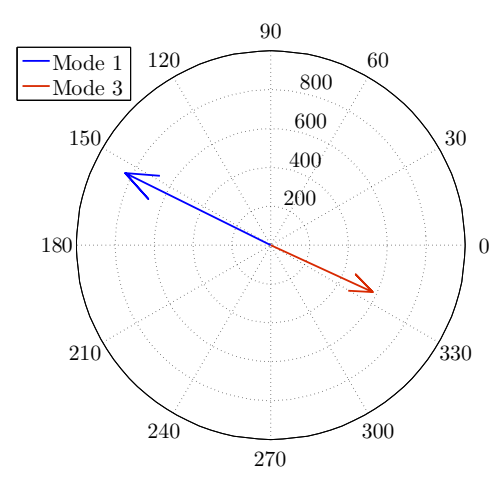
(a) Centre Phase Coupling



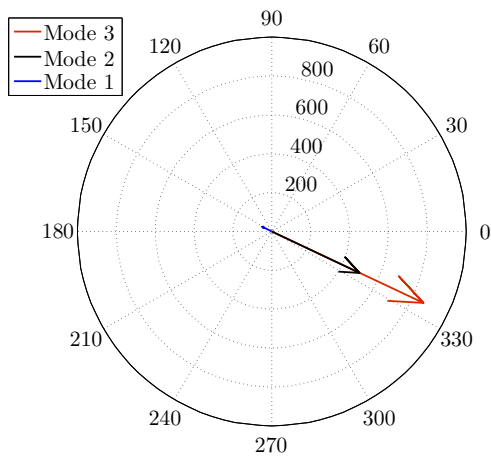
(b) Outer Phase Coupling



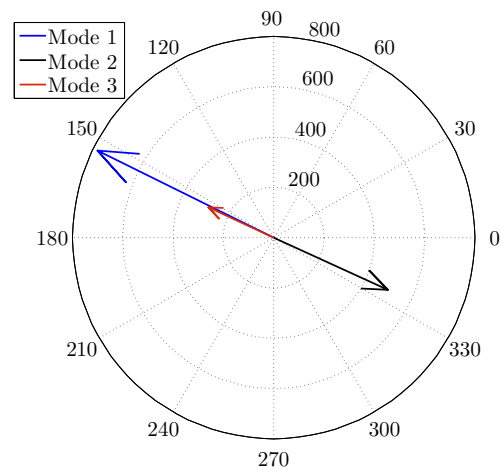
(c) Outer Phase to Outer Phase (Push-Pull)



(d) Outer Phase to Outer Phase (Push-Push)



(e) Outer Phase to Centre Phase (Push-Pull)



(f) Outer Phase to Centre Phase (Push-Push)

Figure 4.19: Voltage phasors induced into the modes for different coupling schemes

the offset is positive or negative. For negative timing errors (i.e. starting the FFT early), there is a period of grace where no BER penalty is imposed. After this period, the BER increases rapidly. For positive timing offsets (i.e. starting the FFT late), there is an immediate BER penalty. It has been shown that using denser constellation modulation schemes decreases the period of grace for negative timing offsets and has a higher BER for positive timing offsets.

- The performance of the Schmidl/Cox timing estimator is significantly improved by using an LPF to ensure that early peaks on the plateau are not used. Furthermore, the presence of a back-off of several samples increases the robustness of the timing estimator by steering the estimate away from positive timing estimates.
- It was demonstrated that it is possible to achieve efficient coupling into one of the aerial modes using a single coupler on one of the outer conductors. If more couplers are available, there is a possibility for even higher efficiency into the aerial modes.

## 4.9 Proposed OFDM Modulation Scheme

Based on the results in this Chapter, a proposal for a communication system is now made. The system should ideally be a 512 subcarrier system, though 256 subcarrier and, to an extent, 128 subcarriers may still be used provided DBPSK is used for subcarrier modulation. The cyclic prefix should be no less than the RMS delay spread of the channel which, in the 166.7 kHz system, amounts to

around 150 samples. The subcarrier modulation scheme has been shown to greatly affect the BER. If DBPSK is able to meet the information requirements of the implemented system, DBPSK should be chosen because it provides the greatest robustness to multipath effects and AWGN. The use of DQPSK and D8PSK could be implemented in channels exhibiting a high SNR and in combination with an efficient error-correction coding scheme at the receiver.

#### 4.10 Conclusion

The channel response of radial HV networks is dominated by multipath effects. The consequence of this is an extremely large RMS delay and a small coherence bandwidth. This poses a significant challenge in the design of a communication scheme to cope with such channel impairments. It has been shown that an optimised form of OFDM is capable of providing robust communication between remote nodes on the HV rural network. The unfortunate consequence of ensuring robust communication on the HV channel is the requirement for a large cyclic prefix, which is a waste of power and time. Another practical problem is the requirement for a synchronisation symbol so the receiver can detect the arrival of a symbol. It has been shown that a synchronisation scheme based on autocorrelation is a reliable method. The synchronisation symbol, however, does not carry information but increases the OHMS symbol duration. A possible mitigating measure that has not been discussed in this Chapter, would be to use the synchronisation symbol to send information, an idea that to the author's knowledge has not been considered in conventional OFDM

schemes but may nonetheless be useful in this niche application.

## Chapter 5

### Application of the OHMS Concept for Fault Location on 11 kV

#### Networks

##### 5.1 Introduction

The use of travelling waves as a means of identifying the faulted part of a distribution feeder is not a new concept. For example, in [75], the measured travelling wave is compared to known reflection points on the network. Other methods of using travelling waves to locate faults are described in [76] [77].

In this chapter, a theoretical examination of possible applications for the OHMS system is carried out. The main application considered is a new fault location scheme based on the synchronous measurement of the fault induced transient and the execution of an algorithm to triangulate the location of the fault based on the network topology.

##### 5.2 Proposal for a New Multi-ended Fault Location Scheme

###### 5.2.1 Principles of Proposed Approach

There is increasing pressure on network operators to improve the reliability of their networks [78] [79]. Faults are a major cause of outages leading to customer minutes lost (CMLs) which are penalised by the regulator, OFGEM, in the UK.

Locating faults in a quicker and more efficient way is a means of reducing CMLs and improving the performance of networks. In recognition of this, there has been a significant body of research looking into ways of expediting the location of faults on power networks. It was stated in Chapter 1 that it is customary to place each fault location method into one of three categories. First, impedance based methods [80], [81]. Second, travelling wave methods [82] [83] and third, knowledge based methods [84]. Impedance based methods and certain types of travelling wave methods have been shown to work well on point to point (i.e., branchless) type networks. For teed (i.e. branched) networks, existing methods often perform poorly and fail to unambiguously locate a fault. Furthermore, the majority of customer interruptions originate on the 11 kV network (in the UK), which are large, sprawling and almost always radial. There is a case, therefore, for the development of better fault location methods on these type of networks.

The present approach relies on the capture, time-stamping and retrieval of the initial high frequency fault induced component. The combination of the transducer (to capture the fault induced transient), the FPGA (to execute trigger control and perform the function of the MODEM), a method of communicating the timestamp information back to a central point (e.g., Power Line Communication ((PLC)) or wirelessly), and the GPS receiver (for time-stamping the arrival time of the fault induced transient), is termed an Overhead Line Monitoring System (OHMS) device. It is shown that a scheme able to determine unambiguously the location of a fault can be implemented if an OHMS device is placed at each branch termination in a network. The method depends on prior knowledge of the distances between

tee points (where two branches meet) and the branch terminations. It is further assumed that the propagation velocity of the high frequency fault induced transient is a constant, however, correction factors for cable sections may be included to improve accuracy. Further improvements in accuracy can be gained by implementing a calibration scheme that determines the actual velocity of the wave between various points on the network. Here, It is suggested that an optimised form of Power Line Communication (PLC) is an effective way of retrieving the GPS time-stamp information from each OHMS device and additionally provides a means of carrying out the calibration scheme.

The most common type of fault on overhead line networks is line to ground fault. Such faults are associated with a sudden change in voltage caused by the earthing, through an impedance, of one or more of the conductors. Assuming a three-conductor unearthed overhead line system of flat formation, this sudden change gives rise to a high frequency travelling wave that propagates through the power system in three independent modes [85]. Of these three modes, two are characterised as aerial modes and support propagation of the high frequency transient at close to the speed of light with relatively low attenuation. The third mode is termed the ground mode and is characterised by propagation at around half to two thirds the speed of light and a relatively high attenuation [86]. It has been shown that the frequency spectra of the induced travelling wave is not affected by the fault type or the impedance characteristics of the path to ground [87].

Modal theory is often used to transform the phase quantities into modal quantities using the transformation matrices,  $[T_i]$  and  $[T_v]$ , of the line structure, where

$[T_i]$  is the matrix that related the modal and phase currents and  $[T_v]$  the matrix relating the modal and phase voltages:

$$[I_{mode}] = [T_i]^{-1}[I_{phase}] , \quad (5.1)$$

$$[V_{mode}] = [T_v]^{-1}[V_{phase}] \quad (5.2)$$

The following analysis uses the line model shown in Table 3.1 with transformation matrix,  $[T_v]$ , for a typical 11 kV overhead line structure of wood pole construction.

Fig. 5.1(a) shows the modal components resulting from an ATP/EMTP simulation of a centre phase to ground fault occurring on the overhead line structure detailed in Table 3.1. It is observed that modes 1 and 3 are induced by the sudden drop in voltage immediately following the grounding of the conductor ( a result shown in polar form in Fig. 4.19(a)). For an outer phase to ground fault, all three modes are excited (as shown in Fig. 5.1(b)).The signal in each mode propagates away from the fault. The propagation velocity of the three modes differ and are frequency dependent. Thus, over a large enough distance, there will be a separation of the aerial and ground modes that is proportional to the difference in velocity of the respective modes and the distance travelled. The aerial modes themselves, due to their slight difference in propagation velocities, will also separate but to a far lesser extent than the separation between the aerial and ground modes.

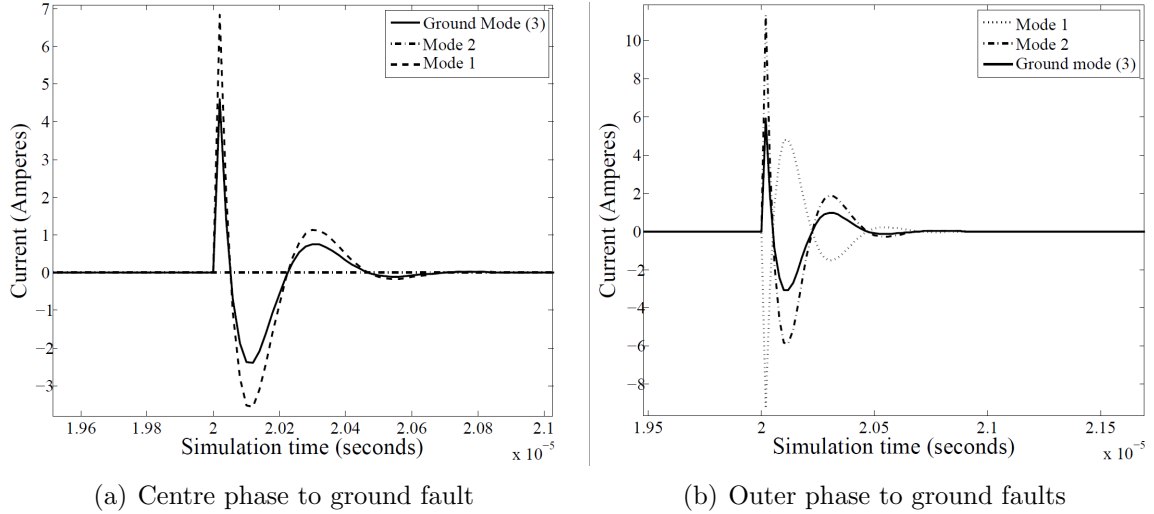


Figure 5.1: Induced modal components for different fault scenarios

### 5.2.2 Network Parameters Required for Proposed Approach

To avoid confusion, it is important to keep a clear and consistent convention, especially for large networks with many branches. It is proposed that the largest point to point distance between any two points on the network is termed the main line and denoted the descriptor of  $j_{zy}$ . A branch is defined as a length of network branching off from the main line. A sub-branch is defined as a length of network branching off from a branch. A situation may arise in which it is unclear which length of network should be considered a branch because of multiple branching off points. In this case, the convention proposed states that the longest point to point length of network, starting from the main line, should be the branch and the sub-branches determined as those lengths of line branching from this. The branch nearest to node  $Z$  is called branch  $X$ , the second nearest is called branch  $W$  and so on. Naming of the sub branches follows a similar convention. If branch  $W$  is the final sub-branch, naming of the sub branches begins with the nearest to the origin

Table 5.1: Definition of Terms

-	Element	Description
1	$Z, Y..A$	Node descriptor (at branch termination)
2	$b_n$	Point at which $n^{th}$ branch begins
3	$j_n$	Length of $n^{th}$ branch
4	$j_{zy}$	Length of main line
5	$n$	Position on network
6	$T_K$	Recorded timestamp at node $k$
7	$F_i$	Position of fault

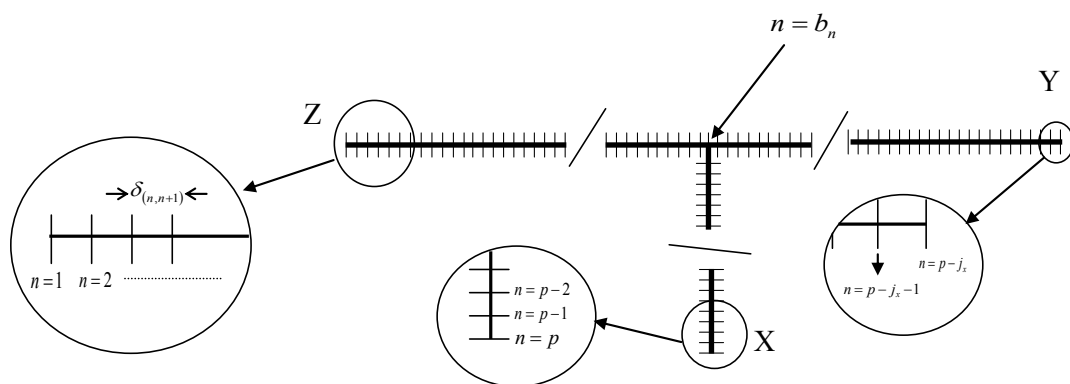


Figure 5.2: Representation of the a discretised one branch network with  $p$  points and a branch,  $X$ , originating at point  $n = b_x$

of branch  $X$ , ( $b_x$ ). Table 5.1 summarises the nomenclature used to describe the example networks and Fig. 5.2 shows a discretised network with one branch.

### 5.2.3 Detailed Aspects of the Proposed Multi-Ended Fault Location

Existing single and double ended fault location algorithms are unable to unambiguously resolve the location of a fault on branched networks. If, however, the arrival time of the fault induced transient at all branch terminations within the network is known, it can be shown that the ambiguity can be removed. Consider

a network consisting of one branch. Assuming that three fault recorders are placed at each branch termination, it follows that a transient originating at any point on the network arrives at OHMS devices 1, 2 and 3 at times  $T_1$ ,  $T_2$  and  $T_3$ . The reflections from the branch terminations are ignored because the OHMS devices are programmed to lock out for a set amount of time when the first transient arrives. To determine the origin of the fault, the difference between timestamps  $T_1$ ,  $T_2$  and  $T_3$  is required.

$$\Delta T_1 = T_1 - T_2 , \quad (5.3)$$

$$\Delta T_2 = T_1 - T_3 , \quad (5.4)$$

$$\Delta T_3 = T_2 - T_3 , \quad (5.5)$$

Furthermore, if the velocity of the transient is assumed to be constant throughout the network and the exact position of the fault locators are known, the origin of the transient can be calculated independent of its velocity. To demonstrate this, an array is constructed with elements representing the distance between a point on the network and the three OHMS devices. From this, and with the assumption that the transient travels at a constant velocity, a further array is constructed showing  $\Delta T_1, \Delta T_2$  and  $\Delta T_3$ . For a known network configuration, three arrays, each containing the distance at any point in the network from the corresponding OHMS device, can be constructed.

$$h_Z(n) = distance(Z, n) , \quad (5.6)$$

$$h_Y(n) = \text{distance}(Y, n) , \quad (5.7)$$

$$h_X(n) = \text{distance}(X, n) , \quad (5.8)$$

It is convenient for computation to discretise the network. To do this, a network of total length  $N$  is split up into  $p$  nodes giving a resolution interval of:

$$\delta(n, n + 1) = \left( \frac{N}{p} \right) \quad (5.9)$$

Where  $p$  is the total number of points the network is split up into. The integer  $n$  exists between 1 and  $p$  and acts as an indicator of position on the network. The distance function returns the distance between point  $n$  and the OHMS devices  $X, Y$  and  $Z$ . If it is assumed that  $X, Y$  and  $Z$  are positioned on the branch terminations, the distance function can be implemented as follows:

$$h_Z(n) = n \left( \frac{N}{p} \right)_{n=1..p-b_x} \quad (5.10)$$

$$h_Y(n) = \left| (p - j_x - n \left( \frac{N}{p} \right)) \right|_{n=1..p-b_x} \quad (5.11)$$

$$h_X(n) = j_x + \left| b_x - n \left( \frac{N}{p} \right) \right|_{n=1..p-b_x} \quad (5.12)$$

Which gives the distance between the OHMS devices and any position on the main branch. This can be extended to include the sub-branch with:

$$h_Z(n) = \left| b_x + n \left( \frac{N}{p} \right) - j_{zy} \right|_{n=(p-b_x+1)..p} \quad (5.13)$$

$$h_Y(n) = \left| -b_x + n \left( \frac{N}{p} \right) \right|_{n=(p-b_x+1)..p} \quad (5.14)$$

$$h_X(n) = \left| j_x - n \left( \frac{N}{p} \right) - j_{zy} \right|_{n=(p-b_x+1)..p} \quad (5.15)$$

The rapid disturbance in the voltage on the faulted conductor initiates a high frequency transient that propagates in both directions away from the faulted point. The velocity of the transient,  $u$  is governed by the properties of the transmission line structure. In general, the distance travelled,  $s$ , the velocity of the transient,  $u$  and the time the transient has travelled,  $t$ , are related by:

$$s = ut \quad (5.16)$$

The OHMS devices at points  $X$ ,  $Y$  and  $Z$  timestamp the arrival time of the transient at times  $T_z$ ,  $T_y$  and  $T_x$ . The time of initialisation of the fault is defined as  $T_0$ . Given an average velocity of  $u_z$ ,  $u_y$  and  $u_x$  for the path between the faulted point and the OHMS devices at points  $Z$ ,  $Y$  and  $X$ , the following equations apply:

$$T_z = T_0 + \frac{s_z}{u_z} \quad (5.17)$$

$$T_y = T_0 + \frac{s_y}{u_y} \quad (5.18)$$

$$T_x = T_0 + \frac{s_x}{u_x} \quad (5.19)$$

At this stage, it is not possible to calculate the position of the fault.  $T_0$  is a

common factor and can be easily removed by subtraction, leading to the following set of equations.

$$T_z - T_y = \Delta T_{zy} = \frac{s_z}{u_z} - \frac{s_y}{u_y} \quad (5.20)$$

$$T_z - T_x = \Delta T_{zx} = \frac{s_z}{u_z} - \frac{s_x}{u_x} \quad (5.21)$$

$$T_y - T_x = \Delta T_{yx} = \frac{s_y}{u_y} - \frac{s_x}{u_x} \quad (5.22)$$

Suppose that the average velocities between the fault and the three fault recorders are approximately equal, i.e:

$$u_z \approx u_y \approx u_x \quad (5.23)$$

From the assumption in Equation (5.23), a further set of equations are constructed, this time eliminating the velocity terms:

$$R_{1-2} = \frac{\Delta T_{zy}}{\Delta T_{zx}} = \frac{s_z - s_y}{s_z - s_x} \quad (5.24)$$

$$R_{1-3} = \frac{\Delta T_{zy}}{\Delta T_{yx}} = \frac{s_z - s_y}{s_y - s_x} \quad (5.25)$$

$$R_{1-3} = \frac{\Delta T_{zx}}{\Delta T_{yx}} = \frac{s_z - s_x}{s_y - s_x} \quad (5.26)$$

Examination of Equations (5.24) - (5.26) reveals that the timestamp derived 'R-ratios' ( $R_{1-2}$ ,  $R_{1-3}$  and  $R_{2-3}$ ) contain only distance terms. Furthermore, for a given fault position, the R-ratios should be of a specific value. It is possible to assess what these values should be for any given fault location by computing the relative distances between each point on the network and the OHMS devices. This is achieved by returning to Equations (5.13)-(5.15) and forming another set of equations:

$$\Delta D_1(n) = h_Z(n) - h_Y(n) , \quad (5.27)$$

$$\Delta D_2(n) = h_Z(n) - h_X(n) , \quad (5.28)$$

$$\Delta D_3(n) = h_Y(n) - h_X(n) , \quad (5.29)$$

Then, the R-ratios as a function of  $n$ , termed the network derived R-ratios, can be expressed as:

$$R_{1-2}(n) = \frac{\Delta D_1(n)}{\Delta D_2(n)} , \quad (5.30)$$

$$R_{1-3}(n) = \frac{\Delta D_1(n)}{\Delta D_3(n)} , \quad (5.31)$$

$$R_{2-3}(n) = \frac{\Delta D_2(n)}{\Delta D_3(n)} , \quad (5.32)$$

The analysis is furthered by considering the one branch network shown in Fig. 5.3. Here, the total number of nodes,  $p$ , is 125, There is a branch with a length of 25 nodes and originating at node 40. The total length of the network is 1250 m giving a node length of 10 m. Suppose a fault event occurs at node 27 on the example

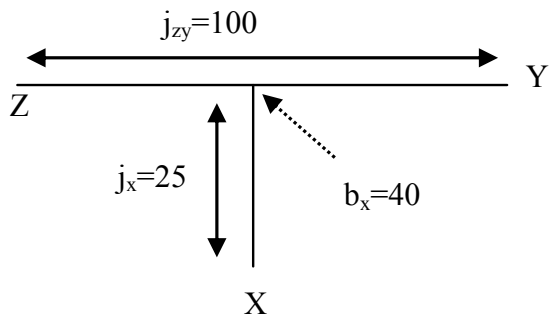


Figure 5.3: Example Network

network ( $F_n=27$ ). The timestamps at  $Z$ ,  $Y$  and  $X$  are calculated by using Equations (5.17)-(5.19). If the condition that the average velocities between the fault and the OHMS devices holds, the fault location estimate is obtained by finding the node,  $n$ , from the network derived R-ratios that are equal to the timestamp derived R-ratios. If a fault event occurs and the resulting high frequency transients are timestamped and registered at OHMS devices  $X$ ,  $Y$  and  $Z$ , the timestamps are converted to R-ratios using Equations (5.24) - (5.26), giving values for  $R_{1-2}$ ,  $R_{1-3}$  and  $R_{2-3}$  of 4.18, -1.31 and -0.31 respectively. The next step in the fault estimation process is to search for the position index,  $n$ , that gives the same network derived R-ratios as the timestamp derived R-values. In this idealised example, the fault estimation is precise.

The analysis for a one branch network can be easily generalised for an  $M$  branch network. For  $M$  branches,  $M + 2$  fault recorders are required with the condition that one is placed at each branch termination. Satisfying this condition guarantees the unambiguous location of a fault provided that each timestamp is

known and the distance arrays are correctly constructed. The correct construction of the distance array means that the distance travelled by the transient is proportional to the time it takes to travel that distance. On non-homogeneous networks, transients travel at variable speeds depending on the propagation constant of the particular part of the network. It will be explained later how the distance array can be modified to compensate partially for this. The procedure for finding a fault using a multi-ended method is summarised in Fig. 5.4.

To estimate the fault location, it is required to find the timestamp derived

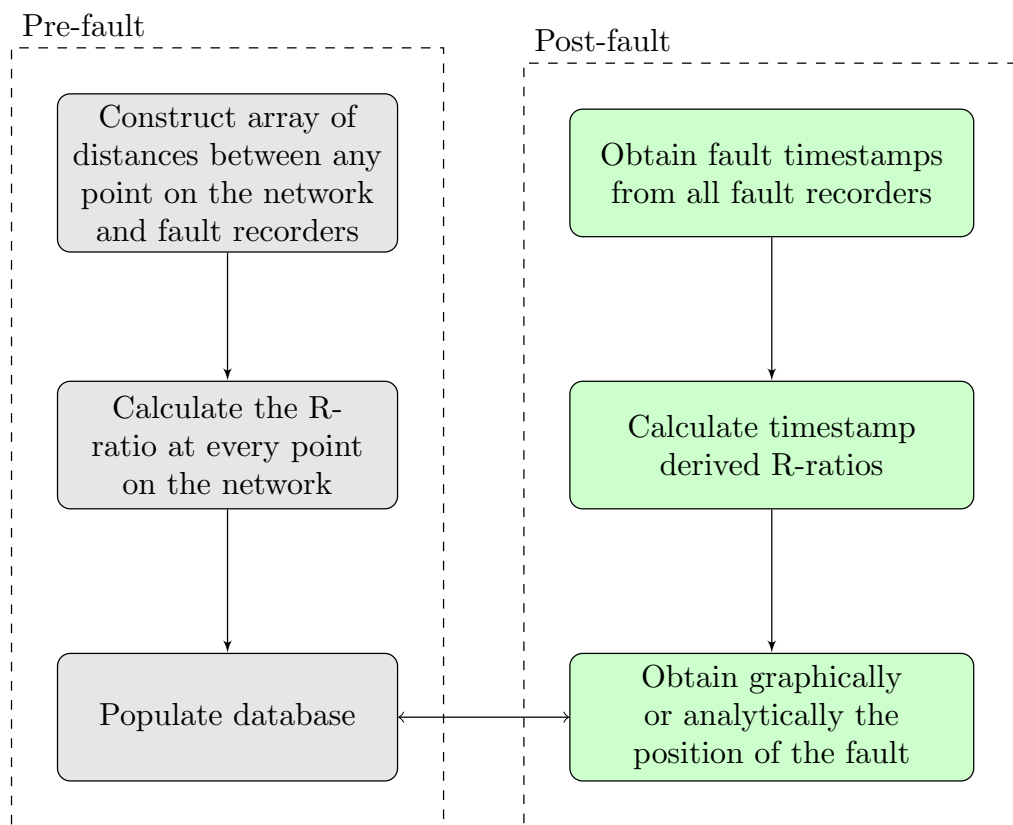


Figure 5.4: Procedure for finding the location of a fault using the multi-ended method

R-ratios before finding a position,  $n$ , that gives the same network derived R-ratios. (e.g., those shown in [5.30]-[5.32]). This can be done graphically or analytically but for ease of use, it is suggested that a metric,  $W(n)$  be used to quantify the departure at each network node from the timestamp derived R-ratios. The fault estimate is defined as the network position,  $n$ , that minimises  $W(n)$ .

$$\begin{aligned}
 W(n) = & (R_{1-2}(n) - (\Delta T_1/\Delta T_2))^2 + \\
 & (R_{1-3}(n) - (\Delta T_1/\Delta T_3))^2 + \\
 & (R_{2-3}(n) - (\Delta T_2/\Delta T_3))^2
 \end{aligned} \tag{5.33}$$

The solution to the problem may also suit neural network solution methods. Future work looking into this, and other possible solutions to the minimisation problem is planned.

## 5.3 Application of Proposed Method to Distribution Networks

### 5.3.1 One Branch Network

Consider a one branch network with a main line length of 17 km and a branch, originating at 7 km along the main line, is 7.5 km in length. It is assumed that OHMS devices capable of detecting the high frequency fault induced transient are placed at positions  $X$ ,  $Y$  and  $Z$ , i.e. at the branch terminations. The distance matrix is calculated using the method outlined previously. Then, using Equations (5.30)-

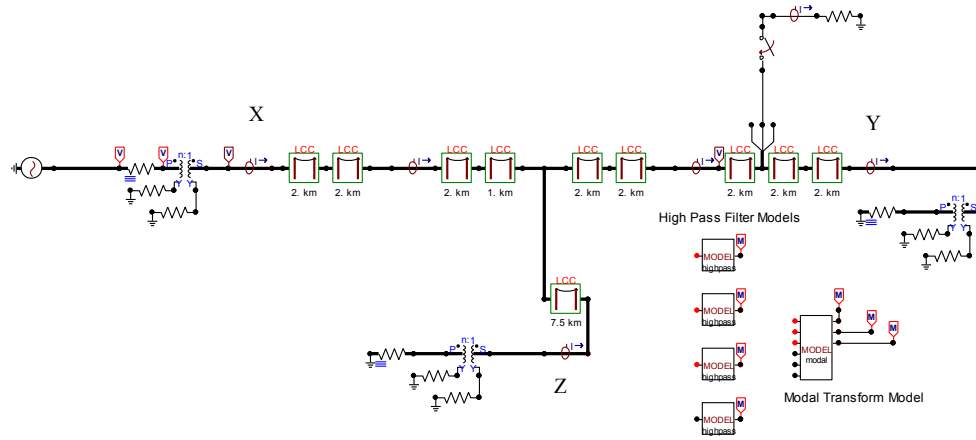


Figure 5.5: ATP/EMTP representation of one branch network, including high pass filter and modal transform models ( $F_i=130$ ).

(5.32), the matrices of ratios for  $\Delta D$  are computed. The matrices of ratios,  $R_{1-2}(n)$ ,  $R_{1-3}(n)$  and  $R_{2-3}(n)$  can be plotted as a function of position on the network,  $n$ . It is then possible, graphically or using the minimum of the metric  $W(n)$ , to estimate the location of the fault. To test the method, the described network is implemented in the ATP/EMTP (see Fig. 5.5).

A fault is simulated at position index 130 ( $F_i=130$ ) using a time controlled switch and the OHMS devices are modelled by a current probe and a 4<sup>th</sup> order high pass filter implemented with the Z-transform command in the ATP Models language. The filter's cut-off frequency is set, through trial and error, to a value that completely removes the 50 Hz power frequency component but does not attenuate the high frequency travelling wave. With the 50 Hz component removed, the high frequency, fault induced transient is clearly identifiable at all three OHMS device locations. The time at which the peak of the first transient arrives at each fault recorder point is dependent on the distance of the fault recorder from the origin

Table 5.2: Timestamps  $T_X$ ,  $T_Y$ ,  $T_Z$ ,  $\Delta T$  and Timestamp derived R ratios for one branch network

T/ $\Delta T$ ( $\mu s$ )		R ratios	
$T_Z$	243.28		
$T_Y$	213.32		
$T_X$	244.94	$R_{1-2}$	-18.0482
$\Delta T_{ZY}$	30.28	$R_{1-3}$	-0.9475
$\Delta T_{ZX}$	-1.66	$R_{2-3}$	0.0525
$\Delta T_{YX}$	-31.62		

of the transient. Table 5.2 shows the recorded timestamps and the difference in timestamps,  $\Delta T$ , for each combination pair. Equations (5.30)-(5.32) are then used to compute the timestamp derived R-ratios (also shown in Table 5.2).

The network defined R-ratios are pre-calculated and plotted as a function of position index (Fig. 5.6). In this example, a resolution of 1 position index per metre is used.

Three estimates of the fault location are obtained, one from each of the R-ratio graphs. All three estimates, i.e. the points where the point on x-axis where the y-axis values of  $R_{1-2}$ ,  $R_{1-3}$  and  $R_{2-3}$  plotted from the network data are equal to the values obtained from the timestamp derived information, yield a fault estimate of 130. The W metric is plotted in Fig. 5.7

### 5.3.2 Multiple Branch Networks

The method can be extended and used for any number of branches. The network shown in Fig. 5.5 is modified to include an additional branch. Nodes  $W$ ,  $X$ ,  $Y$  and  $Z$  are placed at all branch terminations of the 2 branch network. The

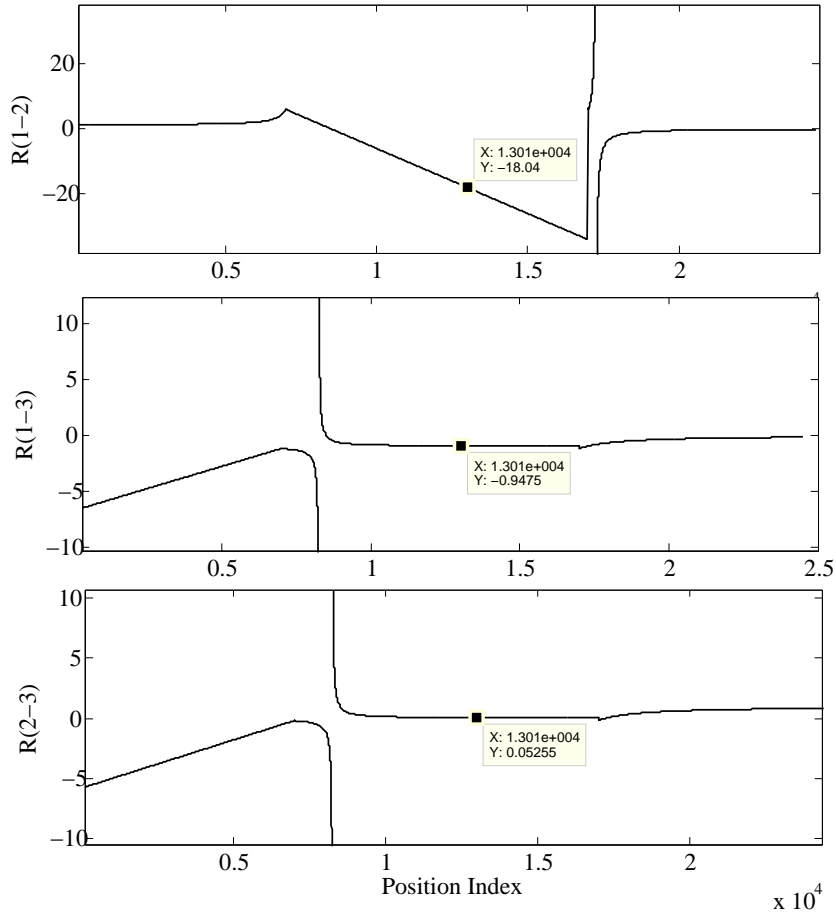


Figure 5.6: R-ratios plotted as a function of position index for one branch network convention of setting  $ZY$  as the main branch is again followed. The branches are denoted a branch letter in reverse alphabetical order the further away from position  $Z$  they originate. The network now has a main line length,  $j_{zy}$  of 17 km, a first branch position,  $b_x$  of 4 km, a first branch length,  $j_x$  of 7.5 km, a second branch position,  $b_w$  of 13 km and a second branch length,  $j_w$  of 4 km. The distance arrays and R ratios are shown in Fig. 5.8. The W metric is shown in Fig. 5.9 . It is noted that the method now yields 6 separate R-ratio graphs corresponding to  $R_{1-2}$ ,

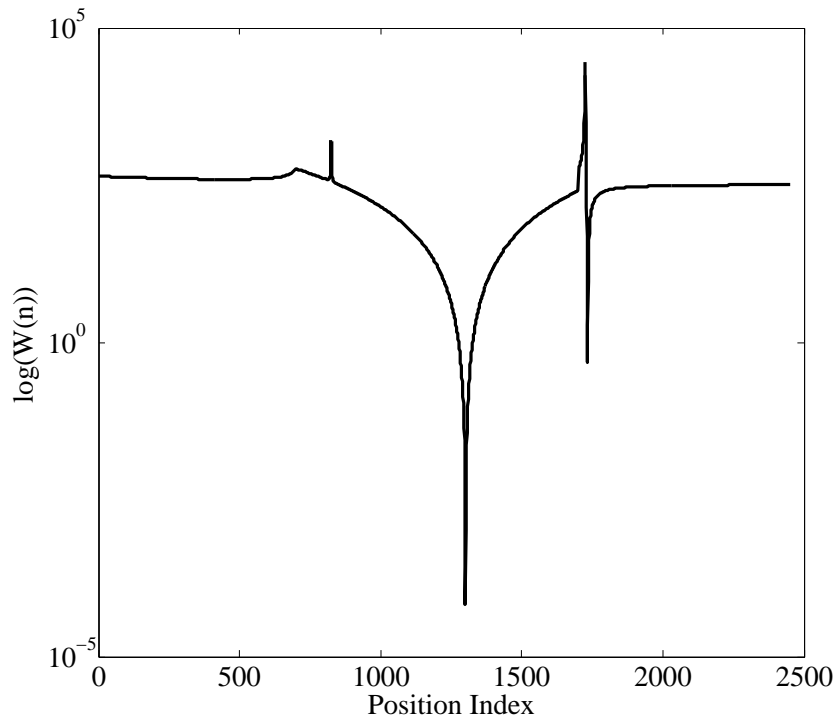


Figure 5.7: W metric for one branch network

$R_{1-3}$ ,  $R_{1-4}$ ,  $R_{2-3}$ ,  $R_{2-4}$  and  $R_{3-4}$ . The described network is once again modelled using the ATP/EMTP. A time-controlled switch through a small resistance is used to simulate the fault at a position of  $F_i = 40$ . The full code listing for calculation of the R-values and determination of an estimate is shown in Appendix A.7. Table 5.3 shows the timestamp values and the calculated R-ratios.

As networks become larger and more branched, the generation of the matrix of distance becomes increasingly complex. It is recommended that a more general approach is developed to generate the R-ratios more easily for an arbitrary network. This is explained in more detail in Section 5.6.1.

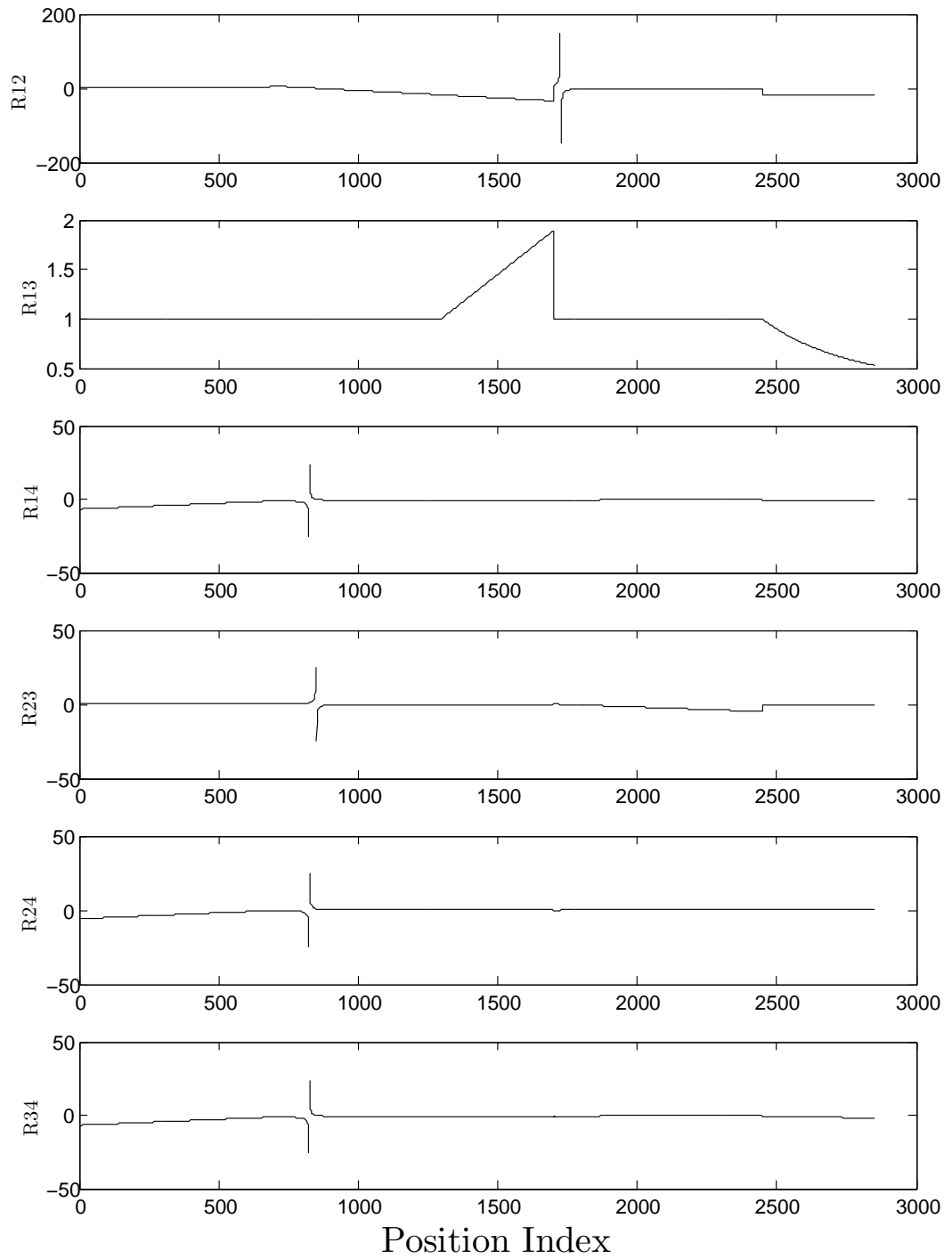


Figure 5.8: R-ratios plotted as a function of position index for two branch network

Table 5.3: Timestamps  $T_X$ ,  $T_Y$ ,  $T_Z$ ,  $\Delta T$  and Timestamp derived R ratios for two branch network

T/ $\Delta T$ ( $\mu s$ )		R ratios	
$T_Z$	113.32		
$T_Y$	143.28		
$T_X$	134.96	$R_{1-2}$	1.3845
$T_W$	143.28	$R_{1-3}$	1
$\Delta T_{ZY}$	-29.96	$R_{1-4}$	-3.6010
$\Delta T_{ZX}$	-21.64	$R_{2-3}$	0.7223
$\Delta T_{ZW}$	-29.96	$R_{2-4}$	-2.601
$\Delta T_{YX}$	8.32	$R_{3-4}$	-3.601
$\Delta T_{YW}$	0		
$\Delta T_{XW}$	-8.32		

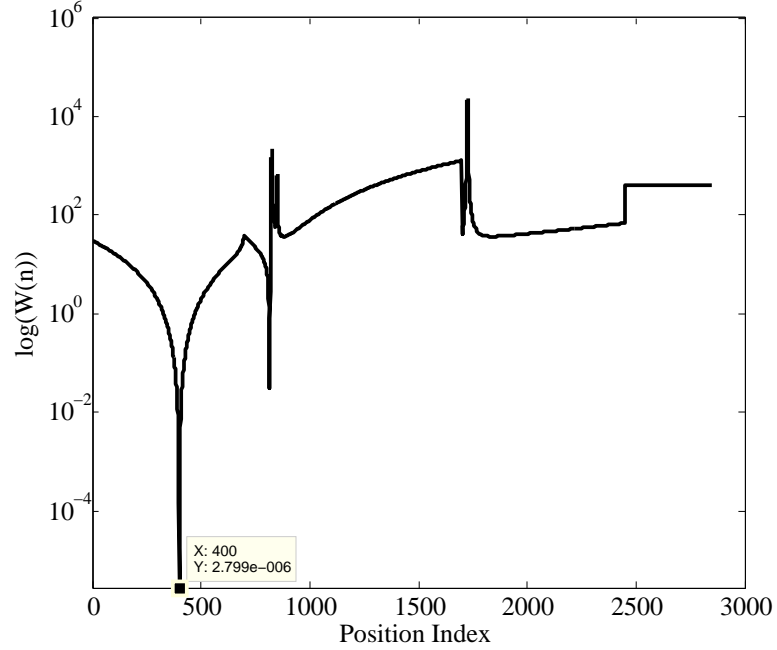


Figure 5.9: W metric for two branch network

## 5.4 Sensitivity to Errors in Networks with the Same Line Configuration

The described method relies on the accurate time-stamping of a transient at branch terminations. An obvious source of error is the inaccurate time-stamping of the arrival time of the transient. For an arrival time of the peak of the transient of  $T_{arrival}$ , the recorded time-stamp will also include an error term,  $T_{err}$ . This error term is made of the error associated with the GPS clock or the clock speed of the processor, noise and the error associated with the interpretation of the received transient. If a clock speed of 100 MHz is assumed for the processor in the receiver, samples will be taken every 10 ns. Given a typical 1 pulse per second (PPS) GPS timing receiver (e.g. [88]), a reported timing accuracy of  $\pm 2$  ns (to 1 standard deviation) can be achieved (in combination with the clock granularity message). In combination with clock uncertainty (for 100 MHz), this gives a maximum error of around 12 ns. Also to be considered, however, is the uncertainty in the interpretation of the received transient, i.e. the question of where the peak value of the transient may be difficult to answer, especially in the presence of noise. It is difficult, without field results, to attribute a value to this portion of the error term. The recorded time-stamp is expressed mathematically as:

$$T_{recorded} = T_{arrival} + T_{err}, \quad (5.34)$$

For the sensitivity analysis, it is assumed that  $T_{err}$  is a random variable with

a normal probability density function. That is:

$$T_{err} = \mathcal{N}(\mu_e, \sigma_e^2) \quad (5.35)$$

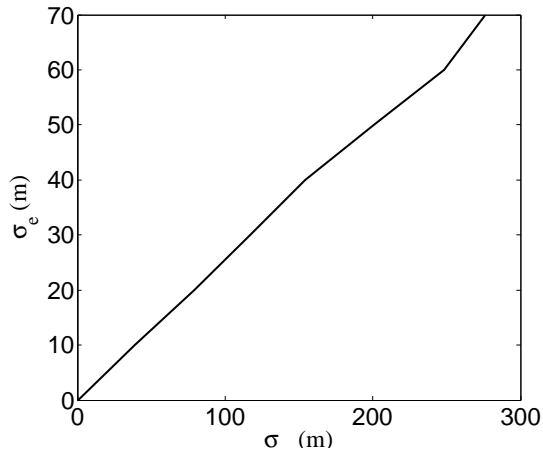
Assuming that  $T_{arrival}$  is the precise arrival time (i.e. error free),  $T_{recorded}$  will also be normally distributed:

$$T_{recorded} = \mathcal{N}(\mu_r, \sigma_r^2) \quad (5.36)$$

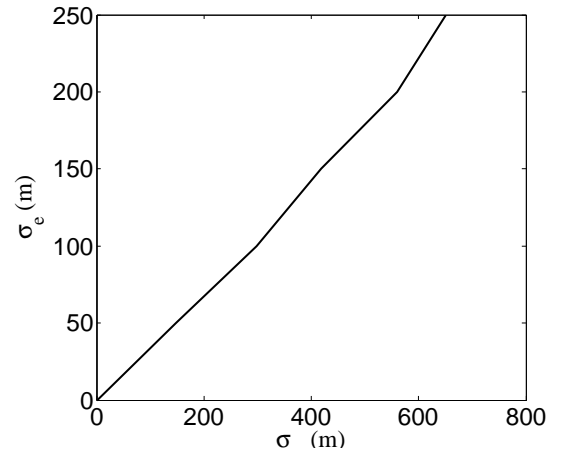
Where the mean,  $\mu_r$ , is the error free arrival time and the standard deviation,  $\sigma_r$ , is the result of the dispersion caused by the error processes in the fault recorder. By the central limit theorem, the fault estimation will also be normally distributed. A sensitivity analysis is carried out by running the fault estimation process 1000 times with the error term,  $T_{err}$ , repeating with varying values of  $\sigma_e$ . The fault estimation is chosen automatically as the position node nearest the minimum of the metric  $W$ . Fig. 5.10 exhibits the results of the analysis for the one branch and two branch networks.

## 5.5 Adaptation of Method for Networks with Cable sections

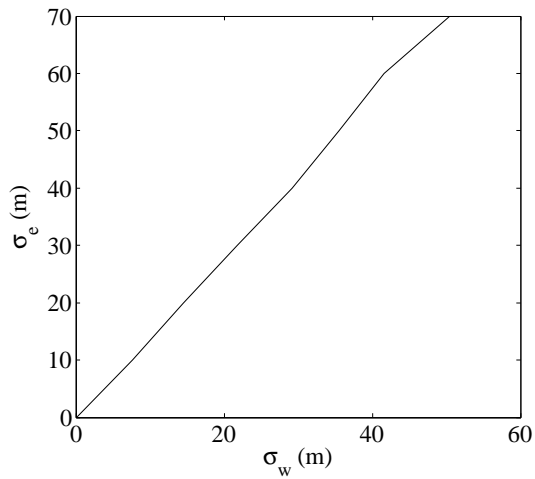
11 kV rural networks are frequently a mixture of overhead line and underground cable sections. The number of underground sections depends on the local geography and the level of urbanisation. Underground sections have a significant effect on travelling waves. At the underground/overhead line junction, the travel-



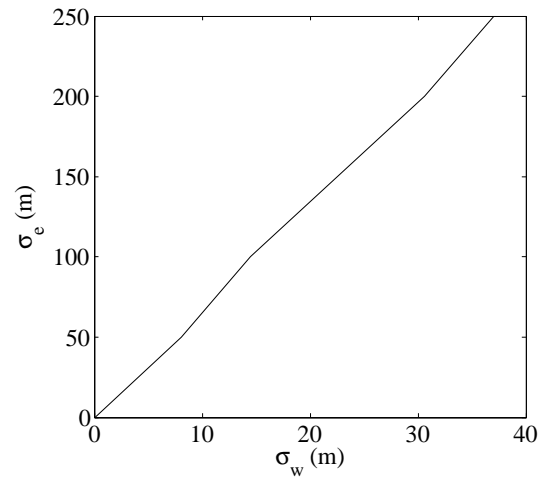
(a) Error in all OHMS devices in the two branch network



(b) Error in one OHMS device (at position Z) in the one branch network



(c) Error in all OHMS devices in the one branch network



(d) Error in one OHMS device (at position Z) in the one branch network

Figure 5.10: Sensitivity analysis in the one branch and two branch network

ling wave responds to the difference in characteristic impedance by splitting into an incident wave (i.e. a continuation of the transient into the cable) and a reflected wave. Furthermore, the wave travelling through the cable section will travel at a significantly reduced velocity, testing the assumption that the speed of the transient is uniform throughout the network.

To compensate for the reduction in velocity of the transient through the cable section, the position index associated with the cable can be multiplied by a correction term. For example, if a cable exists between position index 11 and 20 and it is known that the velocity of the transient is reduced by a factor of 0.66, a correction can be made by multiplying the position index by 1.5. Therefore, instead of taking on position index 11 to 20, the cable now exists between position indexes 11 and 25. This correction relies on the correct multiplication factor being used so will introduce a degree of error. To include cable sections with accuracy, the velocity of the transient through the cable section must be known. A difficulty arises because of the frequency dependency of the aerial mode velocities in cables.

The velocities for the three modes in a three phase overhead line system and a three phase, single core underground cable are calculated using the line/cable constants (LCC) routine of the EMTP. It must be remarked that the accuracy of the EMTP LCC routine at frequencies beyond 100 kHz is questionable. For the overhead line system, however, the indication that the velocity approaches very near to the speed of light at frequencies above about 50 kHz is probably correct because the skin depth in aluminium and copper is very small ( $240 \mu m$  at 100 kHz for copper). Most of the field excited by a fault induced transient is in the air separating the conductors

Table 5.4: Physical data of underground cable used as test case

Parameter	Value
Number of Cores	3
Depth	2 <i>m</i>
Overall diameter	900 <i>mm</i>
Diameter over armour	800 <i>mm</i>
Diameter over outer PVC sheath	740 <i>mm</i>
Diameter over copper screen	340 <i>mm</i>
Diameter over XLPE insulation	270 <i>mm</i>
Core diameter	7.6 <i>mm</i>

and the earth (as opposed to the case of power frequency, where a non-negligible portion of the field is within the conductor). The situation is more interesting in the case of an underground cable. Here, the velocity is highly frequency dependent and has been shown to be extremely difficult to model or predict accurately [89]. For the analysis in this section, the wave velocity, as calculated by the LCC routine in the EMTP, is used. The network shown in Fig. 5.5 is modified such that the 2 km line section closest to point X is replaced by a 2 km cable section with the physical parameters outlined in Table 5.4. Table 5.5 shows the results of the cable compensation method.

[H]

## 5.6 Improved Accuracy using Travel Times Between Installed OHMS Devices

The assumption of a homogenous network is clearly over optimistic for practical distribution networks. The presence of multiple feeder taps, laterals, and con-

Table 5.5: Analysis of cable compensation method

Parameter	Value
Aerial Mode (1) Velocity	299,878 m/s
Mode 1 Cable velocity	156,876 m/s
Correction Factor	1.91
Old section length	2 km
New section length	3.82 km
Fault Position	Point Index 130
Fault estimate without cable adaptation	120
Fault estimate (with cable adaptation)	129.9

ductor size changes have the potential to change the characteristic impedance,  $Z_0$ , seen by the high frequency fault induced transient. This inevitably leads to changes in the velocity of the wave and, therefore, decreases the accuracy of the method outlined earlier. It is proposed that accuracy can be improved if a further, stronger assumption is introduced; that the travel time between any two OHMS devices is unchanging over time. At the expense of a small 'calibration time', information about the velocity characteristics in the path between any two fault recorder devices can be easily determined without the need for additional hardware.

For this, the "OHMS" Transmitter" device is assumed. This device consists of a fault recorder with timestamp mechanism, PLC capabilities and coupling to the power line. During the calibration time and in sequence, each OHMS device transmits a high frequency signal similar in frequency to a fault induced transient (e.g. 400 kHz). Alternatively, an OFDM synchronisation symbol can be sent carrying the information relating to which OHMS device is transmitting and the fact that it is a calibration symbol. It is suggested that a symbol with two identical parts in the time domain is sent, leading to a peak when a cross correlation is performed (similar

to the Schmidl and Cox method of symbol timing [71]). By doing this, any ambiguity associated with the interpretation of the incoming signal is reduced. While one OHMS device transmits, the remaining devices listen and record the arrival time. For a network with  $N$  OHMS devices,  $N$  transmissions are required and each OHMS device will obtain  $N - 1$  timestamps and  $N - 1$  associated identification tags. This information is subsequently sent back to the “OHMS receiver” using PLC.

Consider the three node network of Fig. 5.2. Node Z transmits a synchronisation symbol at time  $t_Z$ . At time  $t_{ZY}$  and  $t_{ZX}$ , nodes Y and X receive the calibration symbol sent from node Z. From the network information, the distance between node Z and the point at which node X begins ( $j_x$ ), and the distance between node Y and  $j_x$  are calculated (including the cable adaptation adjustments). The distances are defined as  $D_{(XZY),Z}$  for the distance between node Z and  $j_x$ , and  $D_{(XYZ),Y}$  for the distance between node Y and  $j_x$ . With the GPS time-stamped sending and arrival times known, the distances (in light seconds) between nodes is defined as  $D_{XZ}$  and  $D_{XY}$ , or generally as  $D_{AB}$ , where A is the transmitting node and B is the receiving node. The difference in the recorded timestamps at the two receiving nodes is defined generally as  $\Delta_{AB:AC}$ , where A is the sending node. For a one branch network, the following equations can be constructed:

$$D_{(XYZ),Z} = D_{XZ} - D_{(XYZ),X}, \quad (5.37)$$

$$D_{(XYZ),Y} = D_{XY} - D_{(XYZ),X}, \quad (5.38)$$

$$D_{(XYZ),X} = D_{XY} - D_{(XYZ),Y}, \quad (5.39)$$

$$D_{(XYZ),Z} = D_{(XYZ),Y} + \Delta_{XY:YZ}, \quad (5.40)$$

$$D_{(XYZ),Y} = D_{(XYZ),Z} + \Delta_{XZ:XY}, \quad (5.41)$$

$$D_{(XYZ),X} = D_{(XYZ),Y} + \Delta_{ZX:ZY}, \quad (5.42)$$

After all three calibration symbols are sent and received (or N calibrations symbols in an N node system), a set of simultaneous equations result. Solving for  $D_{(XYZ),Z}$ ,  $D_{(XYZ),Y}$  and  $D_{(XYZ),X}$  yields:

$$D_{(XYZ),X} = \frac{D_{XY} - \Delta_{ZX:ZY}}{2} \quad (5.43)$$

$$D_{(XYZ),Y} = \frac{D_{XY} - \Delta_{ZX:ZY}}{2} \quad (5.44)$$

$$D_{(XYZ),Z} = \frac{D_{XZ} - \Delta_{YX:YZ}}{2} \quad (5.45)$$

With detailed knowledge of the travelling time between any two OHMS devices known, adjustments can be made to the array of distances for the particular network.

If an assumption is made that the velocity in the overhead line part of the network is approximately the speed of light, it is possible to calculate the time taken for the high frequency signal to travel through the combined underground cable sections in the network. If the underground cable used in a particular part of the network are the same, the velocity through the cable can be calculated directly:

$$V_{cable} = \frac{L_{cable}}{t_{total} - \frac{L_{ohl}}{V_{ohl}}} \quad (5.46)$$

Where  $V_{cable}$  and  $V_{ohl}$  are the cable and overhead line velocities and  $L_{cable}$  and  $L_{ohl}$  are the lengths of the cable and overhead line sections in a particular part of the network.  $t_{total}$  is the total time it takes for the high frequency signal to travel between two points on the network. The calibration stage ensures that these times are known between the two points connecting (for the one branch network)  $D_{XYZ,X}$ ,  $D_{XYZ,Y}$  and  $D_{XYZ,Z}$ .

For the one branch network, three node network, the calibration time must include three transmissions. For more complex networks, a longer calibration period is required. It is possible, however, to use the results of the calibration time to determine the high frequency travel time between any branch point and any node. An obvious weakness in the calibration method is the failure to deal with the frequency dependency of the propagation velocity in cables. A best guess must be used when choosing the frequency of the high frequency signal to be used in the calibration time. In reality, the fault induced high frequency signal is made up of a spread of frequencies. One possible solution would be to bandpass the fault transient signal

to include only energy at around the frequency used in the calibration routine. The described method, however, does not utilise the velocity of the transient directly. Instead, the relative ratios of the propagation times for each path are used to modify the cable sections.

### 5.6.1 Generalisation for Large Networks

For large networks, a general approach is necessary to avoid the onerous task of manually calculating the network derived R-ratios. First, define an  $i$  by  $j$  matrix,  $\mathbf{A}$ , whose entries denote the distance between the  $i^{th}$  and  $j^{th}$  branches (here, we consider the main line to be a branch). Where  $i = j$ , i.e. the diagonals of  $\mathbf{A}$ , the entry should denote the length of branch  $i/j$ . Another  $i$  by  $j$  matrix,  $\mathbf{B}$ , is defined as the branching off point between the  $i^{th}$  and  $j^{th}$  branches. As an example, the entry in the  $2^{nd}$  row and  $4^{th}$  column is the distance between the start of branch 2 and the point at which branch 4 connects to branch 2. For a typical network, many branches will share no connective points. In this case, the entry should be zero. Next, a column vector,  $\mathbf{c}$ , is defined. The value in the first column of  $\mathbf{c}$  is zero. The second column is the length of the main line. The third column is the length of the main line plus the length of the first branch. The fourth column is equal to the third column plus the length of the second branch, and so on. This number of entries in this “accumulator” vector should be one more than there are branches (including the main line) in the network. Therefore, a network with a main line and 6 branches should be described by a  $\mathbf{c}$  with 8 entries.

For a network with  $N_b$  branches, the aim is to arrive at a  $\mathbf{c}[N_b + 1]$  by  $\mathbf{c}[N_b + 1]$  matrix,  $\mathbf{D}$ , whose entry in the  $i^{th}$  row and  $j^{th}$  column denotes the distance between points  $i$  and  $j$  on the network. To achieve this,  $\mathbf{D}$  is populated in a step-by-step manner. Fig. 5.11 shows that  $\mathbf{D}$  can be split up into a number of sections. The diagonal elements (where  $h_i=h_j$ ) represent the elements in  $\mathbf{D}$  whereby  $i$  and  $j$  reside on the same branch. The distance function in this case is simply the absolute value of  $i$  subtracted by  $j$ . For elements in  $\mathbf{D}$  where  $h_i=h_j$ , the distance between  $i$  and  $j$  depends on whether the branch containing  $i$  and the branch containing  $j$  are connected directly. If this is not the case, the distance between the two branches (represented in  $\mathbf{A}$ ) is required. If there is a direct connection, the branching off point (represented in  $\mathbf{B}$ ) is required. The required calculations are summarised in Equation 5.47.

$$\mathbf{D}[i, j] = \begin{cases} |i - j| & \text{if } h_i = h_j \\ \hline |\mathbf{B}[h_i, h_j] - i + \mathbf{c}[h_i]| + |\mathbf{c}[h_j] - j| & \text{if } \mathbf{A}[h_i, h_j] = 0 \text{ and } h_j > h_i \\ \hline |\mathbf{B}[h_i, h_j] - j + \mathbf{c}[h_j]| + |\mathbf{c}[h_i] - i| & \text{if } \mathbf{A}[h_i, h_j] = 0 \text{ and } h_i > h_j \\ \hline |\mathbf{B}[h_i, h_j] - j + \mathbf{c}[h_j]| \dots & \\ \hline +|\mathbf{c}[h_i] - i| + \mathbf{A}[h_i, h_j] & \text{if } \mathbf{A}[h_i, h_j] > 0 \text{ and } h_j > h_i \\ \hline |\mathbf{B}[h_i, h_j] - i + \mathbf{c}[h_i]| \dots & \\ \hline +|\mathbf{c}[h_j] - j| + \mathbf{A}[h_i, h_j] & \text{if } \mathbf{A}[h_i, h_j] > 0 \text{ and } h_i > h_j \end{cases} \quad (5.47)$$

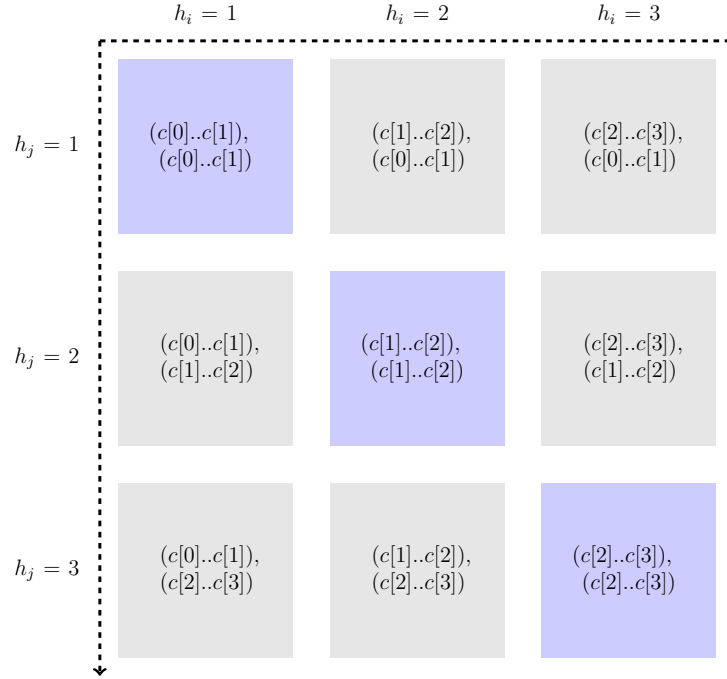


Figure 5.11: Elements of the Matrix **D**

## 5.7 Optimisation of the Number of OHMS Devices for Fault Location

The multi-ended fault location method is able to detect a fault at any position in a network if an OHMS device is situated at every branch termination. For large networks, the required number of OHMS devices may be too great to justify. Should they method be implemented with fewer OHMS devices, fault location in some positions of the network may be possible. However, in some parts of the network, the method is only able to narrow down the location to a branch or sub-branch. In general, the fault location capability at a particular position on the network depends on whether there is a unique (non-recurring) network derived R-ratio. Similarities or duplicates in the value of the R-ratios leads to ambiguity because the timestamp derived R-ratio could be produced by a fault at more than one position on the

network. An OHMS device at each branch termination removes this possibility. Consider the hypothetical network shown in Fig. 5.12. It is assumed that OHMS devices are positioned at the branch terminations,  $A$ ,  $B$ ,  $C$ ,  $D$  and  $E$ . Should a fault occur at the position marked “FP1”, the algorithm requires a minimum of two timestamps from two OHMS devices, provided that there is no ambiguity in the network derived R-ratio for that network position. The only node pairing not satisfying this condition is formed by the OHMS devices at positions  $C$  and  $E$ . The network derived R-ratio involving these two devices is the same for any network position beyond the point where the branch terminated by position  $C$  joins the main line (starting at  $A$  and ending at  $B$ ). Similarly, to locate a fault at “FP2”, the OHMS device at position  $D$  is required because the network derived R-ratios for all position indexes on branch  $D$  are the same for all pairings not including  $D$ . Therefore, without an OHMS device at  $D$ , the algorithm would only be able to detect that a fault has occurred *somewhere* on the branch terminated by  $D$ .

In general, it can be asserted that a precise fault location estimate can only be obtained when an OHMS device terminates the branch on which the fault has occurred. For large networks, it may be acceptable to omit OHMS devices on small branches with the understanding that the algorithm would still be able to narrow down the position of a fault to *somewhere* on these branches.

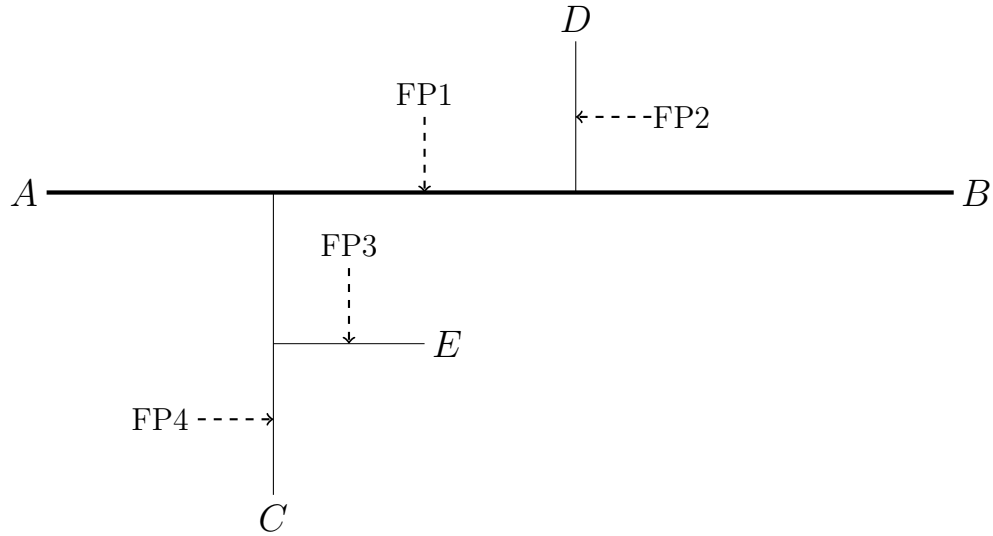


Figure 5.12: Hypothetical network with OHMS devices at positions  $A$ ,  $B$ ,  $C$ ,  $D$  and  $E$  and four possible fault positions labelled  $FP1$ ,  $FP2$ ,  $FP3$  and  $FP4$

## 5.8 Timestamping of Fault Induced Transients

Implementation of the fault location scheme proposed earlier in this chapter relies on the accurate timestamping of the initial high frequency component induced by the fault process. Simplistically, the nature of the high frequency transient depends on the voltage at the inception of the fault and the impedance between the faulted conductor and ground. Often, an arc is generated between the HV conductor and earth, introducing a non-linear impedance on the path to ground. Despite this, previous research has indicated that the spectra of the high frequency fault induced travelling wave is not affected by the path impedance to ground [87].

There is a lack of good quality information regarding high frequency (ns rise time) impulse transients in the published literature, with most of the research focused on transients that can be detected with kHz sampling frequencies.

If the disturbance is made up of a wide range of frequencies, a problem may arise due to dispersion of the frequency content as it travels around the network. This may lead to inaccurate timestamping because of differences in the shape of the wave fronts at different points in the network.

A recent attempt was made to capture transient events on a distribution network in Brazil [90]. The FPGA based fault recorders used a 17 MHz sampling frequency fed by a Rogowski coil. The study found that high fidelity measurements were possible using a high bandwidth ADC, however it was difficult to set the trigger because of the high number of wave fronts of unknown origin. The approach suggested in this thesis may partly resolve this problem by neglecting events that are not observed to have a resolvable origin. If an origin can be deduced, the information should be stored and post-analysis carried out to determine if the event is important, by, for example, checking if the same event has occurred previously or determining if the origin is an important part of the network (e.g. a transformer).

Fig. 5.14 shows a peak detection algorithm. The algorithm is based on the time domain sampling at a frequency,  $F_s$ . The frequency of  $F_s$  determines the maximum rise time that can be detected. The high frequency sampled signal is low pass filtered and analysed by two processes simultaneously. One of these processes calculates the first difference by a simple subtraction of the current sample by the previous sample. The other process monitors the magnitude of the signal. The peak detect flag is triggered if two conditions are satisfied. First, the magnitude must be greater than a pre-selected threshold value. Second, the first difference must be close to zero, exploiting that the first difference at the peak of an impulse will be

Table 5.6: Mean ( $\mu$ ) and standard deviation ( $\sigma$ ) for various impulse waveshapes from 1000 simulation runs under different AWGN conditions

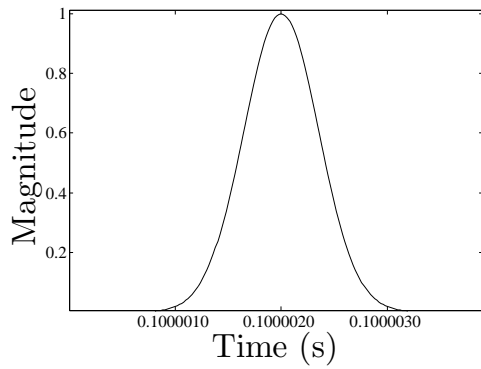
Impulse		$\mu$ v. SNR			$\sigma$ v. SNR		
Type	$T_{rise}(\mu s)$	15dB	10dB	5dB	15dB	10dB	5dB
Gaussian Pulse	4	+0.404	+0.384	+0.402	0.658	0.835	1.21
	0.4	-0.02	-0.34	-0.98	0.109	0.182	0.304
Sinc Pulse	4	-0.791	-0.767	-0.618	0.458	0.472	0.486
	0.4	-0.543	-0.399	-0.419	0.178	0.223	0.34
Lightning Impulse	1.2/50	-3.943	-3.68	-3.27	74	75	89.9
	8/20	4.6	5.81	6.24	2.16	11.22	81.6

zero.

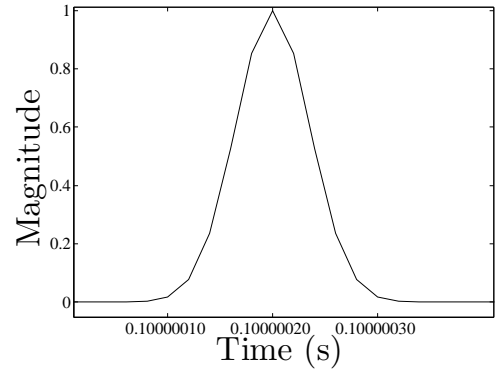
The algorithm is tested for three types of impulse waveshape: Gaussian pulse, Sinc pulse and standard lightning waveshapes, as shown in Fig. 5.13. Following the results of empirical investigations of noise characteristics on HV (10kV) lines published in [63] [64], the noise is modelled as Gaussian. Each impulse type is sent to the peak detect algorithm with differing levels of AWGN. Fig. 5.15 shows an example of the magnitude, the low pass filtered signal and the first difference for a Gaussian pulse with a rise time of 4  $\mu s$  and an SNR of 15 dB. The mean,  $\mu$  and the standard deviation,  $\sigma$  are calculated from 1000 simulation runs (see program listing in Appendix A.8) The results of the analysis are shown in Table 5.6.

## 5.9 Conclusion

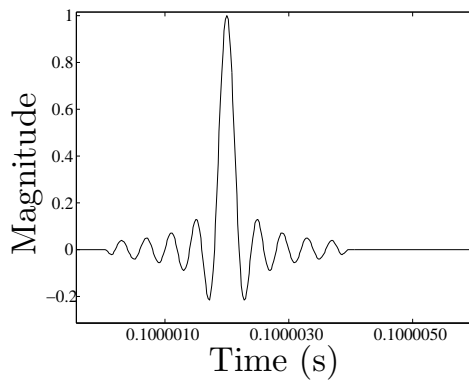
In this chapter, the fault location aspect of the OHMS concept have been examined from a theoretical viewpoint. The method has the potential to locate faults extremely accurately, even in highly branched networks where existing fault



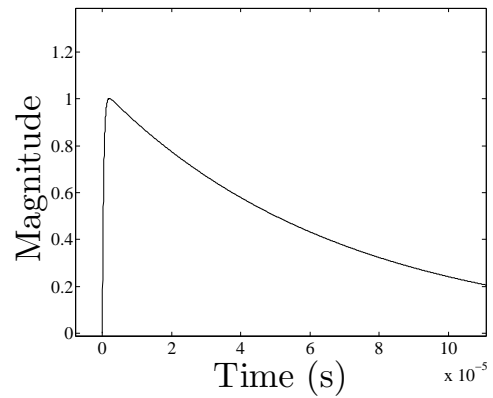
(a) Slow Gaussian Pulse (Rise time=4  $\mu$ s)



(b) Fast Gaussian Pulse (Rise time=400 ns)



(c) Sinc Pulse (Rise time=2  $\mu$ s)



(d) Lightning Impulse (1.2  $\mu$ s/50  $\mu$ s)

Figure 5.13: Generation of transients in Matlab for testing the peak detector algorithm (all magnitudes are normalised to 1,  $F_s=50$  MHz)

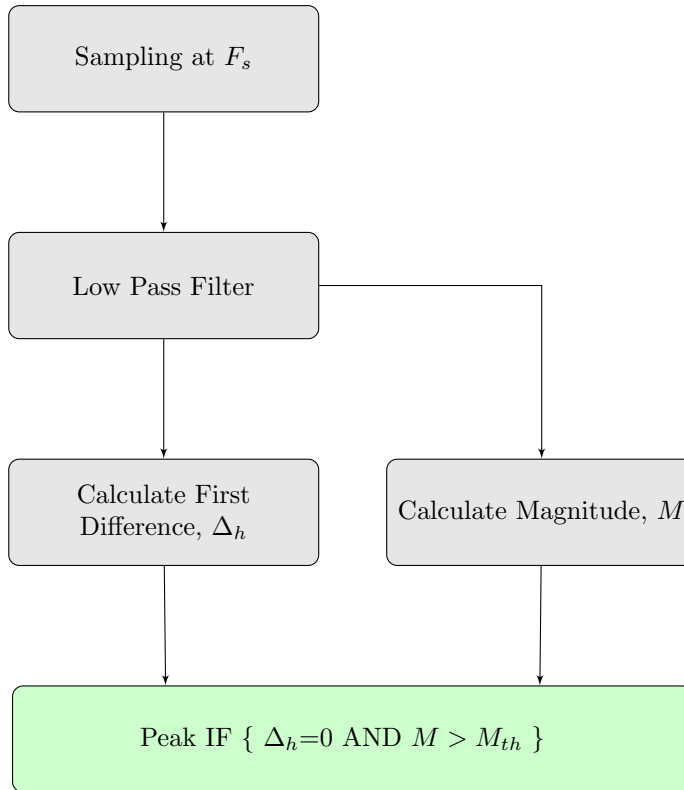
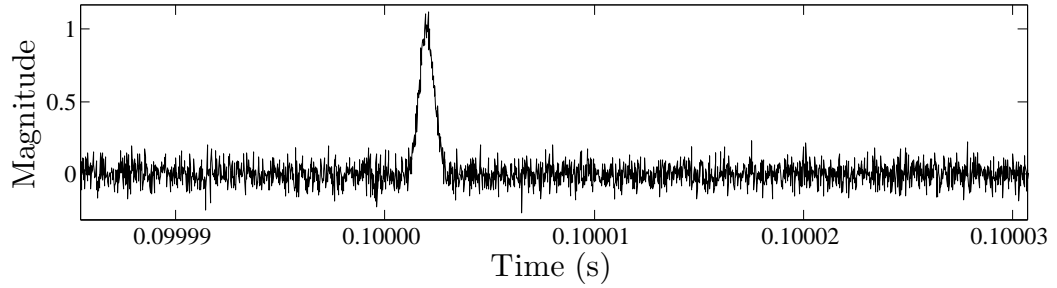
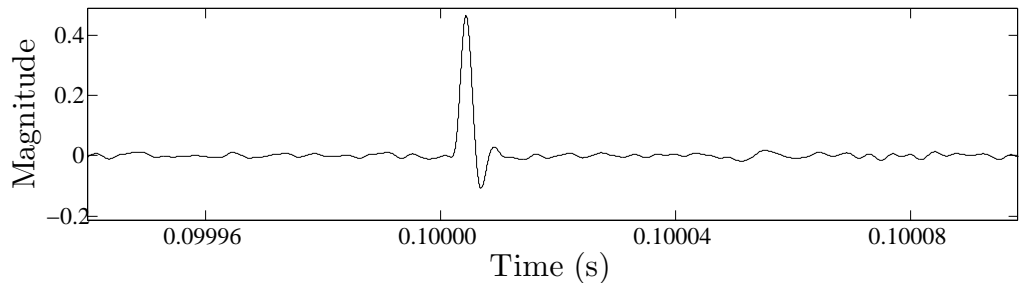


Figure 5.14: Peak detect algorithm with sampling frequency,  $F_s$

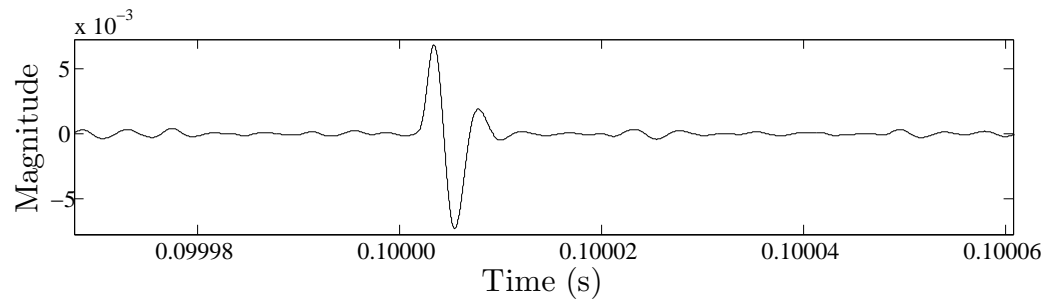
location algorithms tend to perform poorly. The new fault location scheme has been tested using a model in the ATP/EMTP. The results show that the accuracy of the new fault location scheme is only limited by the accuracy of the timestamping process and the transducers. It is recognised, however, that real world conditions will introduce additional sources of inaccuracy not accounted for in the simulation environment, for example a non-constant speed of the transient throughout the network, although this factor can partly be resolved with automated calibration steps. Another source of inaccuracy is the interpretation of the transient shape. The goal of the timestamping unit, across the system, is to detect consistently some



(a) Magntude of incoming signal,  $M$



(b) Low pass filtered signal (cutoff = 500 KHz)



(c) First Difference ( $\Delta_h$ )

Figure 5.15: Example waveforms from Matlab simulation of a Gaussian pulse with rise time of  $4 \mu\text{s}$  and a sampling frequency,  $F_s$ , of 50 MHz. The SNR of the transient is 10 dB.

attribute of the arriving transient and to subsequently timestamp the precise time of this event. It is recognised that this process could be a major source of error, however, a variety of transient waveshapes have been inputted into a candidate timestamping algorithm, and initial results are promising. Despite this, it may be difficult to timestamp the arrival time of “real life” transients because they may be irregular in shape (i.e. with no defined peak) or could be mixed with transients from other sources.

## Chapter 6

### Appraisal of Proposed Modes of Operation for the OHMS Device

#### 6.1 Introduction

In Chapter 4, a communication system based on highly optimised OFDM MODEMs was developed. Chapter 5 introduced a fault location method based on multi-ended measurements of the fault induced transient. Overall, the aim is to combine GPS based timestamping capability with a low latency, highly robust communication link between remote nodes. These nodes are called OHMS devices, and the new possibilities resulting from the rapid sharing of network information between these devices is called the OHMS concept. The sharing of recorded timestamps in the aftermath of a transient event (e.g. a permanent or incipient fault) allows the multi-ended fault location to be implemented, and is considered to be the main focus of the OHMS concept in this thesis. Also to be considered, however, is the implementation of a cost-effective PMU network based on the measurement and processing of voltage and current. Further to this, part of the communication capability inherent to the OHMS concept could be used to transport condition monitoring information back to a central point (e.g. a control room) or, potentially, to other OHMS devices in the network to facilitate better “decision making”.

In this Chapter, the intended modes of operation and the communication limitations/capabilities set out in Chapters 3 and 4 are reconciled to arrive at a

formal description of the prototype OHMS concept and the requirements of each OHMS device.

## 6.2 Possible Modes of Operation for the OHMS Device

In the many transmitter, single receiver configuration, several OHMS transmitters will take turns to transmit to a single receiver. The communication requirements depend on the amount of information to be transferred and how frequently this information is sent. In recognition of this, three separate schemes are considered. The first scheme is the least demanding in terms of communication requirements because it only transmits information following the detection of a transient. The second scheme, in addition to the timestamp information, also incorporates a synchrophasor unit transmitting voltage and current readings corresponding to standards on PMU systems [91]. The third type is the most demanding because in addition to the synchrophasor information, condition monitoring information is also to be sent.

The multiplexing scheme is based on accurate time multiplexing from the clock generated by the GPS receiver. Each OHMS transmitter is allocated a timeslot to transmit a synchronisation symbol and an information symbol. To enable the timestamp based fault location method, it is important to send all timestamps before the protection scheme operates. In light of this, the complete cycle, defined as the time it takes for all OHMS transmitters to transmit, should be kept significantly lower than the operating time of the protection scheme.

Consider a system with  $N_t$  OHMS transmitters spread across a distribution network. Each OHMS transmitter is given a timeslot,  $t_{ohm}$ . The OHMS transmitter uses this timeslot to send a synchronisation symbol and a minimum of one information symbol. It was shown in Chapter 3 and 4 that there are restrictions on the minimum size of the symbols. Each symbol, for instance, must include a cyclic prefix that is greater than the RMS delay spread of the channel,  $\tau_{rms}$ . The complete cycle of all transmitting nodes,  $t_{tot}$ , is defined as  $t_{ohm} \cdot N_{ohm}$ . A diagrammatic representation of the suggested multiplexing scheme is shown in Fig. 6.1.

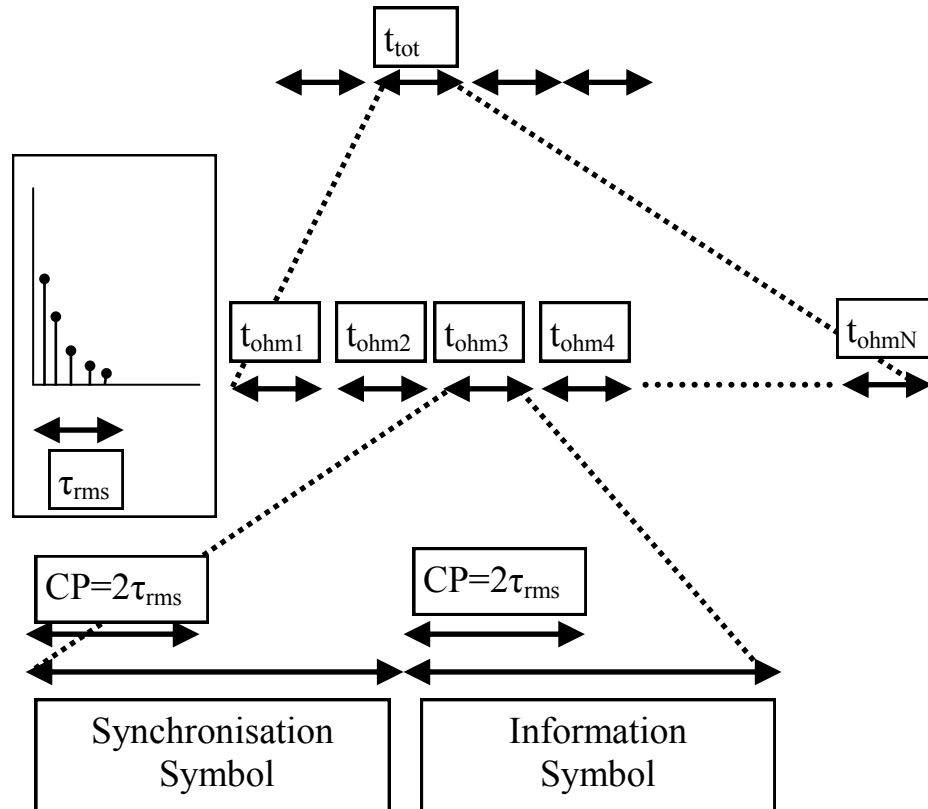


Figure 6.1: Diagrammatic representation of the proposed multiplexing scheme

Based on the results of Chapter 4,  $\tau_{rms}$  is assumed to be around 500  $\mu\text{s}$ , leading to a required cyclic prefix of approximately 1 ms. Table 6.1 shows the symbol duration (including cyclic prefix) and the information carrying capacity of DBPSK, DQPSK and D8PSK. As can be seen from the results, increasing the number of subcarriers increases the information carrying capacity at the expense of an increase in the symbol duration. It would be desirable to minimise the symbol duration whilst still ensuring the information carrying capacity to implement the desired scheme.

For Scheme 1 (timestamp information only), the critical factor is the speed at which all nodes can transmit following a transient event. To implement the fault location scheme outlined in Chapter 5, OHMS transmitters at all branch terminations should transmit before the circuit breaker of the protection scheme operates (although there may be further opportunities to transmit later on during the autore-close sequences). There may be times when a transient event has been detected, but the protection does not operate. In this case, even though there is no time limit on

Table 6.1: Symbol duration and information carrying capacity by modulation scheme

Modulation Scheme	Subcarriers	Symbol Duration	Information
DBPSK	128	1768 $\mu\text{s}$	128 Bits
	256	2500 $\mu\text{s}$	256 Bits
	512	4070 $\mu\text{s}$	512 Bits
DQPSK	128	1768 $\mu\text{s}$	256 Bits
	256	2500 $\mu\text{s}$	512 Bits
	512	4070 $\mu\text{s}$	768 Bits
D8PSK	128	1768 $\mu\text{s}$	128 Bits
	256	2500 $\mu\text{s}$	768 Bits
	512	4070 $\mu\text{s}$	1536 Bits

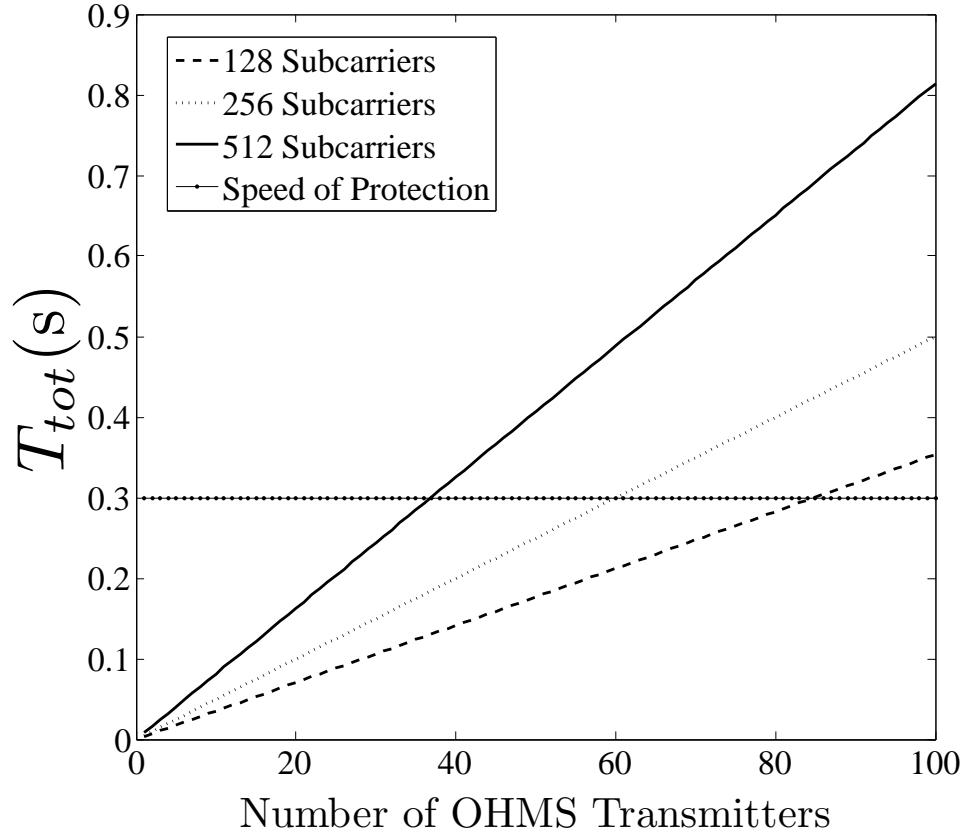


Figure 6.2: Number of OHMS Transmitters versus  $T_{tot}$

the retrieval of information, it is impossible to determine if the transient will result in a trip of the circuit breaker. Fig. 6.2 shows  $T_{tot}$  as a function of the total number of OHMS transmitters for symbol durations of '128', '256' and '512' samples in an OFDM system with a 167 kHz sampling frequency and a cyclic prefix of  $2 \cdot \tau_{rms}$ .

Fig. 6.2 shows that there is a limit imposed on  $T_{tot}$ . This limit is based on the response time of the circuit breaker following a fault. In this case, it is assumed that the protection scheme has an operation time of 0.3 s, allowing approximately 85 OHMS transmitters when using a 128 subcarrier symbol. Fewer OHMS transmitters are permissible when larger subcarrier symbols are used.

## 6.2.1 Mode 1: Transient Timestamp Only

The crucial information to be transmitted following a transient event<sup>1</sup> is the precise time of the peak of the transient and, optionally, the voltage or current of the transient at that point. At the OHMS transmitter, an internal counter running at 100 MHz is reset immediately after receiving a Pulse Per Second (PPS) signal from the GPS receiver. A short time after sending the PPS signal, the GPS module sends a serial string to the OHMS transmitter via the RS-232 interface. This serial string contains the date, hour, minute and the second commenced at the time the PPS signal was sent. The embedded processor within the OHMS transmitter processes this string and is able to place an extremely accurate timestamp on the peak of a transient by noting the value of the internal counter. The exact content of the serial string sent by the GPS module is shown in Table 6.3.

The GPS string shown in Table 6.3 is made up of both relevant and superfluous information. If it is assumed that the month, day and year is already known at the receiver, only the hour, minute, second and fractional second is needed from the GPS string. The fractional second itself becomes superfluous if it is assumed that the PPS is sent at exactly the top of a second. Now, the only extra requirement is the counter value. This counter value, running of a 100 Mhz clock, has a maximum value of 100,000,000, requiring 27 bits ( $2^{27} = 134,217,728$ ) to encode this information in a binary format.

Table 6.2 shows a breakdown of the necessary information to be sent to enable implementation of the fault location scheme outlined in Chapter 5. A total of 109

---

<sup>1</sup>Here, a transient event is defined as any disturbance that produces a travelling wave

Table 6.2: Breakdown of Short Position Message Char string [88]

Identifier	@@Hb	Short Position Message
Date	m	Month (1..12)
	d	Day (1..31)
	yy	Year (1998..2079)
Time	h	Hours (0..23)
	m	Minutes (00..59)
	s	Seconds (0..60)
	ffff	Fractional Second (0..999,999,999 ns)
Position	aaaa	Latitude in mas (-324,000,000..324,000,000)
	oooo	Longitude in mas (-648,000,000..648,000,000)
	hhhh	GPS Height in cm (-1000..+18,000m)
	mmmm	MSL Height in cm (0,000,000 with M12M)
Speed/Heading	VV	3D Speed in cm/s (0 to 514 m/s)
	vv	2D Speed in cm/s (0 to 514 m/s)
	hh	2D Heading (0 to 359.9°)
Geometry	dd	current DOP (0 to 99.9 DOP)
Satellite Data	n	Visible Satellites(0 to 12)
	t	Tracked Satellites (0 to 514 m/s)
Receiver Status	vvvvvv	ID Tag
	C	Checksum

bits are required to convey a timestamp information block with nanosecond accuracy. Also included is the latitude and longitude information, allowing the node to be mapped extremely accurately. Because the latitude and longitude information is unchanging, it may be possible only to send this information once, reducing the necessary number of bits to be transmitted from 109 to 45. Also included in the timestamp information block is the value of the current at the transient peak. This assumes a 14 bit ADC so has a maximum resolution of  $\pm 8192$ . Therefore, if the system is calibrated to a maximum transient current of 10,000 A, the system can record this transient to an accuracy of  $\pm 10,000/8192 = 1.22$  A.

Table 6.3: Breakdown of Timestamp Information Requirements

Timestamp	Fractional Second	27 bits
	Second	8 bits
	Minute	8 bits
	Hour	8 bits
Current	Transient Peak	14 bits ( $\pm$ 8192 resolution)
Device	Latitude	32 bits
	Longitude	32 bits
Total	All	109 bits
	Without Lat. and Long.	45 bits

A high level design showing a possible implementation of Scheme 1 is shown in Fig. 6.3. The decision diagram assumes that a counter controlled by an accurate GPS clock determines the timeslot allocated to that device, and restricts transmission to only this timeslot. The system distinguishes between two types of transient: high priority and low priority. A high priority transient is defined by a large peak value, indicative of a short circuit or low impedance fault. Low priority faults are defined by a lower peak value and may be regarded as earth faults and unlikely to trip the relay. High priority faults must be sent back to the OHMS receiver before the circuit breaker operates, so will be sent out first. Low priority timestamp information may contain important information about the location of an incipient fault, a short term disturbance or an ongoing high impedance fault that has not been detected by the protection operating on the network. Low priority timestamps are only sent if there are no high priority timestamps to send at the scheduled timeslot of the OHMS transmitter. It is important to note that the priority system is designed to ensure delivery of all timestamps before circuit breaker operation and makes no assertion about the severity of the fault itself, For example, earth faults are known

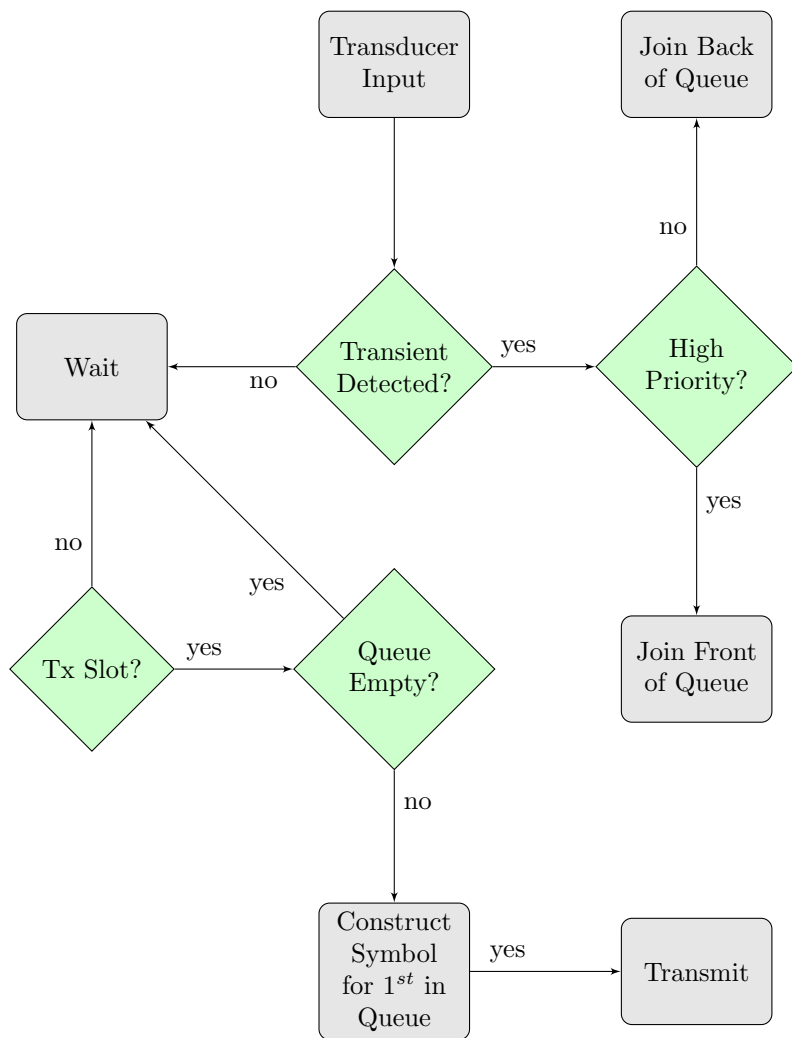


Figure 6.3: Decision diagram to implement scheme 1: timestamp only

to be notoriously difficult to detect and may lead to very dangerous and potentially hazardous conditions on the power system. The only reason these types of fault should be low priority is because they are unlikely to trip the relays as fast as low impedance faults.

## 6.2.2 Mode 2: Transient Timestamp and Synchrophasor

Assume that the OHMS transmitters are capable of measuring power frequency voltage and current. A synchrophasor can be set up if hardware for calculating the phase between the voltage and current signals is implemented. Table 6.4 shows the information requirements to send one synchrophasor message from the synchrophasor unit. Each message contains 14 bit voltage and current readings and a 14 bit phase angle reading, giving a resolution of  $0.02^\circ$ .

The reporting rate of synchrophasors have been standardised in the IEEE Standard C37.118-2005. The standard recommends a reporting rate of either 10 or 25 messages per second in a power system operating at a 50 Hz nominal frequency. To achieve this reporting rate, each OHMS transmitter must transmit at least every 100 ms (for a reporting rate of 10 per second) and 40 ms (for a reporting rate of 25 per second). This requirement places a limit on  $T_{tot}$  and subsequently introduces a limit on the total number of OHMS transmitters that can be used in the same network. It may be possible to increase  $T_{tot}$  by halving the reporting rate and doubling the information sent per message, for example by moving from a DBPSK to DQPSK scheme.

Table 6.4: Breakdown of Synchrophasor Information Requirements

Signals	Voltage	14 bits
	Current	14 bits
Phase Angle	Degrees	14 bits
Total	Synchrophasor	42 bits
	With Timestamp	87 bits

### 6.2.3 Mode 3: Transient Timestamp, Synchrophasor and Condition Monitoring

The third scheme allows a portion of the sent information to be reserved for a dedicated condition monitoring link. It is difficult to predict how much information is required to satisfy a particular condition monitoring service, but here, it is assumed that the information requirement is 100 bits and is sent once per second. This pushes up the information requirement to 187 bits per transmitter per second.

## 6.3 Appraisal of Operating Mode 1

### 6.3.1 Proof of Concept

It is assumed that operating mode 1 is to be implemented on the test network, providing full fault location capability. The multiplexing scheme is based on an OHMS system comprising 14 OHMS transmitters and a single OHMS receiver at position index 1. Therefore, 14 transmissions are required to send all timestamps to the OHMS receiver following a fault. In this case, a 512 subcarrier scheme with DBPSK modulation and a sampling frequency of 166.7 kHz is used. The cyclic prefix

is set to 167 samples giving a total OHMS symbol duration of  $(512+167)+(512+167)$  samples, or 8.15 ms. The total transmission time,  $T_{tot}$ , is 114 ms. The OHMS transmitters are time multiplexed to a transmission window of 8.15 ms every 114 ms. It is now possible to test the concept by simulating fault scenarios on the test network.

### 6.3.2 Pre-fault Calculations

The fault location aspect of the OHMS concept is appraised using the test network. In Fig. 6.4, the test network is modified to include fifteen possible OHMS device locations at the termination of each branch. These are labelled A-O. The resolution is chosen as 10 m per point index<sup>2</sup>. A summary of the branch lengths and position indexing is shown in Table 6.5. The matrices  $\mathbf{A}$  (shown in Equation (6.1)),  $\mathbf{B}$  (shown in Equation (6.2)) and the array  $\mathbf{c}$  (shown in Equation (6.3)) are calculated directly from the network and pre-fault calculations are carried out in accordance with the method set out in Sections 5.2.3 and 5.6.1.  $\mathbf{D}$ , not shown, is a 1947 by 1947 matrix.

---

<sup>2</sup>Choosing 1 m per point index would increase the size of  $\mathbf{D}$  by 100, increasing computation time.

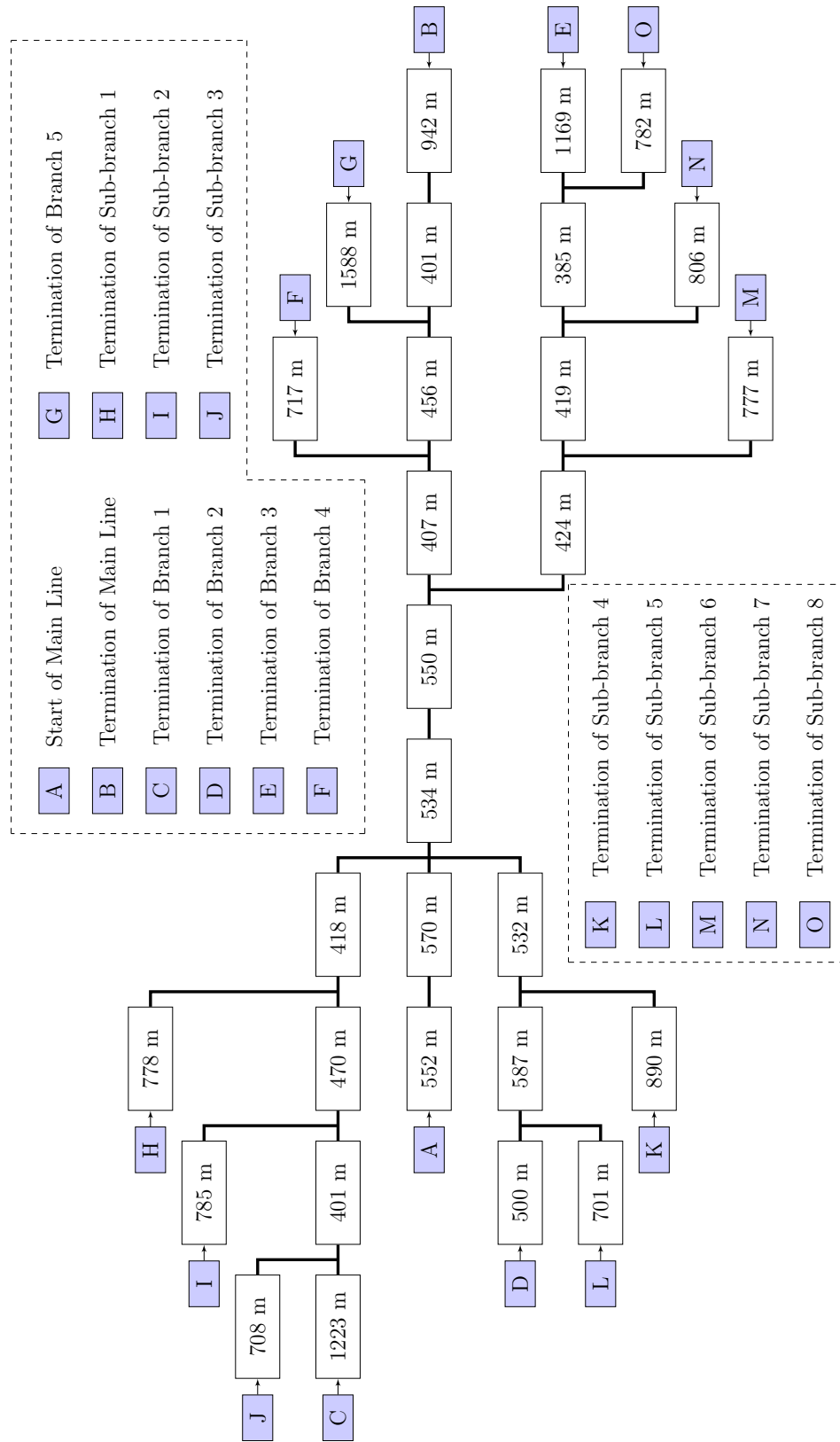


Figure 6.4: Test network showing positions of the OHMS devices

$$\mathbf{A} = \begin{bmatrix}
441 & 0 & 0 & 0 & 0 & 0 & 42 & 89 & 129 & 53 & 112 & 42 & 84 & 123 \\
0 & 251 & 0 & 108 & 149 & 195 & 0 & 0 & 0 & 53 & 112 & 151 & 193 & 231 \\
0 & 0 & 162 & 108 & 149 & 195 & 42 & 89 & 129 & 0 & 0 & 151 & 193 & 231 \\
0 & 108 & 108 & 240 & 41 & 86 & 150 & 197 & 237 & 162 & 220 & 0 & 0 & 0 \\
0 & 149 & 149 & 41 & 72 & 46 & 191 & 238 & 278 & 202 & 261 & 83 & 125 & 164 \\
0 & 195 & 195 & 86 & 46 & 159 & 237 & 284 & 324 & 248 & 307 & 129 & 171 & 209 \\
42 & 0 & 42 & 150 & 191 & 237 & 78 & 47 & 87 & 95 & 154 & 193 & 235 & 273 \\
89 & 0 & 89 & 197 & 238 & 284 & 47 & 79 & 40 & 142 & 201 & 240 & 282 & 320 \\
129 & 0 & 129 & 237 & 278 & 324 & 87 & 40 & 71 & 182 & 241 & 280 & 322 & 360 \\
53 & 53 & 0 & 162 & 202 & 248 & 95 & 142 & 182 & 89 & 59 & 204 & 246 & 284 \\
112 & 112 & 0 & 220 & 261 & 307 & 154 & 201 & 241 & 59 & 70 & 263 & 305 & 343 \\
42 & 151 & 151 & 0 & 83 & 129 & 193 & 240 & 280 & 204 & 263 & 78 & 42 & 80 \\
84 & 193 & 193 & 0 & 125 & 171 & 235 & 282 & 322 & 246 & 305 & 42 & 81 & 39 \\
123 & 231 & 231 & 0 & 164 & 209 & 273 & 320 & 360 & 284 & 343 & 80 & 39 & 78
\end{bmatrix}$$

(6.1)

$$\mathbf{B} = \begin{bmatrix}
441 & 112 & 112 & 221 & 261 & 307 & 112 & 112 & 112 & 112 & 112 & 221 & 221 & 221 \\
112 & 251 & 0 & 0 & 0 & 0 & 42 & 89 & 129 & 0 & 0 & 0 & 0 & 0 \\
112 & 0 & 162 & 0 & 0 & 0 & 0 & 0 & 0 & 53 & 112 & 0 & 0 & 0 \\
221 & 0 & 0 & 240 & 0 & 0 & 0 & 0 & 0 & 0 & 0 & 42 & 84 & 123 \\
261 & 0 & 0 & 0 & 72 & 0 & 0 & 0 & 0 & 0 & 0 & 0 & 0 & 0 \\
307 & 0 & 0 & 0 & 0 & 159 & 0 & 0 & 0 & 0 & 0 & 0 & 0 & 0 \\
112 & 42 & 0 & 0 & 0 & 0 & 78 & 0 & 0 & 0 & 0 & 0 & 0 & 0 \\
112 & 89 & 0 & 0 & 0 & 0 & 0 & 79 & 0 & 0 & 0 & 0 & 0 & 0 \\
112 & 129 & 0 & 0 & 0 & 0 & 0 & 0 & 71 & 0 & 0 & 0 & 0 & 0 \\
112 & 0 & 53 & 0 & 0 & 0 & 0 & 0 & 0 & 89 & 0 & 0 & 0 & 0 \\
112 & 0 & 112 & 0 & 0 & 0 & 0 & 0 & 0 & 0 & 70 & 0 & 0 & 0 \\
221 & 0 & 0 & 42 & 0 & 0 & 0 & 0 & 0 & 0 & 0 & 78 & 0 & 0 \\
221 & 0 & 0 & 84 & 0 & 0 & 0 & 0 & 0 & 0 & 0 & 0 & 81 & 0 \\
221 & 0 & 0 & 123 & 0 & 0 & 0 & 0 & 0 & 0 & 0 & 0 & 39 & 78
\end{bmatrix}$$

(6.2)

Table 6.5: Branch lengths and position indexing for the example network

Branch	Length (m)	Position Index	Starting Point	End Point
Main Line	4412	1..441	A	B
Branch 1	2512	442..692	-	C
Branch 2	1619	693..854	-	D
Branch 3	2397	855..1090	-	E
Branch 4	717	1095..1166	-	F
Branch 5	1588	1167..1325	-	G
Sub-branch 1	778	1326..1402	-	H
Sub-branch 2	785	1403..1481	-	I
Sub-branch 3	708	1482..1552	-	J
Sub-branch 4	890	1553..1641	-	K
Sub branch 5	701	1642..1711	-	L
Sub-branch 6	777	1712..1788	-	M
Sub branch 7	806	1789..1869	-	N
Sub-branch 8	702	1870..1947	-	O

$$\mathbf{c} = \begin{bmatrix} 0 \\ 441 \\ 692 \\ 854 \\ 1094 \\ 1166 \\ 1325 \\ 1402 \\ 1481 \\ 1552 \\ 1641 \\ 1711 \\ 1788 \\ 1869 \\ 1947 \end{bmatrix} \quad (6.3)$$

### 6.3.3 Scenario 1: Fault on the main line (all overhead line network)

A single line to ground fault is simulated at position index 166 using a time controlled switch between the centre conductor and earth. Table 6.6 shows the time

Table 6.6: Arrival of fault induced transient for fault at position index 166 (fault initialisation time=0.0001 s)

OHMS Location	Time of Arrival (s)
A	0.00010552
B	0.00010918
C	0.00011015
D	0.00010717
E	0.00010982
F	0.00010558
G	0.00011000
H	0.00010577
I	0.00010735
J	0.00010843
K	0.00010652
L	0.00010785
M	0.00010584
N	0.00010733
O	0.00010853

of arrival of the high frequency fault induced transient for all fifteen possible OHMS device locations. The timestamp derived R-ratios can now be calculated, followed by calculation of  $W(n)$  using Equation 5.33. The plot of  $W(n)$  for the situation when all 15 OHMS devices are included in the method is plotted in Fig. 6.5. The Matlab m-file used for this simulation is in Appendix C.7.

The metric is observed to minimise at the faulted index point of 166. To explore the effect of timing errors on the performance fault estimator, an error variable with a zero mean and a specified variance is added to the timestamp for each OHMS device. It is observed from Fig. 6.6, which shows the spread of fault estimates for standard deviations of between 10 and 60 ns, that the accuracy of the fault locator is diminished as the standard deviation of the error term increases. The spread of the fault estimation error approximates to a normal distribution

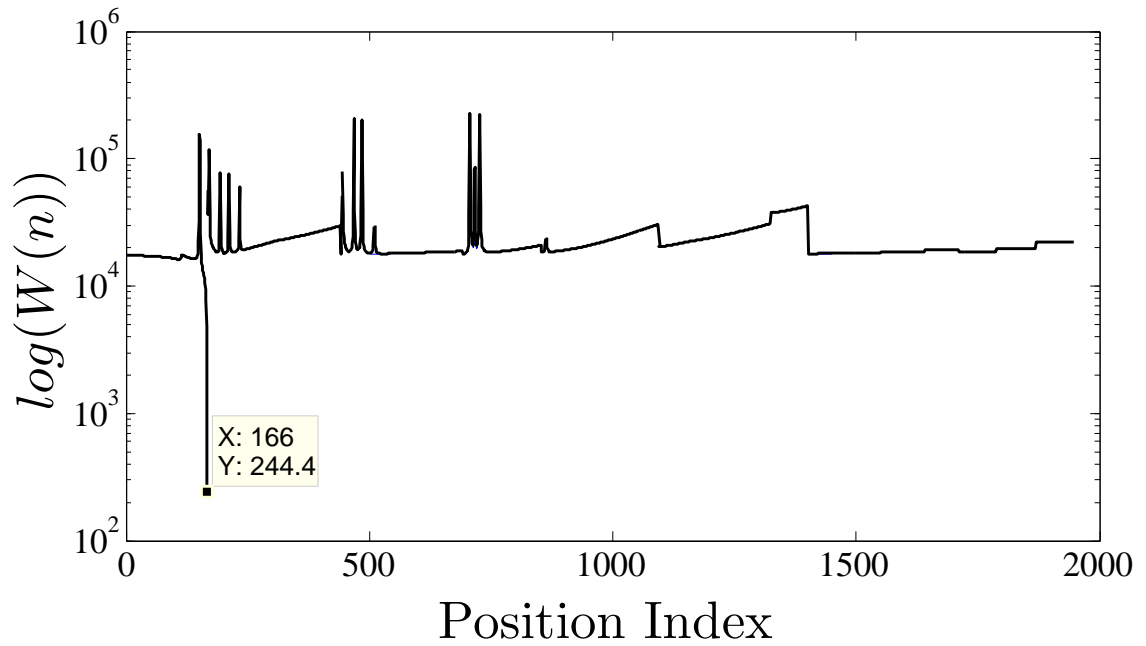
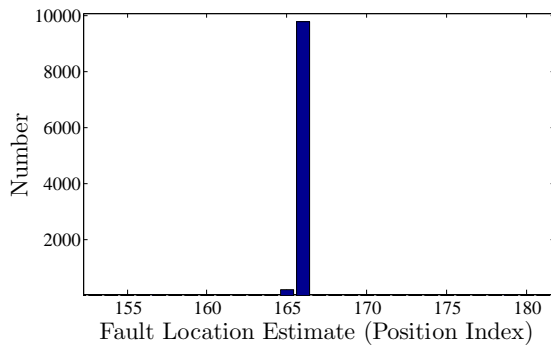


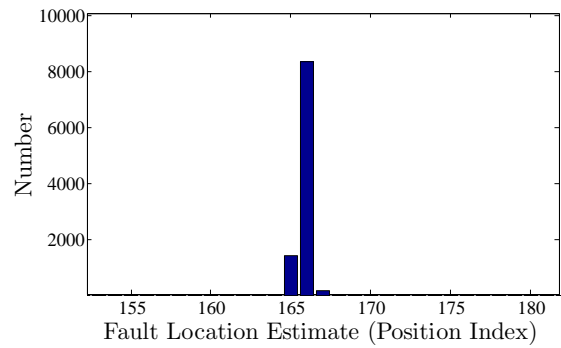
Figure 6.5:  $W$  metric from the multi-ended method for the fault at position index 166.

with the mean value centred on the position index of the correct fault position. This agrees with the earlier analysis of error sensitivity in the one and two branch networks (shown in Fig. 5.10), where the fault estimation error was proportional to the timestamping error.

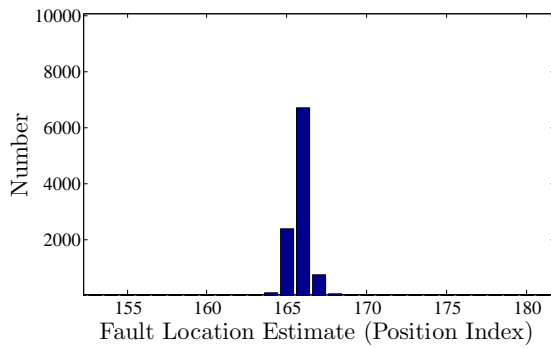
It is interesting to note that as the error standard deviation increases, there is a tendency for fault estimates to move away from the mean and form new clusters. This is shown in Fig. 6.7(a) and Fig. 6.7(b) for standard deviations of 180 ns and 350 ns respectively. It is observed that the outliers cluster at specific position indices, in this case 100 and 442. It is worth noting that position index 442 is the end of the main line. It is unclear why these outliers cluster in such a manner, but it is



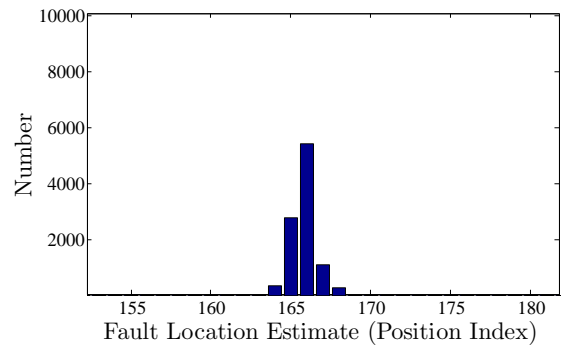
(a)  $\sigma=10$  ns



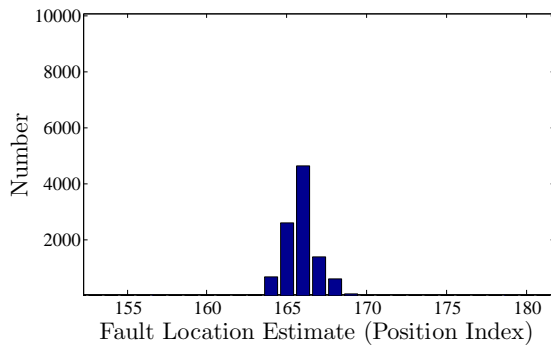
(b)  $\sigma=20$  ns



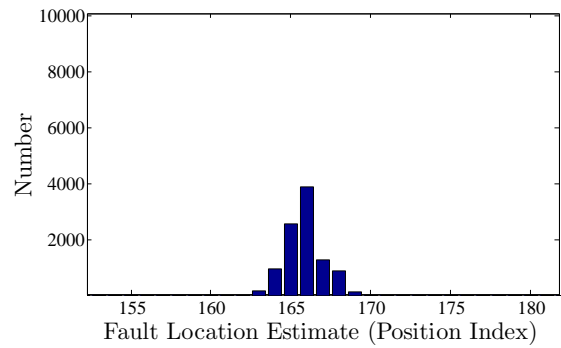
(c)  $\sigma=30$  ns



(d)  $\sigma=40$  ns

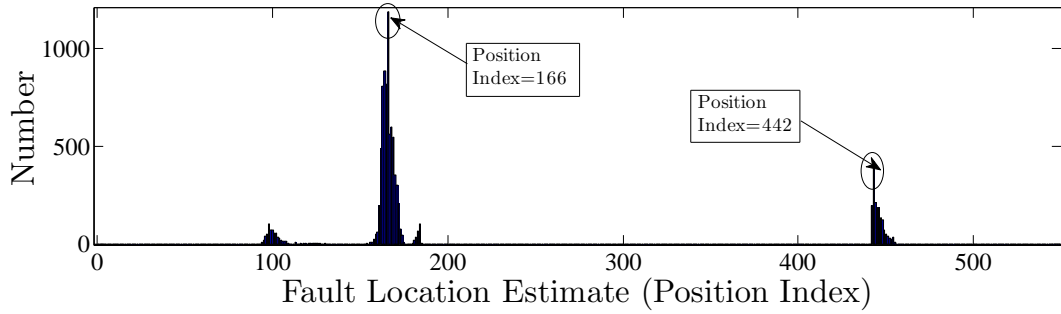


(e)  $\sigma=50$  ns

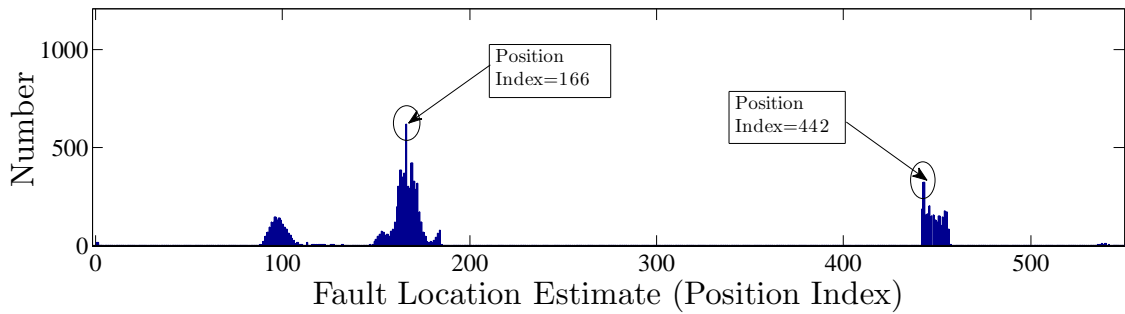


(f)  $\sigma=60$  ns

Figure 6.6: Histograms derived from 10,000 simulation runs at differing values of standard deviation,  $\sigma$ , of the imposed error on each of the 15 OHMS devices involved in the multi-ended fault location method for the fault at position index 166.



(a)  $\sigma=180$  ns



(b)  $\sigma=350$  ns

Figure 6.7: Histograms derived from 10,000 simulation runs at differing values of standard deviation,  $\sigma$ , of the imposed error on each of the 15 OHMS devices involved in the multi-ended fault location method for the fault at position index 166.

suspected that as the error term increases, the fault location estimate may deviate away from the branch of the faulted position and move to the branch that has the most similar R-ratios.

In a practical implementation of the multi-ended method, it is difficult to estimate the standard deviation of the error term at each OHMS device. It will depend on many factors including the GPS clock accuracy, the timestamping accuracy and possible distortion of the travelling wave as it propagates through the network. These types of error can, by the central limit theorem, be modelled to a reason-

able degree of accuracy as a random variable with a Gaussian distribution and zero mean<sup>3</sup>. It is possible to envisage another type of error that does not conform to the gaussian distribution, rather it will only effect a single, or small number of OHMS device(s). An example of this is a situation whereby one of the OHMS devices has a large timestamping error (due, perhaps to a burst of noise local to that device), but the rest of the devices are otherwise unaffected. Although the multi-ended method is somewhat immune to extremely large errors<sup>4</sup>, it may not be possible to distinguish small individual errors. To examine this effect, one of the OHMS devices is given a large error and the remaining devices are left free from error. Two cases are examined. The first case, shown in Fig. 6.8(a) is for the OHMS device at location B. i.e. on the same branch as the fault. The other case, shown in Fig. 6.8(b), is for an OHMS device deemed to be insignificant in the fault location process (for main line faults). Here, the OHMS device at position “N” is chosen.

On comparison of Fig. 6.8(a) and Fig. 6.8(b), it is evident that the effect on  $W(n)$  is far more pronounced when there is a large individual error in OHMS device B than in OHMS device N. The effect of an individual error is to increase the value of the  $W$  metric at the position of the fault. Eventually, the value of  $W$  increases such that there is no longer a minimum at the faulted position. Fortunately, the movement of  $W$  at the faulted position index is graceful in the sense that the minimum is conserved until a critical point is reached.

---

<sup>3</sup>This assumes that each error contributor is an independent random variable.

<sup>4</sup>This is because outliers can be automatically removed from the analysis once all the timestamps are collected.

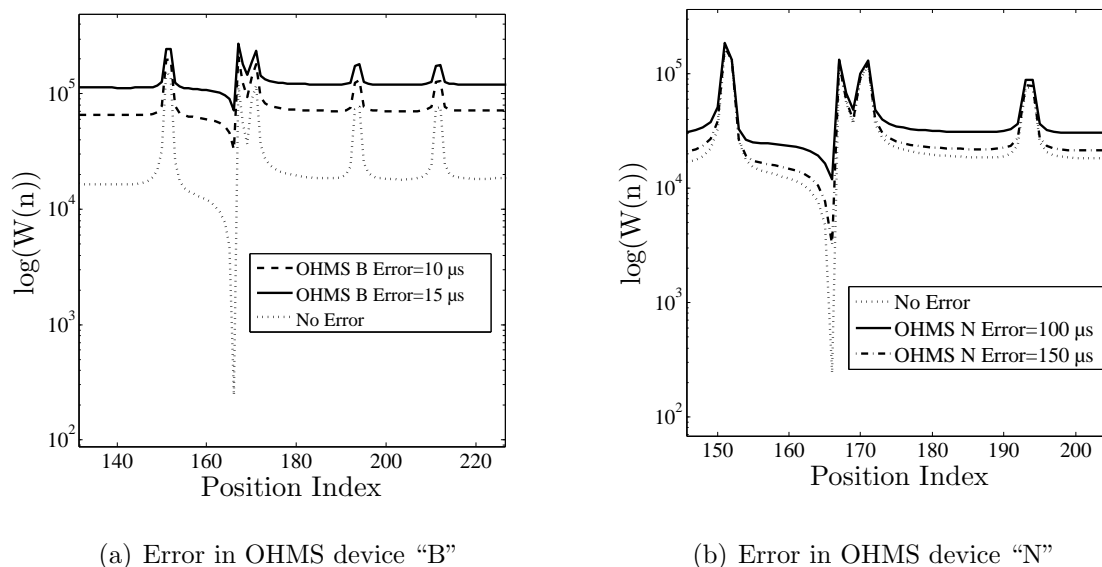


Figure 6.8: Plots to show effect of a large individual error on the resultant  $W(n)$  (all 15 OHMS devices involved in the method).

### 6.3.4 Scenario 2: Fault on a Sub-branch

A similar analysis to that conducted in Scenario 1 is now carried out for a fault position on a branch in the test network. The new fault position is chosen, arbitrarily, as position index 642. This is close to OHMS device C on branch 1. The pre-fault calculations remain the same but it is now necessary to process a new set of timestamp derived R-ratios based on the new arrival times listed in Table 6.7.

Fig. 6.9 shows the  $W$  metric resulting from the multi-ended method with all 15 OHMS devices involved (and no errors). Again, the method has successfully located the position of the fault. To analyse the effect of Gaussian type errors, an error term is introduced to all OHMS devices and the distributions of fault estimates after 10,000 simulation runs for different values of standard deviation are plotted in Fig. 6.10.

Table 6.7: Arrival of fault induced transient for fault at position index 642 (fault initialisation time=0.0001 s)

OHMS Location	Time of Arrival (s)
A	0.00011047
B	0.00011434
C	0.00010168
D	0.00011212
E	0.00011833
F	0.00011408
G	0.00011850
H	0.00010793
I	0.00010639
J	0.00010481
K	0.00011147
L	0.00011279
M	0.00011434
N	0.00011583
O	0.00011703

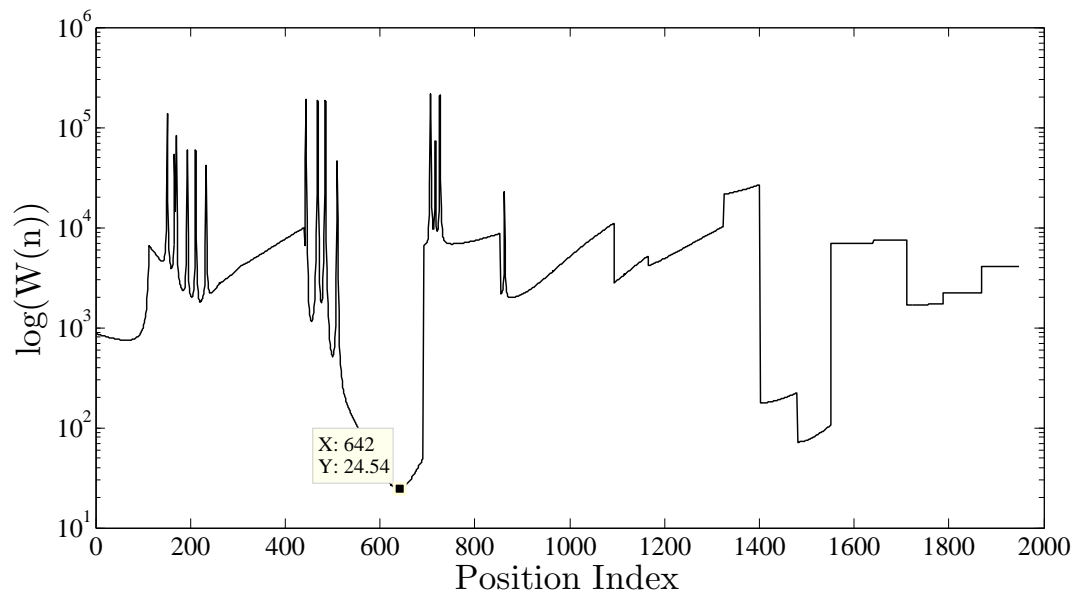
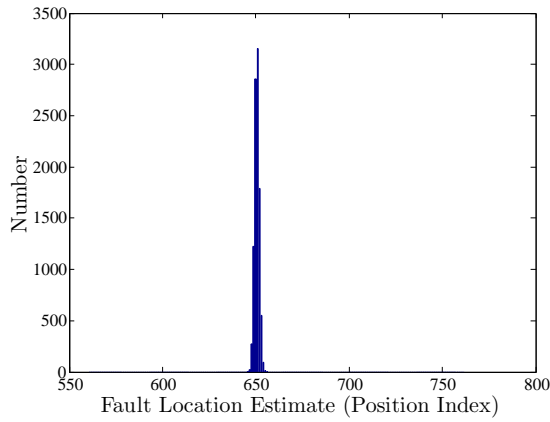
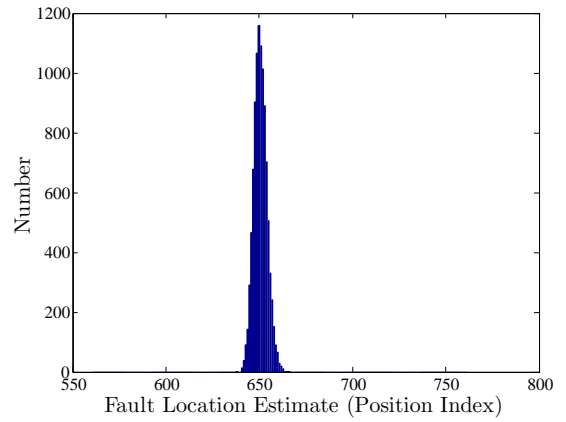


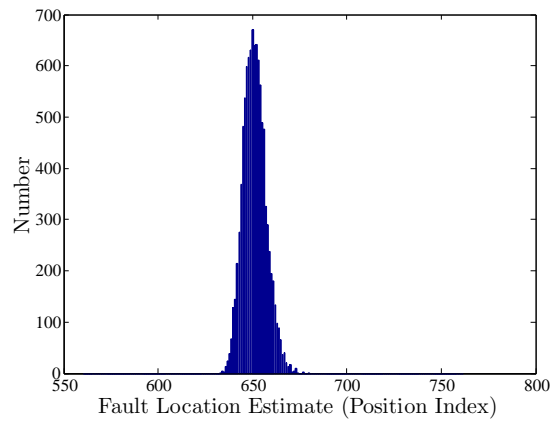
Figure 6.9: W metric from the multi-ended method for the fault at position index 642.



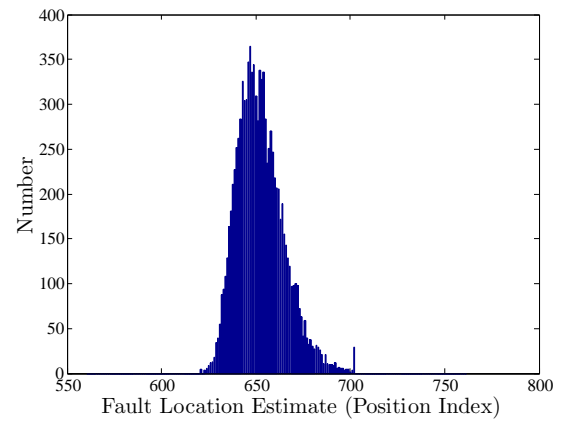
(a)  $\sigma=10$  ns



(b)  $\sigma=30$  ns

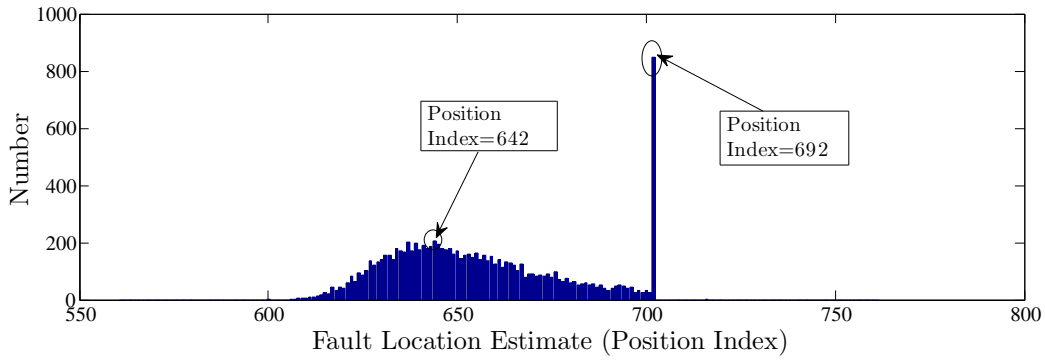


(c)  $\sigma=50$  ns

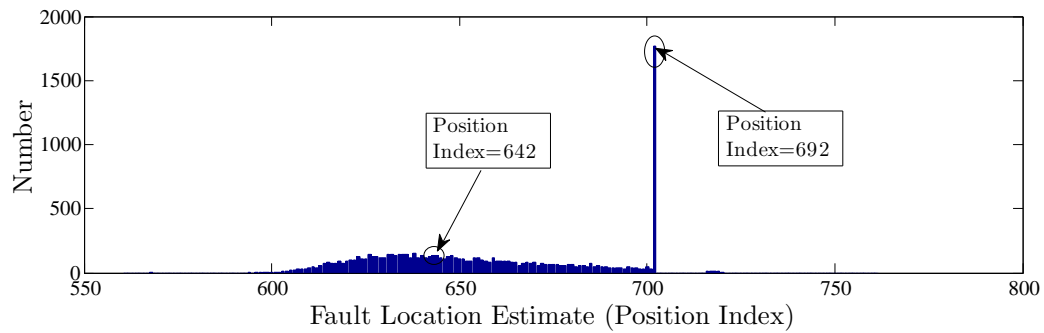


(d)  $\sigma=100$  ns

Figure 6.10: Histograms derived from 10,000 simulation runs at differing values of standard deviation,  $\sigma$ , of the imposed error on each of the 15 OHMS devices involved in the multi-ended fault location method for the fault at position index 642.



(a)  $\sigma = 180$  ns



(b)  $\sigma = 350$  ns

Figure 6.11: Histograms derived from 10,000 simulation runs at differing values of standard deviation,  $\sigma$ , of the imposed error on each of the 15 OHMS devices involved in the multi-ended fault location method for the fault at position index 642.

As was observed in Scenario 1, the distribution is normal with a mean equal to the fault position of 642. In Fig. 6.11, the histogram of fault location estimates is shown for larger standard deviations. Here, a peculiar anomaly is observed at position index 692, a network position that coincides with the end point of branch 1. The error terms combine in all OHMS devices such that the likelihood of a fault estimate of position index 692 is high. This is simply due to the particular evolution of the shape of the  $W$  metric for combinations of error.

### 6.3.5 Scenario 3: Fault on the main line (all overhead line network), reduced number of OHMS devices

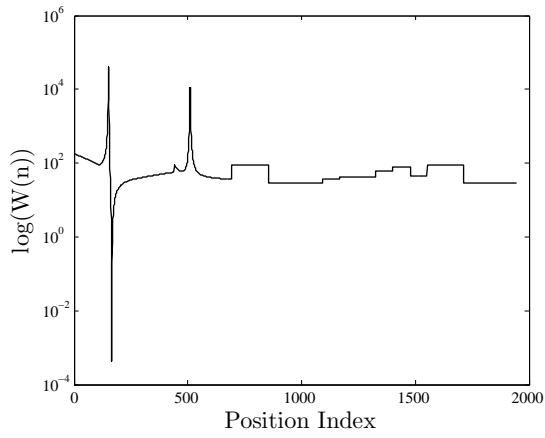
In Section 5.7, it was stated that the fault location capability of the multi-ended method depends on whether there is an OHMS device situated in at least one branch termination in either direction of the faulted network position. In this section, the performance of the fault location algorithm is examined on the test network for reduced numbers of OHMS devices. In Fig. 6.12, the  $W$  metrics resulting from execution of the multi-ended algorithm with different combinations of OHMS devices are shown.

Although the shapes of the  $W$  metrics in Fig. 6.12 may not seem indicative of a pattern, a closer look at them reveals a lot about the behaviour of the multi-ended fault location algorithm. In Fig. 6.12(a), three OHMS devices, positioned at A, B and C are shown to successfully locate the fault. The same analysis for OHMS devices at position A, B and G, as shown in Fig. 6.12(b), still shows a successful fault location estimate, but this time, there is a “rival” minimum at position index 1199, a position index located on branch 5. This means that for this particular arrangement of OHMS devices, position index 1199 exhibits similar R-ratios to those at position index 166 (i.e. the fault position). Increasing the number of OHMS devices decreases the likelihood that 2 points on a network will have similar R-ratios. In Fig. 6.12(d), the multi-ended algorithm is shown to fail to locate the fault. Here, the OHMS devices are positioned at locations A, C and D. Inspection of the test network in Fig. 6.4 explains why this arrangement of OHMS devices has

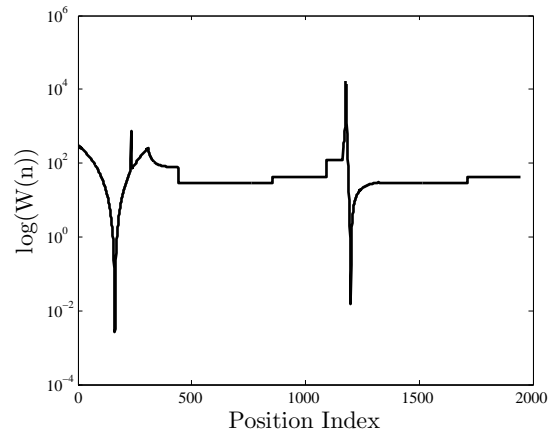
failed to locate the fault. The high frequency travelling wave propagates away, in both directions, from the faulted position index but OHMS devices are only present in one direction. Furthermore, it is observed that the travelling wave splits into three parts (plus a reflection) at the juncture between the main line and branches 1 and 2. It is impossible, even for any number or combination of OHMS devices, to locate faults that are beyond this juncture if there is no OHMS device in the other direction of the faulted point. Although the recorded timestamps will differ for all possible fault positions residing beyond the discussed juncture, the timestamp derived R-ratios will be the same. Furthermore, the network derived R-ratios in this region will be flat. Therefore, the  $W$  metric is flat for these regions. The most that can be inferred from this situation is that the fault has occurred *somewhere* in this flat region of the  $W$  metric. In Fig. 6.12(e), the condition of an OHMS device in both directions of the faulted position is satisfied, and the correct fault estimate is produced. Fig. 6.12(f) shows another example not satisfying this condition and the fault is not located correctly.

## 6.4 Conclusion

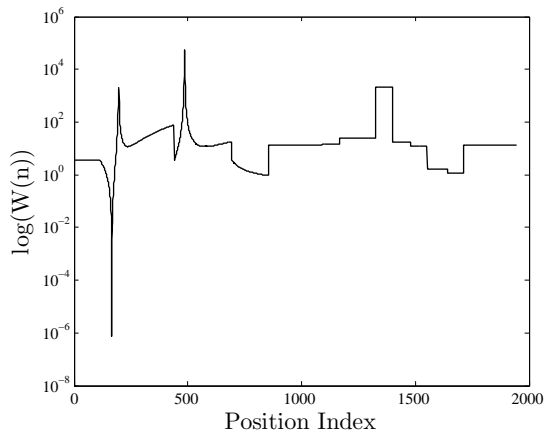
This Chapter has attempted to formalise the OHMS system by recommending a multiplexing scheme allowing a number of OHMS devices to communicate short bursts of information in sequence. Three main operating modes have been suggested. In the first operating mode, the OHMS devices are to send timestamp information following a transient event. It has been shown, through simulation on



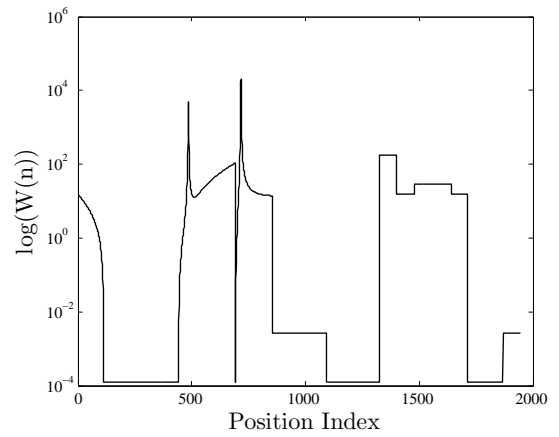
(a) OHMS devices: ABC



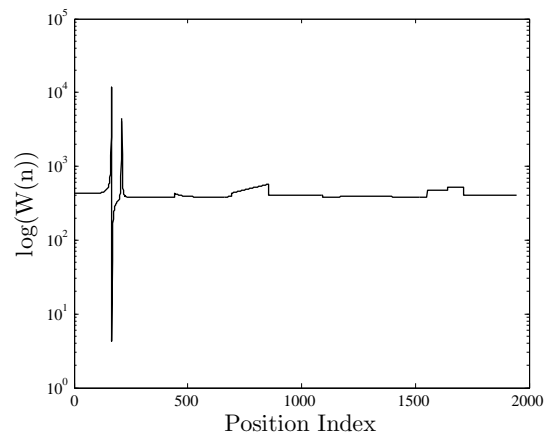
(b) OHMS devices: ABG



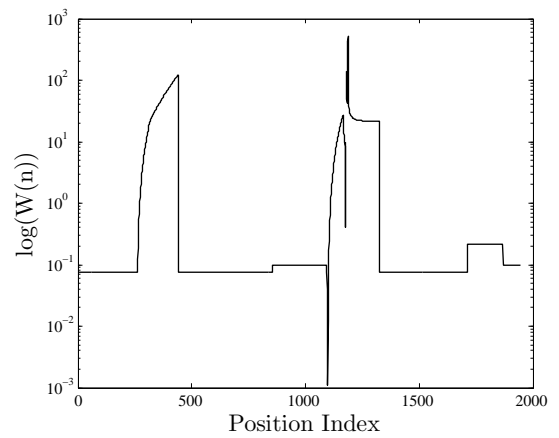
(c) OHMS devices: BCD



(d) OHMS devices: ACD



(e) OHMS devices: CDG



(f) OHMS devices: BGF

Figure 6.12:  $W$  metric for fault at position index 166 for a reduced number of OHMS devices.

the test network, that the multi-ended fault location method introduced in Chapter 5 can be implemented in a typical rural distribution network. To be able to locate faults everywhere on the network, an OHMS device must be located at each branch termination. When fewer OHMS devices are installed, fault location is only possible in parts of the network that satisfy the condition of having an OHMS device in both directions away from that position. An OHMS device at every branch termination explicitly satisfies this condition.

The second and third operating modes can be thought of as extensions to the first operating mode. Operating mode 2 uses on-board computational power to calculate the phasor difference between voltage and current sensor readings. The information is sent back to a central point at regular intervals. If this is achieved at multiple locations on a network, a PMU network has been established on the rural network. Operating mode 3 is a simple bridging of condition monitoring information through the OHMS infrastructure.

## Chapter 7

### Hardware and Software Development

#### 7.1 Introduction

In Chapter 3, it was shown that a multi-carrier communication scheme is well suited to the PLC channel. It was further shown in Chapter 4 that a highly optimised OFDM based system is capable of achieving robust communication between remote nodes on a PLC network. In Chapters 5 and 6, a multi-ended fault location method based on the retrieval of the high frequency fault induced transient was outlined. A further mode of operation incorporates synchrophasors measurements and their retrieval through the OHMS communication network. The final mode discussed in Chapter 6 added the capability of transmitting condition monitoring information.

In this Chapter, the development of the hardware necessary to implement the OHMS concept is discussed.

#### 7.2 Hardware Requirements of the System

##### 7.2.1 Communication Requirements

The starting point to the design of the OFDM MODEM is the set of requirements. Simulation work carried out in Chapter 5 has shown that the robustness of communication is extremely sensitive to a number of key parameters and care-

ful consideration must be given to setting these parameters in hardware. It must be recognised, first, that communication over the HV PLC channel poses a number of unique problems that most “off the shelf” chipsets fail to solve. Second, it must be appreciated that readily available chipsets do not facilitate easy integration into a bespoke multiplexing scheme such as one that is required to facilitate the functionality of the OHMS concept. In response to these factors, the decision was made to design and develop the MODEM independently. This approach offers several advantages, including the ability to customise fully the communication scheme, more intimate integration into the rest of the system and easier integration into a multiplexing scheme. The design cycle begins with the following minimum requirements:

- 128, 256 and 512 subcarrier modes.
- A minimum payload<sup>1</sup> of 90 bits per OHMS symbol for operating mode 1 and 180 bits per OHMS symbol for mode 2.
- Minimum cyclic prefix length of 1 ms (configurable).
- Minimum subcarrier spacing of 300-400 Hz.
- Subcarrier modulation: DBPSK, DQPSK and D8PSK (adaptable).
- Operation time between request to send and ready to send of less than 1 ms.
- Schmidl/Cox timing estimator.

---

<sup>1</sup>Assuming rate  $\frac{1}{2}$  convolutional coding.

- Successful integration into a multiplexing scheme (i.e.the device can only transmit at specified times).

## 7.2.2 Tmestamping Requirements

The GPS time stamping module must be able to detect and timestamp the arrival time of the high frequency fault induced transient to an accuracy that allows successful implementation of the multi-ended fault location method.

## 7.2.3 Processing Requirements

The OHMS concept relies on remote computation at several locations in the distribution network. For operating mode 1 (fault location scheme), it has been shown that a peak detect algorithm is necessary. In Fig. 5.14, a peak detect algorithm based on calculation of the first difference of the samples input signal was suggested. The algorithm also requires a low pass filter. For the OFDM communication system, several computationally intensive functions are required, including the FFT/IFFT and CORDIC engines. The synchrophasor module can also be implemented using the FFT. In general, a high capacity FPGA with a bespoke digital design should be capable of achieving the desired functionality.

## 7.2.4 Transducer Requirements

The OHMS device should include, as a minimum, a means of coupling to the power line (for the PLC communication scheme) and a method of measuring

the high frequency fault induced transient. To enable the synchrophasor operating mode, power frequency sensors are required. It is suggested that a rogowski coil is used to measure the fault induced transient and either a coupling capacitor or inductive coupler is capable of providing coupling to the power line.

### 7.3 Overview of the Design Software for System Development

For the development of the digital hardware residing on the FPGA, Altera's Quartus software was used. This is an industry standard Programmable Logic Device (PLD) design suite used primarily for the design and simulation of digital hardware. Verilog is chosen as the Hardware Description Language (HDL) for the project. During the description of the design process, references will be made Quartus block diagrams. These are visual representations of the digital design and interconnections between design modules. To simulate the design, Modelsim is chosen. The development of the embedded processor was carried out using the System on a Programmable Chip (SOPC) software and the NIOS design environment, allowing code to be executed on an FPGA based embedded processor over a programming cable.

### 7.4 Elements of the OHMS Transmitter

#### 7.4.1 Overview

To achieve the design requirements, the OHMS transmitter is designed as a system on a chip with parallel functionality, meaning that several different functions

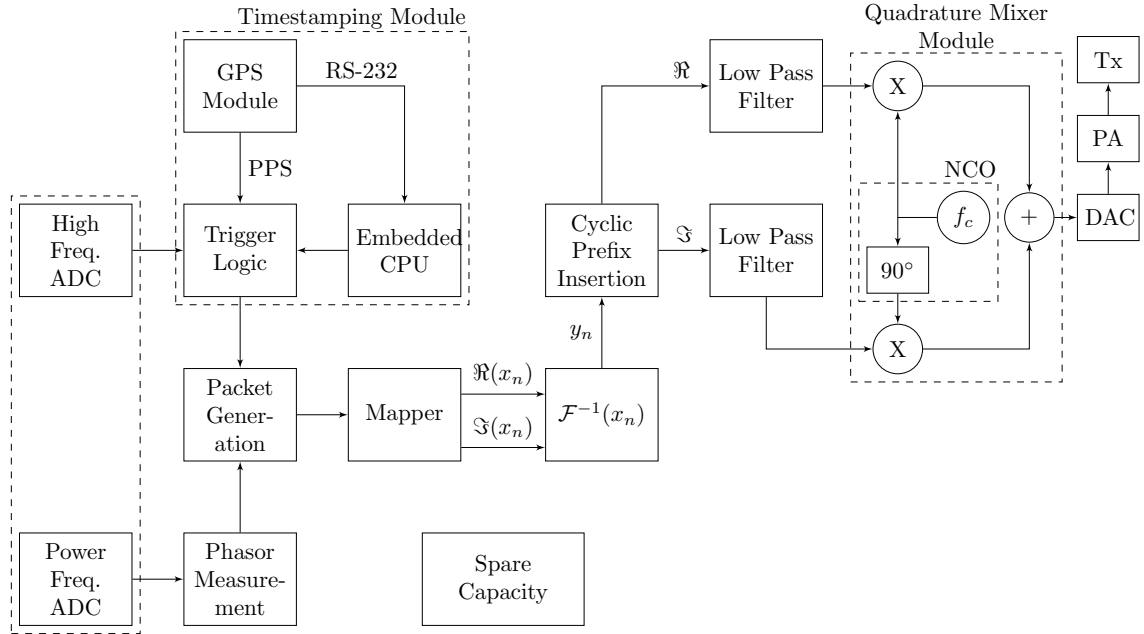


Figure 7.1: High level block diagram of the OHMS transmitter

can be carried out simultaneously. To guarantee speed, parallelism and ease of prototyping, an FPGA platform was chosen. FPGA technology allows the developer to configure hardware after production of the chip. The re-configurability of the FPGA design cycle is a significant advantage over Application Specific Integrated Circuit (ASIC) technology. Although ASIC designs have a lower per-unit cost, there is no opportunity to re-configure once the design has been committed to hardware.

Fig. 7.1 shows a high level block diagram of the proposed OHMS transmitter. The interface to the sensors is through two ADCs, one connected to the high frequency sensor and the other connected to the power frequency sensor. The high frequency part of the system is designed to detect, capture and interpret high frequency, fault induced transients. The trigger logic block, on board the FPGA, is designed to search for transients and record the time and current magnitude at the

peak. To support the trigger logic block, a GPS module is used. This provides to the system an accurate clock reference, a fundamental piece of information used to record the transient arrival time and for the phasor measurement block. The GPS clock also provides a means of supporting a multiplexing scheme, as was discussed in Chapter 6. An embedded CPU, realised in FPGA logic, provides flexibility in processing the RS-232 string sent from the GPS module as a descriptor for the Pulse Per Second (PPS) signal. The PPS signal is sent by the GPS to the FPGA at the start of every new second. This PPS signal is used to reset the master clock within the FPGA. The packet generator block creates an information symbol based on the recorded timestamp (if one is detected) and the phasor measurement information. The information symbol is mapped and sent to the OFDM MODEM part of the FPGA logic.

### 7.4.2 Mapper

The mapper module is used to map the serial stream of information (to be transmitted) to a parallel stream of mapped constellation points. The designed mapper is capable of three modes: DBPSK mode, DQPSK mode and D8PSK mode. It is also possible to assign individual modes to subcarriers to achieve an adaptive OFDM scheme. The digital logic of the mapper is based on a case statement that checks the value of a parallel stream of binary inputs. In DBPSK mode, the stream has a width of 1. In DQPSK and D8PSK, the parallel stream has a width of 2 and 3 bits respectively. Information is to be encoded in the phase difference of

the mapped subcarriers. In DBPSK mode, a binary '1' is encoded as no change between the current and previous subcarrier, whereas a binary '0' is encoded as a 180° phase change. In DQPSK, the 4 possible variations in transmitted bits (11,10,01,00) are encoded as phase shifts of 0°, 90°, 180° or 270°. In D8PSK, 8 variations in transmitted bits and 8 phase changes are used.

To realise the mapper, the case statement checks the current bit(s) required to be encoded and maps to a constellation point to achieve a phase difference from the previous constellation point.

### 7.4.3 Modulator

The design of the MODEM is written in Verilog Hardware Description Language using Altera's Quartus software, targeting the Cyclone family of FPGA devices. The heart of the design is the FFT megacore. This is a customisable megafunction with the option of performing a 64, 128, 256 or 512 point FFT or, when selected, an IFFT. Input and output to the FFT core is handled by the Avalon streaming interface, a standard in Quartus modules.

Fig. 7.2 shows a high level block diagram of the FPGA based implementation of the Modulator part of the MODEM. The mapper, discussed earlier, outputs two arrays of length  $N_{sym}$ , where  $N_{sym}$  is the number of subcarriers. These arrays are arranged in pairs and together represent a constellation mapped subcarrier. A pair of FIFOs holds these arrays and when non-empty, alerts the IFFT controller. The IFFT controller is a parallel to serial converter and feeds the elements of the

constellation mapped subcarriers to the IFFT core, ensuring that the transfer of information follows the criteria required by the Avalon streaming interface. The IFFT core computes the complex IFFT on the loaded complex data samples and outputs, in a serial stream, the computed complex samples. These samples are sent to the block responsible for the cyclic prefix insertion.

The functionality of the IFFT megacore and associated logic was verified using a testbench including a dummy frame of data made up of a synchronisation type symbol immediately followed by a DBPSK information symbol. The IFFT simulation model is a bit accurate gate level model automatically generated during synthesis of the core. In Fig. 7.3, the results of the simulation are plotted. The computation time of the IFFT core is approximately equal to the symbol length, in this case 128 clock cycles. This translates to a transform time of 128  $\mu\text{s}$  when a 1 MHz “slow clock” is used. The transform time can be increased by using a faster clock but this necessitates the use of a buffer between the fast output clock of the IFFT and the slower clock required to output the samples at the sampling frequency of the particular modulation scheme. In this case, the clock used by the IFFT core is the same as the output clock, simplifying the design and leading to an achievable transform time of approximately 700  $\mu\text{s}$ .

#### 7.4.4 Cyclic Prefix Insertion

The cyclic prefix part of the digital logic must be capable of copying the final  $S_g$  samples and then append these samples to the start of the symbol, producing a

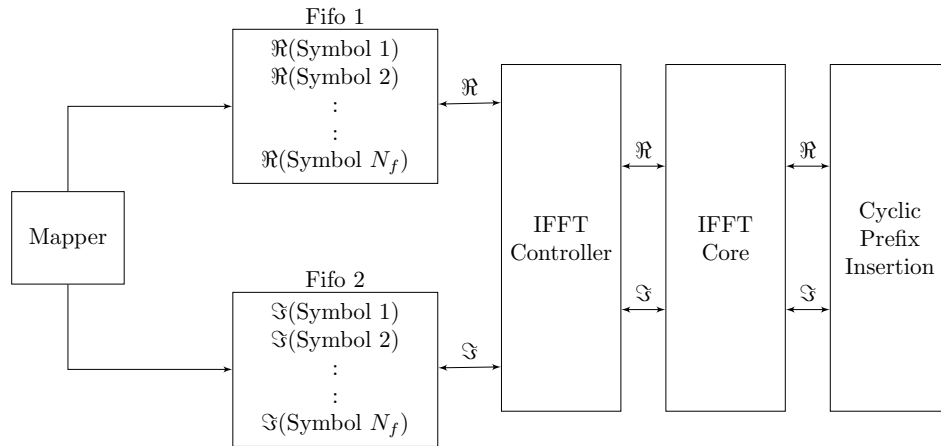


Figure 7.2: Block Diagram showing the design of the OHMS Modulator

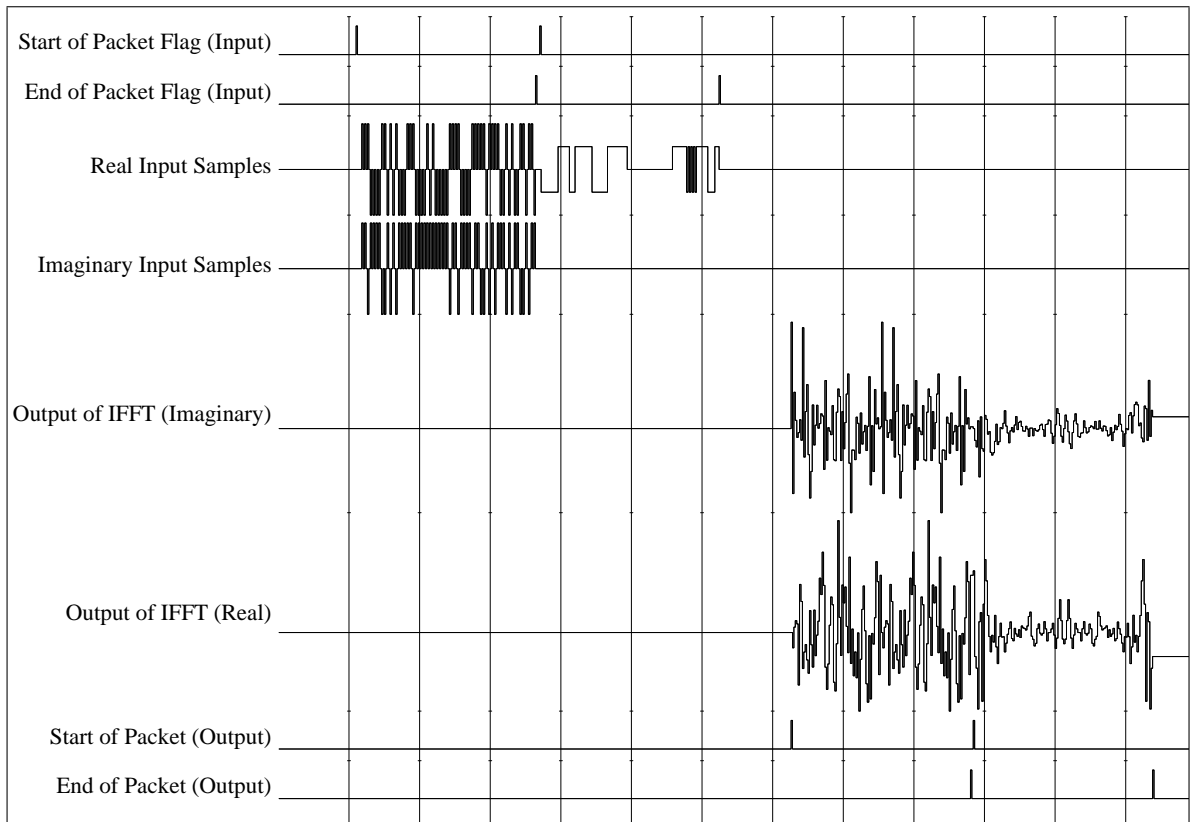


Figure 7.3: Selected waveforms of the simulated IFFT core

symbol of length  $S + S_g$ , where  $S$  is the symbol size before cyclic prefix insertion. This part of the design is achieved using a pair of dual port synchronous RAM functions with a size equal to twice the size of  $S$ . The output of the first IFFT symbol, shown in Fig. 7.3, is written sequentially to the first  $S$  memory spaces in the dual port RAM. This is the synchronisation symbol. The next  $S$  samples are from the information symbol and these values are written into the second half of the dual port RAM. When the dual port RAM is full, a read controller starts by reading the first  $S_g$  samples from the dual port RAM. Following this, the read controller resets the read address and reads the first  $S$  samples, leading to a symbol of length  $S + S_g$ . A similar operation is carried out for the information symbol. The output from the read controller module is two symbols, each with a cyclic prefix of length  $S_g$ . The simulated waveforms are shown in Fig. 7.4. The Quartus block diagram schematic of the cyclic prefix module is shown in Fig. 7.5.

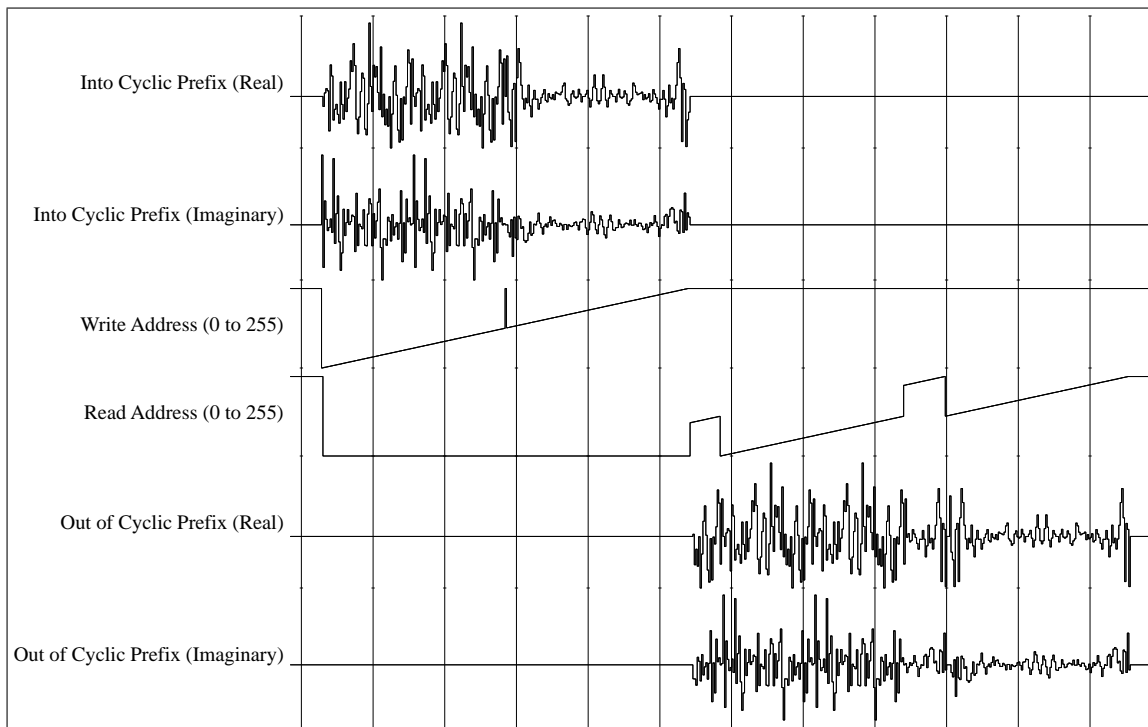


Figure 7.4: Selected waveforms of the simulated Cyclic Prefix module

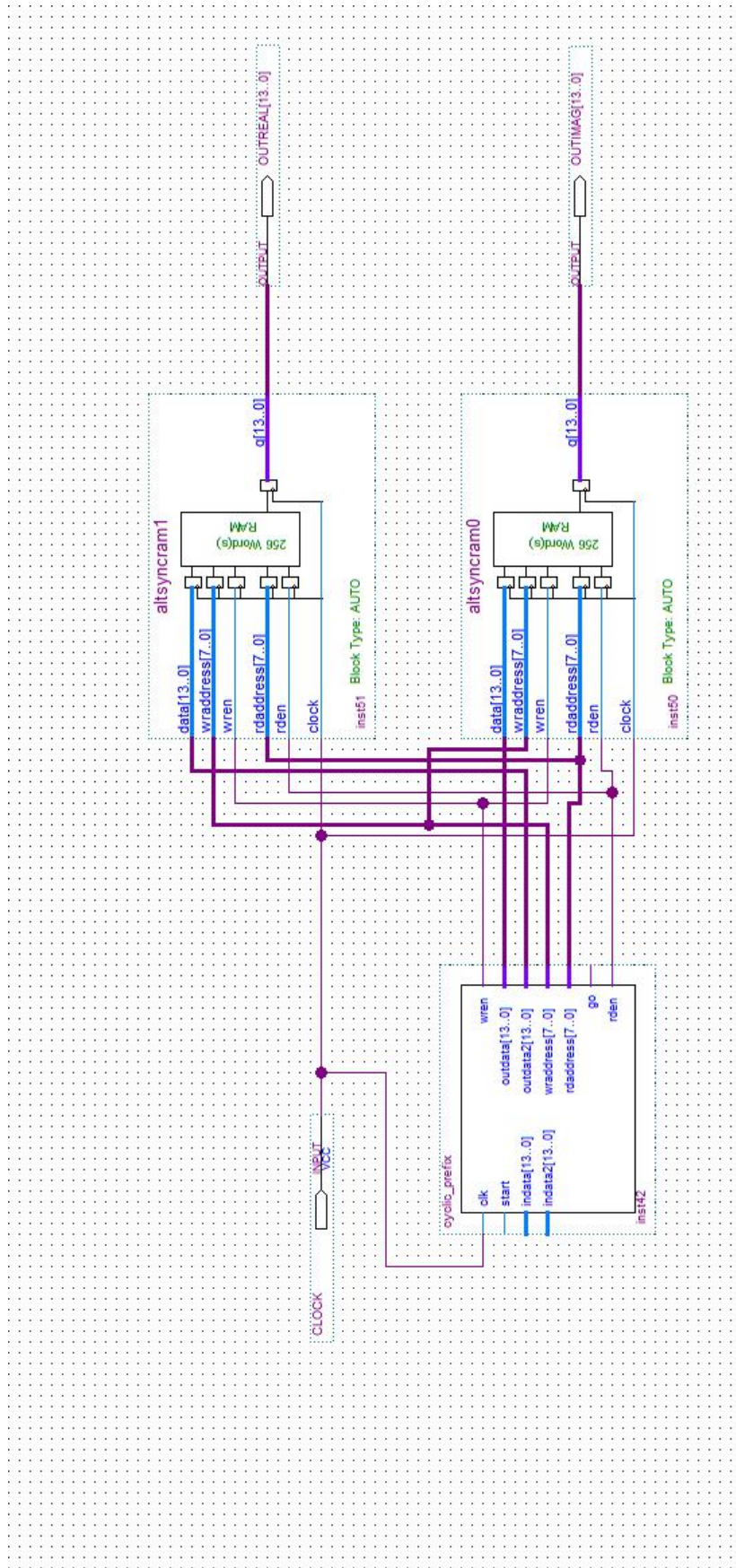


Figure 7.5: Quartus Block Diagram of the Cyclic Prefix Insertion Design. Code for the cyclic prefix block is shown in Appendix C.1

### 7.4.5 Quadrature Mixer and Upconverter

Following the cyclic prefix insertion, the real and imaginary parts of the signal are sent to a quadrature mixer module, as shown in Fig. 7.1. The first part of the module acts as a digital reconstruction filter, increasing the sampling rate of the signals to 60 MHz and filtering out the high frequency aliases from the original signal. This is visualised in Fig 7.6 as a smoothing of the waveforms. The low pass filters are realised in digital logic using Altera's Finite Impulse Response (FIR) compiler megafunction.

Quadrature mixing is achieved by multiplying the real part of the signal by a cosine carrier wave, and the imaginary part of the signal by a sinusoidal carrier wave. Both sinusoids are set to the carrier frequency,  $f_c$ . To generate the sinusoids, a Numerically Controlled Oscillator (NCO) is used. An NCO is able to generate a digital representation of a sinusoid at a chosen frequency. Multiplication and addition is achieved efficiently in digital logic, generating a new signal ready for transmission to the channel. This signal is described as "Mixer Output" in Fig 7.6.

### 7.4.6 GPS Timestamping Module

The GPS timestamping module relies on an internal counter running at 100 MHz. The counter is reset to zero at the start of each new second. The value of this counter can be used to determine the fractional second (to a resolution of 10 ns) of the peak of the detected transient. To implement this, the M12M timing receiver module is interfaced to the FPGA board via an SMA connector (to deliver the 1

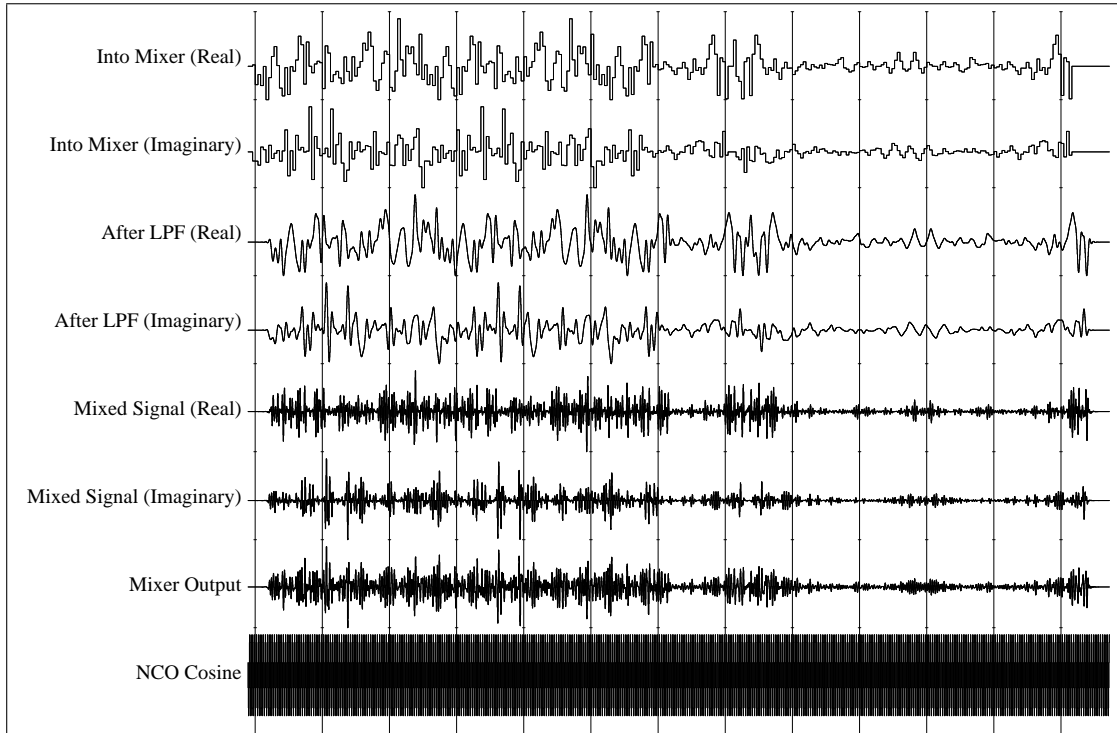


Figure 7.6: Selected waveforms of the Quadrature Mixer Module

pulse per second pulse to determine the start of every new second). There is also an RS-232 interface to receive the information string sent by the module shortly after the PPS signal. This information string contains the time information (date, hour, second) and geographical information (longitude and latitude). To process the string, an embedded processor is included in the FPGA logic of each OHMS receiver. This embedded processor simplifies the task of processing each string and is able to pick off the timing information and store in memory (see Appendix C.2 for the C++ program listing). A memory mapped read master is used to read the memory locations containing the timing information such that an information packet can be constructed when required (for example, when a timestamp information packet is constructed following a transient event).

### 7.4.7 Synchrophasor Module

The synchrophasor module is based on simultaneous sampling of voltage and current. The signals are sent to two separate FFT modules. The result of the FFT is checked at the frequency bin corresponding to the 50 Hz fundamental power frequency and the phase of both the voltage and current signals is obtained by use of the CORDIC algorithm. The CORDIC algorithm is a highly efficient means of converting Cartesian into polar values, and will be further described in Section 7.6.2, where the demapper unit is discussed, for which the CORDIC algorithm also plays an important role. The simultaneous measurement of voltage and current phasors also allows the computation of the power factor. Additionally, if the FFT window is appropriately positioned, it may be possible to gain information on the harmonic content of the voltage and current at that point in the network.

### 7.4.8 Packet Generation

Packet generation is the process of gathering the appropriate information and arranging it into a suitably constructed symbol ready for sending to the transmitter. It was seen in Chapter 6 that a timestamp containing a 27 bit fractional second (allowing a resolution in excess of 10 ns), and the value of the peak of the transient, can be conveyed in 45 bits. The packet is constructed by reading the value of the 27 bit fractional second (at the peak of the transient) and the peak of the transient. This information is appended into a 45 bit register. Also appended is a 7 bit optional “system ID”, a unique code given to each OHMS device.

## 7.5 Elements of the OHMS Receiver

### 7.5.1 Overview

Fig. 7.7 shows a high level block diagram of the OHMS receiver. The receiver is designed to receive information from the OHMS transmitters followed by sending this information to a nearby computer via Bluetooth. The OHMS receiver has a DAC and quadrature mixer module with the carrier frequency generated by a numerically controlled oscillator. The output of the quadrature mixer module is fed into a Schmidl/Cox autocorrelation based timing estimator. The start of the FFT is commanded by a start flag from the timing estimator. After the FFT module, the demapper module passes the received information to an embedded CPU for translation to RS-232 and broadcast over the Bluetooth radio.

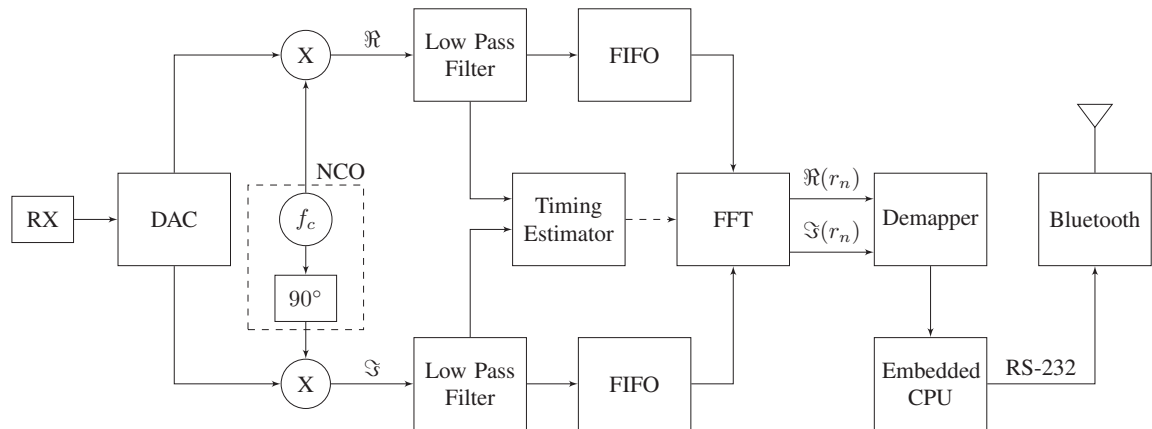


Figure 7.7: High level block diagram of the OHMS receiver

## 7.5.2 Realisation of the Timing Estimator

In Section 4.3.2, the performance of a timing estimator based on the autocorrelation of a repetitive signal was assessed. It was shown that repetition in the time domain provides a way of detecting the arrival time of an information symbol at the receiver, prompting the FFT of the OFDM receiver to begin sampling.

The problem to be faced now is how to implement the functionality of the timing estimator in hardware. In Equation (3.22), the Schmidl/Cox timing metric was defined as:

$$M(d) = \frac{|P(d)|^2}{(R(d))^2}, \quad (7.1)$$

Where  $P(d)$  is the auto-correlation result of the two half symbols and  $R(d)$  is the energy of the half symbol. Simulation results showed that including the normalisation factor,  $R(d)$ , leads to unpredictable peaks in the metric and a far more robust metric was provided by considering  $P(d)$  alone.  $P(d)$  is defined as:

$$P(d) = \sum_{m=0}^{N-1} (r_{d+m}^* r_{d+m+N}), \quad (7.2)$$

Where  $N$  is the number of samples in half a symbol.

The multiplication of  $r_{d+N}^*$  with  $r_{d+2N}$  is performed easily in digital logic with simple delay elements and a multiplier, as is shown in Fig. 7.8.

The moving sum required to arrive at  $P(d)$  has a recursive implementation that lends itself well to implementation in digital hardware:

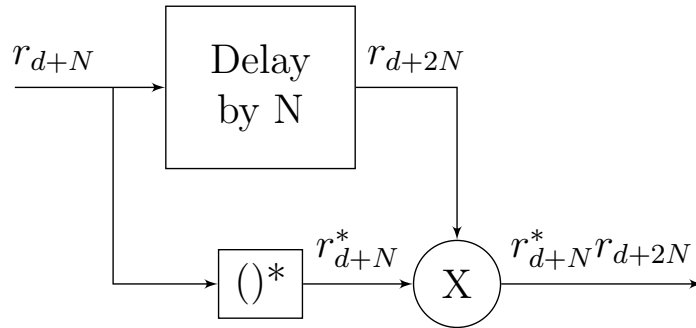


Figure 7.8: Computation of  $r_{d+N}^* r_{d+2N}$

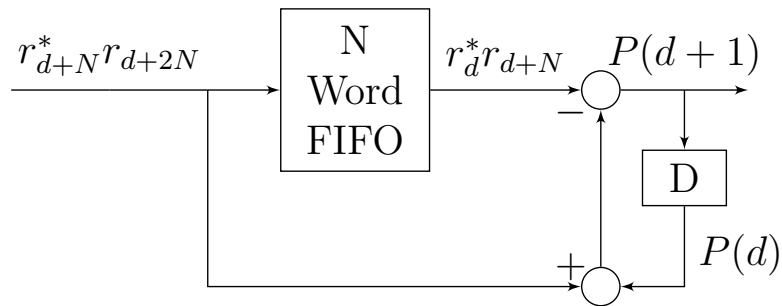


Figure 7.9: Recursive Implementation of the Moving Sum

$$P(d + 1) = P(d) + r_{d+N}^* r_{d+2N} - r_d^* r_{d+N} , \quad (7.3)$$

The recursive implementation can be realised efficiently in hardware at the cost of an N-word FIFO, an adder and a subtractor. This is shown diagrammatically in Fig. 7.9.

In Fig. 7.10, the Quartus block diagram of the moving sum design is shown. For clarity, the signal names in Fig. 7.8 are superimposed on the Quartus block diagram of the moving sum.

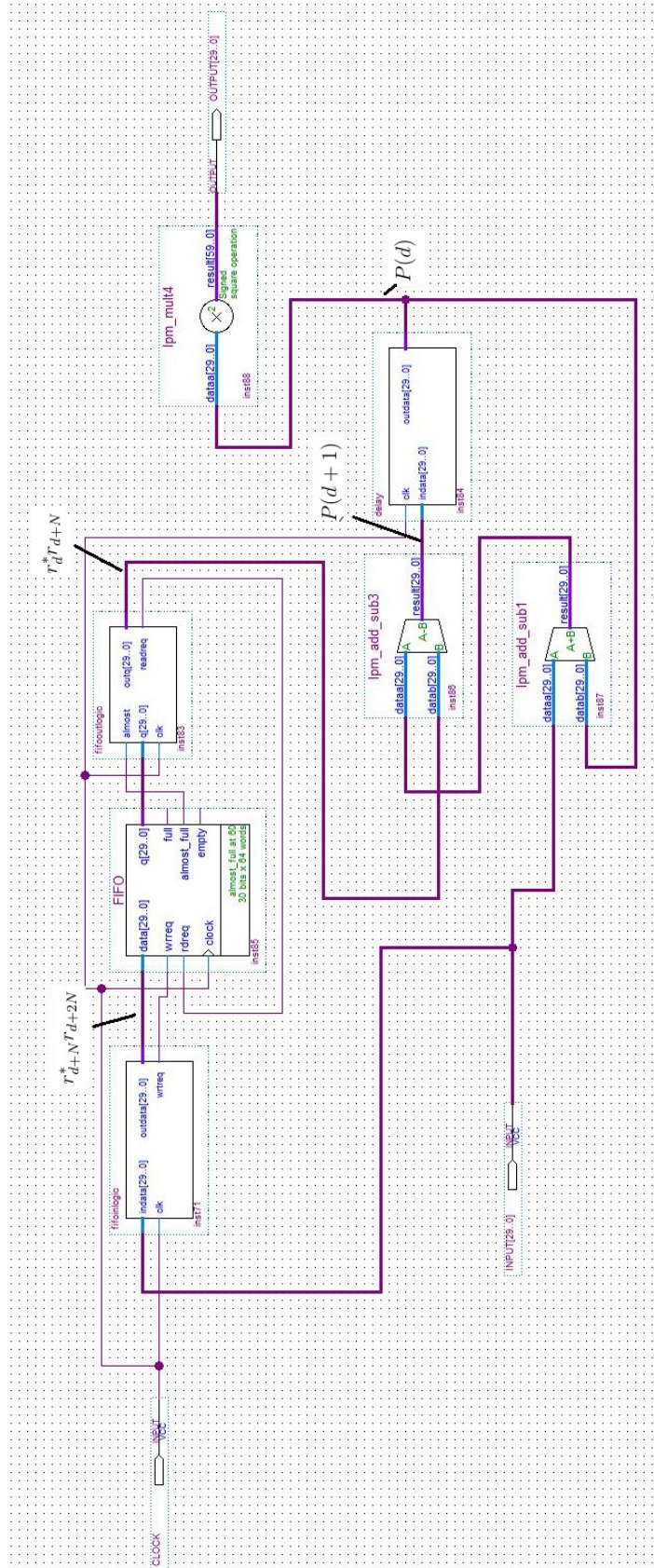


Figure 7.10: Quartus Block Diagram of the Moving Sum Part of the Timing Estimator

It was discovered in Chapter 4 that a significant increase in performance can be achieved by calculating a new metric,  $P_f(d)$ , by passing  $P(d)$  through an LPF with as many taps as there are samples in the cyclic prefix. The LPF should be an averaging filter. This type of filter can be realised using Altera’s FIR compiler and setting the coefficient values to be  $1/N_{cyc}$ , where  $N_{cyc}$  is the number of samples in the cyclic prefix.

Even after the construction of  $P_f(d)$ , it is still required to find the time of the largest sample. This is only possible by keeping “in reserve” a delayed version of the analysed signal.

Consider a symbol with 148 samples, made up of a 128 sample useful part of the symbol and a 20 sample cyclic prefix. The timing estimator has the job of detecting if a symbol has arrived. It does this in two steps. First, dedicated hardware checks if the incoming symbol energy,  $(P(d)^2)$ , exceeds a pre-set threshold value. If this is the case, the second step executes a “find max” routine for two times the number of samples in the useful period (in this example, 256). This simply checks if the current value is greater than the stored maximum value and if so, updates a temporary variable with the time index associated with that sample. After 256 samples, the time index of the maximum value should be known. In a separate part of logic, the signal entering the timing estimator also enters a 256 sample FIFO, resulting in a delay of 256 samples. It can be deduced that the appropriate time to begin the FFT sampling window is when the FIFO delayed signal is delayed by an additional number of samples linked to the time index calculated in the “find max” routine. An overview of the method is shown in Fig. 7.11.

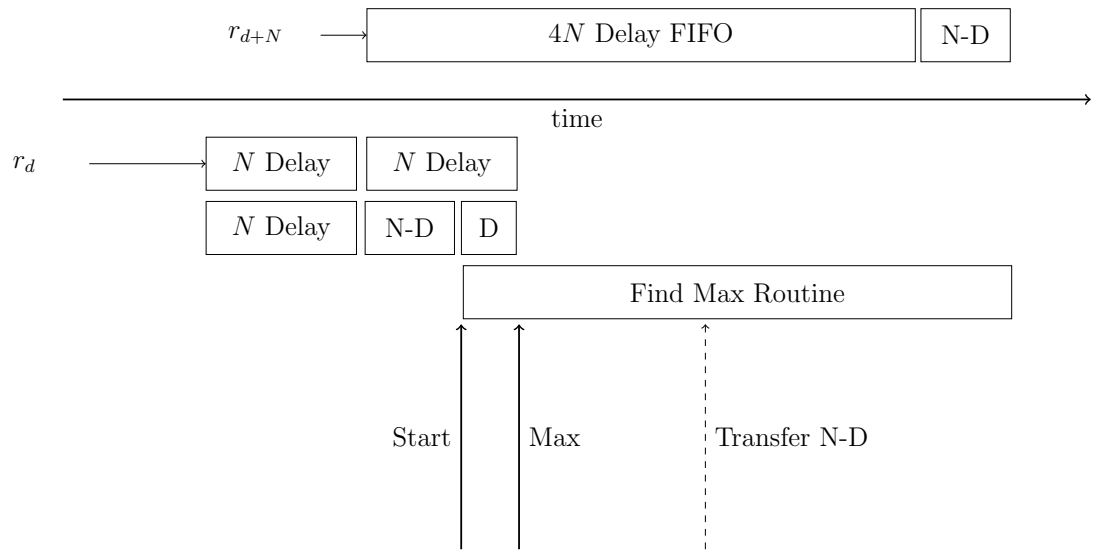


Figure 7.11: Overview of the method used to determine start time of FFT in the OFDM demodulator

To test the functionality of the digital logic of the timing estimator, a complete testbench was written to incorporate the entirety of the OHMS transmitter linked directly to the logic of the timing estimator. In this testbench, a signal consisting of a synchronisation symbol followed by an information symbol is generated using the OHMS transmitter logic. This is sent directly to the OHMS receiver logic. Fig. 7.12 shows selected waveforms to demonstrate the functioning of the discussed logic.

In Fig. 7.12, it is observed that both the “Find Max Counter” and the “Find Max Time Index” counters start to increment once the pre-set threshold value for  $P_f(d)$  is exceeded. The find max counter continues to increment until 255, or 4 times  $N$ , where  $N$  is the number of samples in a half the useful part of a symbol. The “Find Max Time Index” counter, however, stops counting when the maximum value has been reached, in this case at 13. This is equivalent to the value  $D$  in

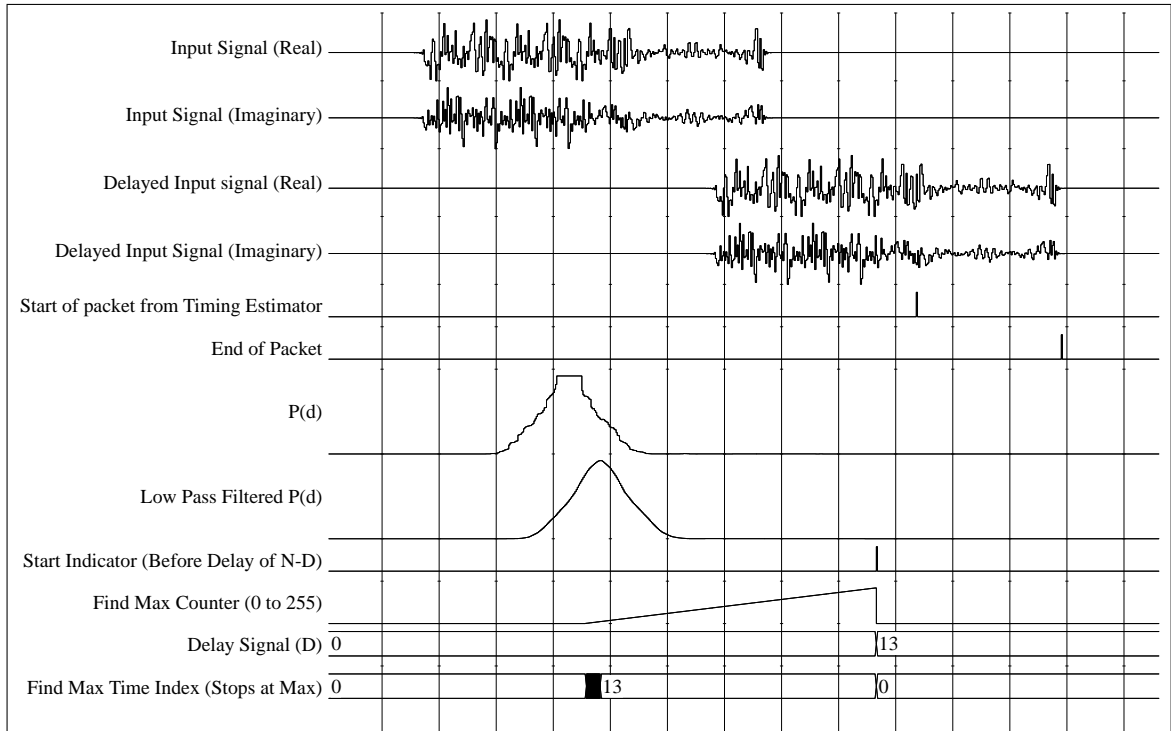


Figure 7.12: Selected waveforms to show functionality of the Find Max logic and generation of the start packet flag

Fig. 7.11. When the find max counter reaches 255, it triggers another counter to begin incrementing. When this counter reaches  $N - D$ , a start of packet flag is generated, informing the FFT to begin sampling. It is noted that if a cyclic prefix is used in the information symbol, the start of packet flag must be delayed by its length (in samples) so that sampling begins at the start of the useful period of the information symbol. The digital logic used to implement the “Find Max” routine is split into two modules. In Appendix C.4, the Verilog code responsible for identifying the threshold to begin counting and the maximum value is shown. In Appendix C.5, the incoming signal is delayed based on the delay signal and therefore the start of the symbol is aligned with the start of the FFT sampling period.

### 7.5.3 FFT and Demapper

The FFT logic is realised in hardware using Altera's FFT megacore. As with the IFFT version of the core, the inputs to the FFT core are the real and imaginary parts of the received signal, and flags to indicate the start and end of the incoming packet. The timing estimator ensures that the start flag coincides, as near as possible, with the start of the useful part of the information symbol(s). The real and imaginary parts of each subcarrier in the FFT output can be mapped onto a constellation diagram, revealing the magnitude and phase of the received points. The first step in the demapping process is to convert the Cartesian representation of these received points (made up by the real and imaginary components) into a polar format, consisting of a magnitude and phase. The OHMS system uses differential encoding, so the information is conveyed in the phase difference between adjacent subcarriers. Therefore, the second step in the demapping process is calculation of the phase differences between adjacent subcarriers. The third step is to decide the most likely bit(s) the symbols convey by decoding the phase differences into a binary stream. This can be thought of as parallel to serial conversion: reconstructing the bit stream that was entered into the mapper at the transmitter.

The process of transforming Cartesian into polar values is non-trivial and expensive in terms of logic usage in digital hardware. One hardware efficient method of Cartesian to polar conversion is the CORDIC (COordinate Rotation DIGital Computer) algorithm [92]. The CORDIC algorithm provides a means of performing vector rotations iteratively using only shift and add operations. A vector in a plane

is rotated by an angle,  $\Phi$  with the following equations:

$$x' = x \cos \Phi - y \sin \Phi \quad (7.4)$$

$$y' = y \cos \Phi + x \sin \Phi \quad (7.5)$$

These can be rearranged to:

$$x' = \cos \Phi(x - y \tan \Phi) \quad (7.6)$$

$$y' = \cos \Phi(y + x \tan \Phi) \quad (7.7)$$

Restricting the rotation angles such that  $\tan \phi = \pm 2^{-w}$ , where  $w$  is the iteration number, means that the multiplication of the tangent term becomes a computationally efficient shift operation in digital logic. With knowledge that  $\cos(\Phi) = \cos(-\Phi)$ , the cosine term is a constant and a new pair of expressions can be formed:

$$x_{w+1} = K_w \{x_w - y_w \cdot d_w \cdot 2^{-w}\} \quad (7.8)$$

$$y_{w+1} = K_w \{y_w + x_w \cdot d_w \cdot 2^{-w}\} \quad (7.9)$$

With:

$$K_w = \cos(\tan^{-1} 2^{-w}) = \frac{1}{\sqrt{1 + 2^{-2w}}} \quad (7.10)$$

$$d_w = \pm 1 \quad (7.11)$$

Another equation, called the angle accumulator, is required:

$$z_{w+1} = z_w - d_w \cdot \tan^{-1}(2^{-w}) \quad (7.12)$$

The CORDIC engine can operate in two modes: Rotation and Vectoring. Rotation mode accepts an angle as an input argument and rotates the input vector by this amount. Vectoring mode accepts a vector as input and outputs the angle required to bring this vector to the x-axis, in other words, the vectoring mode calculates the angle and magnitude of the input vector. The Vectoring mode is, therefore, the necessary mode to carry out the Cartesian to polar conversion required by the demapper. In this design, a first quadrant CORDIC engine is used, meaning it is restricted to calculating angles between 0 and  $\pi/2$  radians. A simple modification of the output angle and tracking of the signs of the input vectors can allow a first quadrant CORDIC to calculate angles spanning the entire range, i.e. 0 to  $2\pi$  radians.

The output of the CORDIC operating in vectoring mode is the angle and magnitude of the input vector, where the input vector is the real and imaginary parts of the FFT output. The difference in the phase of adjacent subcarriers encodes the information, so this information is passed to the demapper and a decision is made

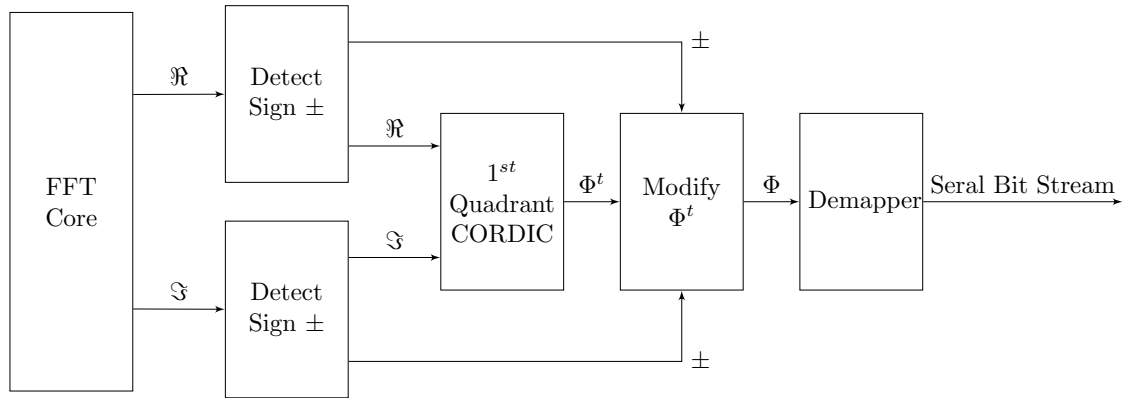


Figure 7.13: Block diagram of the CORDIC and Demapper process

as to what bit(s) were sent. A block diagram showing the use of the CORDIC engine and the demapper is shown in Fig. 7.13. The waveforms from a Modelsim simulation of the CORDIC and demapper logic is shown in Fig 7.14.

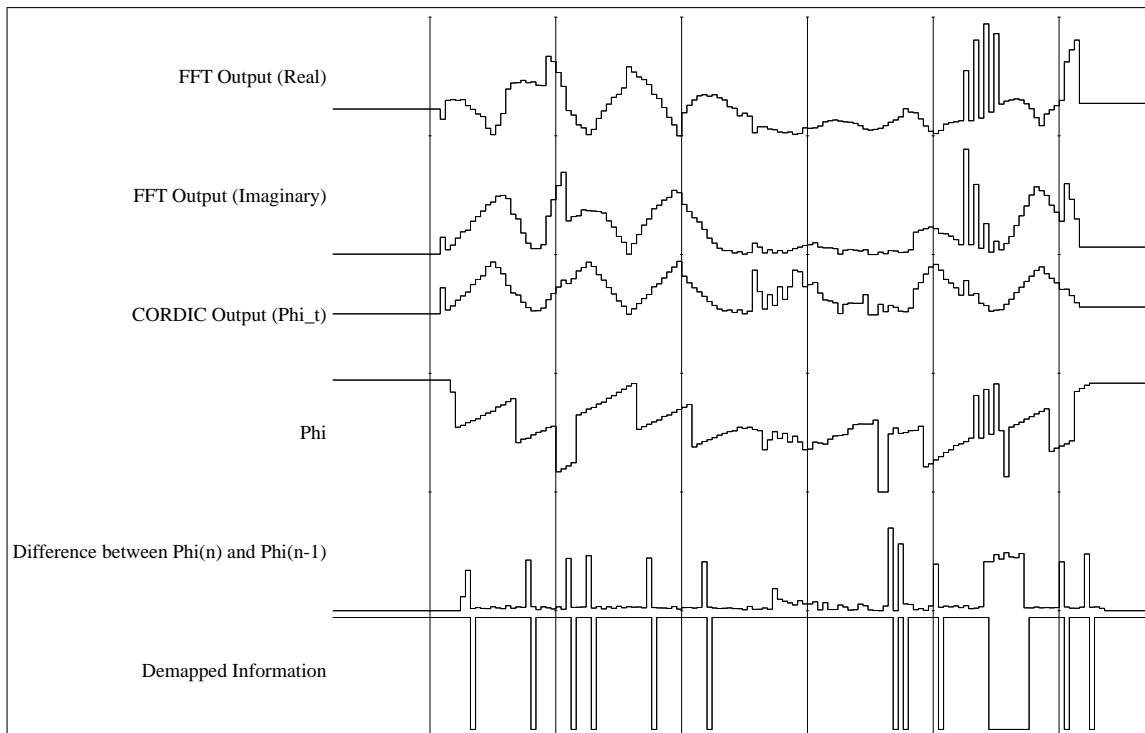


Figure 7.14: Selected waveforms to show functionality of the CORDIC and demapper processes

In Fig. 7.14, CORDIC output,  $\Phi^t$ , is the output of the 1<sup>st</sup> quadrant CORDIC. The 17 bit CORDIC output has a minimum of 0 radians for  $0^\circ$  and a decimal value of 53,955 for an angle of  $\pi/2$ .  $\Phi$  is the modified  $\Phi^t$  to allow for angles that are outside the first quadrant. The range of  $\Phi$  is 0 to 215,820 for a range of 0 to  $2\pi$  radians. The difference between the current and the previous  $\Phi$  determines the output bits from the demapper. The Verilog code implementing the CORDIC algorithm, and the demapper logic, is shown in Appendix C.6.

## 7.6 Implementation of the Bluetooth Interface

The OHMS receiver is designed to be fixed on the wood pole of the 11 kV line. The problem of how to transfer the received information from the HV environment safely to a user interface or communication infrastructure on the ground is, therefore, to be addressed. Due to safety concerns, it is extremely problematic to use directly wired connections from the vicinity of the HV line to ground. An obvious solution is to use a wireless method for making this connection.

Bluetooth is a well established standard for transferring information wirelessly over short distances [93]. The Serial Port Profile (SPP) is a way to connect two Bluetooth devices via an RS-232 bridge. In other words, the Bluetooth SPP is a way to bridge wireless gaps communicating using the RS-232 profile in such a way that no extra coding or interfacing is required. It acts and behaves the same as a conventional wired RS-232 link.

An embedded processor was realised within each OHMS receiver and performs

a conversion between the input bit stream from the demapper module to an RS-232 serial stream ready for transmission over the Bluetooth wireless bridge. The C++ code listing for the code executed on the embedded processor of the OHMS receiver is shown in Appendix C.3.

## 7.7 Development of the Software User Interface

The software user interface, otherwise known as a Human Machine Interface (HMI), is the operator's interface to the physical system, often encompassing a graphical interface on a PC. Significant thought should be put into the design of the network operator's HMI, however, it has been noted that those in use today fail to meet the requirements of expected future smart grid scenarios [94]. As a minimum, the software should be able to log, display and interpret incoming data. At this stage, it is assumed that the OHMS system HMI is to operate completely independent of any other HMI systems (e.g. those associated with SCADA) and that the HMI is to be a convenient means of gathering, displaying and interpreting information in initial trials of the OHMS concept.

To create the HMI, Visual Basic 2010 is chosen as the platform to develop a Windows based PC application. The input to the HMI is delivered via a UART link supported by the Bluetooth interface discussed in the previous section. The HMI processes the incoming serial data from the UART into an events log which displays the demodulated binary stream and arrival time of every message received. The message is deconstructed into the timestamp part, the "transient magnitude" part

and the identification code of the transmitting OHMS device. A separate part of the program is set aside to perform the fault location algorithm introduced in Chapter 5 and store the estimate of the location of any detected faults (or disturbances) into a separate log, and eventually a database. The HMI is also capable of storing and displaying the synchrophasor reporting data (if either of schemes 2 or 3, which were explained in Chapter 6, are being used) either as a log or graphically in a continuously updated chart of phasor angle for each OHMS transmitter position. There is also an additional function allowing GPS co-ordinates to be plotted in an embedded web browser using Google maps, allowing the controller to view a satellite map with the accurate position of the OHMS devices overlaid. An example screenshot of the OHMS HMI is shown in Fig. 7.15.

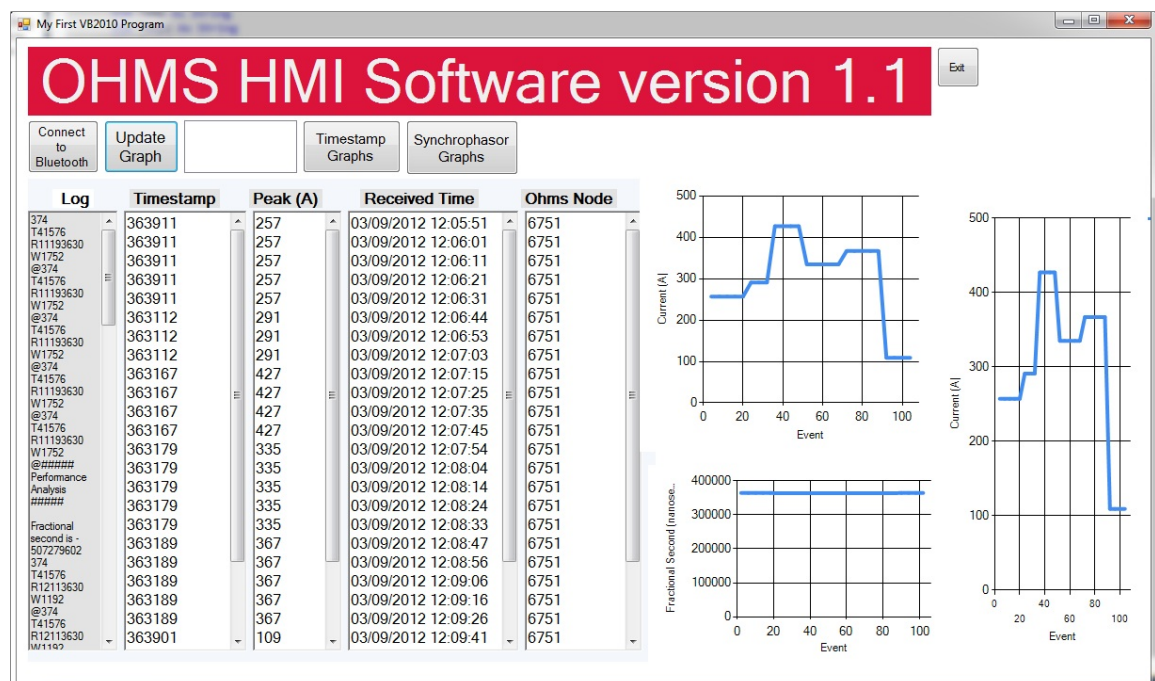


Figure 7.15: Example Screenshot of the OHMS HMI Design



Figure 7.16: Coupling Capacitor

## 7.8 Selection and Implementation of Coupling Device

The OHMS project has acquired a pair of coupling capacitors (in a loan agreement with Power Plus Communications, a Germany based PLC company). The couplers are rated for use on 11 kV lines and are optimised for operation in the kHz and low MHz range. Fig. 7.16 shows one of the coupling capacitors.

## 7.9 External Circuitry

### 7.9.1 ADC/DAC Card

A dual channel, 14 bit ADC/DAC card is used in conjunction with the FPGA devices. The device is capable of a 65 MSPS analog to digital conversion and a 125 MSPS digital to analog conversion.

## 7.9.2 Protective Circuitry

To protect the delicate circuitry from high magnitude voltage or current spikes, each input to the OHMS device is protected by voltage clamping Schottky diodes.

## 7.9.3 GPS Module Circuitry

To interface the M12M GPS timing receiver module to the RS-232 , and to implement the SMA connection to the FPGA input clock, a PCB was designed. The board is made up of a voltage regulator (to supply the M12M module with 3V) and a module to convert the TTL ( $\pm 3V$ ) logic values used by the M12M with RS-232 voltage levels ( $\pm 8V$ ). There is also an SMA connector which outputs the 1PPS signal directly from the relevant pin on the M12M output. A photograph of the GPS timing module is shown in Fig. 7.17.

## 7.9.4 Power Amplifier

To drive the communication signal to the power line, the OPA564 Operational Power Amplifier manufactured by Texas Instruments (TI) is used [95]. The device operates at a maximum bandwidth of 17 MHz and is capable of driving up to 1.5 A. Fig. 7.18 shows the circuit used to bias the op-amp. The performance of the circuit is verified using TI's bespoke TINA-TI software in conjunction with an accurate spice model of the OPA564 device.



Figure 7.17: GPS Timestamping module PCB including the M12M Timing Receiver and the RS-232 interface to to the FPGA

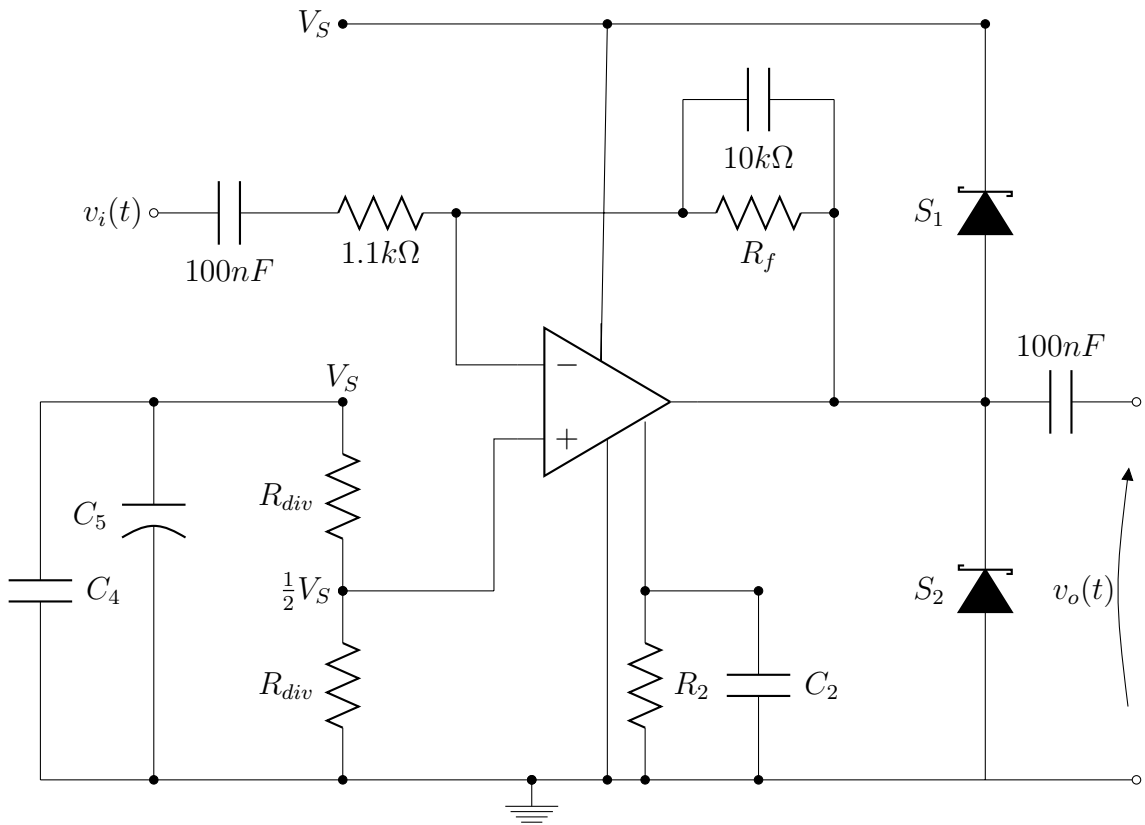


Figure 7.18: Biasing circuitry for the OPA564 Operational Amplifier.  $S_1, S_2=1N4757$  Zener diode.



Figure 7.19: The OPA564 and biasing circuitry PCB board including 24V supply, input/output sma connectors and wires leading to “on/off” switch for external mounting

## 7.10 Timing Performance of the OHMS Elements

It has been discussed in previous sections that the time in which the OHMS transmitter can construct and send an information symbol is crucially important. With a system prototype in place, it is now possible to accurately assess this. It is noted that the communication system has a sampling frequency in the kHz range, whereas the maximum permissible clock frequency of the FPGA is in excess of 100 MHz. The computational time of processing blocks is linked to clock cycles (not time itself), so it is usual in designs requiring high speed to use different clock domains, e.g., a fast clock and a slow clock. In 7.20(a), the timing analysis is carried out using just the slow clock. It is observed that in excess of five times  $N$  (the number of subcarriers) clock cycles are required. For a slow clock operating at 500 KHz and a 128 subcarrier system, this equates to 1.28 ms. If a fast clock of 100 MHz is used (as shown in 7.20(b), this time is reduced to just over  $2N$  slow clock cycles are required, or 512  $\mu$ s. This is the time elapsed between the transient detection and the final sample of the communication symbol being transmitted.

## 7.11 Development of a Prototype

Two prototype devices are produced by combining the necessary electronics into a box. A Fibox enclosure with a clear lid was chosen as the housing for the electronics. For the OHMS transmitter, the FPGA and ADC/DAC boards are fixed to the base of the box using bolts. A similar method is used to fix the amplifier and GPS timing modules. At this stage, it is convenient to use multiple power supplies

time  $\rightarrow$

	Construct Packet	Parallel to Serial Conversion	IFFT	Cyclic Prefix	LPF	Transmit
$T_{slow}$	2	N	2N	$2N + N_{cyc}$	10	0

$$\text{Total} = 5N + 12 + N_{cyc}$$

(a) Timing analysis using only the slow clock

time  $\rightarrow$

	Construct Packet	Parallel to Serial Conversion	IFFT	Cyclic Prefix	LPF	Transmit
$T_{slow}$	-	-	-	-	10	$2N + N_{cyc}$
$T_{fast}$	2	N	2N	$2N + N_{cyc}$	-	-

$$\text{Total} = T_{fast} (5N + 2 + N_{cyc}) + T_{slow} (10 + 2N + N_{cyc})$$

(b) Timing analysis with the introduction of a "fast clock" to perform faster processing

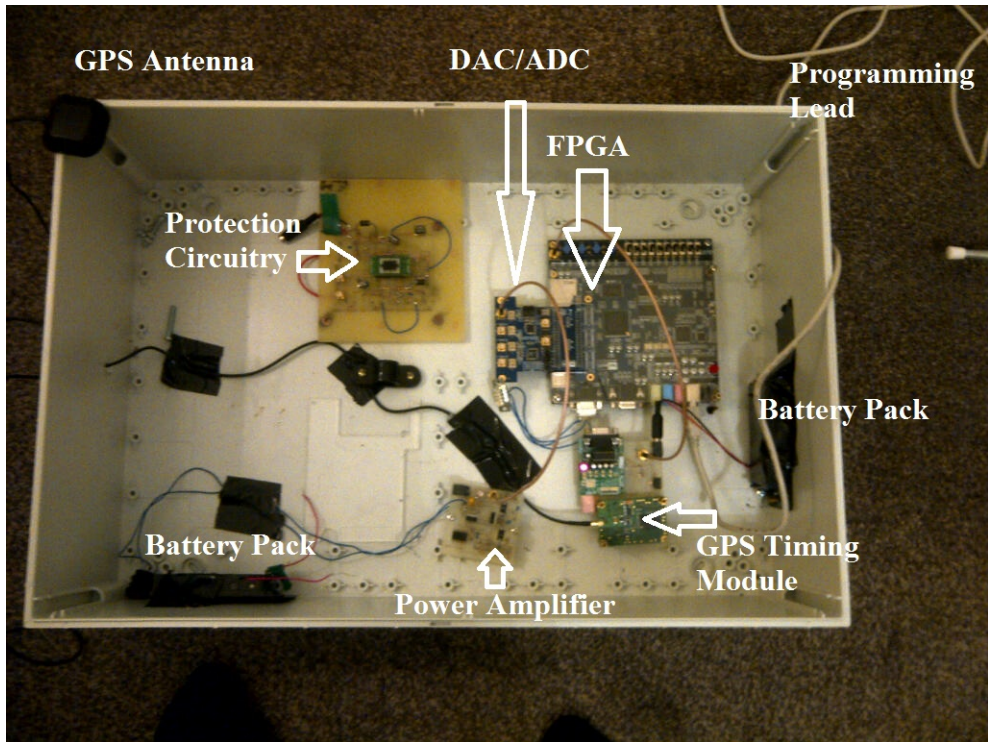
Figure 7.20: Timing analysis from transient detection to communication symbol transmission

in the form of battery packs. Fig. 7.21(a) shows a photograph of the prototype OHMS transmitter. Fig. 7.21(b) shows the prototype with the lid attached.

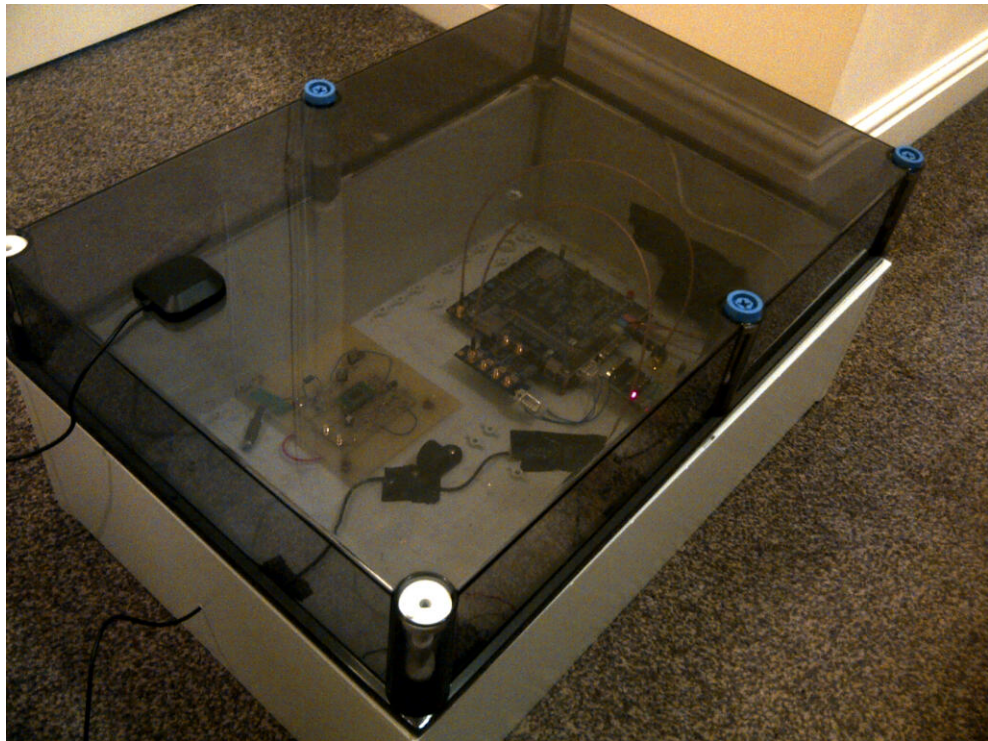
## 7.12 Conclusion

This chapter has discussed the development, in hardware and software, of the OHMS Transmitter, Receiver and the HMI software for use on a Bluetooth connected laptop. The design leverages the parallel nature of FPGAs and utilises highly efficient digital implementations of useful processes, such as moving sums and the FFT algorithm (for FPGA resource usage of the OHMS transmitter and receiver, see Appendix B.1 and Appendix B.2 respectively). The result is a highly integrated fault recorder and timestamping module with the added ability of communication potential, not only between one node and a central point, but between all nodes on a network. Although fault location is the main application discussed in this thesis, it is believed that there are many other potential benefits of such a system. In future trials and improved prototypes, it is hoped that the OHMS concept, with the sharing of information between nodes in a timescale that is unprecedentedly fast, can help to implement more intelligent protection schemes and condition monitoring regimes.

This chapter has also discussed the development of an HMI, designed to display the received information to the user. The HMI, in its basic form, is a log of the received messages but also has extensive visualisation capabilities and the ability to map received co-ordinates on a map using Google Maps. The next step in the



(a) Top down view



(b) Side view with lid

Figure 7.21: OHMS Transmitter prototype

development of the HMI could be the integration into an IP based design suite that is able to gather the information from several other OHMS networks, an important advantage if the networks are rural.

## Chapter 8

### Field Trials and System Testing

#### 8.1 Overview

In Chapter 7, a prototype for an OHMS transmitter and an OHMS receiver was built. It was demonstrated in simulation of the digital logic residing on the FPGAs that the OFDM based communication system and the timestamping module was working correctly. It was further shown that the OHMS transmitter was capable of meeting the necessary timing requirements to implement the OHMS system. For example, it takes just 512  $\mu$ s to process a received timestamp, construct an OHMS symbol and transmit. This was achieved using a design based on the principle of parallel functions, that is, enabling several functions to be carried out simultaneously.

In this Chapter, the performance of the OHMS prototypes are appraised using laboratory based tests.

## 8.2 Laboratory Based Testing of the OHMS concept

### 8.2.1 An FPGA Based Transient Generator and Network Model for Testing Purposes

For the purposes of field trials, an Altera FPGA starter kit and an ADC/DAC daughter card was utilised as a configurable transient generator or as a network model.

Configured as a transient generator, the device is capable of outputting a very fast rise time impulse due to the high sampling frequency of the digital to analogue converter (125 MSPS). The device can be used in conjunction with a bench top broadband amplifier to provide sufficient power in field based tests or used as a direct input into the OHMS devices for laboratory based tests. The FPGA is able to store sampled versions of typical transient types. These transients can be generated elsewhere, for example in Matlab, before being stored in the FPGA memory. Outputting the transient is simply a matter of sending the sampled transient waveform to the DAC at a specified sampling frequency.

Configured as a network model, the device is able to accurately model a PLC network. The relationship between the input of the PLC network (at an arbitrary point) and the output of this network (at some other arbitrary point) is equivalent to the operation of an FIR or IIR filter [96]. The signal arriving at the receiver (at the output) is the sum of a series of time delayed samples, each attenuated by a specified factor. These attenuation factors (tap values) determine the properties

of the channel. For example, a channel dominated by multipath interference will have a large number of taps and very little attenuation, whereas a channel with no multipath will have a low number of taps and high attenuation per tap, except for the "line of sight" tap, which will have a low attenuation factor compared to the others. In the case of the power line channel, the tap values can be obtained from the impulse response of the channel. In this case, the network model is realised as a cascade of several FIR filters with 2000 taps each. The total number of taps should be greater than the impulse response of the channel, but in this case, a total length of 2 times the RMS delay spread of the channel is deemed to be sufficient. Assuming an RMS delay spread of 1 ms and a sampling frequency of 0.1  $\mu$ s, this equates to 20,000 taps. To fit the design into the FPGA, the FIR filters are designed to be fully serial, meaning that an output sample will be constructed every  $n_s$  samples, where  $n_s$  is the bitwidth of the sample. This is compensated for with the use of a "fast clock" running at a multiple of the frequency of the "slow lock", for example, if the input frequency is 10 MHz, the FIR filters run at 100 MHz for a 10 bit ADC.

## 8.2.2 Overview of the Experimental Setup

Fig. 8.1 shows a high level block diagram representing experimental setup possibilities. For the OHMS transmitter prototype, there are three main areas that require investigation. First, packet generation is to be examined. For this, it is to be verified that the information that the OHMS transmitter is required to send (i.e. timestamp values) is being correctly formed into a packet ready to be sent to the

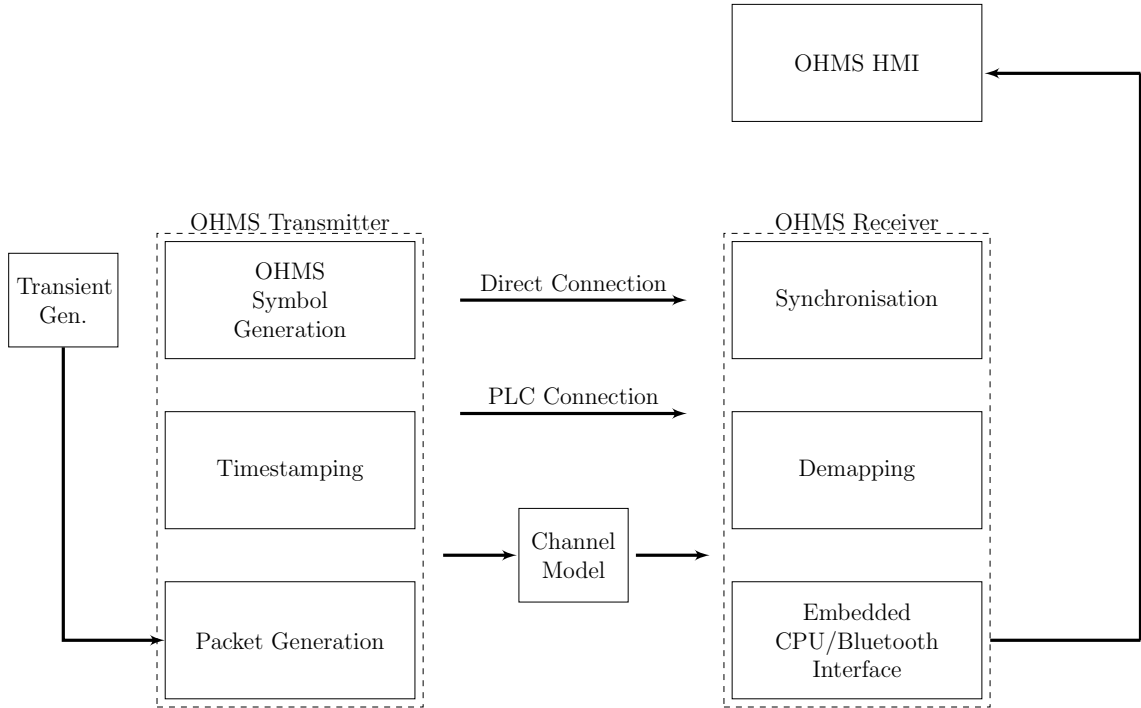


Figure 8.1: Experimental setup possibilities

mapper. Secondly, the operation of the timestamp module is of critical importance. To examine this, the FPGA based transient generator described in Section 8.2.1 is to be used to replicate a high frequency travelling wave. The next important part of the OHMS transmitter prototype to be verified is symbol generation.

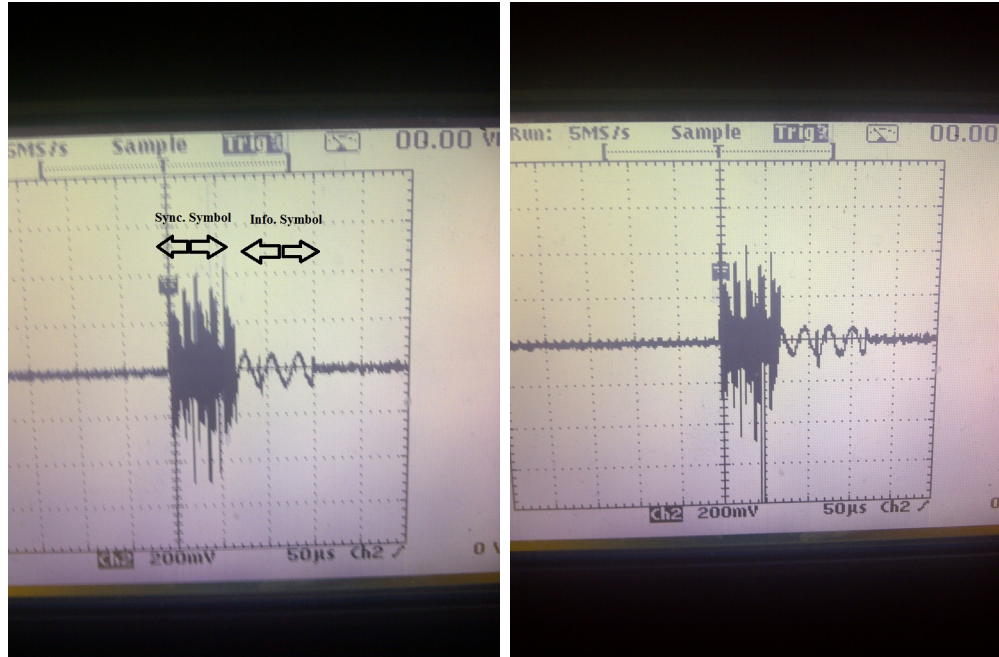
The connection between the OHMS transmitter and OHMS receiver prototypes can be in a number of forms. A direct connection is possible by simply directly connecting the DAC of the transmitter to the ADC of the receiver, thus bypassing the amplifier and protection circuitry. Another option is to couple the signal from the OHMS transmitter to some kind of transmission line, and then use the OHMS receiver to receive this signal through coupling to the same line. A third option is to use of the FPGA based network model as a bridge between the two

devices. The advantage of this method is the ability to replicate realistic network conditions.

At the OHMS receiver prototype, there are also a number of important parts of the device to examine. The synchronisation algorithm should be verified and the reliability of the communication link with the OHMS transmitter evaluated. The connection to the OHMS HMI provides a useful method of retrieving the demodulated signal from the OHMS receiver.

### 8.2.3 Demonstration of OHMS Symbol Generation

The OFDM transmitter is responsible for constructing and sending a synchronisation symbol followed by an information symbol, known collectively as an OHMS symbol. The information encoded in the information symbol is the timestamp information, synchronophasor information, or condition monitoring information, or a combination of all three depending on what operating mode the OHMS system is using. The functioning of the OHMS transmitter modulator is assessed by connecting one of its DAC outputs to an oscilloscope. The synchronisation symbol is constructed using the Schmidl/Cox method, resulting in repetition in the time domain. For demonstrative purposes, only one subcarrier is “switched on” in the information symbol. This way, the output will be a sinusoidal wave at a single frequency. In Fig. 8.2, it is clear to see the distinction between the synchronisation and information symbol. Also clear is the correct operation of the cyclic prefix insertion part of the hardware, indicating that the digital hardware outlined in Section 7.4.4



(a) Cyclic prefix of 50 samples in the information symbol (b) Cyclic prefix of 100 samples in the information symbol

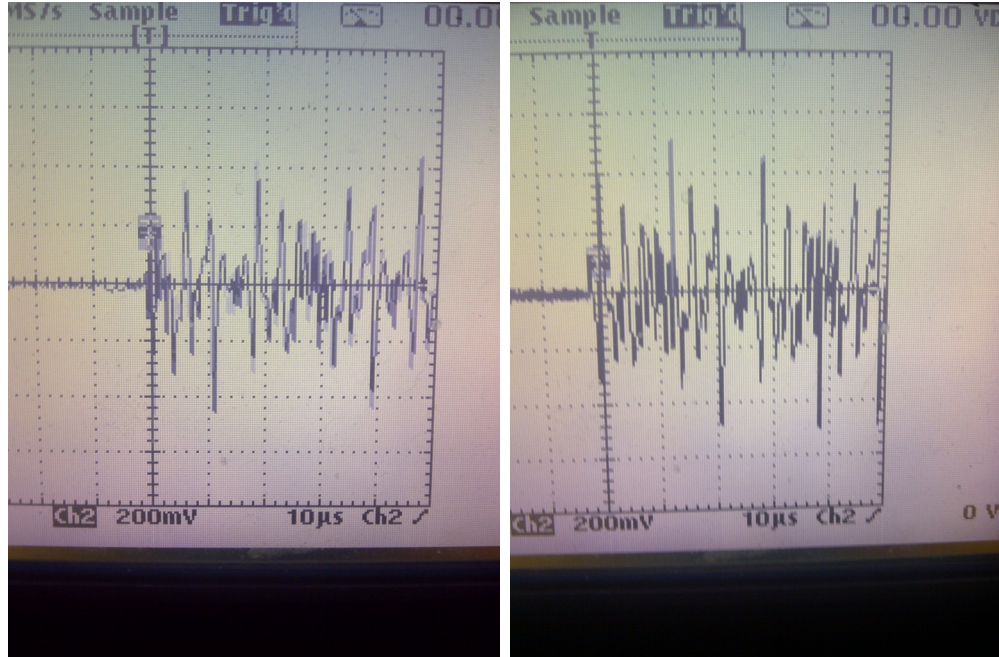
Figure 8.2: OHMS Transmitter message burst: Synchronisation symbol followed by an information symbol (real part, with one subcarrier switched on)

is working correctly.

Fig. 8.3 shows a zoomed in view of the synchronisation symbol. It is obvious from visual inspection that the symbol is equal in two consecutive parts of the time domain. Also demonstrated is the operation, again, of the cyclic prefix insertion, where the end part of the symbol is appended to the start.

#### 8.2.4 Demonstration of the Timestamping Module

To test the digital logic implementation of the timestamping algorithm (shown in in Fig. 5.14 and the interfacing between the GPS module and the FPGA based embedded processor, an experiment is set up involving the FPGA based transient generator and the OHMS transmitter. The transient generator is configured to



(a) Synchronisation Symbol with no cyclic prefix (b) Synchronisation symbol with a cyclic prefix of 50 samples

Figure 8.3: Zoomed view of the real part of the synchronisation symbol, showing repetition in the time domain

output a transient every 10 seconds. The OHMS transmitter is to timestamp this transient and generate a data symbol based on the timestamp information. This data symbol is converted to an RS-232 string and sent directly to the OHMS HMI.

With the resources available, it is difficult to judge the absolute timing of the sent transient from the pulse generator. Instead, the performance of the timestamping module is judged on how consistent the demodulated timestamp values are. This is because a pulse is sent at precisely every 10 seconds and although the absolute timing of the pulses are unknown, the time period between them is known with good accuracy. Fig. 8.4 shows an HMI screenshot of the received fractional second. In Table 8.1, the mean and the standard deviation of the received timestamps are shown for different transient types. Note that the SNR values are due to noise added in

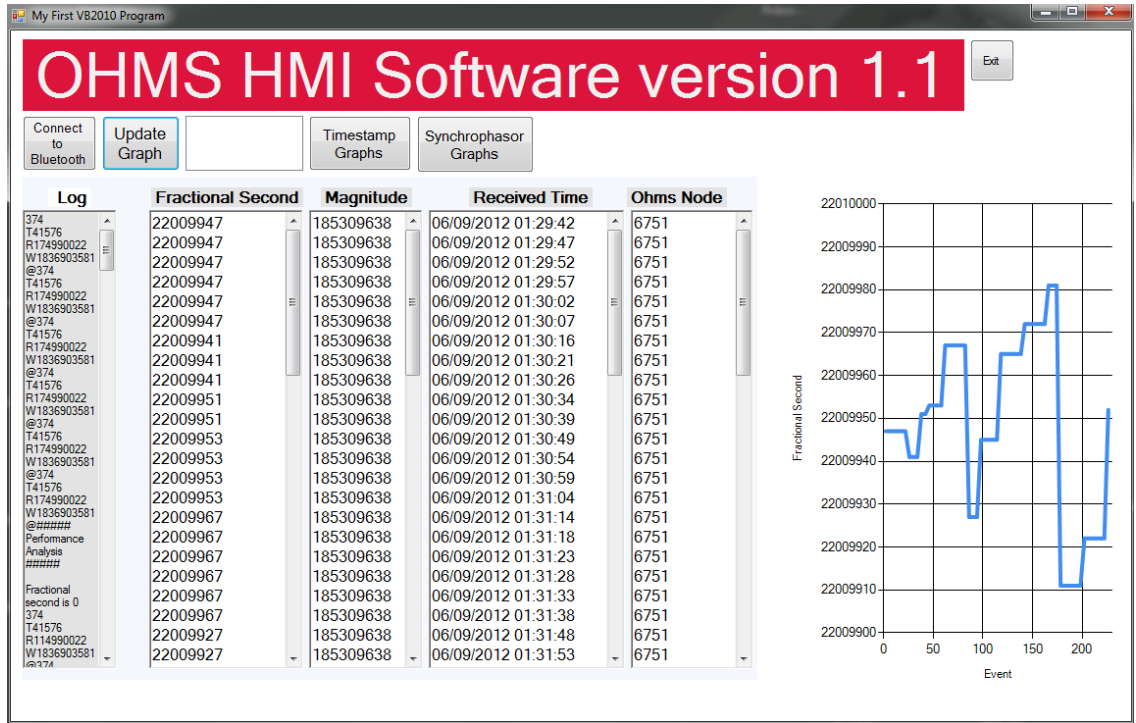


Figure 8.4: Screenshot of HMI plotting the fractional second of the received timestamp

Matlab before the signal is transferred to the memory of the FPGA based transient generator. It is likely that the actual SNR will in fact be lower due to the effects of the coaxial connection between the FPGA generator and the OHMS transmitter.

### 8.2.5 Performance of the OHMS Concept with Direct Connections

The experimental setup shown in Fig. 8.5 is used for initial testing of the OHMS concept. In this setup, a pulse is sent every 10 seconds, prompting the OHMS transmitter to generate a communication symbol for sending immediately to the OHMS receiver. The OHMS receiver is connected via Bluetooth to the HMI running on a laptop. First, a BER experiment is carried out. To do this, the OHMS

Table 8.1: Mean ( $\mu$ ) and standard deviation ( $\sigma$ ) in ns for various impulse waveshapes from 1000 simulation runs under different AWGN conditions

Impulse		$\mu$ v. SNR			$\sigma$ v. SNR		
Type	$T_{rise}(\mu s)$	15dB	10dB	5dB	15dB	10dB	5dB
Gaussian Pulse	4	+13.4	+17.91	+18.79	3.55	2.93	2.78
	0.4	+7.28	+6.27	+5.92	2.01	2.65	3.37
Sinc Pulse	4	+1.33	-3.76	6.82	7.34	8.45	9.12
	0.4	-0.67	-0.58	-0.19	7.23	6.18	14.36
Lightning Impulse	1.2/50	-8.98	-12.83	-14.77	67.4	78.2	79.3
	8/20	-11.1	-9.2	-5.2	18.7	22.1	24.3

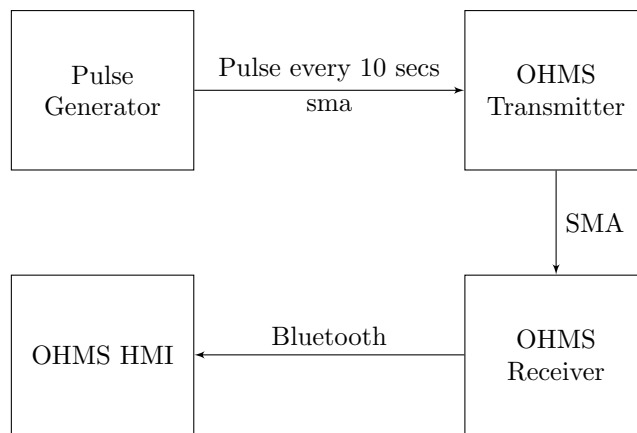


Figure 8.5: Experimental setup with OHMS devices directly connected

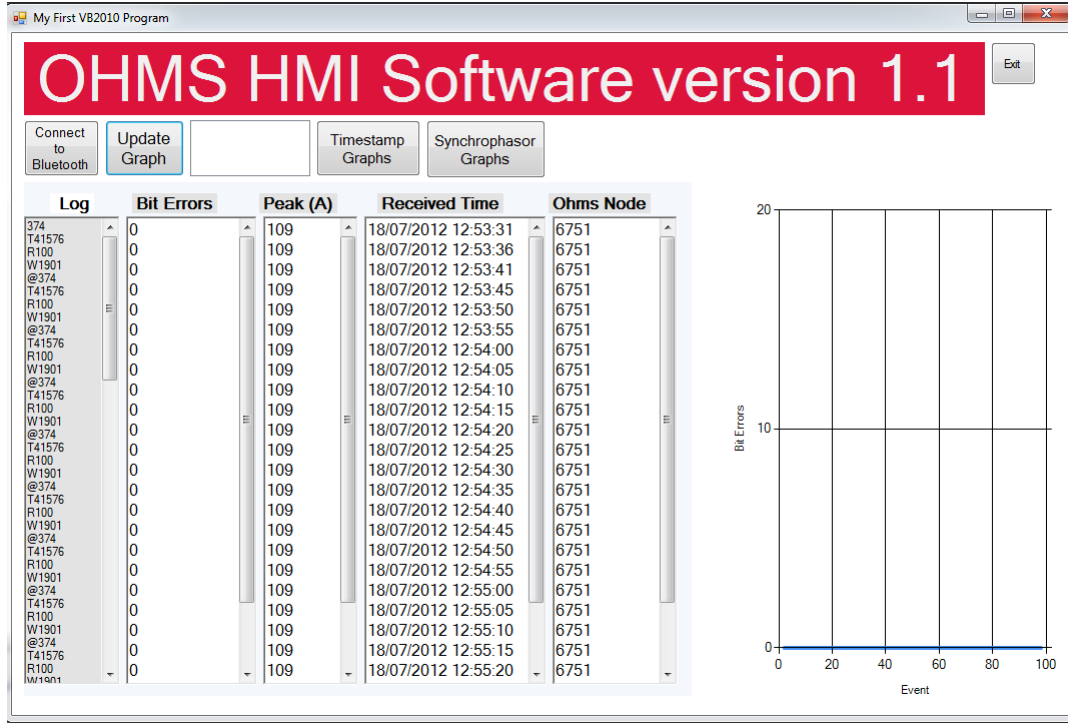


Figure 8.6: OHMS HMI output in the bit errors experiment

transmitter sends a known communication symbol and a comparison is made in the HMI. The HMI then plots the difference between the expected bits and received bits. In Fig. 8.6, it is shown that the BER is zero for a direct connection. This is unsurprising because the SNR is expected to be high and the channel is dominated by AWGN and not affected by multipath interference.

### 8.2.6 Full concept verification using the FPGA based network model

The FPGA based network model is used as a real time model of an 11 kV network to test the performance of the OHMS transmitters and receivers over a realistic channel environment. It is observed that a BER of zero is possible if the cyclic prefix is larger than the RMS delay spread of the channel. Fig. 8.7 shows a

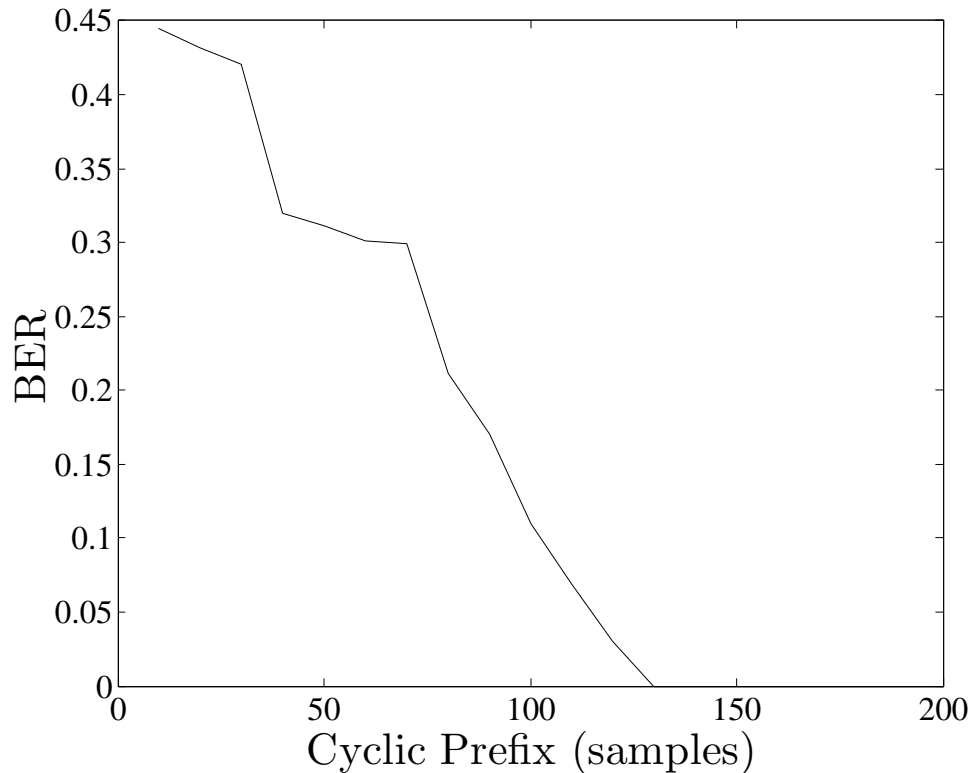


Figure 8.7: Performance on the real time test network with a varying cyclic prefix (166.7 KHz bandwidth system)

result that is in line with the simulated performance discussed in Chapter 4.

### 8.2.7 Partial Demonstration of the OHMS Concept: Sending a Location and Displaying it in the OHMS HMI

The M12M timing module is set up as a precision timing receiver. To validate the correct functioning of the GPS module, it is connected to a PC via the UART and the WinOncore software is used to interpret the received strings. It is verified that the received time and date settings are correct and that the position co-ordinates

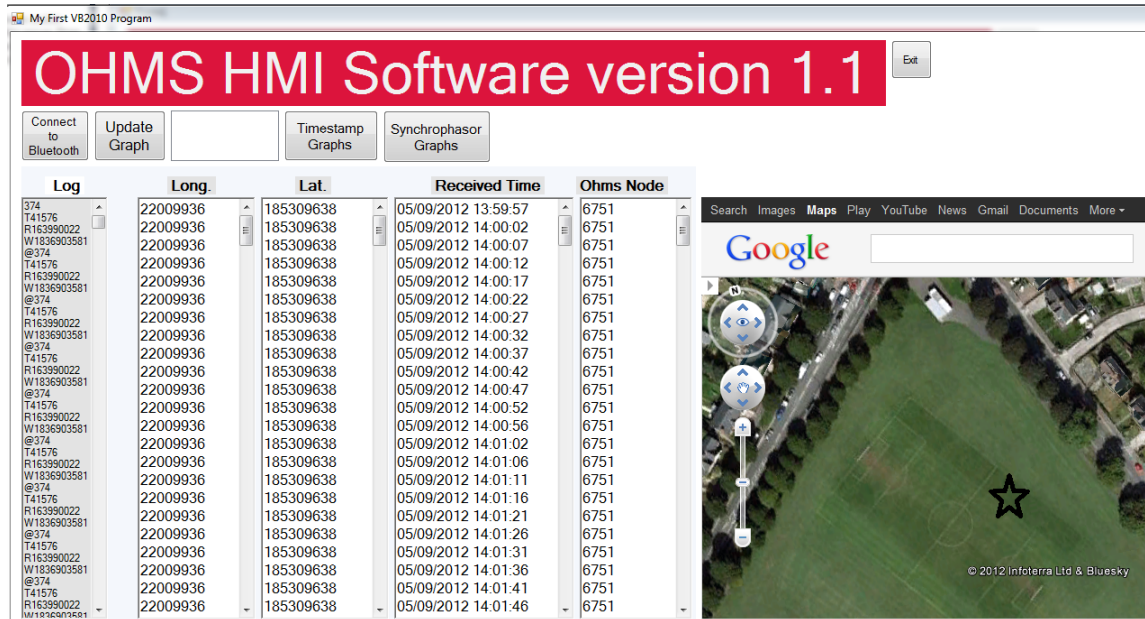


Figure 8.8: Screenshot of the HMI set to detect and display the GPS co-ordinates in the received symbol

are also accurate. The code running on the embedded processor of the OHMS transmitter is designed to extract the relevant information from this input string. To test this, the code is modified (see Appendix C.3) to print the received string over the JTAG-UART (the programming cable connected the FPGA to the PC). The information gathered from the string, namely the longitude and latitude co-ordinates of describing the location of the OHMS transmitter, can now be sent to the OHMS receiver. The OHMS HMI is modified to display the received co-ordinates. Fig. 8.8 shows a screenshot of the OHMS HMI. The location marked with a star on the map is confirmed as the location of the OHMS transmitter.

### 8.3 Field Based Tests on 11 kV Lines

Field trials are due to take place on a rural section of 11 kV network in South East England, just outside the Greater London area. A visit was made to the candidate site on 09/12/2011 to determine the suitability of the site for trial and potential coupling points. A plan has been submitted to carry out trials on this part of the network and final preparations are currently being made.

### 8.4 Conclusion

The laboratory based trials carried out with the prototype OHMS system show that the timing module and MODEM appears to be working as designed. It has been demonstrated that the OHMS transmitter is capable of constructing a symbol based on sensory input and then send it in less than 1 ms. Additionally, the OHMS receiver is able to detect the arrival of the synchronisation symbol and demodulate the information symbol to reveal the decoded information. This has been proven with the prototypes directly connected, and with the use of a real time network model. There are a number of practical factors that should be resolved before the system is capable of deployment on a live network. Firstly, the threshold value for the energy in the autocorrelation function should be dynamically adjusted to reflect local conditions. Secondly, the timing module requires more thorough testing on real networks to calibrate the detection threshold. Thirdly, there is uncertainty over how the ADC will cope with a varying input power of the symbol. It may be helpful to add an automatic gain control function before the ADC input to ensure

the full range of the ADC is used. It has already been shown in Section 4.6 that the frequency selectivity of the channel leads to a phenomenon of varying power in the received symbol sent from different nodes, with the difference being as much as 20 dB. Therefore, a “one size fits all” approach to amplification at the receiver may not be suitable. More will be learnt about this in future trials.

The system concept has been demonstrated with a custom built HMI. The HMI is able to visually display various monitored aspects of the OHMS concept, such as the received timestamp, the magnitude of the transient current and the location of the sending device. The HMI operates independently of any existing monitoring systems. This is both an advantage and disadvantage. On one hand, the software can be carefully tweaked to the precise requirements of the user, but on the other, there is no connectivity to the network operators main infrastructure. In future versions of the HMI, an IP based piece of software will be created to accompany the existing HMI and share the received information with a central hub. This may open up further opportunities in terms of wide area monitoring on a network scale and override the inherent limitation that the OHMS concept is only able to offer low latency communication with devices bounded by the primary transformer.

Field trials have been arranged and it is hoped that the system concept can be proven in more realistic conditions.

## Chapter 9

### General Conclusion and Future Work

#### 9.1 Discussion and Future Work

The OHMS concept is an attempt to use state-of-the-art electronics and modern communication systems to facilitate previously unfeasible applications on electricity networks. Rural networks have been targetted because this is a fault prone part of the network with limited access to conventional communication infrastructure. The main theme of the thesis was to demonstrate that an improved fault location scheme and low latency communication network can be set up at a cost that is not prohibitively expensive. In addition, the extremely fast reaction time of the digital electronics and the potential for very fast sampling rates of local voltage and current opens up new opportunities that have not been fully explored. These include:

- The implementation of fast decision making at protection devices based on post-fault (but pre-protective device operation) information. The low latency communication link between multiple remote nodes may allow auto-reclosers and sectionalisers to make an intelligent decision immediately, removing the need to stress the network with unnecessary reclosures.
- With the widely held belief that the best way to eradicate vulnerabilities in

electricity networks is by extensive WAM [97], the use of a low latency, highly robust communication link may be necessary. It has been demonstrated that depending on the number of devices participating in the OHMS system, a reporting rate that satisfies current IEEE standards for WAM can be achieved. The role of WAM may become increasingly important in rural networks in future decades due to the increasing penetration of embedded generation, furthering the call for effective, low latency communication in these types of networks.

- The traditional approach of a centralised concentrator receiving information from a vast number of remotely positioned sensors may become inadequate. The benefits of utilising the information remotely, “as it is received” may contribute to the implementation of self healing methods. This approach can be thought of as the network reacting to situations dynamically. Admittedly, this does pose risks and further research should be carried out on the possibilities and consequences of this type of approach.
- Further applications may naturally arise from a network of nodes with GPS capability. Could a permanent fault more accurately be resolved by sending a pulse from each OHMS node and measuring any difference between the rebounding pulses on the healthy network and the faulted network? This type of fault location method is already used successfully in the form of Time Domain Reflectometry (TDR).

There are numerous other unexplored applications that a system-wide deployment of communicating GPS connected nodes can provide. It is hoped that future trials and deployment opportunities of the OHMS concept can help to realise some of these potential applications.

Underpinning the OHMS concept is a low latency communication network, enabling communication between OHMS devices. It was found that a high optimised form of OFDM, in a “burst like” format is capable of achieving such a low latency link. Care must be taken, however, to ensure that the cyclic prefix is set to be greater than the RMS delay spread of the channel. It is both a weakness and an opportunity that the HV power line is a good medium for signals in the sub-MHz range. On one hand, it is possible to communicate over large networks without the need for repeaters, but on the other, the signal in the aerial modes bounces around the network and may interfere with subsequent symbols. This manifests itself as a high RMS delay spread and is the reason such a long cyclic prefix is required for robust communication.

It is recognised that the feasibility of the OHMS system will ultimately be driven by a cost/benefit analysis. Appendix B.3 shows the cost breakdown of the OHMS transmitter and receiver designs. The cost is dominated in both devices by the coupling capacitor. It may be possible to replace the coupling capacitor with an inductive coupler, which may reduce this part of the cost somewhat. In general, a network of 25 OHMS transmitters and a single OHMS receiver would cost in the region of a one off payment of 35,000 with no annual subscription charge (as may be the case in the procurement of wireless services). It is difficult to assess what kind

of value this would represent to the network operator, however, the answer would depend on the benefits of the applications the system could support.

An opportunity is recognised to reduce costs by “sharing” a single GPS clock at a given OHMS transmitter with all other OHMS transmitters. Clock sharing schemes already exist in ethernet type networks (with the IEEE 1588 standard [98]) and sensor networks [99]. The IEEE 1588 has even been extended specifically for power system applications, though an ethernet network is still required [2]. The IEEE 1588 Precision Time Protocol (PTP) shares the clock by broadcasting periodically the local time. Each node on the network notes this time and calculates an adjustment factor by calculating the “time of flight” between themselves and the GPS-connected node. This time of flight is obtained by timestamping the sending time and arrival time of a signal with the assumption that the GPS-connected node re-broadcasts the node immediately, or after a pre-set time. In ethernet type networks, this method is fairly easy to implement. In PLC networks not equipped with IP based technology, the same algorithm can be performed by using a Schmidl/Cox synchronisation symbol, with the knowledge that timestamping of the arrival time of a signal can be calculated to within one sample of accuracy, where the sample rate is set by the communication scheme. This concept would be an interesting topic of future research.

Laboratory based experiments have shown promising results and the OHMS systems have been shown to be capable of achieving the low latency link and the timestamping accuracy needed to implement a range of new applications. The focus, in this work, was on the development of a multi-ended fault location method

to take advantage of the ability to retrieve information from branch terminations. The multi-ended fault location algorithm displayed high accuracy in the simulation environment. A weakness of the method, however, was the requirement for an OHMS device at every branch termination to be able to locate faults anywhere in the network. For highly branched networks, the cost of installing so many devices may be too great. For this reason, the author does not think this method will be suitable for urban areas.

## 9.2 Conclusion

In this thesis, a prototype of a new type of remote monitoring device designed for wide area deployment on rural 11 kV distribution lines has been developed. Further to this, the possibilities in terms of useful applications such a system can enable has also been discussed. One of the most promising applications is the implementation of an extremely accurate fault location scheme, with the ability to pinpoint the location of a fault, or even a temporary disturbance, to anywhere on a branched network. To enable the system, a low latency communication scheme has been designed and developed with a highly optimised form of a multi-carrier communication scheme. The possible benefits of a reliable, low latency communication network between numerous remote nodes on a distribution network stretch beyond what is discussed in this thesis, and clever manipulation of this "shared information" could provide a way forward in the implementation of several key areas seen as critical in the movement towards a smart grid that can cope with the challenges

of the coming decades.

## Appendix A

### Code Listings

Listing A.1: EMTP Models code for modal transformation (Fortran)

```
comment
Author: Stephen Robson (robson.stephen@gmail.com)
Modal transform model
5  endcomment

MODEL modal
INPUT realX , realY ,realZ,imagX,imagY,imagZ
OUTPUT MODE1, MODE2, MODE3
10 VAR MODE1, MODE2,MODE3, T11, T12, T13, T21,
    T22, T23, T31,T32,T33,a,b,c,
    MAGM1, MAGM2, MAGM3
INIT
T11:=0.5782
15 T12:=0.5796
    T13:=0.5782
    T21:=-0.7071
    T22:=0
    T23:=0.7071
20 T31:=-0.3706
    T32:=0.8642
    T33:=-0.3706
ENDINIT
EXEC
25 MODE1:=sqrt(2)*((realX*T11)+(realY*T12)+(realZ*T13))
    MODE2:=sqrt(2)*((realX*T21)+(realY*T22)+(realZ*T23))
    MODE3:=sqrt(2)*((realX*T31)+(realY*T32)+(realZ*T33))
ENDEXEC
ENDMODEL
```

Listing A.2: Matlab code for implementing an OFDM demodulator

```
%Code created by Stephen Robson
%(robson.stephen@gmail.com)
5 %This is an OFDM demodulator.It works
```

```

%in tandem with the tsync2.m
%function.

10 %-----Definitions-----
clear
AtoCshort2; %Load file from ATP/EMTP
s=cell2mat(vXX0012);
s=cell2mat(iMODELSM2C); %signal from circuit in atp
15 p=cell2mat(iMODELSIM);
q=cell2mat(iMODELSRE);
R=cell2mat(iMODELSINPHA);
IM=cell2mat(iMODELSQUADI);
t=cell2mat(t);
20 fc=440000; %carrier frequency
y2=167; %cyclic prefix length (samples)
sFFT=512; %FFT size
ncarr=80; %number of used carriers
nsymb=1; %number of symbols
25 %-----Calculate sent signal-----

bitsent=R+1i*IM; %bits from atp
bitsent1=bitsent(1:60:length(bitsent));
30 %decimate to baseband

bitsentc=bitsent1(sFFT+y2+1:length(bitsent1)-1);
rebit=reshape(bitsentc(sFFT+y2+1:(sFFT+y2)...
+(nsymb*(sFFT+y2)))) , sFFT+y2, nsymb);
35 rebit2=[rebit(1:(ncarr),:)]'
rebit((sFFT-ncarr+1):(sFFT),:)]';
rebit3=rebit2';

sendiff=((rebit2(1,:)));
40 sendiff=sendiff';
sendiffconj=angle(conj(rebit2(1,:)));
sendiffconj=sendiffconj';

sentalphabet=dpskdemod(rebit2',4);
45 sentalphabet2=[sentalphabet((2:ncarr),:)]'
sentalphabet(((ncarr+2):length(sentalphabet)),:)]';
sentalphabet2=sentalphabet2';

for j=2:length(sendiff(:,1))
50 hsent(j)=angle(((sendiff(j)))*(conj(sendiff(j-1)))));
end

```

```

%-----Receiver-----
kkk=200;
55 estimate = zeros(1, kkk);
   % for kk=1:kkk %Optional loop for testing influence of
   %noise on timing estimates.

nt = 0.000350*(1/sqrt(2))*[randn(1, prod(size(s))) ...
60   + i*randn(1, prod(size(s)))];
sre3=exp(1i*2*pi*fc*t).*s;
sre2=exp(1i*2*pi*fc*t).*s;
%quadrature mixing/downconversion
[bb, aa]=butter(13, 0.09);
65 %filter out the double frequencies
afterdec=filter(bb, aa, sre2);
afterdec=afterdec+nt';
afterdecnoise=filter(bb, aa, sre3);

70 afterdec2=afterdec(1:60:length(afterdec)); %sample

tocorrel=real(afterdec2)+1i*(imag(afterdec2));
tcorr=(1:1:length(tocorrel))';

75 [F]=tsync2(tocorrel', sFFT, y2); %Timing control
   estimate(kk)=F; %for use in optional loop
signal_size = size(tocorrel', 2);
L = sFFT/2;

80 %end %end of optional loop

a=1;
MM=filter(b, a, PP);
[B, AA] = butter(11, 0.05);

85 ab=reshape(tocorrel(F+(sFFT+y2):((sFFT+y2)...
+(nsymb*(sFFT+y2))+F-1)), sFFT+y2, nsymb);
ab2=ab(1:sFFT, :);
aa2=fft(ab2);
90 aa3=[aa2(1:(ncarr), :) aa2((sFFT-ncarr+1):(sFFT), :)]';
aa3=aa3';

r_data=real(tocorrel(F+sFFT+y2:1:F+sFFT+y2+(sFFT-1)))...
+1i*imag(tocorrel(F+sFFT+y2:1:F+sFFT+y2+(sFFT-1)));
95

g=(aa3(:, 1));
for j=2:length(aa3(:, 1))

```

```

100     h(j)=angle((g(j)*conj((g(j-1)))));
end

recalphabet=dpskdemod(aa3,4);
recalphabet2=[recalphabet((2:ncarr),:)'
105     recalphabet((ncarr+2):length(recalphabet)),:]'];
recalphabet2=recalphabet2';

%calculate errors
[number,ratio,individual]=...
110 biterr(sentalphabet2,recalphabet2)
%-----figures-----
%optional

```

Listing A.3: Timing Module

```

%% Time Synchronisation (RECEIVER)
% -----
%This code implements the SCHMIDL/COX timing estimator

5 function [index] = tsync2(signal, size_of_fft,G)
%%
    signal_size = size(signal,2); % Signal size
    L = size_of_fft/2; % Length of sliding window
    slide_length = signal_size-size_of_fft+1;
10    % Total window slide length
    P = zeros(1,slide_length); % Inititalize the arrays
    R = zeros(1,slide_length);

    for n=1:slide_length
15        for m=1:L
            P(n) = P(n) + conj(signal(n+m-1))...
                *signal(n+m+L-1);

            % Conjugate pair
20            R(n) = R(n) +...
                abs(signal(L+n+m-1))^2;
            %Normalizing factor

        end
    end
25    M = (abs(P).^2)./(R.^2);
    PP= (abs(P).^2);
    b=ones(1,G)/G;
    a=1;
30    MM=filter(b,a,PP);

    for n=1:slide_length

```

```

    [value index] = max(MM); % Find peak
    if((index+2*size_of_fft-1) > signal_size)
35         MM =MM(1:index-1);
        %If peak is near the end, and the symbols
        %cut off, back up and pick another one.
        else
            break
40         end
    end
end
end

```

Listing A.4: Matlab code to calculate channel response and fades

```

%Code by Stephen Robson
%This m file performs the following tasks:
% 1) reads in the impulse test data from matlab
5 % 2) Calculates the magnitude response
% 3) Calculates the fades occuring in freq. domain
% 4) Calculates the RMS delay spread per mode

clear all

10
atpsampT=1E-8; %delta T in atp
sampfreq=1/atpsampT; %1/T = sampling frequency
samples=500001; %number of atp points
halfFFTlength=(samples+1)/2;
15 %half the fft because it is symmetric

AtoBchannel;
%file from ATP/EMTP Impulse response test
inp1=cell2mat(iMODELSM1A); %convert to matrix format
20 inp2=cell2mat(iMODELSM2A);
inp3=cell2mat(iMODELSM3A);
one=cell2mat(iMODELSM1B);
two=cell2mat(iMODELSM2B);
thre=cell2mat(iMODELSM3B);
25 inp1=zeros(samples,1); %set up a matrix of all zeros
inp2=zeros(samples,1); %set up a matrix of all zeros
inp3=zeros(samples,1); %set up a matrix of all zeros
inp1(1)=inp1(3);
inp1(2)=inp1(4);
30 inp1(3)=inp1(5);
inp1(4)=inp1(6);
inp1(5)=inp1(7);
inp1(6)=inp1(8); %Shift

```

```

imp1(7)=inp1(9);
35 imp1(8)=inp1(10);
imp1(9)=inp1(11);
imp1(10)=inp1(12);
imp1(11)=inp1(13);
imp1(12)=inp1(14);
40 imp1(13)=inp1(15);
imp1(14)=inp1(16);
imp1(15)=inp1(17);
imp1(16)=inp1(18);
imp1(17)=inp1(19);
45 imp1(18)=inp1(20);
imp1(19)=inp1(21);
imp1(20)=inp1(22);
imp1(21)=inp1(23);
imp1(22)=inp1(24);
50 imp1(23)=inp1(25);
imp2(1)=inp2(3);
imp2(2)=inp2(4);
imp2(3)=inp2(5);
imp2(4)=inp2(6);
55 imp2(5)=inp2(7);
imp2(6)=inp2(8);
imp2(7)=inp2(9);
imp2(8)=inp2(10);
imp2(9)=inp2(11);
60 imp2(10)=inp2(12);
imp2(11)=inp2(13);
imp2(12)=inp2(14);
imp2(13)=inp2(15);
imp2(14)=inp2(16);
65 imp2(15)=inp2(17);
imp2(16)=inp2(18);
imp2(17)=inp2(19);
imp2(18)=inp2(20);
imp2(19)=inp2(21);
70 imp2(20)=inp2(22);
imp2(21)=inp2(23);
imp2(22)=inp2(24);
imp2(23)=inp2(25);

75 imp3(1)=inp3(3);
%A pulse was injected into the atp circuit.
% Just take this, reject the reflections
imp3(2)=inp3(4);
imp3(3)=inp3(5);
80 imp3(4)=inp3(6);

```

```

imp3(5)=inp3(7);
imp3(6)=inp3(8);
imp3(7)=inp3(9);
imp3(8)=inp3(10);
85 imp3(9)=inp3(11);
imp3(10)=inp3(12);
imp3(11)=inp3(13);
imp3(12)=inp3(14);
imp3(13)=inp3(15);
90 imp3(14)=inp3(16);
imp3(15)=inp3(17);
imp3(16)=inp3(18);
imp3(17)=inp3(19);
imp3(18)=inp3(20);
95 imp3(19)=inp3(21);
imp3(20)=inp3(22);
imp3(21)=inp3(23);
imp3(22)=inp3(24);
imp3(23)=inp3(25);
100

inpf1=fft(imp1);
inpf2=fft(imp2);
inpf3=fft(imp3);
105

onef=fft(one); %position 1 in atp circuit
twof=fft(two); %2
thref=fft(thre); %3
110 chrespone=20*log10(abs(onef./inpf1));
%channel response is FFT(OUTPUT)/FFT(INPUT)
phaseone=angle(onef./inpf1); %phase response

chresptwo=20*log10(abs(twof./inpf2));
115 phasetwo=angle(twof./inpf2);

chrespthre=20*log10(abs(thref./inpf3));
phasethre=angle(thref./inpf3);
120

chrespone=chrespone(1:(halfFFTlength/5));
%reject second half of FFT for plotting
phaseone=phaseone(1:(halfFFTlength/5));
chresptwo=chresptwo(1:halfFFTlength/5);
125 phasetwo=phasetwo(1:halfFFTlength/5);
chrespthre=chrespthre(1:(halfFFTlength/5));
phasethre=phasethre(1:(halfFFTlength/5));

```

```

f = (1:(halfFFTlength/5))*sampfreq/samples;
130 %convert from 0:samples/2 to 0:samplingfrequency/2
f2=f(1:10000);

b=10;

135 phasetwo2=phasetwo(2:b:length(phasetwo));

frel = (1:(length(phasetwo2))*5000000/length(phasetwo2));
%convert from 0:samples/2 to 0:samplingfrequency/2

140

% Next part checks the phase rotation between
% adjacent subcarriers assuming that Differential
% BPSK, QPSK or 8PSK is used
145 for j = 2:1:length(phasetwo2)

    if (phasetwo2(j) < -(pi/2)) && (phasetwo2(j-1)>(pi/2))
        pr2(j)=phasetwo2(j)-phasetwo2(j-1)+(2*pi);
        pr(j)=1;
150

    elseif (phasetwo2(j-1) < -(pi/2)) &&...
        (phasetwo2(j)>(pi/2))
        pr2(j)=phasetwo2(j)-phasetwo2(j-1)-(2*pi);
        pr(j)=2;
155

    elseif ((phasetwo2(j)< (pi/2))&&(phasetwo2(j)>0)...
        && ((phasetwo2(j-1)< (pi/2))...
        &&(phasetwo2(j-1)>0)))
        pr2(j)=phasetwo2(j)-phasetwo2(j-1);
160        pr(j)=3;

    elseif (phasetwo2(j) < (0)) &&...
        (phasetwo2(j) > (-pi/2))...
165        && (phasetwo2(j-1) < (0)) &&...
        (phasetwo2(j-1) > (-pi/2))
        pr2(j)=phasetwo2(j)-phasetwo2(j-1);
        pr(j)=4;

170    elseif ((phasetwo2(j) > pi/2) && ((phasetwo2(j-1)<0)...
        && (phasetwo2(j-1)>(-pi/2))))
        pr(j)=5;
        if ((phasetwo2(j)-phasetwo2(j-1)))>pi
            pr2(j)=(2*pi) - ((phasetwo2(j)-phasetwo2(j-1)));

```

```

175         else
                pr2(j)= ((phasetwo2(j)-phasetwo2(j-1)));
        end

180     elseif (phasetwo2(j-1) < -(pi/2)) &&...
            (phasetwo2(j)<(pi/2)) && (phasetwo2(j)>0)

            if ((phasetwo2(j)-phasetwo2(j-1))>pi
                pr2(j)= (2*pi)-((phasetwo2(j)-phasetwo2(j-1)));
185         pr(j)=6;
            else
                pr2(j)= ((phasetwo2(j)-phasetwo2(j-1)));
                pr(j)=7;
            end

190

        elseif phasetwo2(j)>-(pi/2)) && (phasetwo2(j)<0)...
            && (phasetwo2(j-1)>(pi/2))
                pr2(j)=phasetwo2(j)-phasetwo2(j-1);
195         pr(j)=8;

        elseif phasetwo2(j)<((pi/2)) && (phasetwo2(j)>0)...
            && (phasetwo2(j-1)>(pi/2))
                pr2(j)=phasetwo2(j)-phasetwo2(j-1);
200         pr(j)=9;

        elseif phasetwo2(j)>-(pi/2)) && (phasetwo2(j)<0)...
            && (phasetwo2(j-1)>(pi/2))
                pr2(j)=phasetwo2(j)-phasetwo2(j-1);
205         pr(j)=10;

            elseif (phasetwo2(j) < -(pi/2)) && ...
                (phasetwo2(j-1)<(pi/2)) &&...
                (phasetwo2(j-1)>0)
210         if ((phasetwo2(j)-phasetwo2(j-1))<(-pi)
            pr2(j)=phasetwo2(j)-phasetwo2(j-1)+(2*pi);
            pr(j)=11;
            else
                pr2(j)=phasetwo2(j)-phasetwo2(j-1);
215         pr(j)=12;
            end

        end

        else

220         pr2(j)=phasetwo2(j)-phasetwo2(j-1);
        pr(j)=13;

```

```

        end
    end
    ff=0;
225 for hh = 1:1:length(pr2)
        if (frel(hh)>200000) && (frel(hh)<600000)
            ff=ff+1;
        end
    end
230 for h = 1:1:length(pr2)

        if (frel(h)>200000) && (frel(h)<600000) &&...
            ((pr2(h) > (pi/4) || pr2(h) < -(pi/4)))
235         %+-pi/4 is for QPSK schemes
            err(h)=1;
        else
            err(h)=0;
        end
240 end

fades=sum(err)/ff

%Calculate the RMS delay spreads%%%%%%%%%%%%%%%%%%%%%%%%%%%%%%%%%%%%%%%%%%
245 %%%%%%%%%%%%%%%%%%%%%%%%%%%%%%%%%%%%%%%%%%%
%calculate RMS delay spread for mode 2
twoab=two.^2;
t=cell2mat(t);
twoabt=twoab.*t;
250 excess=sum(twoabt);
twoabtd=sum(twoab);
excess2=excess/twoabtd;

der=((t-excess2).^2).*twoab;
255 dersum=sum(der);

tsmall=t(1:50000);

rmstwo=sqrt(dersum/twoabtd)
260 %%%%%%%%%%%%%%%%%%%%%%%%%%%%%%%%%%%%%%%%%%%
%calculate RMS delay spread for mode 3
threab=thre.^2;
threabt=threab.*t;
excess3=sum(threabt);
265 threabtd=sum(threab);
excess4=excess3/threabtd;

derthre=((t-excess4).^2).*threab;

```

```

dersum3=sum(derthre);
270
rmsthre=sqrt(dersum3/threabtd)
%%%%%%%%%%%%%%%%%%%%%%%%%%%%%%%%%%%%%%%%%%%%%%%%%%%%%%%%%%%%%%%%%%%%%%%%
%calculate RMS delay spread for mode 1
oneab=one.^2;
275 oneabt=oneab.*t;
excess5=sum(oneabt);
oneabtd=sum(oneab);
excess6=excess5/oneabtd;

280 derone=((t-excess6).^2).*oneab;
dersum1=sum(derone);

rmsone=sqrt(dersum1/oneabtd)
%%%%%%%%%%%%%%%%%%%%%%%%%%%%%%%%%%%%%%%%%%%%%%%%%%%%%%%%%%%%%%%%%%%%%%%%

```

Listing A.5: EMTP Models code for the OFDM Transmitter (Fortran)

```

MODEL ofdm

comment
Author: Stephen Robson (robson.stephen@gmail.com)
5 This model replicates an OFDM modulator. It begins
by constructing a 'training symbol' of two identical
halves in the time domain by taking the IDFT
comprising only EVEN subcarriers. The next symbol(s)
is/are the IDFT of a random bitstream mapped onto a
10 BPSK constellation. The number of used subcarriers is
set by the 'c' parameter. This parameter determines
how far either side of DC the subcarriers should be
mapped with data. For instance, for 512 subcarriers
(y=511) and 'c' set to 200, subcarriers 0 to 199 and
15 subcarriers 313 to 512 will carry data. The
other subcarriers are set to zero. The setting of
high frequency subcarriers to zero is common in
practical OFDM systems because it eases the
roll-off requirements of the low pass filter at the
20 output. The output of the DAC will be a staircase type
shape containing frequency components
that are higher than intended. The low pass filter
removes these higher frequency 'aliases' and leaves a
visibly smooth waveform. The distance between the
25 intended signal (centred at DC) and the first alias
is increased if you set the high subcarriers to zero.
Thus, a less complex filter is required to remove this
first alias whilst conserving the baseband data.

```

```

30 Other parameters:
      Cyc: Cyclic prefix length. Note, for 512
        subcarriers, input 511 because the array runs from zero.
        y: Number of subcarriers
Variables:
35      FFr, FFi: These are the real and
        imaginary parts mapped into the IDFT. The value depends
        on the outcome of a random test, or are set to zero if
        they are mapping onto an unused subcarrier.
40      FFrrr, FFiii: These are the outputs of
        the IDFT and outputted sequentially to the
        DAC/low pass filter.
      R2: Starts at zero and increments
        with every timestep. When it reaches y+cyc+1, it
        the code to output the training symbol. Anything above
45 this, the code outputs a normal data symbol.
      r: Resets to zero after every
        y+cyc+1 so the code knows when to calculate another symbol
        to be sent. The counter output allows plotting
        of r.
50      TIMESTEP MAX: Determines how often in
        time an IDFT output is sent, therefore, how much
        bandwidth the baseband signal occupies.

endcomment

55

INPUT X
60 OUTPUT IMAG,REAL, INPHASE,QUADIN,SIGOUT,counter
DATA cyc,y,c
VAR n, SIGOUT, IMAG,REAL,INPHASE, QUADIN,MAG,
  counter,
  FFi[0..y+cyc],
65 FFfin[0..y+cyc],FFq[0..y+cyc], FFr[0..y+cyc],
  FFrr[0..y+cyc],
  FFii[0..y+cyc],FFrpret[0..y+cyc],FFipret[0..y+cyc],
  a,i,p,r,u, D1r,D1i,D2,TS,f,FFrrr[0..y+cyc],
  FFiii[0..y+cyc],
70 SR,SI,R2
TIMESTEP MAX: 1.2E-5
MIN: 1.2E-5
INIT

75 r:=0
R2:=0

```

```

ENDINIT

EXEC

80   IF R2=0 AND r=0 THEN    --Starting condition, nosie
FOR a:=0 to y+cyc DO
FFr[a]:=0
FFi[a]:=0.
85   FFrr[a]:=0.01*random()
FFii[a]:=0.01*random()
FFrrr[a]:=0.01*random()
FFiii[a]:=0.01*random()
ENDFOR
90   ELSIF R2=y+cyc+1 AND r=0 THEN  -Construct training
-- symbol
FOR a:=0 to (c-1) BY 2 DO  --First, map onto the
-- even subcarriers
--up to DC+c

95   IF random()<(1/8) THEN
FFr[a]:=1.404
FFi[a]:=0
ELSIF random()<(2/8) THEN
100  FFr[a]:=1
FFi[a]:=1
ELSIF random()<(3/8) THEN
FFr[a]:=0
FFi[a]:=1.404
105  ELSIF random()<(4/8) THEN
FFr[a]:=-1
FFi[a]:=1
ELSIF random()<(5/8) THEN
FFr[a]:=-1.404
FFi[a]:=0
110  ELSIF random()<(6/8) THEN
FFr[a]:=-1
FFi[a]:=-1
ELSIF random()<(7/8) THEN
FFr[a]:=0
115  FFi[a]:=-1.404
ELSIF random()<(8/8) THEN
FFr[a]:=1
FFi[a]:=-1
ENDIF
120  FFrr[a]:=0
FFii[a]:=0
FFrrr[a]:=0
FFiii[a]:=0

```

```

        ENDFOR
125     FOR a:=1 to (c-1) BY 2 DO      --set odd subcarriers
to zero.

        FFr[a]:=0
        FFi[a]:=0
        FFrr[a]:=0
130     FFii[a]:=0
        FFrrr[a]:=0
        FFiii[a]:=0
        ENDFOR
135     FOR a:=(y-c+1) to y BY 2 DO  --Map onto the even
        -- subcarriers
        -- from y-c to c.

        IF random()<(1/8) THEN
        FFr[a]:=1.404
        FFi[a]:=0
140     ELSIF random()<(2/8) THEN
        FFr[a]:=1
        FFi[a]:=1
        ELSIF random()<(3/8) THEN
        FFr[a]:=0
145     FFi[a]:=1.404
        ELSIF random()<(4/8) THEN
        FFr[a]:=-1
        FFi[a]:=0
        ELSIF random()<(5/8) THEN
150     FFr[a]:=-1.404
        FFi[a]:=0
        ELSIF random()<(6/8) THEN
        FFr[a]:=-1
        FFi[a]:=-1
155     ELSIF random()<(7/8) THEN
        FFr[a]:=0
        FFi[a]:=-1.404
        ELSIF random()<(8/8) THEN
        FFr[a]:=1
160     FFi[a]:=-1
        ENDIF
        FFrr[a]:=0
        FFii[a]:=0
        FFrrr[a]:=0
165     FFiii[a]:=0
        ENDFOR
        FOR a:=(y-c+2) to y BY 2 DO
        --set odd subcarriers in training
        --symbol to zero.

```

```

170      FFr[a]:=0
      FFi[a]:=0
      FFrr[a]:=0
      FFii[a]:=0
175      FFrrr[a]:=0
      FFiii[a]:=0
      ENDFOR
      FOR a:= c to (y-c) DO
      FFr[a]:=0
180      FFi[a]:=0
      FFrr[a]:=0
      FFii[a]:=0
      FFrrr[a]:=0
      FFiii[a]:=0
185      ENDFOR
      FOR a:= y+1 to y+cyc DO
      FFr[a]:=0
      FFi[a]:=0
      FFrr[a]:=0
190      FFii[a]:=0
      FFiii[a]:=0
      FFrrr[a]:=0
      ENDFOR

195      FOR p:=0 to y DO
      FFrrr[p]:=0
      FFiii[p]:=0
      ENDFOR
      FOR n:=0 to y DO
200
      FFi[n]:=-FFi[n]
      ENDFOR

      FOR p:=0 to y DO
205      FOR n:=0 to y DO
      SR:=cos(p*(n/(y+1))*2*PI)
      SI:=-sin(p*(n/(y+1))*2*PI)

      FFrrr[p]:= (FFrrr[p]+FFr[n]*SR)-((FFi[n]*SI))
210      --This is the IDFT
      FFiii[p]:= (FFiii[p]+FFr[n]*SI)+((FFi[n]*SR))
      ENDFOR
      ENDFOR

215      FOR p:=0 to y DO
      --Scaling of the IDFT output

```

```

FFrrr[p]:=((1/(y+1))*FFrrr[p])*3
FFiii[p]:=-((1/(y+1))*FFiii[p])*3
ENDFOR

220
FOR p:=0 to y DO
  --To check it works, FFT the IFFT to see if
  --you get back what you put in
  FOR n:=0 to y DO
225
    SR:=cos(p*(n/(y+1))*2*PI)
    SI:=-sin(p*(n/(y+1))*2*PI)
    FFrr[p]:= (FFrr[p]+FFrrr[n]*SR)-((FFiii[n]*SI))
    FFii[p]:= (FFii[p]+FFrrr[n]*SI)+((FFiii[n]*SR))
230
  ENDFOR
ENDFOR

                                --Cyclic prefix insertion
  FFiii[cyc..y+cyc]:=FFiii[0..y]
  FFrrr[cyc..y+cyc]:=FFrrr[0..y]
235
  FFiii[0..cyc-1]:=FFiii[y+1..y+cyc]
  FFrrr[0..cyc-1]:=FFrrr[y+1..y+cyc]

  ELSIF r=0 AND R2>=y+cyc+3 THEN
    --This condition instructs
240
    -- the code to output a data symbol
FOR a:= 0 to (c-1) DO
  IF random()<(1/8) THEN
    FFrr[a]:=1.404
    FFii[a]:=0
245
  ELSIF random()<(2/8) THEN
    FFrr[a]:=1
    FFii[a]:=1
  ELSIF random()<(3/8) THEN
    FFrr[a]:=0
    FFii[a]:=1.404
250
  ELSIF random()<(4/8) THEN
    FFrr[a]:=-1
    FFii[a]:=0
  ELSIF random()<(5/8) THEN
255
    FFrr[a]:=-1.404
    FFii[a]:=0
  ELSIF random()<(6/8) THEN
    FFrr[a]:=-1
    FFii[a]:=-1
260
  ELSIF random()<(7/8) THEN
    FFrr[a]:=0
    FFii[a]:=-1.404
  ELSIF random()<(8/8) THEN

```

```

265         FFr[a]:=1
           FFi[a]:=-1
           ENDIF

FFrr[a]:=0
FFii[a]:=0
270 FFrrr[a]:=0
FFiii[a]:=0
ENDFOR
FOR a:= (y-c+1) to y DO
IF random()<(1/8) THEN
275     FFr[a]:=1.404
        FFi[a]:=0
        ELSIF random()<(2/8) THEN
        FFr[a]:=1
        FFi[a]:=1
280     ELSIF random()<(3/8) THEN
        FFr[a]:=0
        FFi[a]:=1.404
        ELSIF random()<(4/8) THEN
        FFr[a]:=-1
285     FFi[a]:=0
        ELSIF random()<(5/8) THEN
        FFr[a]:=-1.404
        FFi[a]:=0
        ELSIF random()<(6/8) THEN
290     FFr[a]:=-1
        FFi[a]:=-1
        ELSIF random()<(7/8) THEN
        FFr[a]:=0
        FFi[a]:=-1.404
295     ELSIF random()<(8/8) THEN
        FFr[a]:=1
        FFi[a]:=-1
        ENDIF

300 FFrr[a]:=0
        FFii[a]:=0
        FFrrr[a]:=0
        FFiii[a]:=0
        ENDFOR
305 FOR a:= c to (y-c) DO
        FFr[a]:=0
        FFi[a]:=0
        FFrr[a]:=0
        FFii[a]:=0
310 FFrrr[a]:=0

```

```

FFiii[a]:=0
ENDFOR
FOR a:= (y+1) to y+cyc DO
FFr[a]:=0
315 FFi[a]:=0
FFrr[a]:=0
FFii[a]:=0
FFrrr[a]:=0
FFiii[a]:=0
320 ENDFOR
FOR p:=0 to y DO
FFrrr[p]:=0
FFiii[p]:=0
ENDFOR
325 FOR n:=0 to y DO
FFi[n]:=-FFi[n]
ENDFOR
FOR p:=0 to y DO
FOR n:=0 to y DO
330 SR:=cos(p*(n/(y+1))*2*PI)
SI:=-sin(p*(n/(y+1))*2*PI)
FFrrr[p]:= (FFrrr[p]+FFr[n]*SR)-((FFi[n]*SI))
FFiii[p]:= (FFiii[p]+FFr[n]*SI)+((FFi[n]*SR))
ENDFOR
335 ENDFOR
FOR p:=0 to y DO
FFrrr[p]:= (1/(y+1))*FFrrr[p]
FFiii[p]:= -(1/(y+1))*FFiii[p]
ENDFOR
340 FOR p:=0 to y DO
FOR n:=0 to y DO
SR:=cos(p*(n/(y+1))*2*PI)
SI:=-sin(p*(n/(y+1))*2*PI)
FFrr[p]:= (FFrr[p]+FFrrr[n]*SR)-((FFiii[n]*SI))
345 FFi[p]:= (FFii[p]+FFrrr[n]*SI)+((FFiii[n]*SR))
ENDFOR
ENDFOR
FFiii[cyc..y+cyc]:=FFiii[0..y]
FFrrr[cyc..y+cyc]:=FFrrr[0..y]
350 FFiii[0..cyc-1]:=FFiii[y+1..y+cyc]
FFrrr[0..cyc-1]:=FFrrr[y+1..y+cyc]
ENDIF
IMAG:=FFiii[r]
REAL:=FFrrr[r]
355 INPHASE:=FFrr[r]
QUADIN:=FFii[r]
counter:=r

```

```

    SIGOUT:=(IMAG+REAL)
    r:=r+1
360 R2:=R2+1
    IF r=(y+cyc+1) THEN
    r:=0
    FOR p:=0 to y+cyc DO
    FFrr[p]:=0
365 FFii[p]:=0
    FFrrr[p]:=0
    FFiii[p]:=0
    ENDFOR
    ENDIF
370 ENDEXEC
    ENDMODEL

```

Listing A.6: EMTP Models code for reconstruction filter and quadrature mixer/upconverter (Fortran)

```

MODEL filter

comment
Author: Stephen Robson (robson.stephen@gmail.com).
5 This model represents a reconstruction filter and
quadrature mixer. To see the input and output, plot
the input to the model (im, or re) alongside the
output of the model (JUMP). Otherwise, set jump to
equal sig. The carrier frequency is 440 kHz. In this
10 case, if the bandwidth of the OFDM baseband signal
is 100kHz, the quadrature mixer shifts the signal up
to sit between 390 kHz - 490 kHz. The only explanation
for this is that the baseband signal contains negative
frequencies!
15 endcomment

INPUT A, B
    OUTPUT JUMP
20 VAR ar, br, JUMP, sig, h, p, q
    HISTORY br {dflt: t}
    A {dflt: t}
    B {dflt: t}
    ar {dflt: t}
25 INIT
    h:=timestep/2
    ENDINIT
    EXEC
    COMBINE AS po
30 zfun(br/A) := (0.0000954|z0 +0.0002863|z-1

```

```

+0.0002863|z-2
+0.0000954E-3|z-3)/(1|z0 -2.8116|z-1
+2.6405|z-2 -0.8281|z-3)
ENDCOMBINE
35 COMBINE AS po2
zfun(ar/B) := (0.0000954|z0 +0.0002863|z-1
+0.0002863|z-2
+0.0000954E-3|z-3)/(1|z0 -2.8116|z-1
+2.6405|z-2 -0.8281|z-3)
40 ENDCOMBINE
p:=br*sin(2*pi*T*460000)
q:=ar*cos(2*pi*T*460000)
sig:= p+q
JUMP:=100*sig
45 comment
set jump = br, or ar and plot im/re against jump
to see model smooths out the staircase like wave.
JUMP should be set to sig (p+q) to represent the
quadrature mixed output wave to send onto the channel.
50 Amplification can be set by making sig larger,
i.e., 100*sig.
endcomment

55 ENDEXEC
ENDMODEL

```

Listing A.7: Matlab code for Fault location algorithm and derivation of network derived R-values in two branch network

```

%Stephen Robson (robson.stephen@gmail.com)
%2 branch network fault location process

5 clear all
m=1700; %length of main branch
b1=700; %point at which the first branch begins
b2= 1300 %point at which second branch begins
lenb1=750; %length of the first branch
10 lenb2=400; %length of second branch
mm=m+lenb1;
mmm=mm+lenb2;

T1=0.00011332; %PA
15 T2=0.00014328; %PB
T3=0.00013496; %PC
T4=0.00014328; %PD

```

```

Tt1=T1+0.00000006; %PA
20 Tt2=T2-0.00000000; %PB
Tt3=T3+0.00000000; %PC
Tt4=T4-0.00000000; %PD

Ttt1=T1+0.00000012; %PA
25 Ttt2=T2+0.00000000; %PB
Ttt3=T3+0.00000000; %PC
Ttt4=T4-0.00000000; %PD

Tttt1=T1+0.00000018; %PA
30 Tttt2=T2+0.00000000; %PB
Tttt3= T3+0.00000000; %PC
Tttt4=T4-0.00000000; %PD

35 %-----

for i=1:m

    x(i)=abs(i);
40 end

for i = (m+1):mm
    x(i)=abs(b1+(i-m));
end
45

for i=(mm+1):mmm
    x(i)=abs(b2+(i-mm))
end

50 %-----

for i=1:m

    y(i)=abs(m-i);
55 end

for i = (m+1):mm
    y(i)=abs((m-b1)+(i-m));
end

60

for i=(mm+1):mmm
    y(i)=abs((m-b2)+(i-mm));
end

65 %-----

```

```

for i=1:m
    z(i)=lenb1+abs(b1-i);
70 end

for i = (m+1):mm
    z(i)=abs(lenb1-(i-m));
end
75

for i=(mm+1):mmm
    z(i)=abs(lenb1+(b2-b1)+i-mm);
end

80 %-----

for i=1:m
    z1(i)=lenb2+abs(b2-i);
85 end

for i = (mm+1):mmm
    z1(i)=abs(lenb2-(i-mm));
end

90

for i=(m+1):mm
    z1(i)=abs(lenb2+(b2-b1)+i-m);
end

95 %-----

f1=T1-T2;
f2=T1-T3;
f3=T1-T4;
100 f4=T2-T3;
f5=T2-T4;
f6=T3-T4;

e1=f1/f2;
105 e2=f1/f3;
e3=f1/f4;
e4=f2/f3;
e5=f2/f4;
e6=f3/f4;

110
ff1=Tt1-Tt2;
ff2=Tt1-Tt3;

```

```

ff3=Tt1-Tt4;
ff4=Tt2-Tt3;
115 ff5=Tt2-Tt4;
ff6=Tt3-Tt4;

fff1=Ttt1-Ttt2;
fff2=Ttt1-Ttt3;
120 fff3=Ttt1-Ttt4;
fff4=Ttt2-Ttt3;
fff5=Ttt2-Ttt4;
fff6=Ttt3-Ttt4;

125 ffff1=Tttt1-Tttt2;
ffff2=Tttt1-Tttt3;
ffff3=Tttt1-Tttt4;
ffff4=Tttt2-Tttt3;
ffff5=Tttt2-Tttt4;
130 ffff6=Tttt3-Tttt4;

ee1=ff1/ff2;
ee2=ff1/ff3;
ee3=ff1/ff4;
135 ee4=ff2/ff3;
ee5=ff2/ff4;
ee6=ff3/ff4;

fff1=Ttt1-Ttt2;
140 fff2=Ttt1-Ttt3;
fff3=Ttt1-Ttt4;
fff4=Ttt2-Ttt3;
fff5=Ttt2-Ttt4;
fff6=Ttt3-Ttt4;

145 eee1=fff1/fff2;
eee2=fff1/fff3;
eee3=fff1/fff4;
eee4=fff2/fff3;
150 eee5=fff2/fff4;
eee6=fff3/fff4;

ffff1=Tttt1-Tttt2;
ffff2=Tttt1-Tttt3;
155 ffff3=Tttt1-Tttt4;
ffff4=Tttt2-Tttt3;
ffff5=Tttt2-Tttt4;
ffff6=Tttt3-Tttt4;

```

```

160 eeee1=ffff1/ffff2;
    eeee2=ffff1/ffff3;
    eeee3=ffff1/ffff4;
    eeee4=ffff2/ffff3;
    eeee5=ffff2/ffff4;
165 eeee6=ffff3/ffff4;

    s1=x-y;
    s2=x-z;
    s3=x-z1;
170 s4=y-z;
    s5=y-z1;
    s6=z-z1;

    d1=s1./s2;
175 d2=s1./s3;
    d3=s1./s4;
    d4=s2./s3;
    d5=s2./s4;
    d6=s3./s4;

180 figure (1)
    subplot (6,1,1)
    plot (d1)
    ylabel ('R12')
185 subplot (6,1,2)
    plot (d2)
    ylabel ('R13')
    subplot (6,1,3)
    plot (d3)
190 ylabel ('R14')
    subplot (6,1,4)
    plot (d4)
    ylabel ('R23')
    subplot (6,1,5)
195 plot (d5)
    ylabel ('R24')
    subplot (6,1,6)
    plot (d6)
    ylabel ('R34')
200 xlabel ('Position Index')

figure (2)
for h=1:mmm
ra(h)=((e1-d1(h)))^2 + ((e2-d2(h)))^2 + ...
205      ((e3-d3(h)))^2 ...
+ ((e4-d4(h)))^2 + ((e5-d5(h)))^2 + ...

```

```

((e6-d6(h)))^2;
end
plot(ra)
210 hold on

for h=1:mmm
ra2(h)=((ee1-d1(h)))^2 + ((ee2-d2(h)))^2 ...
215 + ((ee3-d3(h)))^2 + ((ee4-d4(h)))^2 + ...
      ((ee5-d5(h)))^2 + ((ee6-d6(h)))^2;
end
plot(ra2)

220 for h=1:mmm
ra3(h)=((eee1-d1(h)))^2 + ((eee2-d2(h)))^2+...
      ((eee3-d3(h)))^2 ...
      + ((eee4-d4(h)))^2 + ((eee5-d5(h)))^2 +...
      ((eee6-d6(h)))^2;
225 end
plot(ra3)

for h=1:mmm
ra4(h)=((eeee1-d1(h)))^2 + ((eeee2-d2(h)))^2 +...
230      ((eeee3-d3(h)))^2 + ((eeee4-d4(h)))^2 + ...
      ((eeee5-d5(h)))^2 + ((eeee6-d6(h)))^2;
end
plot(ra4)

235 hold off

for p=1:1000
240      tn1=T1+0.00000001*randn(1);
      tn2=T2+0.00000001*randn(1);
      tn3=T3+0.00000001*randn(1);
      tn4=T4+0.00000001*randn(1);

245      fn1=tn1-tn2;
      fn2=tn1-tn3;
      fn3=tn1-tn4;
      fn4=tn2-tn3;
      fn5=tn2-tn4;
250      fn6=tn3-tn4;

      en1=fn1/fn2;
      en2=fn1/fn3;

```

```

en3=fn1/fn4;
255 en4=fn2/fn3;
en5=fn2/fn4;
en6=fn3/fn4;

260     for h=1:mmm
ran(h)=((en1-d1(h)))^2 + ((en2-d2(h)))^2 + ...
        ((en3-d3(h)))^2 + ((en4-d4(h)))^2 +...
        ((en5-d5(h)))^2 + ((en6-d6(h)))^2;

265     end

        [v,c]=find(ran==min(min(ran)));
        xx(p)=c;
270     dd(p)=0.01*randn(1);
end

```

Listing A.8: Impulse Generation and Peak Detect Algorithm

```

%This m file generates a variety of impulses and
%implements the peak detect algorithm
clear all
5

%%%%%%%%%%%%%%%%%%%%%%%%%%%%%%%%%%%%%%%%%%%%%%%%%%%%%%%%%%%%%%%%%%%%%%%%

Fs=50000000;           %Sampling Frequency
10 T=1/Fs;
risetime1=0.000001; %risetime of gaussian pulse
risetime2=0.000001; %risetime of gaussian pulse 2

%%%%%%%%%%%%%%%%%%%%%%%%%%%%%%%%%%%%%%%%%%%%%%%%%%%%%%%%%%%%%%%%%%%%%%%%

15 [bb,aa]=butter(5,0.02);
longsignal1=zeros(1,5000000);
longsignal2=zeros(1,5000000);

%%%%%%%%%%%%%%%%%%%%%%%%%%%%%%%%%%%%%%%%%%%%%%%%%%%%%%%%%%%%%%%%%%%%%%%%

20 N=(risetime1*4)/(Fs*T);
signal=pulsegen(Fs,N,1,'gaussian');

for p=1:1:500 %Optional loop to test influence of noise

25 sig=[longsignal1 signal longsignal2];
%construct long signal

```

```

% nt = 0.06950*randn(1,prod(size(sig))); %15db
nt = 0.1*randn(1,prod(size(sig))); %10db
30 % nt = 0.12950*randn(1,prod(size(sig))); %5db

sig2=sig+nt;

tslow=0:(1/Fs):(1/Fs)*(length(sig)-1);
35 tslowdiff=0:(1/Fs):(1/Fs)*(length(sig)-2);

g=diff(sig2);
g2=diff(sig);
afterdec=filter(bb,aa,sig2);
40 g3=diff(afterdec);

slide_length=length(afterdec)-5;

%Peak detect algorithm
45 for n=1:slide_length
    if (g3(n)<0.001) && (g3(n)>-0.001) && ...
        (afterdec(n)>0.4)
        if afterdec(n)>afterdec(n-1)
            f(p)=n;
50         end
        end
    end
end
end
55

%%%%%%%%%%%%%%%%%%%%%%%%%%%%%%%%%%%%%%%%%%%%%%%%%%%%%%%%%%%%%%%%%%%%%%%%

N2=(risetime2*4)/(Fs*T);

60 signalfast=pulsegen(Fs,N2,1,'gaussian');
sigfast=[longsignal1 signalfast longsignal2];

for p = 1:1:500 %Optional loop to test influence of noise
65

%ntfast = 0.06950*randn(1,prod(size(sigfast))); %15db
%ntfast = 0.1*randn(1,prod(size(sigfast))); %10db
70 ntfast = 0.12950*randn(1,prod(size(sigfast))); %5db

sig2fast=sigfast+ntfast;

tfast=0:(1/Fs):(1/Fs)*(length(sigfast)-1);

```

```

75 gfast=diff(sig2fast);

[bb,aa]=butter(5,0.15); %works with 200khz
afterdecfast=filter(bb,aa,sig2fast);

80
g3fast=diff(afterdecfast);
slide_length=length(afterdecfast)-5;

%Peak detect algorithm
85 for n=1:slide_length
    if (g3fast(n)<0.5) && (g3fast(n)>-0.5) &&...
        (afterdecfast(n)>0.4)
        if afterdecfast(n)>afterdecfast(n-1)
            f(p)=n;
90         end
    end
end

end

95

%%%%%%%%%%%%%%%%%%%%%%%%%%%%%%%%%%%%%%%%%%%%%%%%%%%%%%%%%%%%%%%%%%%%%%%%%%
%%%%%%%%%%%%%%%%%%%%%%%%%%%%%%%%%%%%%%%%%%%%%%%%%%%%%%%%%%%%%%%%%%%%%%%%%%SINC%%%%%%%%%%%%%%%%%%%%%%%%%%%%%%%%%%%%%%%%%%%%%%%%%%%%%%%%%%%%%%%%%%%%%%%%%%

100 for p = 1:1:500

sinc=pulsegen(Fs,N,1,'sinc');
sig sinc=[longsignal1 sinc longsignal2];

105 %ntsinc = 0.06950*randn(1,prod(size(sig sinc)));%15db
%ntsinc = 0.1*randn(1,prod(size(sig sinc))); %10db
ntsinc = 0.12950*randn(1,prod(size(sig sinc))); %5db

110 sincnoise=sig sinc+ntsinc;
afterdecsinc=filter(bb,aa,sincnoise);

tsinc=0:(1/Fs):(1/Fs)*(length(sig sinc)-1);

115 gsinc=diff(afterdecsinc);

slide_length=length(afterdecsinc)-5;

%Peak detect algorithm
120 for n=2:slide_length
    if (gsinc(n)<0.1) && (gsinc(n)>-0.1)...

```

```

        && (afterdecsinc(n)>0.6)
        if afterdecsinc(n)>afterdecsinc(n-1)
f(p)=n;
125     end
        end
    end
end
130
% %%%%%%%%%%%%%%%Lightning%%%%%%%%%%%%%%
% %%%%%%%%%%%%%%%Impulse%%%%%%%%%%%%%%

% alpha=0.0146; % 1.2/50
135 % beta=2.467; %1.2/50
% Vo=1.04; %1.2/50

alpha=0.0535; % 2/20
beta=0.113; %2/20
140 Vo=4.01; %2/20
Simtime=500; %in microseconds

step=(1/Fs)/(0.000001);
t=0:step:Simtime;
145 t2=0:(1/Fs):Simtime*10^-6;

V1=Vo*(exp(alpha*t));
V2=Vo*(exp(-beta*t));

150 V3=Vo*(exp(-alpha*t)-exp(-beta*t));
siglightning=[longsignal1 V3 longsignal2];

for p = 1:1:200

155 %nt2 = 0.06950*randn(1,prod(size(siglightning)));%15db
%nt2 = 0.1*randn(1,prod(size(siglightning))); %10db
nt2 = 0.12950*randn(1,prod(size(siglightning))); %5db

siglightningnoise=siglightning+nt2;
160 afterdec2=filter(bb,aa,siglightningnoise);

g4=diff(afterdec2);

165 slide_length=length(afterdec2)-5;

%Peak detect algorithm
for n=3:slide_length

```

```

170     if (g4(n)<0.1) && (g4(n)>-0.1) && (afterdec2(n)>0.6)
        if afterdec2(n)>afterdec2(n-1)
            f(p)=n;
        end
    end
end
175 end
end

```

Listing A.9: Matlab code for Fault location algorithm and derivation of network derived R-values in one branch network

```

%Stephen Robson (robson.stephen@gmail.com)

5 clear all
m=1700+(200); %length of main branch (plus cable correction)
b1=700+(200); %point at which the second branch begins
lenb1=750; %length of the second branch
mm=m+lenb1;

10 %130
%T1=0.00024328; %PA
%T2=0.00021332; %PB
%T3=0.00024494; %PC
15 %%%%%%%%%%%%%%%%%%%%%%%%%%%%%%%%%%%%%%%%%%%%%%%%%%%%%%%%%%%%%%%%%%%%%%%%%

T1=0.0002506; %Measured timestamps
T2=0.0002134;
T3=0.0002452;

20

Tt1=T1; %PA
Tt2=T2; %PB
Tt3=T3; %PC

25

Ttt1=T1; %PA
Ttt2=T2; %PB
Ttt3=T3; %PC

30

for i=1:m

35     x(i)=abs(i);
end

```

```

40 for i = (m+1):mm
        x(i)=abs(b1+(i-m));
end

45 for i=1:m
        y(i)=abs(m-i);
end

50 for i = (m+1):mm
        y(i)=abs((m-b1)+(i-m));
end

55 for i=1:m
        z(i)=lenb1+abs(b1-i);
end

60 for i = (m+1):mm
        z(i)=abs(lenb1-(i-m));
end

f1=T1-T2;
f2=T1-T3;
f3=T2-T3;

65 e1=f1/f2;
    e2=f1/f3;
    e3=f2/f3;

70 ff1=Tt1-Tt2;
    ff2=Tt1-Tt3;
    ff3=Tt2-Tt3;

75 ee1=ff1/ff2;
    ee2=ff1/ff3;
    ee3=ff2/ff3;

80 fff1=Ttt1-Ttt2;
    fff2=Ttt1-Ttt3;
    fff3=Ttt2-Ttt3;

eee1=fff1/fff2;

```

```

eee2=fff1/fff3;
85 eee3=fff2/fff3;

s1=x-y;
s2=x-z;
90 s3=y-z;
d1=s1./s2;
d2=s1./s3;
d3=s2./s3;

95 figure(1)
subplot(3,1,1)
plot(d1)
xlabel('Position Index')
ylabel('R Ratio (X)')
100 subplot(3,1,2)
plot(d2)
xlabel('Position Index')
ylabel('R Ratio (Y)')
subplot(3,1,3)
105 plot(d3)
xlabel('Position Index')
ylabel('R Ratio (Z)')

h=0;
110

%for n=1:2;

115
for p=1:1000
    tn1=T1+0.000000020*randn(1);
    tn2=T2+0.000000000*randn(1);
    tn3=T3+0.000000000*randn(1);
120

    fn1=tn1-tn2;
    fn2=tn1-tn3;
    fn3=tn2-tn3;
125

en1=fn1/fn2;
en2=fn1/fn3;
en3=fn2/fn3;
130

```

```

    for h=1:mm
ran(h)=((en1-d1(h)))^2 + ((en2-d2(h)))^2 ...
+ ((en3-d3(h)))^2;
135

    end
    [v,c]=find(ran==min(min(ran)));
    if c>1500
140         c=1300;
    end
    xx(p)=c;

end
145
figure(2)
for h=1:mm
ra(h)=((e1-d1(h)))^2 + ((e2-d2(h)))^2 ...
+ ((e3-d3(h)))^2;
150 end
plot(ra)

hold on

155 for h=1:mm
ra2(h)=((ee1-d1(h)))^2 + ((ee2-d2(h)))^2 ...
+ ((ee3-d3(h)))^2;
end
%plot(ra2)
160
for h=1:mm
ra3(h)=((eee1-d1(h)))^2 + ((eee2-d2(h)))^2 ...
+ ((eee3-d3(h)))^2;
end
165 %plot(ra3)

hold off

```

Total logic elements	25,878 / 114,480 ( 23 % )	
Logic element usage by number of LUT inputs		
-- 4 input functions		4374
-- 3 input functions		10658
-- <=2 input functions		4310
register only		6536
Logic elements by mode		
normal mode		10536
arithmetic mode		8806
Total registers*	19,942 / 117,053 ( 17 % )	
Dedicated logic registers	19,823 / 114,480 ( 17 % )	
I/O registers	119 / 2,573 ( 5 % )	
Total LABs: partially or completely used	1,859 / 7,155 ( 26 % )	
User inserted logic elements		0
Virtual pins		0
I/O pins	168 / 529 ( 32 % )	
Clock pins	4 / 7 ( 57 % )	
Dedicated input pins	3 / 9 ( 33 % )	
Global signals		11
M9Ks	69 / 432 ( 16 % )	
Total block memory bits	174,496 / 3,981,312 ( 4 % )	
Total block memory implementation bits	635,904 / 3,981,312 ( 16 % )	
Embedded Multiplier 9-bit elements	46 / 532 ( 9 % )	
PLLs	2 / 4 ( 50 % )	
Global clocks	11 / 20 ( 55 % )	
JTAGs	1 / 1 ( 100 % )	
CRC blocks	0 / 1 ( 0 % )	
ASMI blocks	0 / 1 ( 0 % )	
Impedance control blocks	0 / 4 ( 0 % )	
Average interconnect usage (total/H/V)	10% / 9% / 10%	
Peak interconnect usage (total/H/V)	50% / 51% / 49%	
Maximum fan-out node		
Maximum fan-out		12702
Highest non-global fan-out signal		
Highest non-global fan-out		3023
Total fan-out		127330
Average fan-out		2.88

Figure A.1: Resources used in the OHMS Receiver FPGA

## Appendix B

### Resource Usage

Total logic elements	17,229 / 18,752 ( 92 % )	
Combinational with no register		2880
register only		3430
Combinational with a register		10919
Logic element usage by number of LUT inputs		
-- 4 input functions		3863
-- 3 input functions		7126
-- <=2 input functions		2810
register only		3430
Logic elements by mode		
normal mode		8131
arithmetic mode		5668
Total registers*	14,462 / 19,649 ( 74 % )	
Dedicated logic registers	14,349 / 18,752 ( 77 % )	
I/O registers	113 / 897 ( 13 % )	
Total LABs: partially or completely used	1,170 / 1,172 ( 100 % )	
User inserted logic elements		0
Virtual pins		0
I/O pins	175 / 315 ( 56 % )	
Clock pins	3 / 8 ( 38 % )	
Global signals		16
M4Ks	49 / 52 ( 94 % )	
Total block memory bits	88,160 / 239,616 ( 37 % )	
Total block memory implementation bits	225,792 / 239,616 ( 94 % )	
Embedded Multiplier 9-bit elements	28 / 52 ( 54 % )	
PLLs	2 / 4 ( 50 % )	
Global clocks	16 / 16 ( 100 % )	
JTAGs	1 / 1 ( 100 % )	
ASMI blocks	0 / 1 ( 0 % )	
CRC blocks	0 / 1 ( 0 % )	
Average interconnect usage (total/H/V)	30% / 28% / 34%	
Peak interconnect usage (total/H/V)	46% / 45% / 47%	
Maximum fan-out node		
Maximum fan-out		8545
Highest non-global fan-out signal		
Highest non-global fan-out		3023
Total fan-out		90644
Average fan-out		2.93

Figure B.1: Resources used in the OHMS Transmitterr FPGA

Total logic elements	25,878 / 114,480 ( 23 % )	
Logic element usage by number of LUT inputs		
-- 4 input functions		4374
-- 3 input functions		10658
-- <=2 input functions		4310
register only		6536
Logic elements by mode		
normal mode		10536
arithmetic mode		8806
Total registers*	19,942 / 117,053 ( 17 % )	
Dedicated logic registers	19,823 / 114,480 ( 17 % )	
I/O registers	119 / 2,573 ( 5 % )	
Total LABs: partially or completely used	1,859 / 7,155 ( 26 % )	
User inserted logic elements		0
Virtual pins		0
I/O pins	168 / 529 ( 32 % )	
Clock pins	4 / 7 ( 57 % )	
Dedicated input pins	3 / 9 ( 33 % )	
Global signals		11
M9Ks	69 / 432 ( 16 % )	
Total block memory bits	174,496 / 3,981,312 ( 4 % )	
Total block memory implementation bits	635,904 / 3,981,312 ( 16 % )	
Embedded Multiplier 9-bit elements	46 / 532 ( 9 % )	
PLLs	2 / 4 ( 50 % )	
Global clocks	11 / 20 ( 55 % )	
JTAGs	1 / 1 ( 100 % )	
CRC blocks	0 / 1 ( 0 % )	
ASMI blocks	0 / 1 ( 0 % )	
Impedance control blocks	0 / 4 ( 0 % )	
Average interconnect usage (total/H/V)	10% / 9% / 10%	
Peak interconnect usage (total/H/V)	50% / 51% / 49%	
Maximum fan-out node		
Maximum fan-out		12702
Highest non-global fan-out signal		
Highest non-global fan-out		3023
Total fan-out		127330
Average fan-out		2.88

Figure B.2: Resources used in the OHMS Receiver FPGA

<b>OHMS Transmitter</b>	
Cyclone 2 FPGA	£100
14 Bit Dual Channel ADC/DAC	£200
M12M GPS Timing Module and Patch Antenna	£60
Fibox Enclosure	£90
Power Amplifier Board	£15
Potective Circuitry	£15
Battery Power Supply	£40
Coupling Capacitor	£800
Rogowski Coil (custom made)	£40
<b>Total</b>	<b>£1,360</b>
<b>OHMS Receiver</b>	
Cyclone 4 FPGA	£140
14 Bit Dual Channel ADC/DAC	£200
Fibox Enclosure	£90
Potective Circuitry	£15
Battery Power Supply	£40
Coupling Capacitor	£800
Bluetooth Wireless Bridge	£40
<b>Total</b>	<b>£1,325</b>

Figure B.3: Illustrative cost breakdown of the OHMS Transmitter and Receiver

## Appendix C

### Contents of the Accompanying CD

- C.1: Cyclic Prefix Code
- C.2: C++ code for OHMS Transmitter Embedded Processor
- C.3: C++ code for OHMS Receiver Embedded Processor
- C.4: Selectime Module (Part of the Timing Estimator Module)
- C.5: Whentostart Module (Part of the Timing Estimator Module)
- C.6: Demapper Logic and Cordic Algorithm
- C.7: Matlab Software for Calculating R-ratios and Fault Estimates on Example Network

## References

- [1] J. Carroll, "Vulnerability assessment of the us transportation infrastructure that relies on the global positioning system," *Journal of Navigation*, vol. 56, no. 2, pp. 185–194, 2003.
- [2] "Ieee standard profile for use of ieee 1588 precision time protocol in power system applications," *IEEE Std C37.238-2011*, pp. 1 –66, 14 2011.
- [3] X. Meng, P. Zerfos, V. Samanta, S. Wong, and S. Lu, "Analysis of the reliability of a nationwide short message service," in *INFOCOM 2007. 26th IEEE International Conference on Computer Communications. IEEE*, pp. 1811 –1819, may 2007.
- [4] M. Judd, L. Yang, and I. Hunter, "Partial discharge monitoring of power transformers using uhf sensors. part i: sensors and signal interpretation," *Electrical Insulation Magazine, IEEE*, vol. 21, pp. 5 –14, March-April 2005.
- [5] M. Judd, L. Yang, and I. Hunter, "Partial discharge monitoring for power transformer using uhf sensors. part 2: field experience," *Electrical Insulation Magazine, IEEE*, vol. 21, pp. 5 –13, May-June 2005.
- [6] P. Taylor, "The use of global positioning satellites in the location of lightning storms as used by the met office's arrival time difference sferics detection system," in *Developments in the Use of Global Positioning Systems*, pp. 3/1 –3/5, Feb 1994.
- [7] J. Burnett, R.O., M. Butts, and P. Sterlina, "Power system applications for phasor measurement units," *Computer Applications in Power, IEEE*, vol. 7, pp. 8 –13, Jan. 1994.
- [8] P. M. Ashton, G. A. Taylor, P. M. Ashton, A. M. Carter, and H. Renner, "Opportunities to exploit phasor measurement units (pmus) and synchrophasor measurements on the gb transmission network," *Universities' Power Engineering Conference (UPEC), Proceedings of 2011 46th International*, pp. 1 –6, Sept. 2011.
- [9] "Ieee standard for scada and automation systems," *IEEE Std C37.1-2007 (Revision of IEEE Std C37.1-1994)*, pp. 1 –143, 8 2008.
- [10] M. Childers and M. Borrielli, "Iec61850 substation experiences dpsp 2012," in *Developments in Power Systems Protection, 2012. DPSP 2012. 11th International Conference on*, pp. 1 –5, April 2012.
- [11] A. Wilson, "The use of gprs technology for electricity network telecontrol," *Computing Control Engineering Journal*, vol. 16, pp. 40 –45, April-May 2005.

- [12] N. Sadanandan and A. Eltom, "Power donut system laboratory test and data analysis," in *Southeastcon '90. Proceedings., IEEE*, pp. 675 –679 vol.2, Apr 1990.
- [13] Y.-C. Wu, L.-F. Cheung, K.-S. Lui, and P. W. T. Pong, "Efficient communication of sensors monitoring overhead transmission lines," *Smart Grid, IEEE Transactions on*, vol. 3, pp. 1130 –1136, Sept. 2012.
- [14] C. A. Boddie and R. C. Curtis, "The transmission of high-frequency currents for communication over existing power networks," *American Institute of Electrical Engineers, Transactions of the*, vol. 48, pp. 227 –235, Jan. 1929.
- [15] C. Boddie, "Telephone communication over power lines by high frequency currents," *Proceedings of the Institute of Radio Engineers*, vol. 15, pp. 559 – 640, July 1927.
- [16] M. J. Brown, "Power-line carrier channels," *American Institute of Electrical Engineers, Transactions of the*, vol. 64, pp. 246 –251, May 1945.
- [17] G. W. Hampe and B. W. Storer, "Power-line carrier for relaying and joint usage; part ii. a survey of modern power-line carrier systems," *Power Apparatus and Systems, Part III. Transactions of the American Institute of Electrical Engineers*, vol. 71, pp. 661 –670, Jan. 1952.
- [18] D. E. Jones, "Staged fault tests with power-line carrier transferred-trip relaying for line protection," *Power Apparatus and Systems, Part III. Transactions of the American Institute of Electrical Engineers*, vol. 78, pp. 588 –593, April 1959.
- [19] W. Jones, "Amped up and ready to go [broadband over power lines]," *Spectrum, IEEE*, vol. 41, pp. 14 – 16, 18, Sept. 2004.
- [20] R. Bansai, "Broadband over power line: once more unto the breach," *Antennas and Propagation Magazine, IEEE*, vol. 46, pp. 88 – 89, June 2004.
- [21] F. J. S. Miravalles, "Opera 2: standardization of broadband plc," in *Power Line Communications and Its Applications, 2007. ISPLC '07. IEEE International Symposium on*, p. 11, March 2007.
- [22] G. Bmiller, "Evaluation and integrated diagnostic of high speed narrow band power-line chipset," in *Power Line Communications and Its Applications, 2005 International Symposium on*, pp. 371 – 375, april 2005.
- [23] A. Haidine, A. Portnoy, S. Mudriievskiyi, and R. Lehnert, "Dlc x002b;vit4ip project: High-speed nb-plc for smart grid communication x2014; design of field trial," in *Power Line Communications and Its Applications (ISPLC), 2012 16th IEEE International Symposium on*, pp. 88 –93, march 2012.

- [24] W. A. Lewis and L. S. Tippet, "Fundamental basis for distance relaying on 3-phase systems," *American Institute of Electrical Engineers, Transactions of the*, vol. 66, pp. 694 –709, Jan. 1947.
- [25] T. Takagi, Y. Yamakoshi, M. Yamaura, R. Kondow, and T. Matsushima, "Development of a new type fault locator using the one-terminal voltage and current data," *Power Apparatus and Systems, IEEE Transactions on*, vol. PAS-101, pp. 2892 –2898, Aug. 1982.
- [26] L. Eriksson, M. Saha, and G. Rockefeller, "An accurate fault locator with compensation for apparent reactance in the fault resistance resulting from remote-end infeed," *Power Apparatus and Systems, IEEE Transactions on*, vol. PAS-104, pp. 423 –436, Feb. 1985.
- [27] R. Salim, K. Salim, and A. Bretas, "Further improvements on impedance-based fault location for power distribution systems," *Generation, Transmission Distribution, IET*, vol. 5, pp. 467 –478, April 2011.
- [28] R. Das, M. Sachdev, and T. Sidhu, "A fault locator for radial subtransmission and distribution lines," in *Power Engineering Society Summer Meeting, 2000. IEEE*, vol. 1, pp. 443 –448 vol. 1, 2000.
- [29] P. Crossley and P. McLaren, "Distance protection based on travelling waves," *Power Apparatus and Systems, IEEE Transactions on*, vol. PAS-102, pp. 2971 –2983, sept. 1983.
- [30] P. Gale, P. Crossley, X. Bingyin, G. Yaozhong, B. Cory, and J. Barker, "Fault location based on travelling waves," in *Developments in Power System Protection, 1993., Fifth International Conference on*, pp. 54 –59, 1993.
- [31] Z. Bo, G. Weller, and M. Redfern, "Accurate fault location technique for distribution system using fault-generated high-frequency transient voltage signals," *Generation, Transmission and Distribution, IEE Proceedings-*, vol. 146, pp. 73 –79, jan 1999.
- [32] D. Spoor and J. G. Zhu, "Improved single-ended traveling-wave fault-location algorithm based on experience with conventional substation transducers," *Power Delivery, IEEE Transactions on*, vol. 21, pp. 1714 –1720, July 2006.
- [33] F. Magnago and A. Abur, "Fault location using wavelets," *Power Delivery, IEEE Transactions on*, vol. 13, pp. 1475 –1480, Oct 1998.
- [34] E. Styvaktakis, M. Bollen, and I. Gu, "A fault location technique using high frequency fault clearing transients," *Power Engineering Review, IEEE*, vol. 19, pp. 58 –60, May 1999.
- [35] P. Crossley, M. Davidson, and P. Gale, "Fault location using travelling waves," in *Instrumentation in the Electrical Supply Industry, IEE Colloquium on*, pp. 6/1 –6/3, Jun 1993.

- [36] C. Evrenosoglu and A. Abur, "Travelling wave based fault location for teed circuits," *Power Delivery, IEEE Transactions on*, vol. 20, pp. 1115 – 1121, April 2005.
- [37] A. Borghetti, M. Bosetti, C. Nucci, M. Paolone, and A. Abur, "Integrated use of time-frequency wavelet decompositions for fault location in distribution networks: Theory and experimental validation," *Power Delivery, IEEE Transactions on*, vol. 25, pp. 3139 –3146, Oct. 2010.
- [38] Y.-Y. Hsu, F.-C. Lu, Y. Chien, J. Liu, J. Lin, P. Yu, and R. Kuo, "An expert system for locating distribution system faults," *Power Delivery, IEEE Transactions on*, vol. 6, pp. 366 –372, Jan 1991.
- [39] F. Eickhoff, E. Handschin, and W. Hoffmann, "Knowledge based alarm handling and fault location in distribution networks," *Power Systems, IEEE Transactions on*, vol. 7, pp. 770 –776, May 1992.
- [40] B. Von Herzen, "Signal processing at 250 mhz using high-performance fpga's," *Very Large Scale Integration (VLSI) Systems, IEEE Transactions on*, vol. 6, pp. 238 –246, June 1998.
- [41] J. de Jesus Rangel-Magdaleno, R. de Jesus Romero-Troncoso, R. Osornio-Rios, E. Cabal-Yepez, and A. Dominguez-Gonzalez, "Fpga-based vibration analyzer for continuous cnc machinery monitoring with fused fft-dwt signal processing," *Instrumentation and Measurement, IEEE Transactions on*, vol. 59, pp. 3184 –3194, Dec. 2010.
- [42] A. Schmidt, H. Gemmeke, A. Haungs, K.-H. Kampert, C. Ruhle, and Z. Szadkowski, "Fpga based signal-processing for radio detection of cosmic rays," *Nuclear Science, IEEE Transactions on*, vol. 58, pp. 1621 –1627, Aug. 2011.
- [43] W. Liu, H. Widmer, and P. Raffin, "Broadband plc access systems and field deployment in european power line networks," *Communications Magazine, IEEE*, vol. 41, pp. 114 – 118, May 2003.
- [44] M. Perz, "Natural modes of power line carrier on horizontal three-phase lines," *Power Apparatus and Systems, IEEE Transactions on*, vol. 83, pp. 679 –686, July 1964.
- [45] L. Wedepohl and S. Mohamed, "Multiconductor transmission lines. theory of natural modes and fourier integral applied to transient analysis," *Electrical Engineers, Proceedings of the Institution of*, vol. 116, pp. 1553 –1563, September 1969.
- [46] H. Dommel, *EMTP Theory Book*. Microtran Power System Analysis Corporation, 1996.
- [47] J. R. Carson, "Wave propagation in overhead wires with ground return," vol. 5, pp. 539–554, Oct. 1926.

- [48] G. Bridges, "Definition of the high frequency characteristic impedance of an overhead conductor," *Electronics Letters*, vol. 26, pp. 2079 –2081, dec. 1990.
- [49] A. Semlyen, "Ground return parameters of transmission lines an asymptotic analysis for very high frequencies," *Power Apparatus and Systems, IEEE Transactions on*, vol. PAS-100, pp. 1031 –1038, march 1981.
- [50] P. Amirshahi and M. Kavehrad, "High-frequency characteristics of overhead multiconductor power lines for broadband communications," *Selected Areas in Communications, IEEE Journal on*, vol. 24, pp. 1292 – 1303, july 2006.
- [51] P. Amirshahi and M. Kavehrad, "High-frequency characteristics of overhead multiconductor power lines for broadband communications," *Selected Areas in Communications, IEEE Journal on*, vol. 24, pp. 1292 – 1303, July 2006.
- [52] A. Fernandes and W. Neves, "Phase-domain transmission line models considering frequency-dependent transformation matrices," *Power Delivery, IEEE Transactions on*, vol. 19, pp. 708 – 714, April 2004.
- [53] R. C. Hemminger, L. J. Gale, and J. B. O'Neal, "Signal propagation on single phase power distribution lines at power line carrier frequencies," *Power Delivery, IEEE Transactions on*, vol. 2, pp. 28 –35, Jan. 1987.
- [54] T. Papadopoulos, G. Papagiannis, and P. Dokopoulos, "Low-voltage distribution line performance evaluation for plc signal transmission," *Power Delivery, IEEE Transactions on*, vol. 23, pp. 1903 –1910, Oct. 2008.
- [55] U. of Strathclyde, "United kingdom generic distribution system," poster, University of Strathclyde, June 2009.
- [56] R. C. Hemminger, L. J. Gale, F. Amoura, and J. B. O'Neal, "The effect of distribution transformers on distribution line carrier signals," *Power Delivery, IEEE Transactions on*, vol. 2, pp. 36 –40, Jan. 1987.
- [57] M. Tlich, A. Zeddani, F. Moulin, and F. Gauthier, "Indoor power-line communications channel characterization up to 100 mhz x2014;part ii: Time-frequency analysis," *Power Delivery, IEEE Transactions on*, vol. 23, pp. 1402 –1409, July 2008.
- [58] A. Cataliotti, D. Di Cara, R. Fiorelli, and G. Tine, "Power-line communication in medium-voltage system: Simulation model and onfield experimental tests," *Power Delivery, IEEE Transactions on*, vol. 27, pp. 62 –69, Jan. 2012.
- [59] S. Barmada, A. Musolino, and M. Raugi, "Innovative model for time-varying power line communication channel response evaluation," *Selected Areas in Communications, IEEE Journal on*, vol. 24, pp. 1317 – 1326, July 2006.

- [60] J. Anatory, N. Theethayi, and R. Thottappillil, "Power-line communication channel model for interconnected networks x2014;part ii: Multiconductor system," *Power Delivery, IEEE Transactions on*, vol. 24, pp. 124–128, Jan. 2009.
- [61] M. Zimmermann and K. Dostert, "A multipath model for the powerline channel," *Communications, IEEE Transactions on*, vol. 50, pp. 553–559, Apr 2002.
- [62] C. Shannon, "Communication in the presence of noise," *Proceedings of the IRE*, vol. 37, pp. 10–21, Jan. 1949.
- [63] Z. Tao, Y. Xiaoxian, Z. Baohui, C. Jian, Y. Zhi, and T. Zhihong, "Research of noise characteristics for 10-kv medium-voltage power lines," *Power Delivery, IEEE Transactions on*, vol. 22, pp. 142–150, Jan. 2007.
- [64] Z. Tao, Y. Xiaoxian, Z. Baohui, N. Xu, F. Xiaoqun, and L. Changxin, "Statistical analysis and modeling of noise on 10-kv medium-voltage power lines," *Power Delivery, IEEE Transactions on*, vol. 22, pp. 1433–1439, July 2007.
- [65] M. Lei, P. Zhang, H. Harada, and H. Wakana, "An adaptive power distribution algorithm for improving spectral efficiency in ofdm," *Broadcasting, IEEE Transactions on*, vol. 50, pp. 347–351, Sept. 2004.
- [66] L. Hanzó, W. Webb, and T. Keller, *Single- and multi-carrier quadrature amplitude modulation: principles and applications for personal communications, WLANs and broadcasting*. John Wiley & Sons, 2000.
- [67] R. W. Chang, "Synthesis of Band-Limited Orthogonal Signals for Multichannel Data Transmission," *Bell Systems Technical Journal*, vol. 45, pp. 1775–1796, Dec. 1966.
- [68] S. Weinstein and P. Ebert, "Data transmission by frequency-division multiplexing using the discrete fourier transform," *Communication Technology, IEEE Transactions on*, vol. 19, pp. 628–634, October 1971.
- [69] I. Weber, W., "Differential encoding for multiple amplitude and phase shift keying systems," *Communications, IEEE Transactions on*, vol. 26, pp. 385–391, Mar 1978.
- [70] Y. Mostofi and D. Cox, "Mathematical analysis of the impact of timing synchronization errors on the performance of an ofdm system," *Communications, IEEE Transactions on*, vol. 54, pp. 226–230, Feb. 2006.
- [71] T. Schmidl and D. Cox, "Robust frequency and timing synchronization for ofdm," *Communications, IEEE Transactions on*, vol. 45, pp. 1613–1621, Dec 1997.
- [72] J. Cavers, *Mobile Channel Characteristics*. Kluwer international series in engineering and computer science, Kluwer Academic, 2000.

- [73] T.-C. Yu and J. Marti, "A robust phase-coordinates frequency-dependent underground cable model (zcable) for the emtp," *Power Delivery, IEEE Transactions on*, vol. 18, pp. 189 – 194, Jan 2003.
- [74] L. Hanzó, W. Webb, and T. Keller, *Single- and multi-carrier quadrature amplitude modulation: principles and applications for personal communications, WLANs and broadcasting*. John Wiley & Sons, 2000.
- [75] H. Hizman, P. Crossley, P. Gale, and G. Bryson, "Fault section identification and location on a distribution feeder using travelling waves," in *Power Engineering Society Summer Meeting, 2002 IEEE*, vol. 3, pp. 1107 –1112 vol.3, july 2002.
- [76] M. Korkali, H. Lev-Ari, and A. Abur, "Traveling-wave-based fault-location technique for transmission grids via wide-area synchronized voltage measurements," *Power Systems, IEEE Transactions on*, vol. 27, pp. 1003 –1011, may 2012.
- [77] C. Evrenosoglu and A. Abur, "Travelling wave based fault location for teed circuits," *Power Delivery, IEEE Transactions on*, vol. 20, pp. 1115 – 1121, april 2005.
- [78] V. Levi, G. Strbac, and R. Allan, "Assessment of performance-driven investment strategies of distribution systems using reference networks," *Generation, Transmission and Distribution, IEE Proceedings-*, vol. 152, pp. 1 –10, Jan. 2005.
- [79] F. Li, D. Tolley, N. Padhy, and J. Wang, "Framework for assessing the economic efficiencies of long-run network pricing models," *Power Systems, IEEE Transactions on*, vol. 24, pp. 1641 –1648, Nov. 2009.
- [80] R. Salim, K. Salim, and A. Bretas, "Further improvements on impedance-based fault location for power distribution systems," *Generation, Transmission Distribution, IET*, vol. 5, pp. 467 –478, April 2011.
- [81] A. Girgis, C. Fallon, and D. Lubkeman, "A fault location technique for rural distribution feeders," *Industry Applications, IEEE Transactions on*, vol. 29, pp. 1170 –1175, Nov/Dec 1993.
- [82] C. Evrenosoglu and A. Abur, "Travelling wave based fault location for teed circuits," *Power Delivery, IEEE Transactions on*, vol. 20, pp. 1115 – 1121, April 2005.
- [83] P. Jafarian and M. Sanaye-Pasand, "A traveling-wave-based protection technique using wavelet/pca analysis," *Power Delivery, IEEE Transactions on*, vol. 25, pp. 588 –599, April 2010.
- [84] S. Ebron, D. Lubkeman, and M. White, "A neural network approach to the detection of incipient faults on power distribution feeders," *Power Delivery, IEEE Transactions on*, vol. 5, pp. 905 –914, Apr 1990.

- [85] L. Wedepohl, "Application of matrix methods to the solution of travelling-wave phenomena in polyphase systems," *Electrical Engineers, Proceedings of the Institution of*, vol. 110, pp. 2200 –2212, December 1963.
- [86] B. Oyegoke, P. Hyvonen, M. Aro, and N. Gao, "Application of dielectric response measurement on power cable systems," *Dielectrics and Electrical Insulation, IEEE Transactions on*, vol. 10, pp. 862 – 873, Oct. 2003.
- [87] Z. Bo, G. Weller, and M. Redfern, "Accurate fault location technique for distribution system using fault-generated high-frequency transient voltage signals," *Generation, Transmission and Distribution, IEE Proceedings-*, vol. 146, pp. 73 –79, Jan 1999.
- [88] Motorola, "i-lotus m12m oncore gps receiver user guide," data sheet, Motorola, June 2006.
- [89] L. Marti, "Simulation of transients in underground cables with frequency-dependent modal transformation matrices," *Power Delivery, IEEE Transactions on*, vol. 3, pp. 1099 –1110, Jul 1988.
- [90] D. Coggins, D. Thomas, B. Hayes-Gill, Y. Zhu, E. Pereira, and S. Cabral, "Initial experiences with a new fpga based traveling wave fault recorder installed on a mv distribution network," in *Power System Technology and IEEE Power India Conference, 2008. POWERCON 2008. Joint International Conference on*, pp. 1 –8, Oct. 2008.
- [91] "Ieee standard for synchrophasor data transfer for power systems," *IEEE Std C37.118.2-2011 (Revision of IEEE Std C37.118-2005)*, pp. 1 –53, 28 2011.
- [92] J. E. Volder, "The cordic trigonometric computing technique," *Electronic Computers, IRE Transactions on*, vol. EC-8, pp. 330 –334, Sept. 1959.
- [93] "Ieee standard for telecommunications and information exchange between systems - lan/man - specific requirements - part 15: Wireless medium access control (mac) and physical layer (phy) specifications for wireless personal area networks (wpans)," *IEEE Std 802.15.1-2002*, pp. 1 –473, 14 2002.
- [94] P. Zhang, F. Li, and N. Bhatt, "Next-generation monitoring, analysis, and control for the future smart control center," *Smart Grid, IEEE Transactions on*, vol. 1, pp. 186 –192, Sept. 2010.
- [95] I. Texas Instruments, "1.5a, 24v, 17mhz power operational amplifier," data sheet, Texas Instruments Inc., January 2011.
- [96] L. T. Berger and G. Moreno-Rodrguez, "Power line communication channel modelling through concatenated iir-filter elements," *JCM*, pp. 41–51, 2009.

- [97] C.-C. Liu, J. Jung, G. Heydt, V. Vittal, and A. Phadke, “The strategic power infrastructure defense (spid) system. a conceptual design,” *Control Systems, IEEE*, vol. 20, pp. 40 –52, Aug. 2000.
- [98] “Ieee standard for a precision clock synchronization protocol for networked measurement and control systems,” *IEEE Std 1588-2002*, pp. i –144, 2002.
- [99] F. Sivrikaya and B. Yener, “Time synchronization in sensor networks: a survey,” *Network, IEEE*, vol. 18, pp. 45 – 50, July-Aug. 2004.